

High-Resolution Study of the ${}^4\text{He}(e, e'p)$ Reaction in
the Quasielastic Region

Alexander A. Kozlov

M.Sc., Kharkov State University (1992)

Submitted in total fulfilment of the requirements of the degree of
Doctor of Philosophy

School of Physics

The University of Melbourne

Victoria 3010

Australia

June 10, 2000

Abstract

A high-resolution study of the $(e, e'p)$ reaction on ${}^4\text{He}$ was carried out at the Institut für Kernphysik in Mainz, Germany. The high quality 100 % duty factor electron beam, and the high-resolution three-spectrometer-system of the A1 collaboration were used. The measurements were done in parallel kinematics at a central momentum transfer $|\vec{q}| = 685 \text{ MeV}/c$, and at a central energy transfer $\omega = 334 \text{ MeV}$, corresponding to a value of the y -scaling variable of $+140 \text{ MeV}/c$. In order to enable the Rosenbluth separation of the longitudinal σ_L and transverse σ_T response functions (as defined in [13]), three measurements at different incident beam energies, corresponding to three values of the virtual photon polarization ϵ , were performed. The absolute $(e, e'p)$ cross section for ${}^4\text{He}$ was obtained as a function of missing energy and missing momentum. A distorted spectral functions and momentum distributions were extracted from the data, using the *cc1* prescription for the elementary off-shell $e - p$ cross section (see ref. [14]).

For the two-body breakup channel the experimental results were compared to the theoretical calculations performed by Schiavilla *et al.* [45] and Forest *et al.* [48], and to the earlier experimental momentum distributions measured at NIKHEF by van den Brand *et al.* [52] and the new results from MAMI by Florizone [23]. For the continuum channel, recent calculations for the ${}^4\text{He}$ spectral function by Efros *et al.* [55] were used to study discrepancies between the theory and the experimental results.

A Rosenbluth separation was performed for both the two-body breakup and for continuum channels. The ratio σ_L/σ_T was determined and compared with predictions. The measurements show no significant strength corresponding to the $(e, e'p)$ reaction channel for missing-energy values $E_m \geq 45 - 48 \text{ MeV}$.

This is to certify that

- (i) the thesis comprises only my original work,
- (ii) due acknowledgement has been made in the text to all other material used,
- (iii) the thesis is less than 100,000 words in length, exclusive of tables, bibliographies, appendices and footnotes.

Acknowledgements

I would like to thank first my supervisor, Dr. Maxwell Thompson, who provided me the opportunity to become a PhD student of his group. During the whole period of my work in Melbourne and overseas, he always helped me in my research, and was thoughtful about my private life.

I would like to thank also Prof. K. Nugent, the chairman of the School of Physics, University of Melbourne, for providing a financial support and help.

My special gratitude is for Prof. William Bertozzi and Prof. Thomas Walcher for providing the opportunity to study at Mainz University. I am deeply indebted to Prof. Thomas Walcher, without whose financial support and help this work would not have been completed. He also provided a pleasant working environment and good advice.

I would like to thank Prof. Joerg Friedrich, Prof. Reiner Neuhausen and Dr. Guenther Rosner for their support and help during my work in Mainz.

My special thanks to all the Mainz students and postdocs of A1 Mainz collaboration who spent so much effort in preparing the Spectrometer Hall for my experiment, and for help in taking the data and otherwise during my work in Mainz. I would like to thank Michael Kohl for his work with me on the helium target; also Arnd Liesenfeld, Axel Wagner, Marcus Weis, Ralph Böhm, Dr. Michael Distler, Dr. Harald Merkel, Ingo Ewald, Jan Friedrich and all the others who have assisted.

I would like to thank the US collaborators for their help during my experi-

ment: Dr. Shalev Gilad, Dr. Zilu Zhou, Dr. Kevin Fissum, Dr. David Rowntree, Dr. Jianguo Zhao, Dr. Jian-Ping Chen, Rikki Roche, Prof. Konrad Aniol, Dr. Dan Dale, Prof. Dimitri Margaziotis and Prof. Peter Dragovitsch. My special thanks for Dr. Adam Sarty, who was always ready to help me in my data analysis and Dr. Jeff Templon, who saved me so much time doing the AEEXB simulations, and helped me with physical advice. I thank Dr. Zilu Zhou for his advices and expertise concerning the data analysis. I would like to thank specifically Dr. Shalev Gilad for organizing my MIT visit and other assistance.

I have to mention also the Photonuclear group at the University of Melbourne where I spent the first year of my PhD: Dr. R. Rassool, Sasha Kuzin, Craig, Rob, and Mark. The time I spent with you was very pleasant and important for me.

Thanks for Dr. Victor Kashevarov from The Lebedev Physical Institute in Moscow, who generously shared his expertise in Monte-Carlo simulation techniques and was always ready to help me.

Thanks for Monika Baumbusch, who organized housing and money during my long "visit" at Mainz.

Contents

Acknowledgements	3
1 Introduction	1
1.1 Why Electron Scattering?	1
1.2 History	2
1.3 Inclusive (e, e') cross section	4
1.4 This Experiment: Motivation	5
1.5 Thesis content	8
2 Theoretical overview	10
2.1 Nucleon knockout reactions	10
2.2 y -scaling	11
2.3 Missing energy	12
2.4 Plane Wave Born approximation	14
2.5 Plane Wave Impulse Approximation	16
3 Experimental details	18
3.1 Electron beam	19
3.1.1 MAMI Electron Accelerator	19
3.1.2 Beam Monitoring	21
3.2 Magnetic Spectrometers	23
3.2.1 Collimators	26

3.2.2	Vertical Drift Chambers	27
3.2.3	Scintillators	27
3.2.4	Cherenkov Detectors	29
3.3	Helium Target	29
3.4	Data Acquisition System	33
3.5	${}^4\text{He}(e, e'p)$ experiment	36
4	Calibration of Experimental Components	39
4.1	Overview	39
4.1.1	Calibration of the Spectrometers	39
4.1.2	Helium-Target Density Measurements	41
4.2	Angular and Momentum Resolution	42
4.2.1	Elastic ${}^{12}\text{C}(e, e')$ Measurements with the Sieve Slit	42
4.2.2	Momentum corrections	46
4.3	${}^{12}\text{C}(e, e')$ cross section	49
4.3.1	Theoretical ${}^{12}\text{C}(e, e')$ Elastic-Scattering Cross Sections	50
4.3.2	Measured ${}^{12}\text{C}(e, e')$ Elastic-Scattering Cross Sections	50
4.3.3	Experimental Uncertainty of the Measured Cross Section	56
4.4	Efficiency studies	62
4.5	Elastic electron-scattering measurements on ${}^4\text{He}$	64
4.5.1	Introduction	64
4.5.2	Theoretical helium-elastic cross section.	67
4.5.3	Experimental ${}^4\text{He}(e, e')$ cross section	68
4.5.4	Experimental uncertainties	73
4.5.5	Spectrometer C	75
4.5.6	Summary	78
5	Coincidence (e,e'p) data	79
5.1	Introduction	79

5.2	Missing-energy spectra	81
5.3	Software cuts and background reduction	84
5.3.1	Overview	84
5.3.2	Coincidence timing	88
5.3.3	Background processes	92
5.3.4	Cut on target length	94
5.3.5	Background contribution from the scattering chamber windows	97
5.3.6	Background at $E_m \geq 50 \text{ MeV}$	105
5.3.7	Thickness of the helium target	106
5.3.8	ω -cut	107
5.4	Six-fold differential cross section	110
5.5	Five-fold differential cross section	111
5.6	The experimental spectral function	112
5.7	Radiative corrections with RADCOR	113
5.7.1	Introduction	113
5.7.2	Schwinger radiation	114
5.7.3	External bremsstrahlung	117
5.7.4	Limitations of the unfolding procedure with RADCOR	119
5.8	Monte-Carlo simulations of the radiative tail	125
6	Results	127
6.1	Six-fold differential cross section	128
6.1.1	AEEXB simulations	128
6.1.2	RADCOR unfolding	130
6.2	Two-body-breakup channel	135
6.2.1	Five-fold differential cross section	135
6.2.2	Rosenbluth L/T separation	137
6.2.3	The proton-triton momentum distribution	142
6.3	Three and four-body breakup channels	155

6.3.1	Rosenbluth L/T separation	155
6.3.2	Spectral function	162
6.3.3	The proton-momentum distribution	167
6.4	Systematic error estimate	177
7	Conclusion	179
	Appendices	184
A		184
A.1	GEANT model of the collimators	184
A.1.1	The collimator of Spectrometer A	184
A.1.2	The collimator of Spectrometer B	185
B		190
B.1	DUMP Code	190
B.1.1	Overview	190
B.1.2	Events generation	191
B.1.3	Simulation of physical processes	193
B.1.4	Particles tracking through the collimators	194
B.1.5	Effective solid angle of the spectrometers	195
C		198
C.1	GEANT Monte-Carlo code	198
C.1.1	Modeling of the experimental setup	198
C.1.2	Operation modes	198
D		202
D.1	Helium-target density	202
	References	206

List of Figures

1.1	The cross-section behaviour and reaction mechanisms in inclusive electron scattering	4
1.2	From ref.[6], the R_L and R_T responses of the $^{12}\text{C}(e, e'p)$ cross section . . .	7
1.3	Ref. [8]: S_L^{exp} (L) and S_T^{exp} (T) as functions of \vec{q} (in MeV/c) for ^4He compared to calculations of R. Schiavilla (R.S.) [9]	8
2.1	General diagram of the (e,e'p) reaction	11
2.2	PWBA of the (e,e'p) reaction	13
2.3	PWIA of the (e,e'p) reaction	14
2.4	Initial proton momentum p_i in PWIA	15
3.1	Mainz Microtron and the experimental halls	20
3.2	Racetrack microtron	21
3.3	Beam rastering in both horizontal x and vertical y directions	23
3.4	Magnetic spectrometers	24
3.5	Detector package	25
3.6	Multiplicity, number of wires and drift time in VDC	28
3.7	Helium cryogenic loop	30
3.8	The helium-target density as a function of the beam current for two different densities of the helium gas	31

3.9	The detector system: a particle first crossing VDCs, then dE and ToF detectors (which are the 1 st and 2 nd scintillator layers), the Cherenkov detector (Cer) and the Top scintillator	34
3.10	Experimental setup as it was used for the (e,e'p) measurements	35
3.11	The angle θ_{pq} between the proton momentum \vec{p} and 3-momentum transfer \vec{q}	37
3.12	(E_m, P_m) range covered in the (e,e'p) measurements	38
4.1	The sieve slit picture at $E_{beam} = 495.11$ MeV. The fit of y_0 and ϕ_{tgt} was done for the central hole only.	43
4.2	Sieve slit picture at $E_{beam} = 630.11$ MeV.	44
4.3	The $^{12}C(e, e')$ momentum spectrum before (top) and after the correction for the kinematic broadening.	48
4.4	The $^{12}C(e, e')$ data analysis	49
4.5	The $^{12}C(e, e')$ elastic line in Kinematic 2. The momentum corrected from θ_{focal} dependence (right); uncorrected momentum (left)	51
4.6	The $^{12}C(e, e')$ elastic line correction which compensates dependence on θ_{focal} coordinate	52
4.7	The $^{12}C(e, e')$ elastic data; the correction of the central scattering angle of the spectrometers	57
4.8	Summary of $^{12}C(e, e')$ elastic measurements	58
4.9	The Carbon elastic line in $^{12}C(e, e')$; the solid line shows the ^{12}C elastic peak, and the dashed line is ^{13}C background	60
4.10	The $^{12}C(e, e')$ measurements in Kinematic 2. The electron momentum was corrected for θ_{focal} aberrations	61
4.11	The x -scintillator plane in the $^{12}C(e, e')$ QE measurements; the efficiency losses at the edges of the scintillator segments are well seen (top); a low efficiency of the whole segment (bottom)	65
4.12	N_{eff} counts for the QE $^{12}C(e, e')$ measurements with four different central momenta in Spectrometer A	66

4.13	The ${}^4\text{He}$ elastic peak in Kinematic 2 projected at x scintillator plane; the trigger inefficiency is visible near $x = 395,460$ and 550 mm	70
4.14	The ${}^4\text{He}(e, e')$ measurements, Kinematic 2.1; the kinematically-corrected momentum corrected for θ_{focal} aberrations (left) and the kinematically-corrected momentum without such correction (right)	72
4.15	The ${}^4\text{He}$ elastic peak in Kinematic 1 (solid line); the background from the Al target cell (dashed line)	73
4.16	The measurements with the empty Al cell; Kinematic 1. First two histograms show a large range of the background under the elastic helium peak (positioned at approx. 550 MeV) and outside it. For the first (second) histogram the target mass equal to the ${}^4\text{He}$ (Al) mass was used to perform the kinematic calculations. The bottom histogram shows the background only under the elastic helium line (including the radiative tail.	77
5.1	Analysis of the (e,e'p) data	80
5.2	Raw missing-energy spectrum for ${}^4\text{He}(e, e'p)X$ reaction	83
5.3	Raw missing-energy spectra; (a) the solid line is the corrected missing energy and dashed line is the missing energy not corrected from θ_{focal} dependence; (b) the two-body-breakup peak after the resolution optimization	85
5.4	Two-body-breakup peak after correction for energy loss and θ_{focal} dependence	86
5.5	ADC spectra for scintillator of Spectrometer B before the timing cut (a) and after it (b)	87
5.6	Raw coincidence time (a); corrected timing (b)	89
5.7	Coincidence timing; the foreground and background windows are shown	90
5.8	Dependence of the coincidence timing from the dispersive x-scint. coordinate near the edges of the scintillator segments	91
5.9	Inefficiency of the coincidence-timing cut	93
5.10	$E_{beam} = 570.11\text{ MeV}$, the central momentum in Spectrometer A $P_{cent}^A = 236\text{ MeV}/c$. Pions background in ToF (top); ToF after the Cherenkov cut (bottom)	95

5.11	(a) The missing-energy spectra (from top to bottom): no cut on z , $ z \leq 2.5 \text{ cm}$ and $ z \leq 2.0 \text{ cm}$; (b) z -coordinate at the target for the walls of the empty cell	96
5.12	Simulated missing-energy spectra : solid line - collimator B is opened by 70 mrad in the vertical direction. Hatch style histograms contain the missing-energy spectra for the different values of the vertical acceptance: 60, 55, 50 and 45 mrad. The scattering-chamber position is -3 mm in the vertical direction	99
5.13	Kinematic 3, the measured data; the background at missing energies around 34 MeV from the protons losing energy in the scattering-chamber window	100
5.14	Kinematic 1 & 2, the measured data; the background from the electrons losing their energy in the scattering chamber window	102
5.15	GEANT simulation for the Kinematic 2, of the background contribution at a high missing energy from the electrons and protons losing part of their energy in the scattering chamber window	103
5.16	GEANT simulation for the Kinematic 1, of the background contribution at a high missing energy from the electrons and protons losing part of their energy in the scattering chamber window	104
5.17	Image of Spectrometer B collimator ($E_m \geq 50 \text{ MeV}$)	105
5.18	The cut on ω used to match the phase-space for the different kinematics of the (e,e'p) data	108
5.19	The (E_m, p_m) phase-space after the cut on ω	109
5.20	Radiative correction diagrams for electron-nucleus scattering	115
5.21	Diagrams for photon emission during electron-nucleus scattering	116

5.22	Radiative tails from the incident and scattered electrons (top). Continuum cross section corrected for radiation using RADCOR (bottom); significant radiative contribution (from the two-body-breakup peak at a higher p_m) is expected in the missing-energy region shown as the “2bbu radiative tail” (bottom)	120
5.23	Radiative tails from the incident and scattered electrons (top). Continuum cross section corrected for radiation using RADCOR (bottom); significant radiative contribution (from the two-body-breakup peak at a lower p_m) is expected in the missing-energy region shown as the “2bbu radiative tail” (bottom)	121
5.24	Radiative tails from the incident and scattered electrons (top). Continuum cross section corrected for radiation using RADCOR (bottom); significant radiative contribution (from the two-body-breakup peak at a lower p_m) is expected in the missing-energy region shown as the “2bbu radiative tail” (bottom)	122
5.25	AEEXB simulation of the two-body breakup radiative tail (received from Templon [31]) positioned on top of the radiatively uncorrected six-fold cross section (top); this six-fold cross section after subtraction of the two-body breakup radiative tail (AEEXB)	124
6.1	AEEXB simulation of the 6-fold differential cross section (received from Templon [31]). The solid line shows the simulation result for all channels of the ${}^4He(e, e'p)$ reaction. The dashed line is the theoretical cross section for the continuum without radiation, calculated from the theoretical spectral function [55]	129
6.2	Six-fold differential cross section radiatively corrected with RADCOR	131
6.3	Six-fold differential cross section radiatively corrected with RADCOR	132
6.4	${}^4He(e, e'p){}^3H$ cross section (without the ω -cut)	134
6.5	Rosenbluth plot for the case of the two-body breakup reaction channel	136

6.6	Rosenbluth plot for the case of the two-body breakup reaction channel (the systematic error is included)	138
6.7	The proton-triton momentum distributions (without the ω -cut)	140
6.8	The proton-triton momentum distributions	141
6.9	The proton-triton momentum distributions compared to the averaged over the three kinematics value	143
6.10	The $\langle N \rangle$ value (for each p_m bin) calculated for the proton-triton momentum distributions	145
6.11	The ratio between the experimental data and several theoretical models for proton-triton momentum distributions (without the ω -cut)	147
6.12	The ratio between the experiment and several theoretical models for proton-triton momentum distributions (with the ω -cut)	148
6.13	The ratio between the experiment and several theoretical models for the proton-triton momentum distributions (without the ω -cut)	150
6.14	The ratio between the experiment and several theoretical models for proton-triton momentum distributions (with the ω -cut)	152
6.15	Rosenbluth plots for the continuum region (5 MeV missing-energy bins) .	154
6.16	Ratio σ_L/σ_T as a function of the missing energy (5 MeV missing-energy bins)	155
6.17	Rosenbluth plots for the continuum region (5 MeV missing-energy bins) .	158
6.18	Rosenbluth plots for the continuum region (10 MeV missing-energy bins)	159
6.19	Rosenbluth plots for the continuum region (4 MeV missing-energy bins) .	160
6.20	Measured spectral function in Kinematic 1	161
6.21	Measured spectral function in Kinematic 3	163
6.22	Measured spectral function in Kinematic 2	164
6.23	Measured spectral function for all three kinematics	166
6.24	The proton-momentum distribution $\rho_{3,4}$ as a function of the missing momentum	169

6.25	The proton-momentum distribution $\rho_{3,4}$ as a function of the missing momentum	170
6.26	$\langle N \rangle$ value as a function of the missing momentum (calculated for each missing-momentum bin)	171
6.27	Ratio for the experimental and theoretical momentum distributions as a function of the missing momentum	173
6.28	The proton-momentum distributions compared to the averaged over the three kinematics value	174
6.29	Ratio for the experimental and theoretical momentum distributions as a function of the missing momentum	176
7.1	Results shown as a function of missing energy. (a) Six-fold differential cross section for the three values of the virtual-photon polarization ϵ in the missing-momentum range from 115 to 155 MeV/c. (b) Spectral function. (c) The ratio σ_L/σ_T (both the 2-body and continuum channels)	182
A.1	The collimator of Spectrometer A, the view from the spectrometer side	185
A.2	GEANT simulation of the collimator of Spectrometer A	186
A.3	The geometry of the collimator of Spectrometer B, where θ and ϕ are the angular acceptance values for a point target	187
A.4	GEANT simulation of the vertical collimator of Spectrometer B	188
A.5	GEANT simulation of the horizontal collimator of Spectrometer B	189
B.1	Simplified structure of the <i>DUMP</i> Monte-Carlo code	192
B.2	The solid angle of Spectrometer A(B) as a function of the spectrometer y_0 coordinate in case of 21(5.6) msr collimator	197
C.1	Scattering chamber	199
C.2	General structure of the GEANT Monte-Carlo code	200

List of Tables

3.1	Properties of the magnetic spectrometers	26
3.2	Material (Al7075) of the target cell	33
3.3	${}^4He(e, e'p)$ measurements	36
4.1	The summary for the ${}^{12}C(e, e')$ elastic measurements	56
4.2	The summary of the fit quality parameters from ALLFIT and the individual uncertainties contributed to the total error of the ${}^{12}C(e, e')$ elastic cross sections ($\pm\Delta\sigma/\sigma$)	59
4.3	The ${}^{12}C(e, e')$ quasi-elastic kinematics	62
4.4	Results from AEEXB and <i>DUMP</i> Monte-Carlo codes	68
4.5	Summary of the ${}^4He(e, e')$ elastic measurements	74
4.6	The contribution of the experimental uncertainties to the total error of the 4He target density ($\pm\Delta\rho/\rho$)	76
5.1	Parameters for calculation of the radiation length in RADCOR	118
6.1	${}^4He(e, e'p){}^3H$ cross section (* indicates the cross section calculated with the ω -cut)	137
6.2	The proton-triton momentum distributions (* indicates the momentum distributions calculated with the ω -cut)	144
6.3	$\rho_{3,4}(p_m)$ momentum distributions for ${}^4He(e, e'p)nd$ and ${}^4He(e, e'p)np$ reaction channels (<i>mark*</i> is corresponding to the momentum distributions calculated with the ω -cut)	167

B.1	The horizontal x_i and vertical y_i dimensions of the 21 <i>msr</i> collimator of Spectrometer A and the corresponding distances R_0^i from the target . . .	191
D.1	Helium-target density at $E_{beam} = 570.11 MeV$	203
D.2	Helium-target thickness at $E_{beam} = 570.11 MeV$	203
D.3	Helium-target density at $E_{beam} = 675.11 MeV$	204
D.4	Helium-target thickness at $E_{beam} = 675.11 MeV$	204
D.5	Helium-target density at $E_{beam} = 855.11 MeV$	205
D.6	Helium-target thickness at $E_{beam} = 855.11 MeV$	205

Chapter 1

Introduction

1.1 Why Electron Scattering?

Electron scattering can be used to study various properties of matter. The important property of the electromagnetic interaction is that it is weak, compared to the nuclear force: a coupling constant of $\sim 1/137$ means that the *perturbation* theory can be developed to describe its effect.

Thus, the first main advantage of the electron scattering compared to a nuclear probe is that the electromagnetic interaction is perfectly described by quantum electrodynamics (QED), providing a calculable framework for the interpretation of electron scattering experiments.

The second one is that nuclear matter is practically transparent to the electromagnetic interaction, so that the *entire* nuclear volume can be probed uniformly.

Thirdly, electrons as point particles may probe different distance scales by changing the momentum transfer. It is also very important that the energy and momentum transfer are related, but differ from each other as distinct from reactions with real photons, where energy and momentum transfer are equal. This allows, for example, one to study the spatial distribution of the nuclear currents, for any excitation of the nucleus.

The disadvantage of the electron scattering is that the electron mass is small relative to the mass of a nucleus. Thus, it can be easily deflected during the interaction with a nuclear volume, and radiate virtual or real photons. Consequently complete calculations of the radiative processes must be performed in order to exclude the radiative contribution to the measured cross section. This procedure can become the major source of systematic uncertainty in the measured cross section.

1.2 History

One way to study the internal structure of an object, such as an atom, nucleus or other sub-nuclear particle is to scatter other particles from it and detect the reaction particles. The particles used as the probe, the electrons in our case, must have a wavelength comparable with the geometric size of the investigated object. For example, in order to study the spatial distribution of electrons in atoms, (typically $\sim 10^{-10} m$) a beam of electrons with an adequate resolving power has to be used, otherwise the electrons would "see" atoms as a point-like objects. It is easy to obtain a coarse estimate of the incident electron momentum p that satisfies the following requirements. From the de Broglie relation $\lambda = h/p$:

$$pc \sim \hbar c \cdot 2\pi/10^{-10} m \Rightarrow p \sim 12 KeV/c \quad (1.1)$$

where $\hbar c \approx 200 \times 10^6 eV \cdot fm$. Electrons with such momentum can be treated as non-relativistic particles ($\beta \approx 0.02$) with a kinetic energy $T \approx p^2/2m \approx 140 eV$.

Electron scattering was first used to study the quantum aspects of atoms in 1914, when Frank and Hertz in ref. [10], confirmed the presence of quantized energy levels in atoms by inelastically scattering 200 eV electrons from helium atoms. The scattered-electron spectrum showed not only a peak at 200 eV corresponded to elastic scattering, but also two other peaks at 179 eV and 177 eV. These two additional peaks correspond to an *inelastic* process where electrons gave 21 and 23 eV to the helium atoms, thus providing evidence of quantization in atoms.

Similar experiments such as the classical α -scattering experiment by Rutherford in 1909, revealed the size of the nucleus of the atom. Here α -particles scattered from a thin *Au* foil, led to the first realistic atomic model. In this model the atom consists of point-like electrons interacting via the Coulomb force with each other, and with the point-like nucleus.

As accelerator technology developed, it became possible to provide electrons with energy sufficiently high to probe the nucleus. In the 1950s Hofstadter and collaborators at HEPL performed a series of electron-scattering experiments which revealed the finite extents of the atomic nucleus. They used 126 *MeV* electrons to measure the cross section for elastically scattered electrons from *Au*, and observed that it was significantly below the point-nucleus prediction. They introduced a new factor called the *form factor*, which characterizes the spatial extension of the nuclear charge density. This factor provides corrections to the simple Rutherford formula.

In 1963 Hofstadter published the charge density distribution of ^{12}C , which showed that the nucleus is not point-like, but has a charge radius approximately $1 - 2 \text{ fm}$.

Again, it is easy to estimate the order of magnitude of the electron momentum required to study the spatial charge distribution in the nucleus, using the de Broglie relation:

$$p \sim \frac{\hbar c \cdot 2\pi}{2[\text{fm}]} \approx 600 \text{ MeV}/c \quad (1.2)$$

In 1955 Fregeau and Hofstadter in ref.[11] published a spectrum of inelastically scattered electrons from ^{12}C where three peaks, in addition to the elastic peak, were identified as a sequence of quantized energy states, similar to those observed in atoms.

Inclusive electron scattering - $A(e,e')$

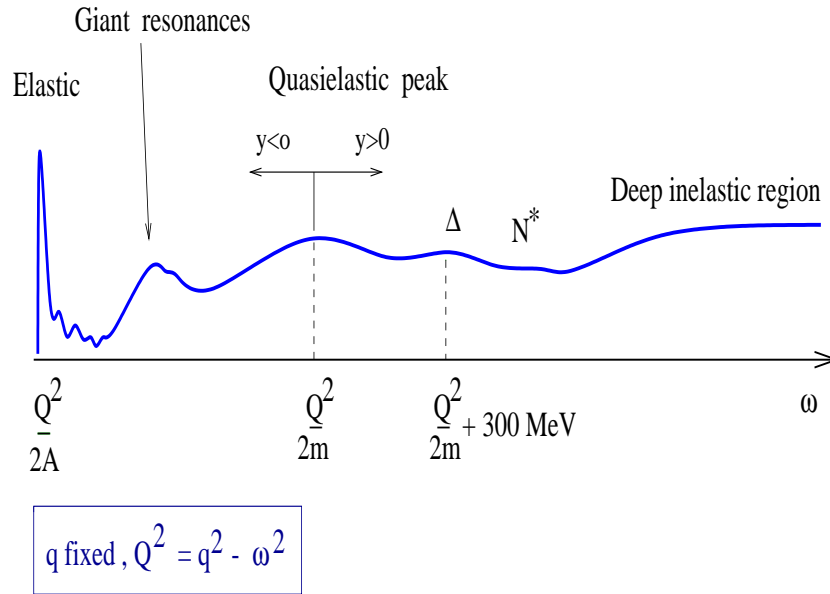


Figure 1.1: The cross-section behaviour and reaction mechanisms in inclusive electron scattering

1.3 Inclusive (e, e') cross section

The cross section for inclusive electron scattering is shown in Figure 1.1 as a function of the energy transfer ω , and a fixed value of the momentum transfer \vec{q} . At successively higher values of ω the following reaction mechanisms can be identified:

- a) The elastic peak (shifted from zero by recoil effects).
- b) In the region $\omega < 20 \text{ MeV}$, narrow peaks appear in the spectrum, which correspond to excitation of discrete nuclear states.
- c) Near $\omega \approx 20 \text{ MeV}$ several broad peaks are visible representing the nuclear giant resonances. They result from collective excitations of the nucleons in the nucleus.
- d) Above the giant resonance region is the quasi-elastic (QE) peak, the region of interest in the present work. It is located at $\omega = Q^2/2m^*$, where m^* is the effective mass of a nucleon inside nucleus, and corresponds to a process where an individual

nucleon is knocked out of the nucleus. Due to the Fermi motion of the nucleons within the nucleus it is not as sharp as it would be for a nucleon at rest.

An estimate can be made from the Heisenberg uncertainty principle of the magnitude of the bound-nucleon momentum:

$$\Delta p = \frac{\hbar c \cdot 2\pi}{2 \cdot R} \sim 150 \text{ MeV}/c \quad (1.3)$$

where R is the nuclear radius, (taken as 2 fm).

e) The first peak beyond the quasi-elastic peak corresponds to the Δ resonance, which was first observed in $\pi - N$ scattering. It is the lowest-energy baryon resonance.

f) The cross-section region marked as N^* is the region of other baryon resonances corresponding to excitations within individual nucleons.

g) The cross section in the deep inelastic region result from scattering from the nucleon constituents: quarks and gluons.

1.4 This Experiment: Motivation

This work is a part of systematic study of the quasi-elastic kinematic region using simple and calculable nuclear systems as ${}^3,{}^4\text{He}$ (see ref. [1]). The first part of the measurements was successfully analysed by R. Florizone [23], whose results are used for comparison in Chapter 6 of this thesis. Florizone measurements were performed in the quasi-elastic region (close to the top of the quasi-elastic peak) on both ${}^3,{}^4\text{He}$ nuclei. This measurement was limited by the ${}^4\text{He}$ nucleus.

The ${}^4\text{He}$ nucleus is a unique and interesting nuclear system. First, this nucleus is a system of only four nucleons, so that theoretical calculations based on nucleon-nucleon (N-N) interaction models are possible. Second, one may expect the onset of many-body nuclear effects for this nucleus. Third, the nuclear density for ${}^4\text{He}$ is very high, so that various effects of the strong interaction between more than two nucleons may be significant for this nucleus than for less tightly bound nuclear

systems.

The kinematical conditions selected for the experiment (so-called “dip” kinematics) emphasized the role of meson exchange currents (MEC) and virtual Δ -resonance excitation in the $(e,e'p)$ cross section. These processes may lead to larger transverse strength than quasi-free nucleon knockout, which dominates near the quasi-elastic peak. In order to estimate the role of MEC and Δ -resonance excitation in the total $(e,e'p)$ cross section, longitudinal/transverse (L/T) cross-section behaviour was studied for both two-body and continuum reaction channels.

Therefore, the most important physical problems discussed in this thesis are the following.

- 1) The nature of the strength for the high-missing-energy kinematic region.

In the earlier $(e, e'p)$ experiments on helium and ^{12}C (see ref. [2] - [7]) unexpectedly large cross sections for nucleon knockout were observed at high missing energies. In reference [6] (MIT/Bates) the measured $^{12}\text{C}(e, e'p)$ cross section was used to extract the longitudinal (R_L) and transverse (R_T) response functions. The measured strength in the high missing-energy region ($E_m \geq 50 \text{ MeV}$) was found to be purely transverse, with R_L equal to zero (see Figure 1.2). A possible explanation for this phenomenon is that the nuclear interaction between two or more nucleons (multi-body current) play a significant role.

In this experiment significant efforts were made to reduce the statistical and systematic uncertainty of the $(e,e'p)$ cross section measured in the high-missing-energy region. This should give a clear answer as to whether the significant strength observed at high missing energies belong to the $(e,e'p)$ reaction mechanism, or to the some background process.

- 2) The second important question involves how the ratio for longitudinal/transverse components for $(e,e'p)$ cross section behave as a function of y -scaling, missing energy, and missing momentum.

Separation of the structure functions for $(e,e'p)$ cross sections for the ^2H , ^3He

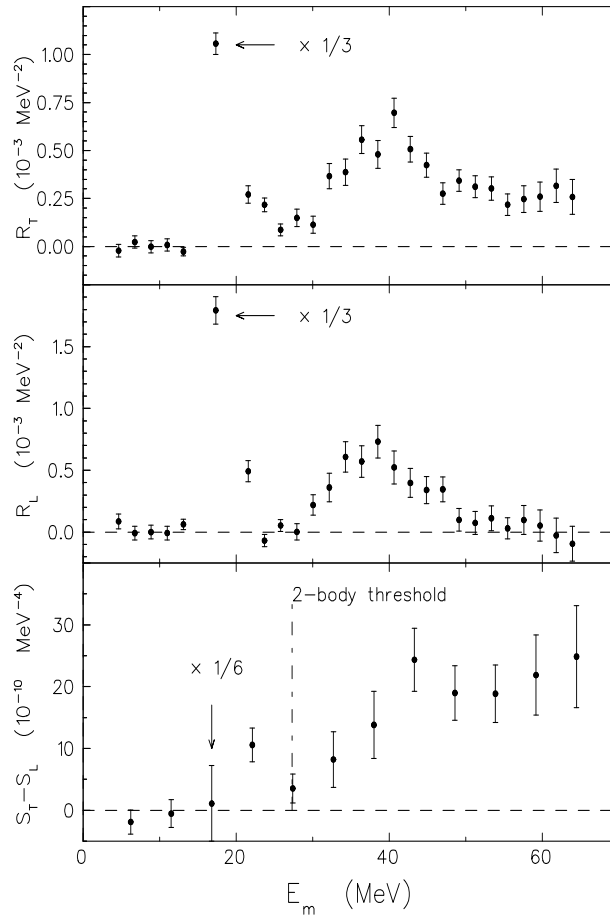


Figure 1.2: From ref.[6], the R_L and R_T responses of the $^{12}\text{C}(e, e'p)$ cross section

and ^4He was performed by Ducret *et al* [8] (Saclay) for an extended range of the momentum transfer \vec{q} . The longitudinal (S_L^{exp}) and transverse (S_T^{exp}), "experimental" spectral function were measured, and the ratio S_L^{exp}/S_T^{exp} for the two-body breakup channel was found to be close to PWIA predictions for \vec{q} values similar to the current measurements for ^2H and ^3He , but significantly below the predictions for ^4He , as shown in Figure 1.3.

Our experiment allows the Rosenbluth separation to be made for the structure functions of the $(e, e'p)$ cross section, not only for the two-body breakup channel, but also for the continuum. In other words, we should be able to answer the questions to whether the L/T ratio for the two-body breakup and the continuum

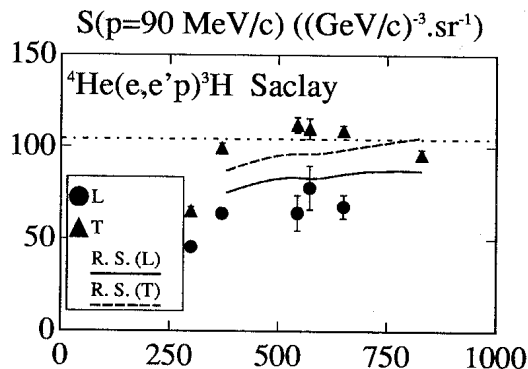


Figure 1.3: Ref. [8]: S_L^{exp} (L) and S_T^{exp} (T) as functions of q (in MeV/c) for ${}^4\text{He}$ compared to calculations of R. Schiavilla (R.S.) [9]

channels for nucleon knockout from ${}^4\text{He}$ is different from that calculated using the simple PWIA model or not.

- 3) the purpose of these studies is also to achieve better statistical and systematic accuracy for results already available in this kinematic region. This would allow a better understanding of the reaction mechanisms involved in the knockout (e,e'p) reactions, by comparing the measured cross sections with modern theoretical calculations, which go beyond the simple PWIA picture.

1.5 Thesis content

This chapter is followed by:

- Chapter 2, which contains a short theoretical overview, together with some kinematical definitions used in the data analysis;
- Chapter 3 describes the experimental setup of the A1 Mainz collaboration and the MAMI electron accelerator. Some details about the kinematics of the coincidence (e, e'p) measurements are also provided;
- Chapter 4 describes in detail all the calibration measurements with carbon and helium targets that were used to determine the spectrometer properties and to

- normalize the (e,e'p) cross section;
- Chapter 5 includes details of the analysis of the coincidence (e,e'p) data;
- Chapter 6, contains the results presented in figures and tables;
- Chapter 7, the final one, gives a brief summary for the results obtained in this experiment;
- Appendices A, B, C and D describe some important details for the new computer codes used in the data analysis, and give tabulated information for the calculated density of the helium target.

Chapter 2

Theoretical overview

2.1 Nucleon knockout reactions

By using electrons with energies between 0.5 and 1 GeV various aspects of nuclei structure, such as momentum distributions, can be effectively studied in nucleon knockout reactions. The general diagram of the (e,e'p) reaction is shown in Figure 2.1. The electron arm of the reaction is characterized by the 4-vectors of the incident electron, $k_i = (E_i, \vec{k}_i)$, and the scattered electron $k_f = (E_f, \vec{k}_f)$. The proton arm is described by the 4-vector of the detected proton $p_p = (E_p, \vec{p}_p)$. The values of these parameters are measured during the experiment, and are determined with an accuracy limited by the spectrometer's resolution.

The other 4-vectors required to describe the (e,e'p) reaction are the target-nucleus momentum $p_A = (E_A, \vec{p}_A)$, the residual-nucleus momentum $p_B = (E_B, \vec{p}_B)$, and the 4-momentum transfer $q = (\omega, \vec{q})$. In the laboratory reference frame the target is at rest, and the 4-vector of the target nucleus reduces to $p_A = (M_A, 0)$.

By definition, the 4-momentum of the virtual photon is:

$$q = k_i - k_f = (\omega, \vec{q}), \quad (2.1)$$

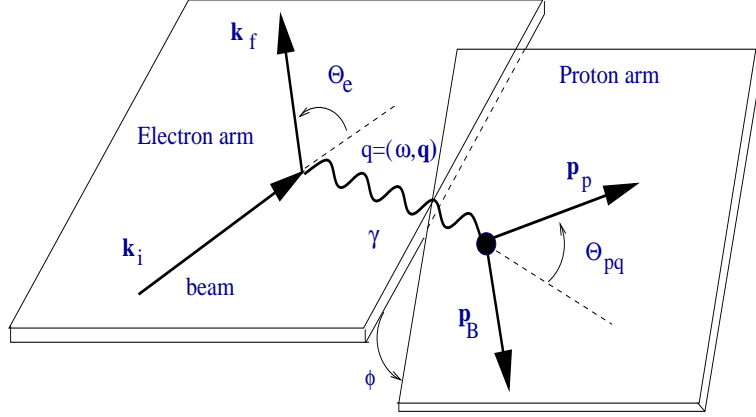


Figure 2.1: General diagram of the (e,e'p) reaction

where the energy transfer $\omega = E_i - E_f$, and the 3-vector of momentum transfer is $\vec{q} = \vec{k}_i - \vec{k}_f$. The 4-momentum transfer is space-like where $q^2 = -Q^2 = \omega^2 - |\vec{q}|^2 \leq 0$; its positive value is defined as Q^2 . In Figure 2.1 the angle of the detected proton with respect to the direction of \vec{q} is labeled as θ_{pq} . The kinematics were selected such that $\theta_{pq} = 0$ when \vec{q} is parallel to the direction of the detected proton. This is the so-called "parallel" kinematics.

2.2 y -scaling

In the simplest version of the impulse approximation for the QE scattering, the inclusive cross section can be factorized as an elementary electron-nucleon cross section for a moving nucleon, times the structure function $f(y)$:

$$\frac{d^3\sigma}{d\omega d\Omega_e} \propto (Z\sigma_{ep} + N\sigma_{en})f(y) \quad (2.2)$$

This function $f(y)$ depends on the nucleon momentum distribution parallel to \vec{q} . For the A(e,e'p)B reaction, energy conservation balance can be written as:

$$E_p + E_B = M_A + \omega \quad (2.3)$$

where M_A is the mass of the target nucleus and E_p is the total proton energy, E_B is the total energy of the recoil system including the internal excitation energy.

This can be rewritten by using particle momenta as:

$$\sqrt{p_p^2 + M_p^2} + \sqrt{p_B^2 + M_B^2} = M_A + \omega \quad (2.4)$$

where p_p is the proton momentum, and p_B is the momentum of recoil nucleus. The *missing momentum* $p_m^{\vec{}}$, which is equal to the 3-momentum of the recoil nucleus $p_B^{\vec{}}$, is defined as:

$$p_m^{\vec{}} = p_B^{\vec{}} = \vec{q} - \vec{p}_p \quad (2.5)$$

In the Plane Wave Impulse Approximation (PWIA), described in more details in the following sections, the missing momentum is equal to the *initial* nucleon momentum p_i (Eq. 2.20 and Figure 2.4). Using this definition, the energy balance can be modified to:

$$\omega = \sqrt{(\vec{q} + \vec{p}_i)^2 + M_p^2} + \sqrt{p_i^2 + (M_B)^2} - M_A \quad (2.6)$$

$$\omega = \sqrt{(q + y)^2 + M_p^2} + \sqrt{y^2 + (M_B)^2} - M_A \quad (2.7)$$

where the variable y is defined to be the minimum value of the initial nucleon momentum consistent with energy conservation.

The sign of the y -scaling variable is positive (negative) for large (small) energy transfer ω . Thus, a large negative value for y , corresponds to high momentum components antiparallel to \vec{q} . They correspond to population of the low- ω side of the QE peak. Large positive values for y , correspond to the *dip region*, (between QE and Δ peaks) and involve large- ω processes that involve pion production or excitation of baryon resonances.

The QE peak occurs when $y = 0$, thus

$$\omega_{QE} = \sqrt{q^2 + M_p^2} + M_B - M_A \quad (2.8)$$

2.3 Missing energy

In reference [12] the *missing energy* E_m is defined as:

$$E_m = M_p + M_B - M_A \quad (2.9)$$

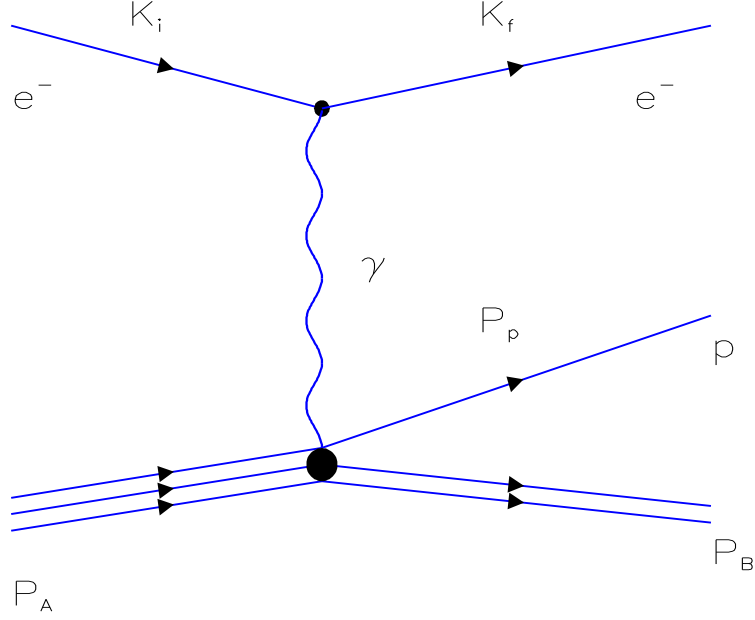


Figure 2.2: PWBA of the (e,e'p) reaction

From this definition and Eq.2.4 the following expression for missing energy can be derived:

$$E_m = \omega - (\sqrt{p_p^2 + M_p^2} - M_p) - (\sqrt{p_B^2 + M_B^2} - M_B) \quad (2.10)$$

Due to historical reasons a slightly different missing-energy definition is used in electron scattering discussions. An approximation is used where $M_B \approx M_{A-1}$, where M_{A-1} is the mass of the product nucleus. Thus, the final missing energy expression is:

$$E_m = \omega - (\sqrt{p_p^2 + M_p^2} - M_p) - (\sqrt{p_B^2 + M_{A-1}^2} - M_{A-1}) \quad (2.11)$$

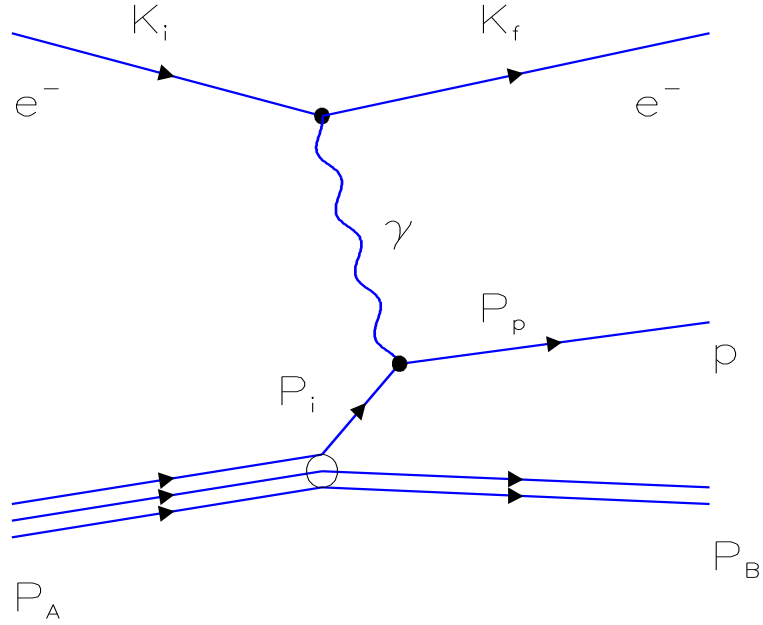


Figure 2.3: PWIA of the (e,e'p) reaction

2.4 Plane Wave Born approximation

The leading-order, one-photon-exchange diagram (first Born approximation), for electron scattering is shown in Figure 2.2. Because the electromagnetic coupling constant α ($\sim 1/137$) is small, higher order terms are suppressed compared to the single photon exchange process. In this approximation, called Plane Wave Born Approximation (PWBA), the cross section can be written as (see ref. [13]):

$$\frac{d^6\sigma}{d\Omega_e d\Omega_p d\omega dp_p} = p_p^2 \frac{e^2 \pi}{2|\vec{q}|} \Gamma \left[\sigma_T + \epsilon \sigma_L + \sqrt{\epsilon(1+\epsilon)} \sigma_{TL} \cos\phi + \epsilon \sigma_{TT} \cos 2\phi \right] \quad (2.12)$$

where the flux of virtual photons Γ , and the polarization ϵ are defined as:

$$\epsilon = \left[1 + 2 \frac{|\vec{q}|^2}{Q^2} \tan^2 \frac{\theta}{2} \right]^{-1} \quad (2.13)$$

$$\Gamma = \frac{\alpha}{2\pi^2} \frac{E'}{E} \frac{|\vec{q}|}{Q^2} \frac{1}{1-\epsilon} \quad (2.14)$$

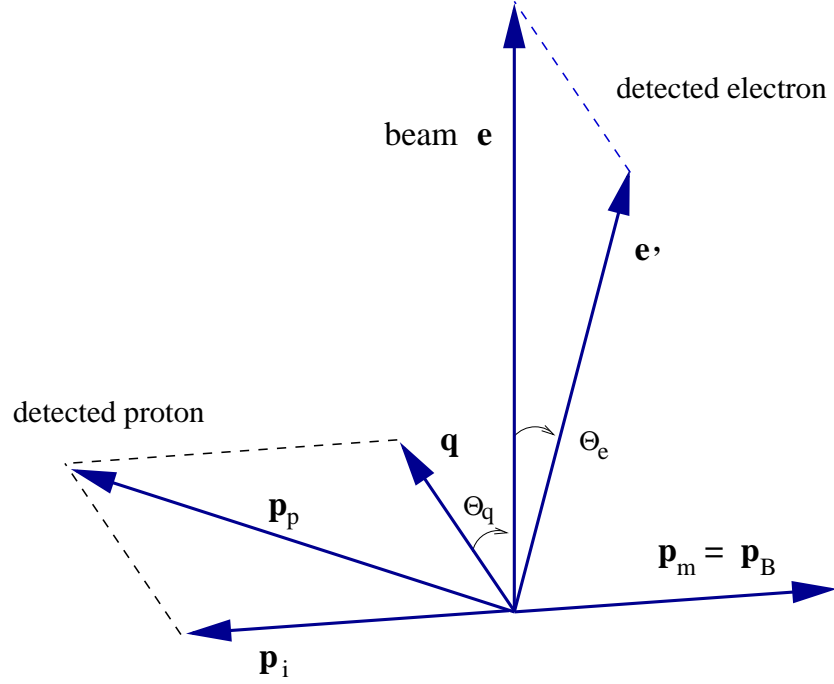


Figure 2.4: Initial proton momentum p_i in PWIA

The response functions $\sigma_T, \sigma_L, \sigma_{TL}$ and σ_{TT} are related to the various components of the nuclear current, \vec{J} :

$$\sigma_L = 2 \frac{Q^2}{\bar{q}^2} |J_0|^2 \quad (2.15)$$

$$\sigma_T = |J_{+1}|^2 + |J_{-1}|^2 \quad (2.16)$$

$$\sigma_{TL} \cos \phi = 2 \left(\frac{Q^2}{|\bar{q}|} \right)^{1/2} \text{Re} \left(J_0^* (J_{+1} - J_{-1}) \right)$$

$$\sigma_{TT} \cos 2\phi = -\text{Re} (J_{+1}^* J_{-1})$$

where J_0 is the longitudinal component of the nuclear current, and $J_{\pm 1}$ are the transverse components.

Sometimes also slightly different definition is used, where the longitudinal and transverse components of the nuclear current are called

$$R_L = |J_0|^2 \quad (2.17)$$

$$R_T = |J_{+1}|^2 + |J_{-1}|^2 \quad (2.18)$$

where R_T is equal to the previously defined σ_T , and R_L differs from σ_L by a kinematical factor $2 \cdot Q^2/\vec{q}^2$.

As mentioned before, in the present kinematics, protons are detected in a direction parallel, or nearly parallel, to the 3-momentum \vec{q} , and thus $\theta_{pq} \approx 0$. The interference structure functions σ_{TL} and σ_{TT} are both proportional to $\sin(\theta_{pq})$, and therefore vanish in parallel kinematics, so that in parallel kinematic the cross section contains only longitudinal and transverse responses:

$$\frac{d^6\sigma}{d\Omega_e d\Omega_p d\omega dp_p} = p_p^2 \frac{e^2 \pi}{2|\vec{q}|} \Gamma [\sigma_T + \epsilon \sigma_L] = K \cdot \Gamma \cdot [\sigma_T + \epsilon \sigma_L] \quad (2.19)$$

where K is a kinematical factor. Measurements of the experimental cross section with two or more different values of ϵ allows determination of both the longitudinal and transverse structure functions σ_L and σ_T from Equation 2.19. This is the so-called Rosenbluth Separation.

2.5 Plane Wave Impulse Approximation

In the Plane Wave Impulse Approximation (PWIA) a virtual photon is absorbed by a single proton, which leaves the nucleus without further interaction, and is detected as illustrated in Figure 2.3. In such a case the missing momentum is equal to the initial proton momentum within the nucleus \vec{p}_i , as shown in Figure 2.4:

$$\vec{p}_m = \vec{p}_B = \vec{q} - \vec{p}_p = -\vec{p}_i \quad (2.20)$$

The (e,e'p) cross section in the PWIA is expressed as:

$$\frac{d^6\sigma}{d\Omega_e d\Omega_p dp_e dp_p} = p_p^2 \sigma_{ep} S(p_i, E_m) \quad (2.21)$$

An experimental spectral function, which is the probability of finding a proton of momentum p_i inside the nucleus, can be determined from the measured (e,e'p) cross section as:

$$S^{exp}(p_i, E_m) = \frac{1}{p_p^2 \sigma_{ep}} \frac{d^6\sigma}{d\Omega_e d\Omega_p dp_e dp_p} \quad (2.22)$$

where σ_{ep} is the off-shell electron-proton cross section.

In the data analysis presented in this work, the *cc1* prescription of de Forest [14] was used to model σ_{ep} in the above equation. The electric and magnetic nucleon form factors were calculated according to the parameterization of Simon [15]. The elementary *ep* cross section for knockout reactions is off-shell because the effective mass of the nucleon is not equal to its invariant rest mass, due to its Fermi motion within the nucleus.

Remark

In this work, the PWIA is used as a main framework for the data interpretation. The experimental (distorted) spectral functions and momentum distributions were extracted using the PWIA form of the cross section.

Chapter 3

Experimental details

Overview

The electron scattering measurements reported in this thesis were performed at the 855 MeV Mainz Microtron. Electrons of energies 570.11, 675.11 and 855.11 MeV and beam currents 20 - 30 μA were used.

The scattered electrons and product protons were detected using the three-spectrometer-system of the A1 Mainz collaboration. Spectrometer A was the electron-arm spectrometer, Spectrometer B was used for protons detection and Spectrometer C was the luminosity monitor.

The Microtron technical overview and the beam parameters are given in Section 3.1. In addition, important beam-control procedures, such as the beam rastering calibration, calculations of the total charge collected at the target, and control of the horizontal and vertical beam-spot positions are described.

General information about the optics and design of the magnetic spectrometers is presented in Section 3.2. In this section the properties of the collimators for each spectrometer and the individual detectors in the focal-plane detector package are also described.

Section 3.3 is dedicated to description of the high pressure helium target,

and Section 3.4 gives a short account of the specific trigger conditions used in this experiment. A short overview of the data acquisition system is also provided.

In Sections 3.5 some details about the kinematic conditions for the (e,e'p) measurements are given.

3.1 Electron beam

3.1.1 MAMI Electron Accelerator

MAMI is a continuous-wave (CW) electron accelerator with 100 % duty factor. It consists of three microtrons (Figure 3.2) connected in series, with a 3.5 MeV linac as the injector (Figure 3.1). The first section (MAMI A1) delivers a 14.35 MeV electron beam after 18 re-circulations. This beam is injected into MAMI A2 which delivers 180 MeV electrons after 51 re-circulations. The final microtron, MAMI B, accelerates the electron beam from 180 MeV to 855 MeV in 90 beam re-circulations of 7.5 MeV. Electron beam can be delivered for each even numbered return path of MAMI B, so that:

$$E = 180 + 2n \cdot 7.5 \text{ MeV} \quad (n = 1 \dots 45) \quad (3.1)$$

where E is the final beam energy [in MeV], n is a path number. MAMI B can deliver a maximum current 110 μA . The lengths of the accelerating sections of these three microtrons are 0.80, 3.55 and 8.87 meters, with a corresponding energy gain of 0.6, 3.2 and 7.5 MeV per section. The beam-energy spread due to synchrotron radiation is 30 keV (FWHM), and it is measured with an absolute accuracy of $\pm 160 \text{ keV}$.

In contrast to earlier linear electron accelerators, which produce a pulsed electron beam, the CW beam delivered by MAMI has no pulse structure (besides its microstructure due to the HF electric field used in the accelerating cavities). The microstructure exists also in the beam of a pulsed accelerator. For coincidence measurements such as are reported in this thesis, the signal-to-noise ratio is one

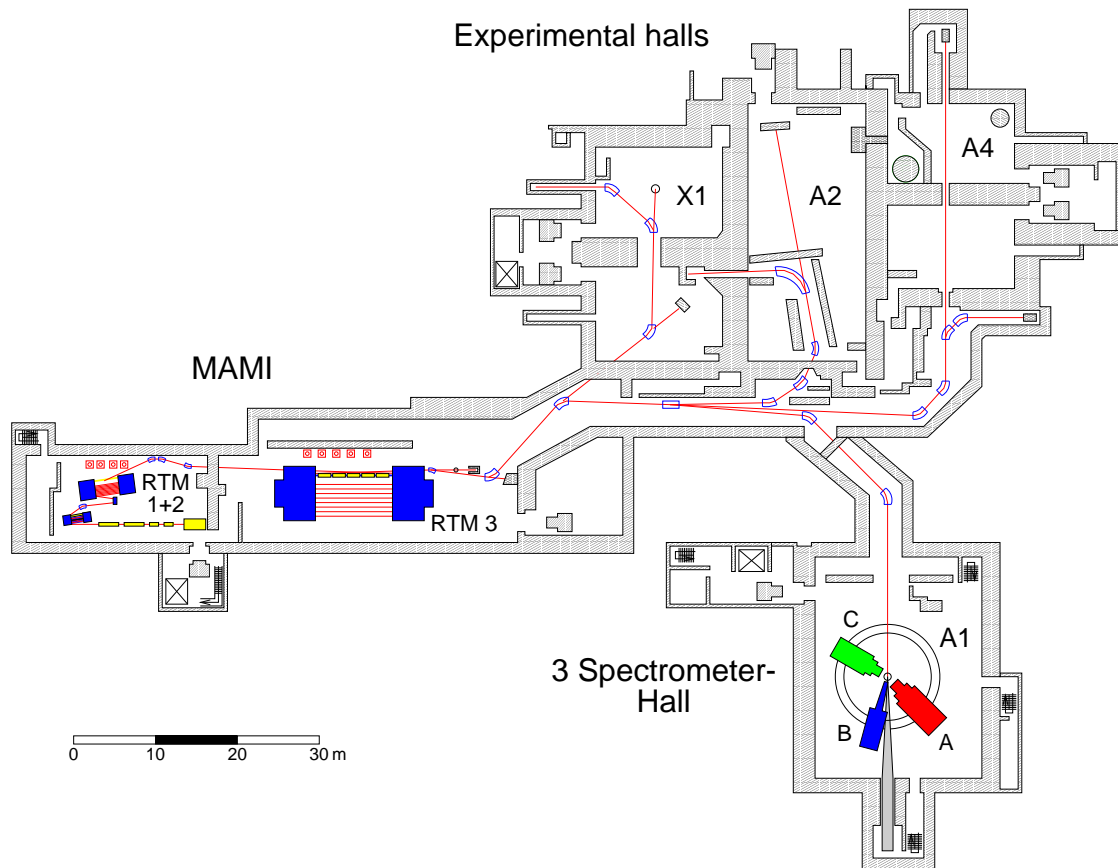


Figure 3.1: Mainz Microtron and the experimental halls

of the most important parameters. The advantage of a CW beam becomes clear by comparing the signal-to-noise ratio $\frac{N_{coinc}}{N_{acc}}$ for a pulsed beam to that for a CW accelerator (see reference [18]):

$$\frac{N_{coinc}}{N_{acc}} \sim \frac{F_d}{I_{ave}}$$

where N_{coinc} is the number of true coincidence events, N_{acc} is the number of accidentals, F_d is the duty factor and I_{ave} is the average beam current. The difference between a CW beam and 1% duty factor linac corresponds to a factor of 100 in the signal-to-noise ratio for the same beam current. Thus a CW beam allows one to study reactions which would be impossible to study with a pulsed beam, due to the small size of the cross section and high accidental coincidence background rates.

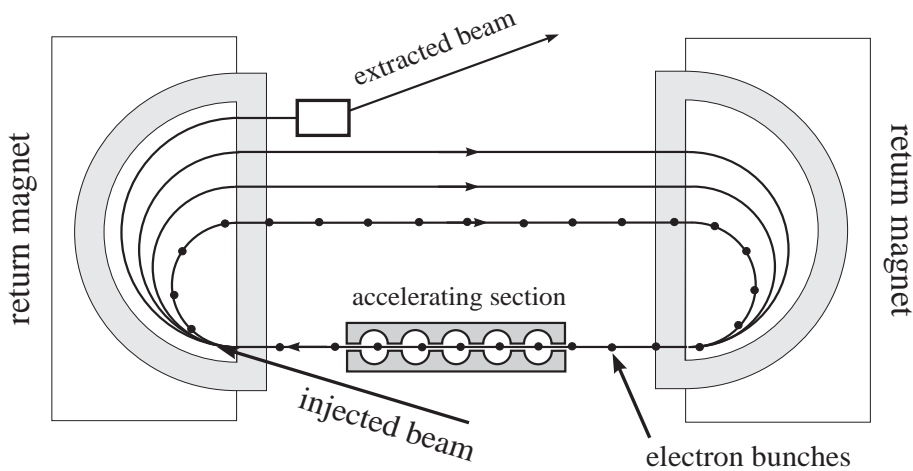


Figure 3.2: Racetrack microtron

3.1.2 Beam Monitoring

A system of magnets delivers the beam from the last microtron into the Spectrometer Hall (Figure 3.1). The electron beam diameter used in experiments is approximately 0.5 mm (FWHM), and its absolute position can be determined with an accuracy of 0.5 mm by remotely monitoring the beam image on BeO or ZnS screens.

Accurate knowledge of the beam position was crucial for the calibration measurements of elastic scattering from carbon or helium. The strong angular dependence of elastic cross sections requires an accurate knowledge of the central scattering angle of the spectrometer, and thus of the beam coordinates at the target. It will be shown in detail in Chapter 4, that even a 0.5-1 mm shift of the beam position from zero can change the measured cross section by 2-4 %.

The average absolute beam position was measured using the beam cavities (described in details in reference [16]) installed at the beam line, a few meters before the scattering chamber. The calibration constant for the beam cavity, used to estimate the average beam position was obtained from [28]. Deviation of the horizontal

beam position Δx from its zero value was calculated as:

$$\Delta x = C(T) \cdot \frac{U}{I} \quad (3.2)$$

where $C(T)$ is the calibration constant (but in reality a function of temperature), U is the cavity output in Volts, and I is the beam current in μA . The temperature dependence of $C(T)$ is unknown and, therefore the accuracy of the resulting Δx value is also uncertain.

For measurements with cryogenic targets the beam is rastered, often at 2.5-3.6 kHz in the both vertical and horizontal directions. This helps to avoid damage of the target cell walls, and reduces the dependence of the target density on beam current by dispersing the heat deposited by the beam over a larger area. The rastering is done by a number of coils installed in the beam line. The rastering amplitudes are adjusted using a visual beam spot on the ZnS target. This calibration is dependent on the beam energy and has to be repeated whenever the beam energy is changed. The actual position of the beam-spot, relative to the undeflected beam position, is determined for each event, and included into the data stream. In this experiment all measurements with the helium cryogenic target were performed with a beam rastering amplitude of $\pm 3 \text{ mm}$ in the horizontal and $\pm 2 \text{ mm}$ in vertical directions, as shown in Figure 3.3.

The beam-current value was obtained using the multi-turn Förster probe installed at MAMI B (see reference [17]). It consists of two toroidal coils that surround the electron beam, and measure its absolute magnetic field. Due to the large number of measurements (equal to the number of beam re-circulations) and negligible beam intensity losses, the accuracy of these measurements is very high and the absolute uncertainty in the charge collected at the target is $\sim 0.1 \%$.

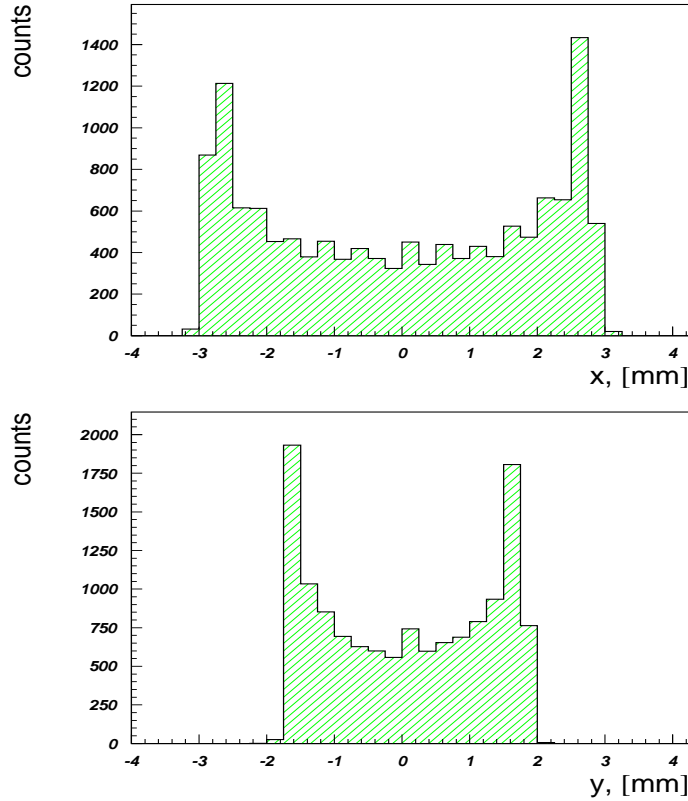


Figure 3.3: Beam rastering in both horizontal x and vertical y directions

3.2 Magnetic Spectrometers

Optics and Design

The Spectrometer Hall used by the A1 collaboration, contains three magnetic spectrometers called A , B and C , which are shown in Figures 3.1 and 3.4. The properties of these spectrometers are summarized in Table 3.1.

Spectrometers A and C are similar, and consist of quadrupole, sextupole and 2 dipole magnets (QSDD). They are characterized by a large solid angle, and point-to-point focusing in the dispersive plane ($x | \theta) = 0$. This makes x_{focal} independent of the initial angle θ_0 , and ensures good momentum resolution ($\sim 10^{-4}$). Both

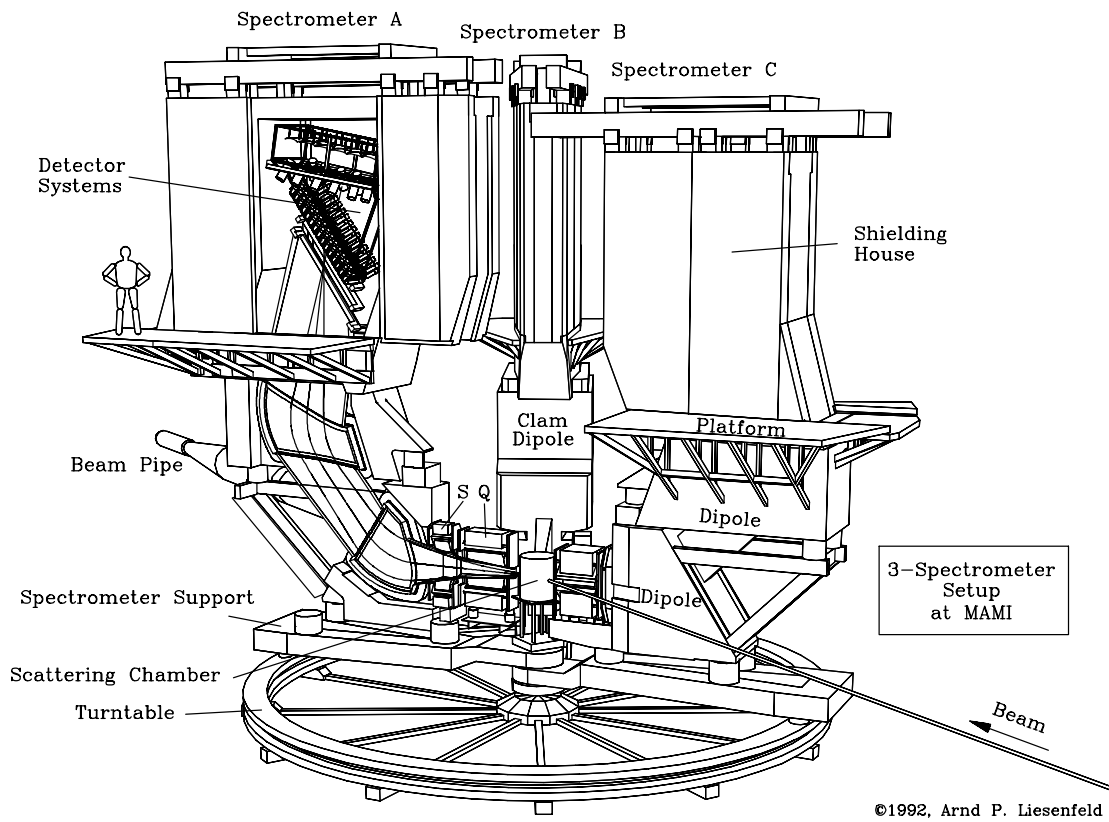


Figure 3.4: Magnetic spectrometers

spectrometers A and C have parallel-to-point focusing in the non-dispersive plane ($y \mid y) = 0$, so that y_{focal} is independent of the initial position y_0 . Parallel-to-point focusing in the non-dispersive plane allows optimal angle determination, but reduces the position resolution at the target.

Spectrometer B has point-to-point focusing in both planes, and as a result has high position resolution at the target, but smaller solid angle and momentum acceptance. It consists of a single dipole magnet.

Detector package

For each spectrometer the detection system included two vertical drift chambers (VDCs), triggered in the electron and proton spectrometers by a coincidence signal derived from two arrays of plastic scintillators. These scintillators were also

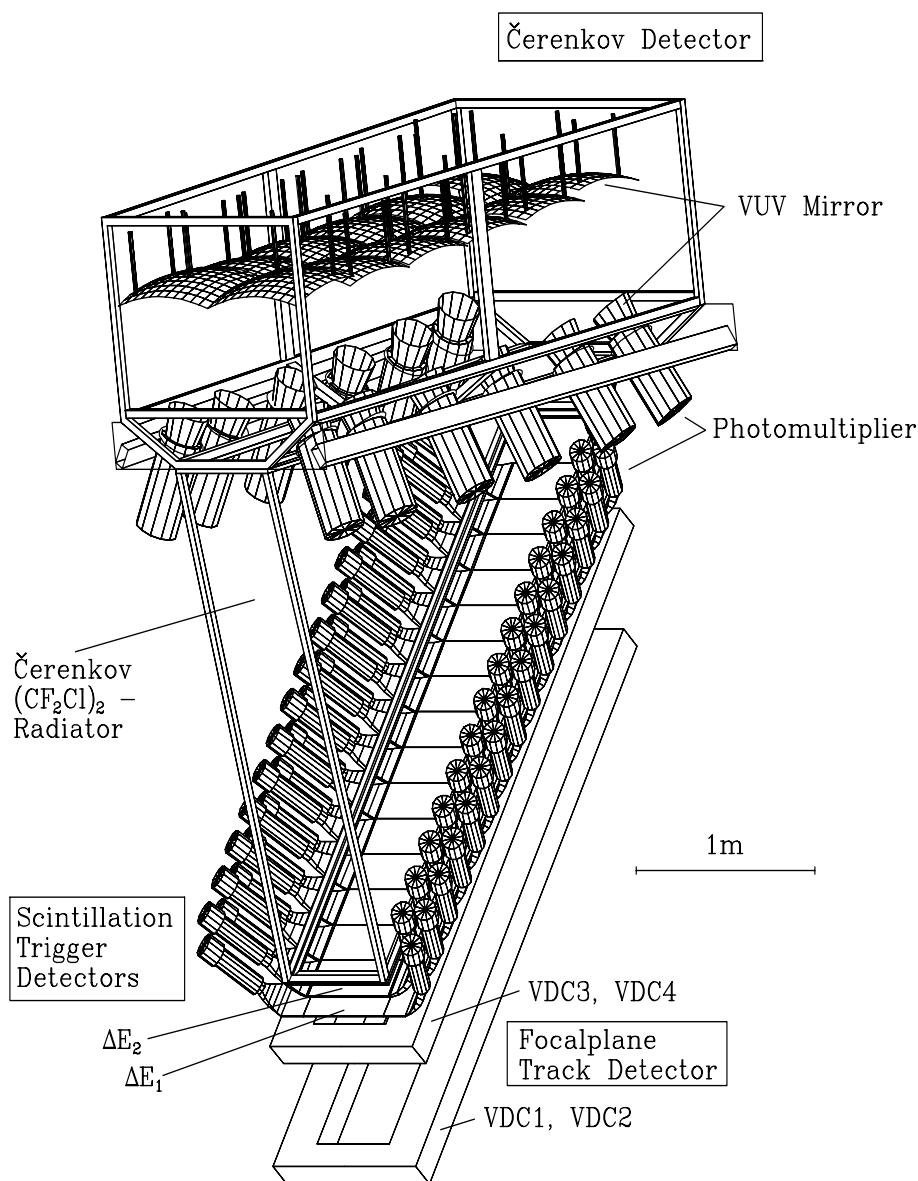


Figure 3.5: Detector package

used for particle identification by measuring specific energy losses. Two VDCs, placed in the focal surface, measured four focal-plane coordinates for each detected particle, and thus permitted full reconstruction of the particle trajectories. The scintillator array is followed by a gas Cherenkov detector used for electron identification (see Figure 3.5). The Mainz experimental setup is described in details in

spectrometer configuration	A QSDD	B <i>D</i>	C QSDD
maximum momentum [MeV/c]	735	870	551
max. centr. momentum [MeV/c]	665	810	490
maximum induction [T]	1.51	1.50	1.40
momentum acceptance [%]	20	15	25
solid angle [msr]	28	5.6	28
horizontal acceptance [mrad]	± 100	± 20	± 100
vertical acceptance [mrad]	± 70	± 70	± 70
long-target acceptance [mm]	50	50	50
scattering angle range [$^{\circ}$]	18-160	7-62	18-160
length of central trajectory [m]	10.76	12.03	8.53
momentum resolution	$\leq 10^{-4}$	$\leq 10^{-4}$	$\leq 10^{-4}$
angular resol. at target [mrad]	≤ 3	≤ 3	≤ 3
position resol. at target [mm]	6	1.5	6

Table 3.1: Properties of the magnetic spectrometers

reference [19].

3.2.1 Collimators

Each spectrometer has a number of available collimators designed to allow measurements with point and extended targets. The solid-angle value listed for Spectrometers A and C in Table 3.1 is the maximum solid angle, obtained using the 28 *msr* collimator. These collimators are used only for measurements with point targets. Spectrometer A, for example, has two other collimators 15 *msr* and 21 *msr* for extended targets.

The spectrometers were designed such that the collimators fully define their angular acceptance. The solid angle, as defined by the collimator geometry, and

the distance from the target to the collimator, is the real acceptance value of the spectrometer. In the measurements presented in this thesis, the 21 *msr* collimator for an extended target was used in Spectrometer A, a 5.6 *msr* collimator in Spectrometer B and a 22.5 *msr* collimator in Spectrometer C.

The collimator for Spectrometer B consists from four independent parts which can be moved separately. Therefore, the angular range defined by this collimator can be assymmetric about the central scattering angle. Additional information about collimation of Spectrometer A and B is given in Appendix A.

3.2.2 Vertical Drift Chambers

Each vertical drift chamber consists of two x -planes (dispersive) and two s -planes (non-dispersive). The VDCs are used to measure focal plane coordinates and the angles of detected particles. Each plane of the VDC has a series of parallel wires positioned between two parallel conducting planes. The wire plane is connected to ground potential, and the cathode foils are set to a negative high voltage (5.6 – 6.5 *kV*). The distance between adjacent signal wires is 5 mm, and particles crossing the VDCs at angles close to 45° , hit on average four cells in the s -plane, and five cells in the x -plane (see *multiplicity* in Figure 3.6). The number of wires varies between 300 and 400 for the s and x -planes, depending on the spectrometer (Figure 3.6). The efficiency of a single plane is normally between 97 % and 99 % and depends strongly on the high voltage, and specific ionization of the particle for the gas mixture (Ar+isobutane). The total efficiency for four of the VDCs planes is close to 100 %.

3.2.3 Scintillators

Each spectrometer has two scintillator planes. For Spectrometers A and C, each plane consists of 15 segments each $45\text{ cm} \times 16\text{ cm}$. For Spectrometer B there are 15 individual segments of area $14\text{ cm} \times 16\text{ cm}$. The small segment size reduces

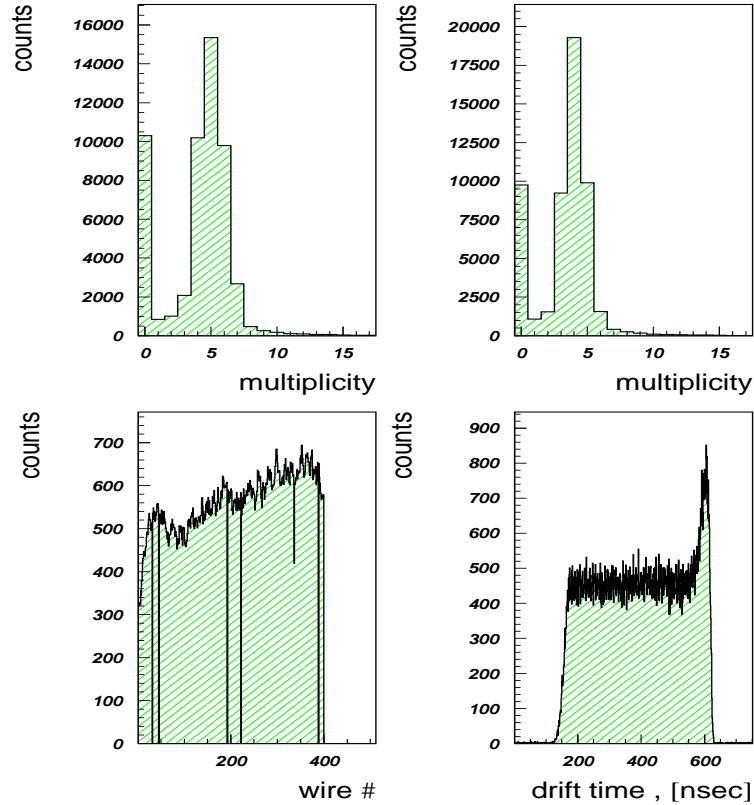


Figure 3.6: Multiplicity, number of wires and drift time in VDC

light losses and background rates, and allows good timing resolution. The thickness of the first layer is 3 mm (NE 102A plastic) and the second layer is 10 mm (NE Pilot U plastic). The second layer usually provides the fast timing signal, except in cases where heavy particles with low energy have to be detected. For Spectrometers A and C, each scintillator segment is viewed by two photomultipliers (PMTs) on opposite sides. For the short segments of Spectrometer B only one PMT is used per segment (Figure 3.5).

Using two layers of ΔE scintillators allows particle identification via measurements of the energy loss of particles with different specific ionizations. Separation of pions from protons can be readily achieved, however it was not possible to separate

electrons and pions since their specific energy losses are too similar. To achieve this a Cherenkov detector is used.

3.2.4 Cherenkov Detectors

The threshold Cherenkov gas detector follows the scintillation detectors (Figure 3.5), and is used to discriminate between minimum-ionizing particles (electrons and pions), and to remove the cosmic background contribution in single-arm measurements. Cherenkov light is generated in the radiator gas (Freon 114) with an index of refraction close to 1.0013. The Cherenkov angle θ_{Cher} can be determined from the simplified equation $\cos(\theta_{Cher}) = 1/(n \cdot \beta)$, where n is the refraction index and β is the particle velocity in units of c . For the known refraction index, the threshold β value is determined to be 0.9987, which for electrons or positrons means momentum ~ 10 MeV/ c , and for pions ~ 2700 MeV/ c . Cherenkov light is collected by a number of mirrors, which reflect light to the PMTs. Special light-collecting funnels at the entrance of the PMTs are used to collect as much light as possible. The efficiency of the Cherenkov detector is ~ 99.98 %.

3.3 Helium Target

Hardware

The Helium target used in this experiment was a high pressure (17-20 bars) and low temperature (20-21 K) 4He cell. The target cell was originally a cylinder with an internal radius equal to 4.00 cm and made from a high strength Al7075 alloy (details are in Table 3.2). The wall thickness of the target cell was approximately $230 \pm 10 \mu m$. After a high pressure test (~ 36 bar) the radius of the cell increased slightly to 4.05 cm .

This cell formed an integral part of the cryogenic loop shown in Figure 3.7. Warm helium gas was cooled in the cryogenic loop after passing through a liquid-

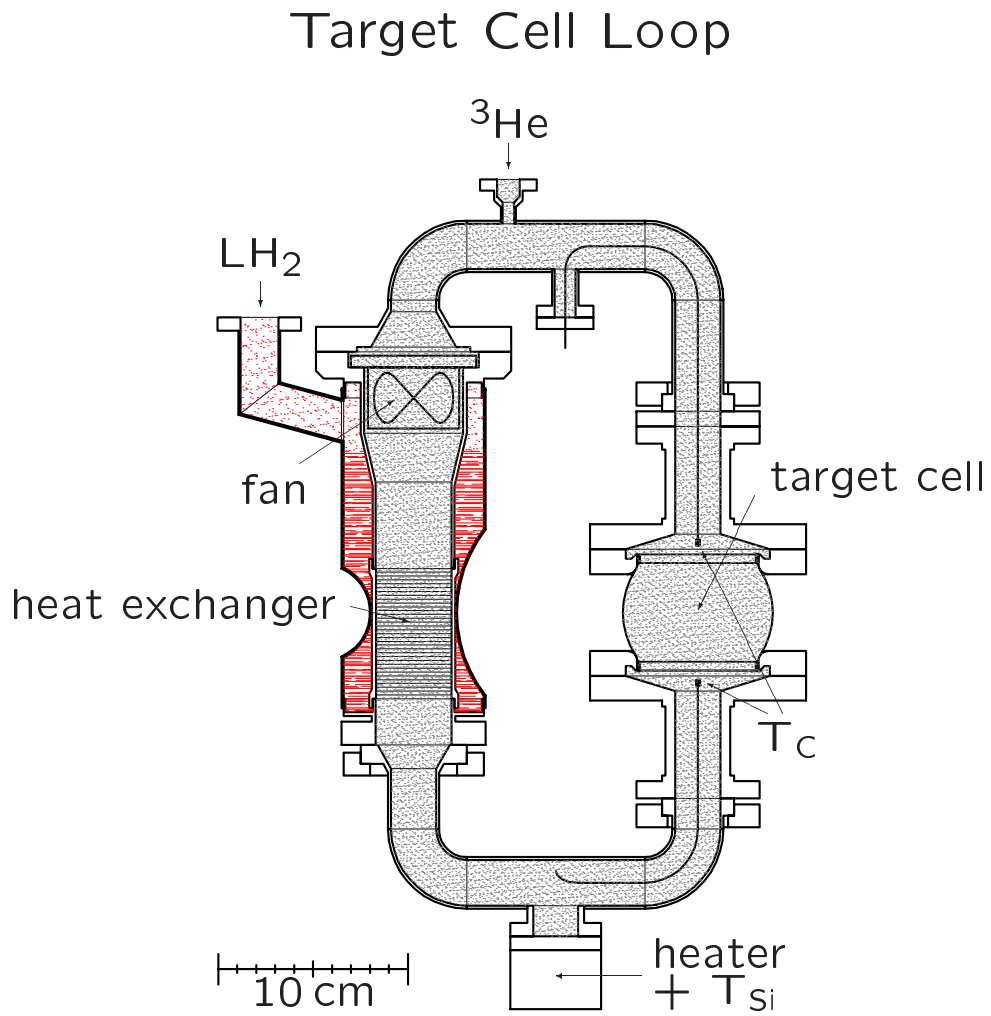


Figure 3.7: Helium cryogenic loop

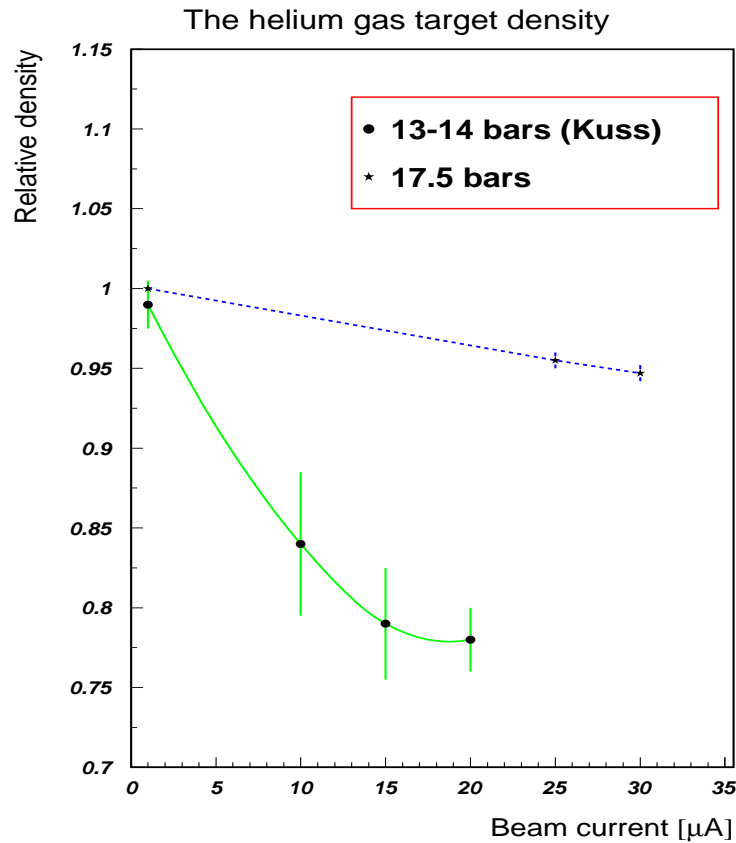


Figure 3.8: The helium-target density as a function of the beam current for two different densities of the helium gas

H_2 heat exchange. The liquid-hydrogen was delivered from the Phillips compressor through a long (~ 12 m) transfer line which was kept at the temperature of LN_2 . Gas circulation inside the cell was provided by a fan installed inside the loop at the top of the heat exchanger. When the loop was filled with the cold helium gas, the operation of the fan kept the whole system in equilibrium. Three resistors (T_C and T_{Si} in Figure 3.7) installed inside the target loop were used to monitor the temperature of the helium gas. They are located at the entrance and the exit of the target cell (T_C), and at the bottom of the target loop (T_{Si}). This latter resistor

can also be used as a heater to warm up the target loop quickly. Video cameras installed in the Spectrometer Hall allowed the gauges for measuring gas temperature and pressure to be monitored from the counting room.

Helium-density fluctuations

The electron beam deposits some energy in the *He* target, thus heating the gas along the beam. Consequently the density of the helium target depends on the beam current. This dependence had been measured by Kuss [20] for a lower pressure (13-14 bars) helium gas target. In Figure 3.8 one can see (lower curve) a strong dependence of the gas density on the beam current. This occurred despite beam rastering amplitudes (7×7 mm) which were supposed to reduce local heating effects. In the measurements presented in this thesis (dashed line) the beam rastering was 6×4 mm and the density reduction was only 5 % for a $30 \mu A$ beam current. This can be explained by a better performance of the new cryogenic system in the A1 Spectrometer Hall.

Helium-target thickness

The average density of the helium gas in the target loop, as a function of temperature and pressure, can be estimated using the ideal gas equation. The gas density, ρ_{He} , is $0.00017846 [g/cm^3]$ ($T_0 = 273$ K; $P_0 = 1$ bar). Thus, the helium gas density ρ_{He} is equal to $0.00017846 \cdot P V_0/V$. This gives a 4He density of $0.0426 [g/cm^3]$ for the pressure ($P = 17.5$ bar) and temperature ($T = 20$ K) used in this experiment. This value is in very good agreement with the helium gas density extracted from the elastic scattering data for the low beam current (details are in Table 4.5, Chapter 4).

Element	%	Z	M	eff.thickness [μm]
Cu	1.6	29	63.5	3.7
Mg	2.5	12	24.3	5.8
Cr	0.3	24	52	0.7
Zn	5.6	30	65.4	12.9
Al	90	13	27	207

Table 3.2: Material (Al7075) of the target cell

3.4 Data Acquisition System

The magnetic spectrometers detect all charged particles in the defined momentum range. When a particle passes through the individual detectors of the spectrometer, it deposits part of its energy and generates a response. The signals from these detectors are processed by the trigger circuit (see Figure 3.9) depending on the defined trigger condition. In general, the minimum trigger condition requires a hit of one of the ΔE scintillators (PMT noise is suppressed by requiring a coincidence between the two PMTs viewing each scintillator).

The signal from each PMT is split; one goes to the leading-edge discriminator (LeCroy 4413), and the other, via a delay ($\sim 550 - 800$ nsec depending on which spectrometer), to the ADC. This delayed signal arrives at the ADC in coincidence with the first signal that has passed the whole logic circuit, and an interrupt is generated to trigger digitalization in the ADCs, and the readout sequence (Figure 3.9). Each spectrometer operates independently, with multiple triggers allowing pre-scaling of various combinations of events. Processing of trigger signals is done by a programmable lookup unit (PLU) which allows different combinations of trigger conditions to be used.

During the (e,e'p) measurements, a specific trigger combination called "ab-MIT" was used. This allows single-event detection in all spectrometers, and coincidences only between Spectrometers A and B. This was done to avoid any coincidence events

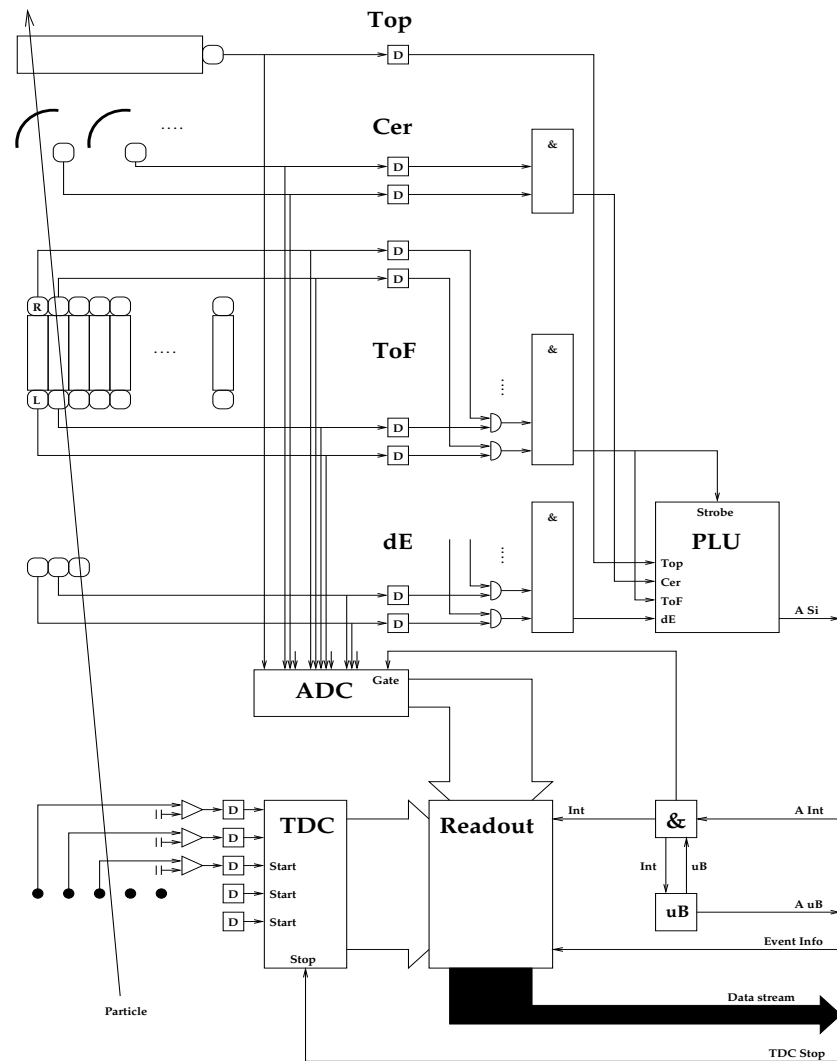


Figure 3.9: The detector system: a particle first crossing VDCs, then dE and ToF detectors (which are the 1st and 2nd scintillator layers), the Cherenkov detector (Cer) and the Top scintillator

between Spectrometers B and C and Spectrometers A and C. The minimum trigger condition for each spectrometer was a coincidence of two segments in the two ΔE scintillator layers. The scaling-factor values were set to obtain a 10-20 Hz single-event rate in Spectrometers A and B, in addition to the coincidence data which were collected without any pre-scaling.

Spectrometer C was used as a luminosity monitor in the present experiment,

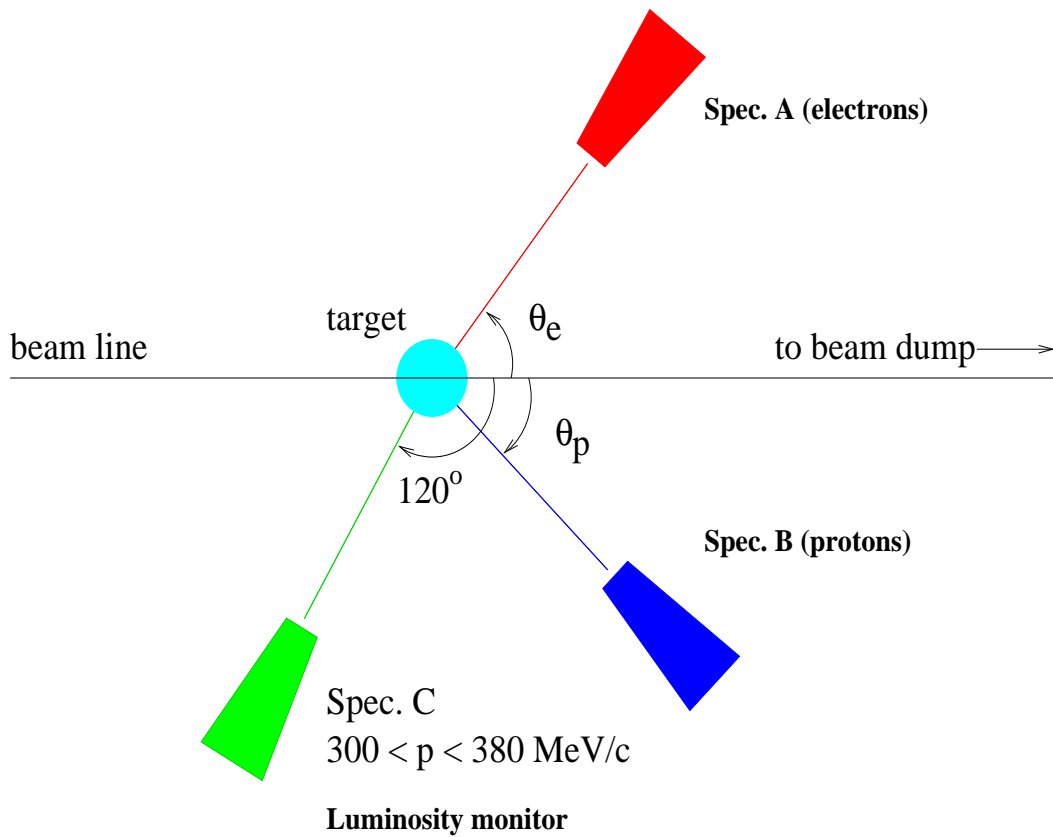


Figure 3.10: Experimental setup as it was used for the $(e,e'p)$ measurements

and the number of electrons detected in this spectrometer defined the statistical uncertainty in the helium-density calculations. In Spectrometer C the minimum trigger condition also included a signal from the Cherenkov detector. This was necessary because of high background (non-electron) rates in this spectrometer. Thus, the scaling factor for Spectrometer C was set to obtain at least 20-25 Hz of singles, and provide enough data for the helium density calculations.

The Mainz experiment control system (ECS), and data acquisition system MECDAS [22], provided the software for diagnosing, controlling and for data handling. On-line and off-line analysis were done with the Mainz COLA++ code [21].

	Kinematic 1	Kinematic 2	Kinematic 3
E_{beam} [MeV]	570.11	675.11	855.11
ϵ	0.160	0.373	0.603
$ \vec{q} $ [MeV/c]	685	685	685
θ_{cent}^A [deg]	109.22	77.11	53.23
θ_{cent}^B [deg]	18.99	29.03	37.54
P_{cent}^A [MeV/c]	236.09	341.09	521.09
P_{cent}^B [MeV/c]	790	790	790

Table 3.3: ${}^4\text{He}(e, e'p)$ measurements

3.5 ${}^4\text{He}(e, e'p)$ experiment

Details of the kinematics used to measure the ${}^4\text{He}(e, e'p)X$ reaction are given in Table 3.3. Spectrometer B was used as a proton detector, Spectrometer A defined the electron arm of the reaction, and Spectrometer C was used as a luminosity monitor, (Figure 3.10). The reason of this selection was that only Spectrometer B could analyse the required high-momentum protons. The measurements were performed at a fixed 3-momentum transfer of $\vec{q} = 685 \text{ MeV}/c$. The energy transfer ω was selected to be 334 MeV , corresponding to the high ω side of the QE peak ($\omega_{QE} = 242.7 \text{ MeV}$ according to the definition given in Equation 2.8). The value of the y -scaling variable corresponding to the required energy and momentum transfer was $+140 \text{ MeV}/c$ (see Eq. 2.7).

The measurements were performed at three different beam energies in order to obtain three independent points with different virtual-photon polarization ϵ , thus allowing Rosenbluth L/T separation to be performed. The proton spectrometer angles were chosen to agree with the definition of "parallel" kinematics, (where the momentum of the detected proton \vec{p}_p is parallel to the 3-momentum transfer \vec{q}). In reality this condition is true only for the central value, and θ_{pq} spans the range

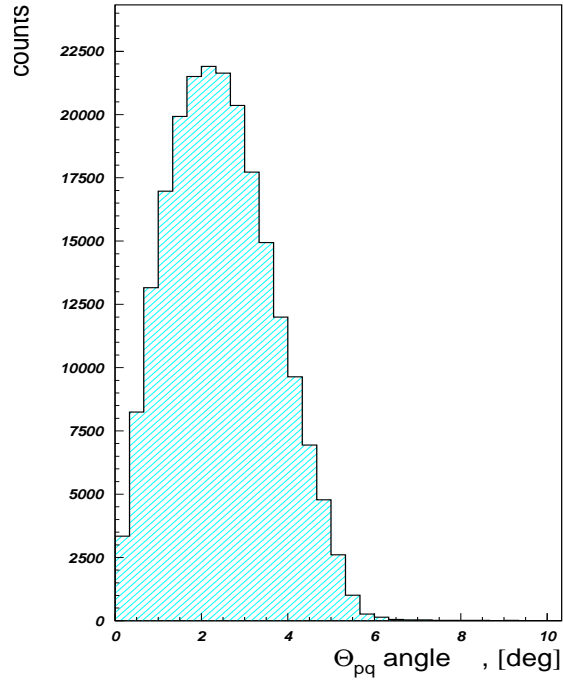


Figure 3.11: The angle θ_{pq} between the proton momentum \vec{p} and 3-momentum transfer \vec{q} between 0 and 5 degrees due to the finite angular acceptance of Spectrometer B (Figure 3.11). The missing-energy and missing-momentum range covered in these kinematics is slightly different and is shown in Figure 3.12.

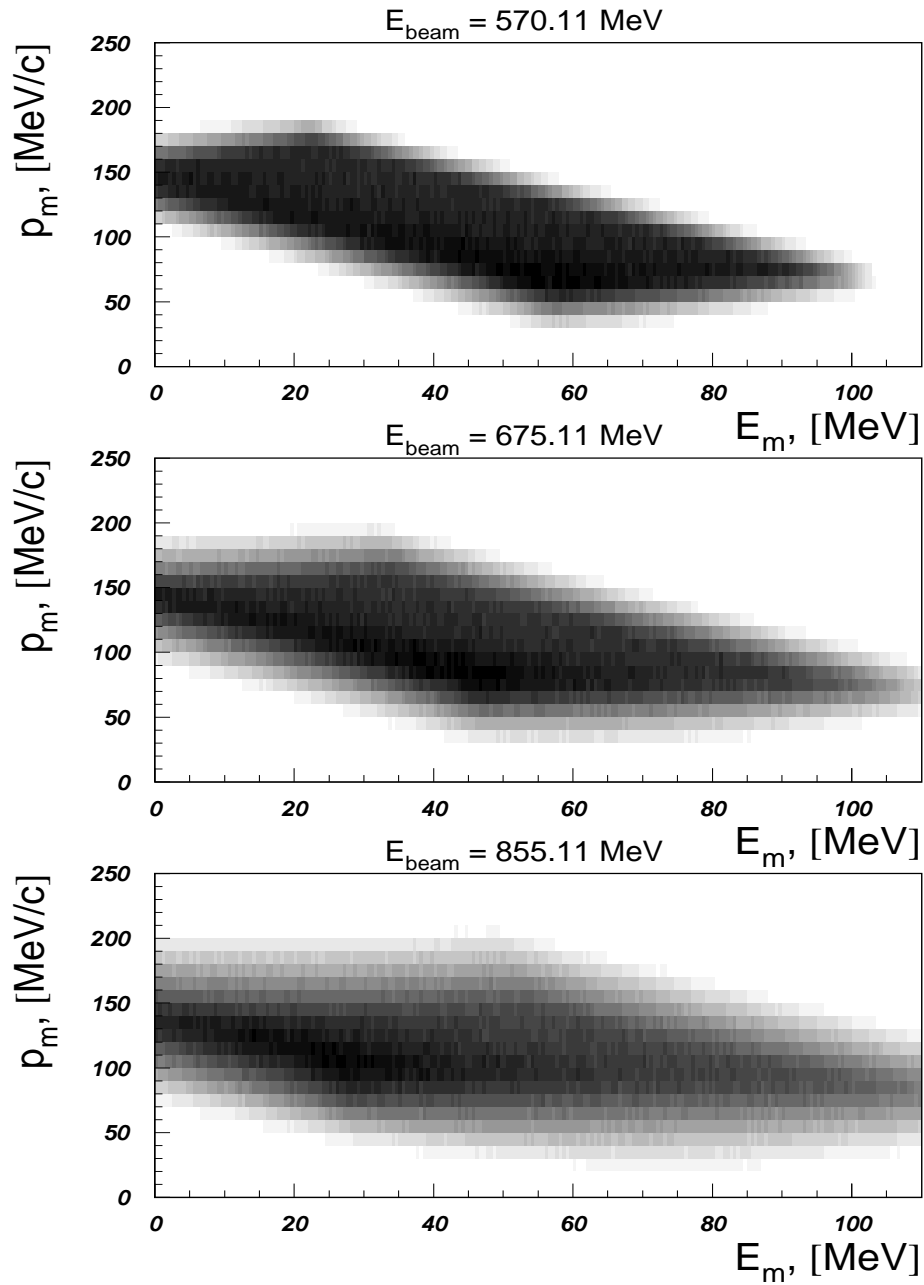


Figure 3.12: (E_m, P_m) range covered in the (e,e'p) measurements

Chapter 4

Calibration of Experimental Components

4.1 Overview

This chapter reports calibration measurements made with carbon and helium targets, which were performed to ensure the quality of the principal experiment of this thesis, viz. the coincidence (e,e'p) data.

4.1.1 Calibration of the Spectrometers

Sections 4.2 and 4.3 describe the measurements with a point carbon target, where the following properties of the magnetic spectrometers and the whole setup were studied:

a) angular and momentum resolution for both Spectrometer A and B (Section 4.2);

Good angular and momentum resolution are important factors, which define, for example, several systematic uncertainties contributing to the (e,e'p) cross section error. The accuracy of the angular software cuts and corresponding angular acceptance values; the missing-energy and missing-momentum resolution are dependent on the angular and momentum resolution of the spectrometers.

Measurements with a sieve slit were made in order to study the angular resolution of Spectrometer A at high detected momentum, and to correct the offsets of the VDCs in the standard matrix elements for an extended target, used in the analysis of the $(e, e'p)$ data. These measurements provided an answer as to whether the standard matrix elements for an extended target are still valid in the saturation region of the spectrometer, or in other words, whether the angular resolution of Spectrometer A becomes worse than its nominal value.

Although Spectrometers A and B are characterized by high momentum and angular resolution, additional studies were required since at one kinematical setting for Spectrometer A, and at all kinematics for Spectrometer B, the momenta of the detected particles were at the limit of the spectrometer's acceptance. This is the region where strong saturation effects, resulting in a reduction of the spectrometers momentum resolution, were observed in both spectrometers.

Measurements with a point carbon target were used to develop a new correction procedure for such physical variables as the *kinematically-corrected* momentum and *missing energy*. This compensates for non-linear aberrations of the detected momentum. In addition, the definition of the *kinematically-corrected* momentum is introduced.

The new offsets of the VDCs for the back-tracing matrix for Spectrometer A were calculated. Use of the standard matrix elements for Spectrometer A in the saturation region was confirmed.

b) absolute normalization (Section 4.3);

The absolute cross section for elastic scattering $^{12}\text{C}(e, e')$ was measured and compared to the theoretical predictions. It was done to investigate the possible acceptance and efficiency losses for both Spectrometers A and B. It was important to know whether the cross section value for a simple point target can be reproduced in the present measurements. The ^{12}C nucleus was selected, since there are many high quality cross section measurements performed by various laboratories.

Moreover, an accurate MEFIT code [29] for the calculation of the elastic scattering cross section was available.

The measured elastic cross section values were found to be in a good agreement with the theoretical predictions.

c) trigger scintillators efficiency (Section 4.4).

These measurements were performed to study the observed focal-plane inefficiency for the electron arm spectrometer. The high-voltage values of the PMTs were not properly adjusted, so that some of the scintillator segments had an efficiency for electron detection of less than 100 %. The relative efficiency of each scintillator segment was obtained, using the quasi-elastic $^{12}C(e, e')$ scattering, and a correction factor was introduced to compensate the observed efficiency loss.

4.1.2 Helium-Target Density Measurements

The measurements of $^4He(e, e')$ elastic scattering were used to determine the absolute density of the helium gas target (Section 4.5). The accuracy of this value directly affects the accuracy of the measured absolute (e,e'p) cross section, thus a reliable value for the target density is crucial for the absolute normalization of the experiment.

The target density was calculated, with a systematic uncertainty of 2.6-3 % by comparing the experimental cross section to that calculated using a new Monte-Carlo program, which is based on the published elastic form factors for 4He (see also Appendix B). These target-density values were used as the reference values for the calculations of the helium-target density during the (e,e'p) measurements.

4.2 Angular and Momentum Resolution of the Spectrometers

4.2.1 Elastic $^{12}\text{C}(e, e')$ Measurements with the Sieve Slit in Spectrometer A

Overview

These measurements were used to solve two independent problems:

- 1) the correct offsets of the VDCs in a standard matrix for an extended target, calculated for a central momentum of $495 \text{ MeV}/c$ for Spectrometer A were obtained. A good knowledge of these offsets is important, since this matrix is used in all data analysis of $(e, e'p)$ and elastic calibration measurements on helium. There are a number of software cuts made in the data analysis, and the angular acceptance of the spectrometers is partially or completely defined by these. Thus, uncertainty in the offset values creates a systematic uncertainty in the $(e, e'p)$ absolute cross section value, and this should be as small as possible. Moreover, the accuracy of the offsets is particularly important for elastic scattering from ^4He , due to the strong angular dependence of the measured cross section. Recall it is this measurement which is used to determine the absolute density of the helium target used in the $(e, e'p)$ measurements.
- 2) The angular resolution of Spectrometer A was measured at a central momentum value of $652.5 \text{ MeV}/c$. The angular resolution of Spectrometer A is important since poorer resolution would cause an increase of the systematic uncertainty of the absolute $(e, e'p)$ cross section value, due to uncertainties resulting from the angular software cuts used in the data analysis.

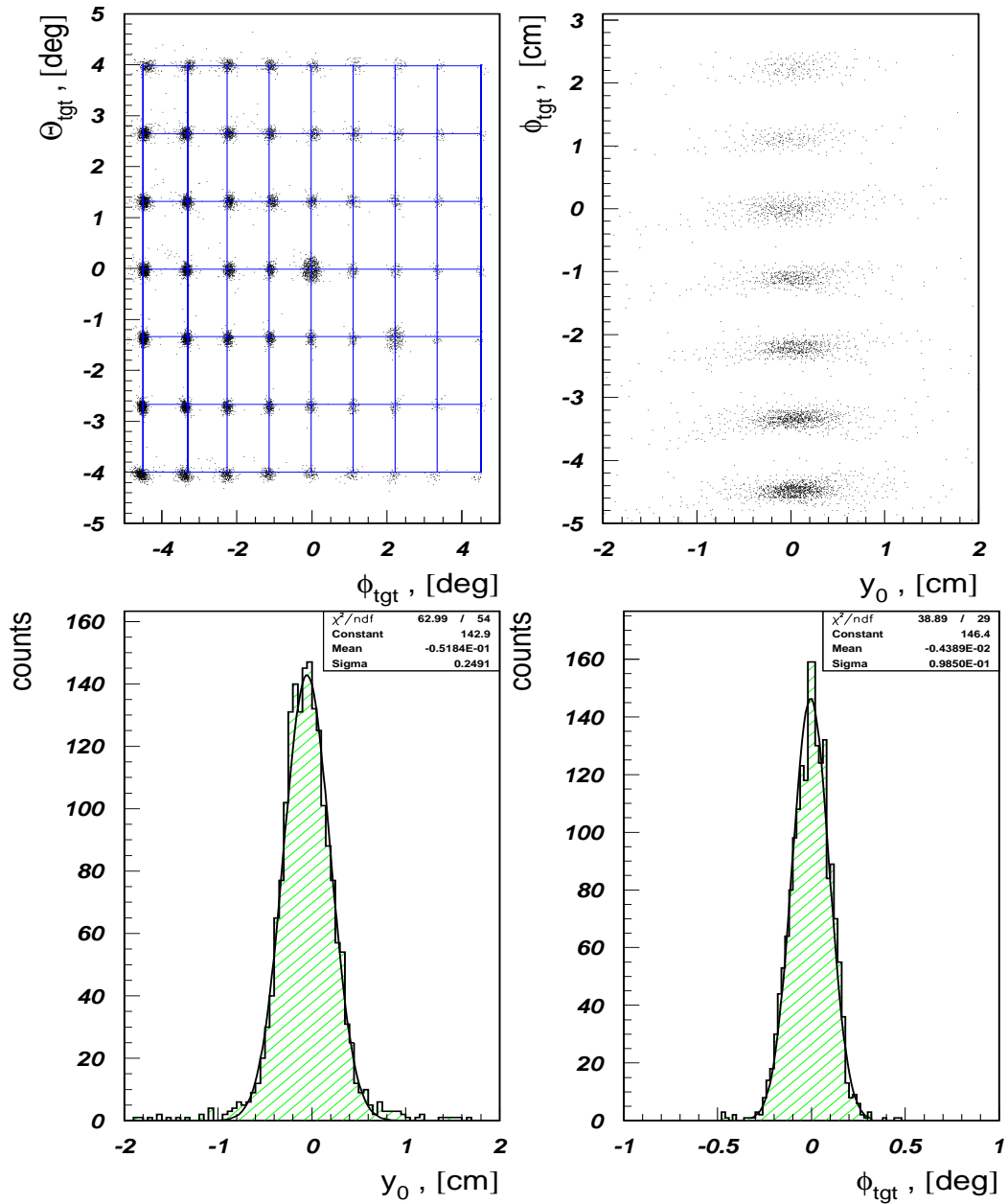
$^{12}\text{C}(e,e')$ 

Figure 4.1: The sieve slit picture at $E_{beam} = 495.11$ MeV. The fit of y_0 and ϕ_{tgt} was done for the central hole only.

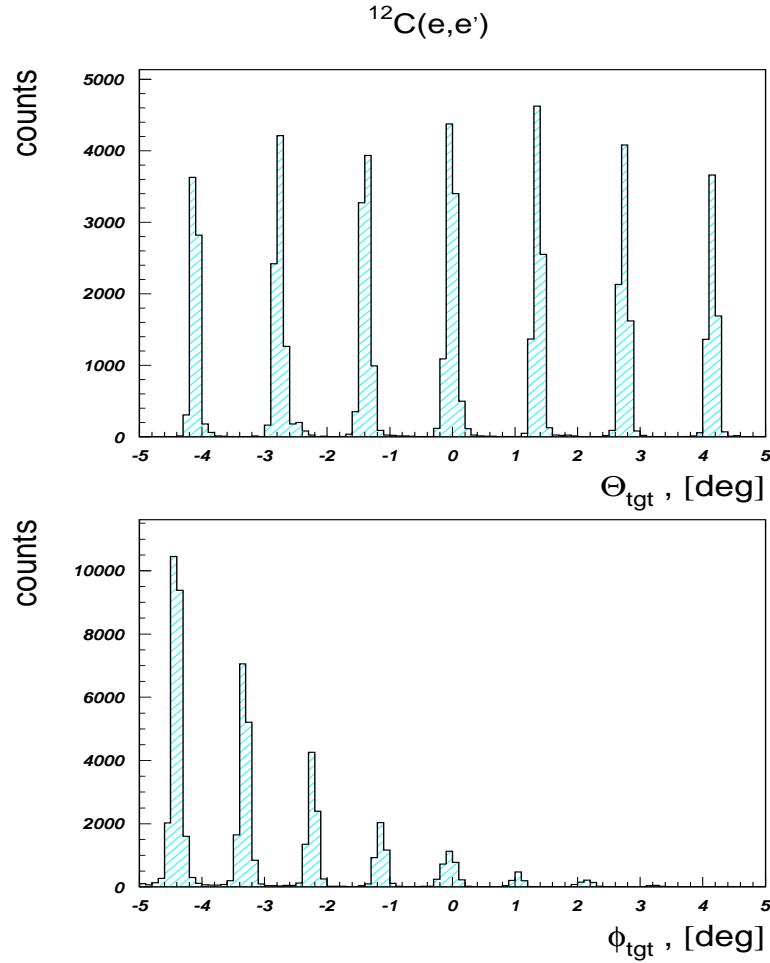


Figure 4.2: Sieve slit picture at $E_{beam} = 630.11$ MeV.

Measurements and results

Measurements with the sieve slit [30] were performed using Spectrometer A at two beam energies (495.11 and 630.11 MeV). During these measurements the absolute beam position was determined as 0 ± 0.1 mm in both the horizontal and vertical directions, using the information from the beam cavities (see Chapter 3). Any uncertainty in the beam position creates an uncertainty in both the vertical and horizontal angles equal to $\Delta = 0.1/R_0 \approx 0.16$ mrad, where $R_0 \sim 600$ mm is the distance to the collimator of Spectrometer A. The value of this uncertainty is thus

an order of magnitude smaller than the nominal angular spectrometer resolution (3 mrad), and was neglected.

$$E_{beam} = 495.11 \text{ MeV}$$

A narrow (0.3 MeV) cut was placed about the elastic peak to reduce the background contribution and to select events which pass through the sieve slit holes without any re-scattering. The position of the carbon target along the beam line was +1 mm towards the beam dump. Therefore, the VDCs offsets were adjusted to keep the θ_{tgt} and ϕ_{tgt} coordinates at zero, and $y_0 \approx z_{tgt} \cdot \sin(\theta_0)$ at -0.5 mm (Figure 4.1). Only the central hole of the sieve slit, which defines the real central scattering angle of the spectrometer, was used to make offset adjustment. Again, only events from the central hole were used to define the y_0 offset, because of the dependence of y_0 on the other coordinates, Figure 4.1.

$$E_{beam} = 630.11 \text{ MeV}$$

During these measurements the central momentum of Spectrometer A was set to 652.5 MeV/c, which is close to the value used in one of the measurements of the elastic scattering cross section from helium. At this central momentum value, which is close to the maximum, saturation effects in the momentum spectra are very strong. No significant *angular* aberrations are visible in Figure 4.2. The angular resolution at the edges of the acceptance, and at the center of the sieve slit is the same, and equal to $\sim 2 \text{ mrad}$ (FWHM), which is the nominal value. That means that the standard matrix elements can be safely used at higher central momenta for Spectrometer A.

Summary

In the measurements with the sieve slit, the new offsets of the VDCs for Spectrometer A were calculated.

No signs of the angular resolution deterioration were observed during the measurements with the sieve slit in the saturation region of Spectrometer A. The mea-

sured angular resolution was $\sim 2 \text{ mrad}$, which is close to its nominal value.

4.2.2 Momentum corrections

Two independent correction procedures for the detected and *kinematically – corrected* momentum are described below.

The first one is a standard correction, which compensates the angular dependence of the particle's detected momentum by introducing a new variable called *kinematically – corrected* momentum.

The second correction is new. It can be applied to the momentum already corrected for angular kinematic broadening, or in case of the (e,e'p) measurements, to the missing-energy value, in order to compensate dependence of these variables on the focal plane θ_{focal} coordinate (see Figures 4.5 and 4.6).

Angular Kinematic Broadening

Due to the finite angular acceptance of the spectrometers, the detected momentum of elastically scattered electrons is dependent on the scattering angle. This is the so-called momentum *kinematic broadening*. By introducing a new variable, normally called *kinematically – corrected* momentum, one can remove this dependence (Figure 4.3). The final energy of an elastically-scattered electron is defined by the Equation:

$$E_f(\theta) = \frac{E_i}{1 + \frac{E_i}{M_A} \cdot \sin^2\theta/2} \quad (4.1)$$

where $E_f(\theta)$ is the energy of the elastically-scattered electron, θ is the scattering angle, E_i the initial electron energy, and M_A the mass of the target nucleus. For relativistic electrons the momentum $p \approx E$, and the kinematically-corrected momentum p_{kin} was calculated as:

$$p_{kin} = p - p(\theta) + p(\theta_0) \quad (4.2)$$

where θ_0 is the central scattering angle of the spectrometer, and p is the momentum of the elastically-scattered electron.

Kinematically-corrected momentum aberrations

The $^{12}\text{C}(e, e')$ elastic measurements were performed using Spectrometer A (Kinematic 1 and 2) and Spectrometer B (Kinematic 3), details are in Table 4.1. The standard matrix elements for an extended target (qsdda495.mxl2 and bclam495.mlx9), obtained at $495 \text{ MeV}/c$ central momentum, were used for the analysis of the data. In Kinematic 2 and 3, the momenta of the particles are in the saturation regions of the spectrometers, and the kinematically-corrected momenta become dependent on θ_{focal} (Figure 4.5). This dependence is found to be a combination of first and second-order aberrations of p_{kin} . Therefore p_{kin} was corrected according to the equation:

$$p_{kin} = p_{kin} + A \cdot (\theta_{focal} - \theta_{focal}^0) + B \cdot (\theta_{focal} - \theta_{focal}^1)^2 \quad (4.3)$$

where θ_{focal}^0 and θ_{focal}^1 are constants, and A and B are the empirical coefficients which were obtained in an iterative procedure by optimizing the width of the elastic line. The definitions of all these variables are fully explained in Figure 4.6.

Summary

The correction procedure used to produce the kinematically-corrected electron momentum (Equation 4.3) was found to be reliable. The momentum corrections worked properly over the whole range of electron momenta. This can be seen in Figure 4.10, which shows the momentum of scattered electrons from $^{12}\text{C}(e, e')$ after kinematic correction and correction for θ_{focal} aberrations. All excited ^{12}C states have similar resolution, and there is no indication that at higher excitation energies these corrections create non-linear effects. The same procedure was used to correct the missing energy spectra for measurements of helium elastic and (e,e'p) reactions.

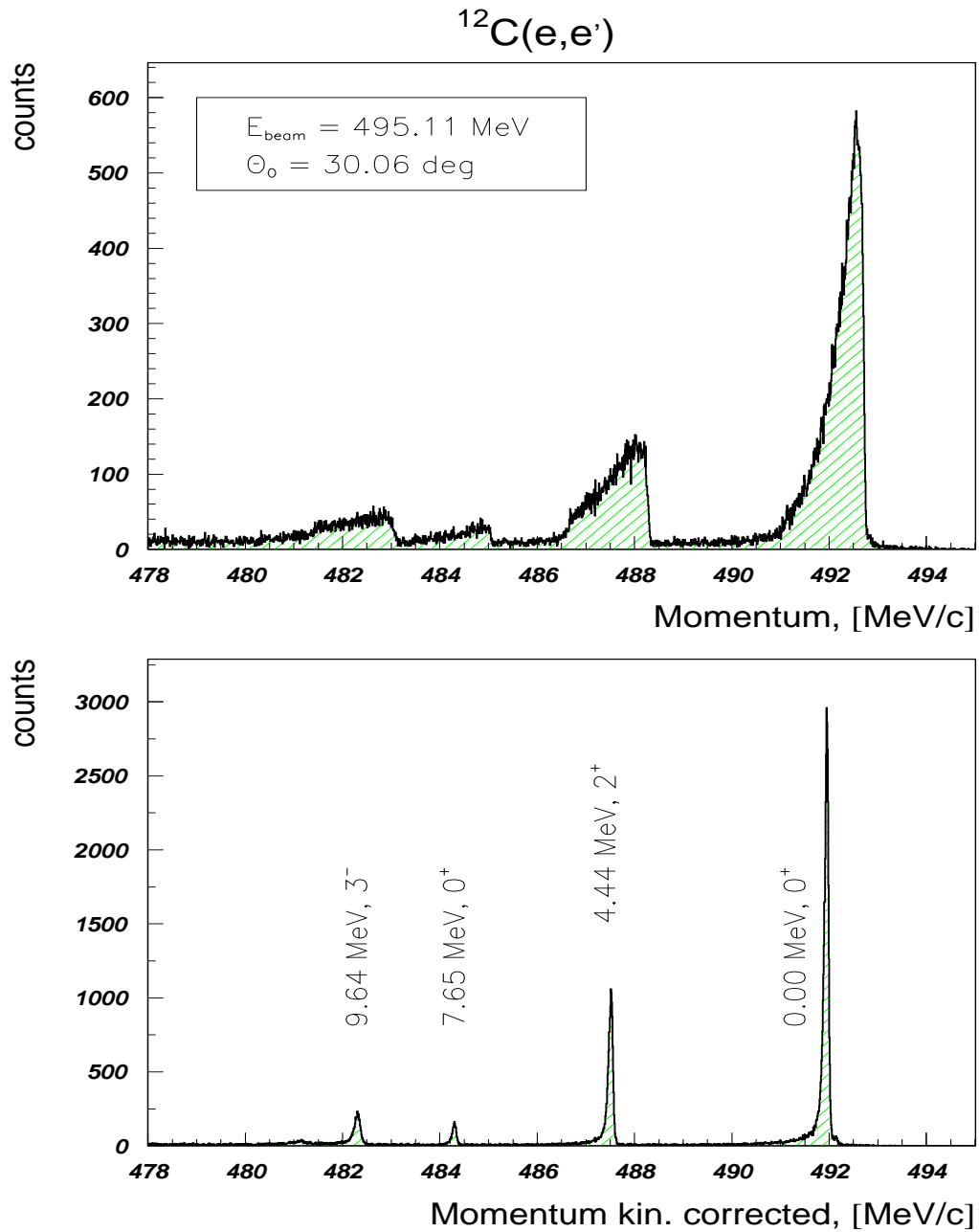


Figure 4.3: The $^{12}\text{C}(e,e')$ momentum spectrum before (top) and after the correction for the kinematic broadening.

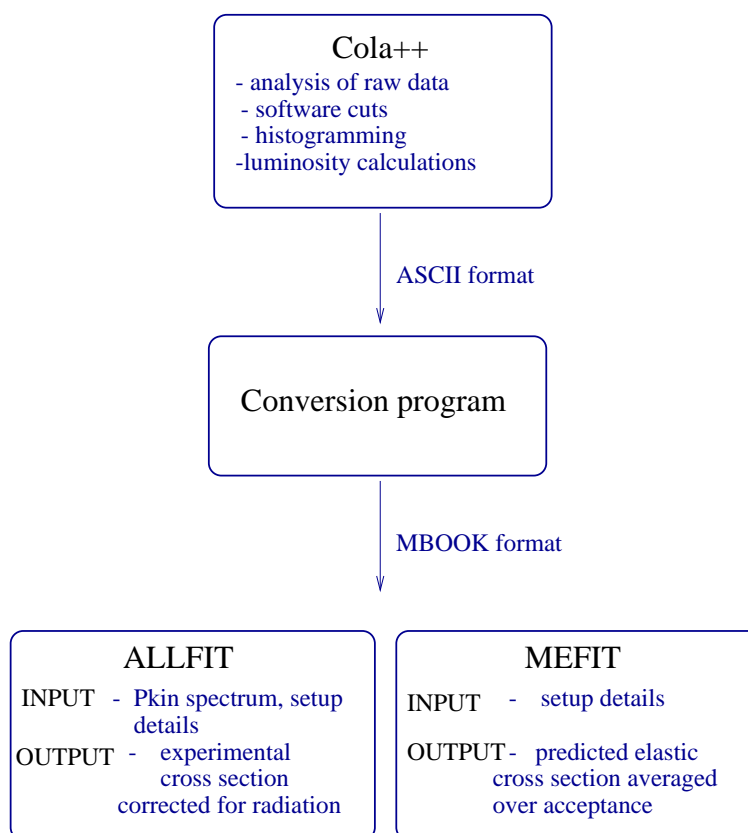


Figure 4.4: The $^{12}\text{C}(e, e')$ data analysis

4.3 Absolute $^{12}\text{C}(e, e')$ cross section for elastic scattering

The purpose of these measurements is to study the absolute efficiency of the experimental setup. To do this, the absolute $^{12}\text{C}(e, e')$ cross sections for elastic scattering, averaged over the spectrometers acceptance, are extracted and compared to the theoretical predictions based on a large number of published experimental data. This procedure provides an independent test of the hardware and software systems and helps to estimate the possible systematic normalization error.

The simplified overview of the analysis steps is presented in Figure 4.4.

4.3.1 Theoretical $^{12}\text{C}(e, e')$ Elastic-Scattering Cross Sections

The predicted ^{12}C elastic scattering cross section was obtained from the phase-shift code *MEFIT* (see ref. [29]). In this program a large collection of the world's measurements of elastic scattering from the ^{12}C is used as an input. Some other experimental parameters, such as the angular acceptance of the spectrometer $\pm\theta_{tgt}$ and $\pm\phi_{tgt}$, the central scattering angle of the spectrometer, the beam energy, and the target thickness have to be defined in the program input. The program determines the charge density through a fit of a large number of the experimental data points, including an additional point where the prediction of the cross section for elastic scattering is required. At this additional kinematic point the cross section value is set to 1.0 and assigned very large error bars, so that any influence of this value on the fit is avoided. The program output is the cross section at this point for elastic scattering (in units fm^2/sr) averaged over the experimental acceptance of the spectrometer, and corrected for Coulomb distortions and energy loss in the target. It is assumed that scattering occurs at the middle of the target. The calculated values of the elastic cross section $\frac{d\sigma_{el}}{d\Omega}$ are given in the Table 4.1.

4.3.2 Measured $^{12}\text{C}(e, e')$ Elastic-Scattering Cross Sections

Cross-section definition

A 32.5 mg/cm^2 carbon foil with an isotopic abundance of $\sim 98.9\%$ ^{12}C was used as the target for these measurements. The carbon purity was better than 99.95% and the density was 1.8 g/cm^3 . The experimental cross section was calculated according to the Equation:

$$\frac{d\sigma_{exp}}{d\Omega} = 10^{26} \times \frac{N_{cor} \cdot A_C \cdot \eta_{eff}}{\Delta\Omega_{spec} \cdot \left(\frac{Q_{tot}}{q_e}\right) \cdot \rho_C \cdot N_A \cdot (1 - \tau_{eff}) \cdot \epsilon_{tot}} \quad (4.4)$$

where

N_{cor} = number of counts, corrected for the radiation by ALLFIT

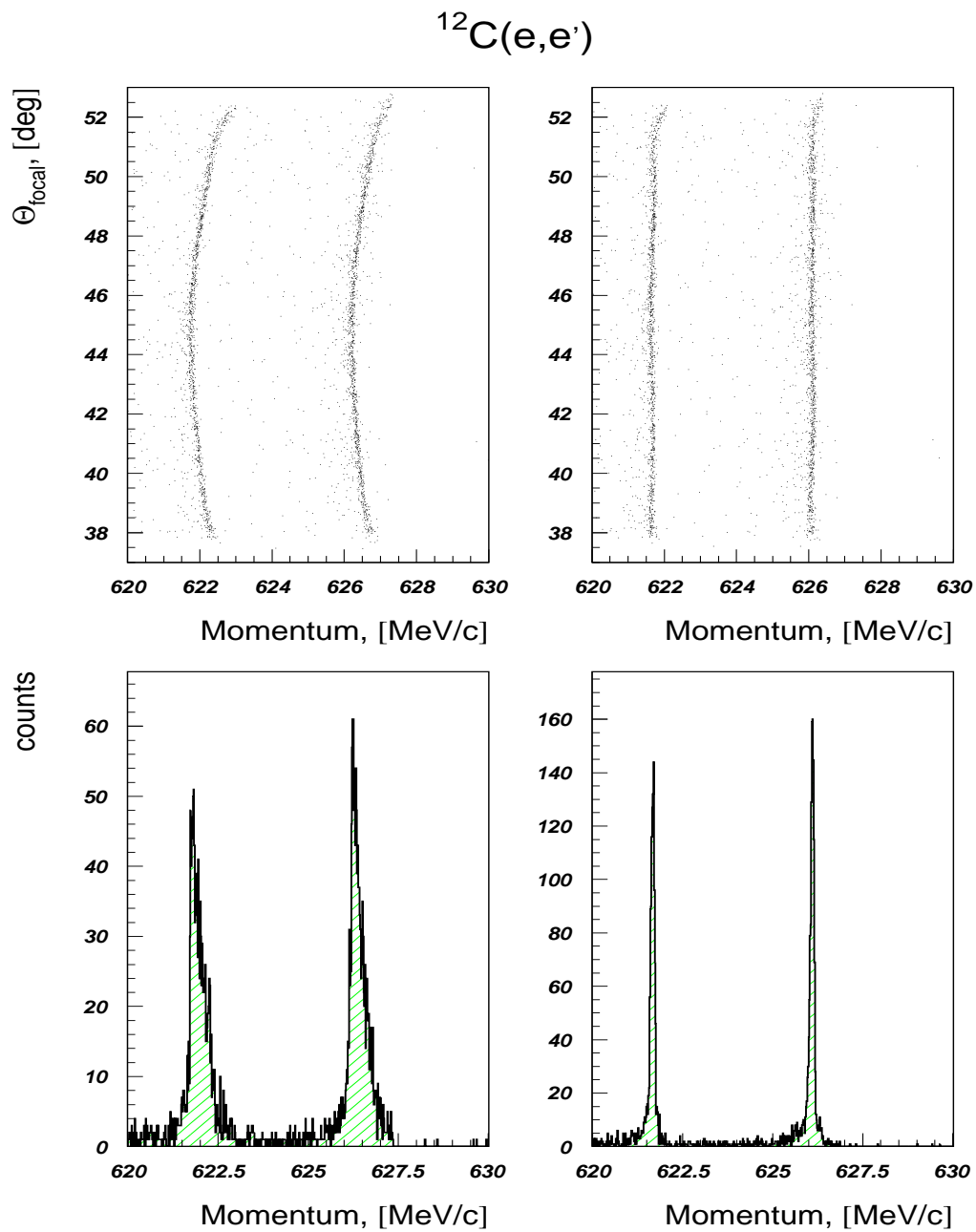


Figure 4.5: The $^{12}\text{C}(e,e')$ elastic line in Kinematic 2. The momentum corrected from θ_{focal} dependence (right); uncorrected momentum (left)

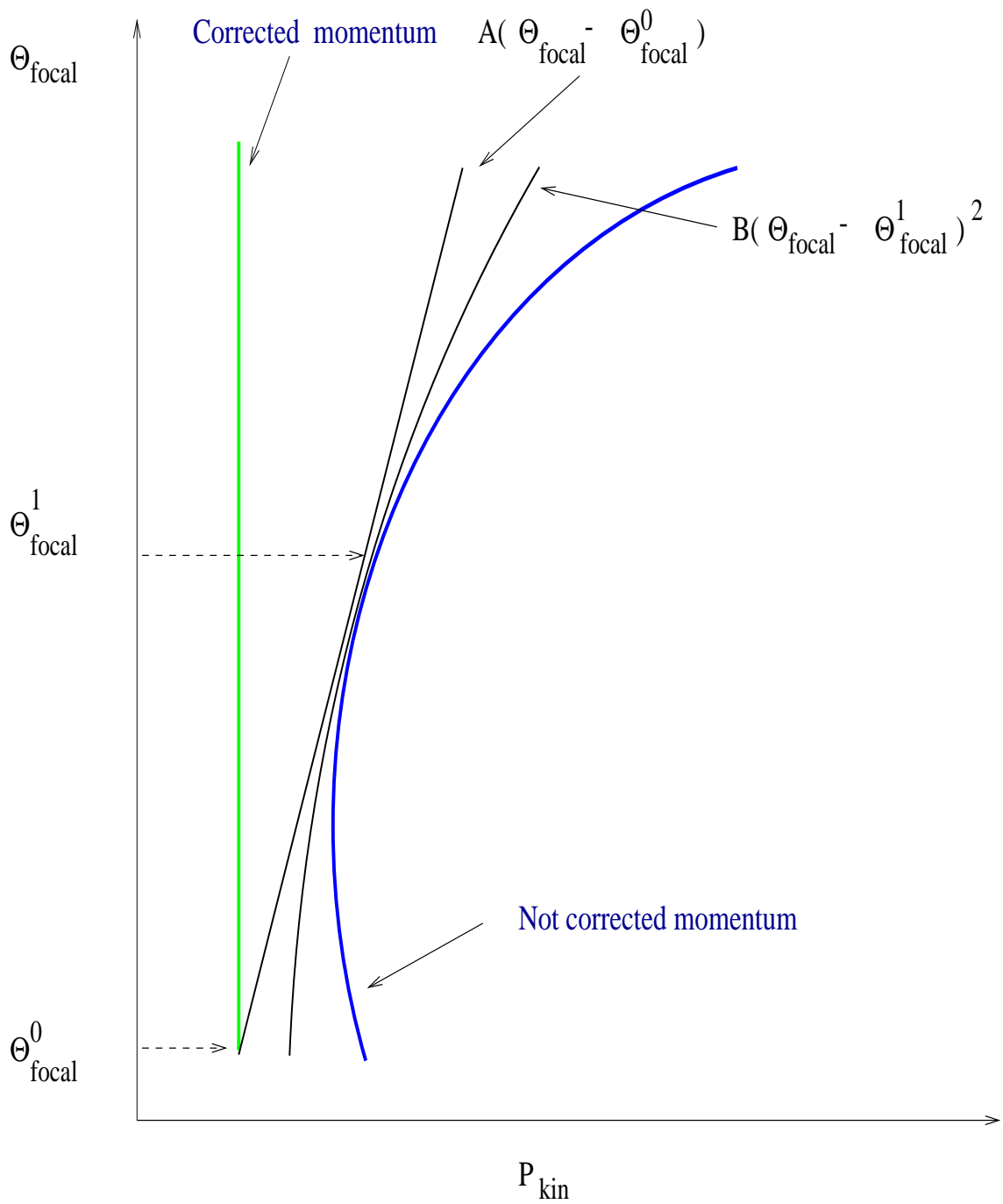


Figure 4.6: The $^{12}C(e, e')$ elastic line correction which compensates dependence on θ_{focal} coordinate

$A_C = 12.0$ [g/mol] the mass of the target

η_{eff} = effective scaling factor (see Eq. 4.5)

$\Delta\Omega_{spec}$ = spectrometer solid angle in [sr]

Q_{tot} = total charge [in C]

$q_e = 1.602 \times 10^{-19}$ [C] elementary charge

$\rho_C = 0.03211$ [g/cm²] the density of the ¹²C isotope in the target

$N_A = 6.022 \times 10^{23}$ [1/mol] Avogadro number

τ_{eff} = effective dead time (see Eq. 4.6)

ϵ_{tot} = detector efficiency

Radiative corrections

Radiative corrections for the elastic scattering cross section were performed using the existing *ALLFIT* code [24]. A sample of the Carbon elastic peak after the *ALLFIT* fitting procedure is shown in Figure 4.9. In this code, the elastic line is treated as an asymmetric hyper-Gaussian in the central region, with two exponential tails; there are nine fitting parameters. *ALLFIT* also makes a correction for the ionization energy loss of the beam electrons, assuming that the scattering occurs in the middle of the target. This corrected beam-energy value is also used in calculations of the radiative corrections.

External and internal bremsstrahlung, and Landau straggling were taken into account in calculating the radiative tail. The target thickness along the beam line was used as an input parameter for the calculations of external bremsstrahlung and Landau straggling of the incident and scattered electrons. *ALLFIT* output includes important fitting parameters such as χ^2 , the percentage of the data used in the fit, the values of the fitting parameters for the peaks and the background, and the absolute and statistical error. All these values were used to monitor the fit quality, and to optimize and reduce errors in the fitting procedure. The final output of *ALLFIT* is the elastic cross section in fm^2/sr units corrected for the radiation.

Luminosity calculations

Some elastic events were detected as random AB coincidence events, and were assigned deadtime and scaling factors corresponding to these AB coincidence events. This effect was corrected for by introducing an effective scaling factor η_{eff} , and deadtime τ_{eff} calculated from their single and double values weighted by the corresponding number of the events in the particular run:

$$\eta_{eff} = \frac{N_{single} \cdot \eta_{single} + N_{double} \cdot \eta_{double}}{N_{double} + N_{single}} \quad (4.5)$$

$$\tau_{eff} = \frac{N_{single} \cdot \tau_{single} + N_{double} \cdot \tau_{double}}{N_{double} + N_{single}} \quad (4.6)$$

The total charge collected, and the dead-time values, were calculated using the Mainz COLA++ program.

Software cuts

The criterion for selection of the elastic events was a coincidence between a hardware scintillator trigger and a signal in the Cherenkov detector. In Kinematic 3, an additional software cut $\phi_{tgt} = \pm 19 \text{ mrad}$ was applied to make the horizontal acceptance of Spectrometer B symmetric, and to properly match the *MEFIT* symmetric angular input.

Trigger inefficiency

It was shown in Chapter 3, that the trigger scintillators are divided into small segments. When a particle crosses the edge of a segment, the path through the scintillator is shorter than normal, and the energy deposition in the segment is less. This reduction in the deposited energy leads to a reduction in trigger efficiency. This effect is clearly seen in the case of quasi-elastic measurements (see Figure 4.11), described below in detail. In this figure the coordinate x of the scintillator plane is a projection of the focal plane x coordinate onto the position of the scintillators

in the spectrometer. In Kinematic 2, a reduction of trigger efficiency in the regions between the scintillator segments was observed, and in this case the reduction in detector efficiency was accounted for in the cross section calculations. The trigger inefficiency was estimated as an average number of events lost in projection of the elastic line to the x -scintillator plane.

Corrections of the spectrometers angular acceptance

The position of the ^{12}C target was $+1\text{ mm}$ along the z axis, and known with an accuracy of $\pm 1\text{ mm}$ (Figure 4.7). These values were obtained during the target alignment with theodolites before the measurements. It is clear from Figure 4.7 that the central scattering angle, and the range of horizontal angles accepted by the spectrometer varies for different target positions. The Monte-Carlo code *DUMP* (details are given in Appendix B) was used to obtain the correct range of the horizontal angles ϕ_{tgt}^{min} and ϕ_{tgt}^{max} corresponding to the target position shifted by $+1\text{ mm}$ (see Table 4.1). These values were used to calculate a symmetric horizontal angular acceptance of the spectrometer $\pm\phi_{tgt}$ as:

$$|\pm\phi_{tgt}| = \frac{(\phi_{tgt}^{min} + \phi_{tgt}^{max})}{2}$$

The change in the central scattering angle θ_0 , due to target displacement, is thus equal to $|\phi_{tgt}| - |\phi_{tgt}^{min}|$. The correct central scattering angle also can be calculated from the formula:

$$\theta_{cent} = \theta_o + \frac{\delta z \cdot \sin\theta_o}{R_o} \quad (4.7)$$

where θ_o is uncorrected central scattering angle, δz is the absolute shift of the carbon target from the zero position, and R_o is the distance to the collimator of Spectrometer A or B from the target (see Figure 4.7). The solid angle of the spectrometer $\Delta\Omega$ can be calculated as:

$$\Delta\Omega \approx 4 |\phi_{tgt}| \cdot |\theta_{tgt}|$$

		Kinematic 1	Kinematic 2	Kinematic 3
E_{beam}	[MeV]	495.11	630.11	810.11
central momentum	[MeV/c]	492.6	652.4	790
ϕ_{tgt}^{min}	[deg]	-4.392	-4.357	-1.089
ϕ_{tgt}^{max}	[deg]	4.241	4.270	1.089
θ_{tgt}	[deg]	4.0095	4.007	4.011
$\theta_{cent} \pm \phi_{tgt}$	[deg]	30.056 ± 4.317	27.023 ± 4.314	18.006 ± 1.089
solid angle $\Delta\Omega$	[msr]	21.044	21.067	5.323
beam position Δx	[mm]	0.35 ± 0.5	0.0 ± 0.5	0.1 ± 0.5
total charge	[mC]	3.214	1.875	4.476
Dead time	[%]	9.0	8.2	4.4
Scaling factor		59.95	22	119.65
trigger efficiency	[%]	100.0	99.7	100.0
$\frac{d\sigma_{exp}}{d\Omega}$	[$10^{-3} fm^2 / sr$]	0.4884	0.1619	1.120
$\frac{d\sigma_{th}}{d\Omega}$	[$10^{-3} fm^2 / sr$]	0.5140	0.1576	1.149
$\frac{d\sigma_{exp}}{d\Omega} / \frac{d\sigma_{th}}{d\Omega}$		0.950	1.028	0.975

Table 4.1: The summary for the $^{12}C(e, e')$ elastic measurements

4.3.3 Experimental Uncertainty of the Measured Cross Section

The systematic uncertainty of the experimental cross section is defined mostly by the target thickness uncertainty, the uncertainty in the central scattering angle, and results from the target and the beam-position error (see Table 4.2 and Figure 4.7).

The target thickness was estimated by measuring the target dimensions and weight (ref. [27]). The uncertainty in these measurements led to an absolute uncertainty of the target thickness of $\pm 2\%$, but the real target thickness at the beam

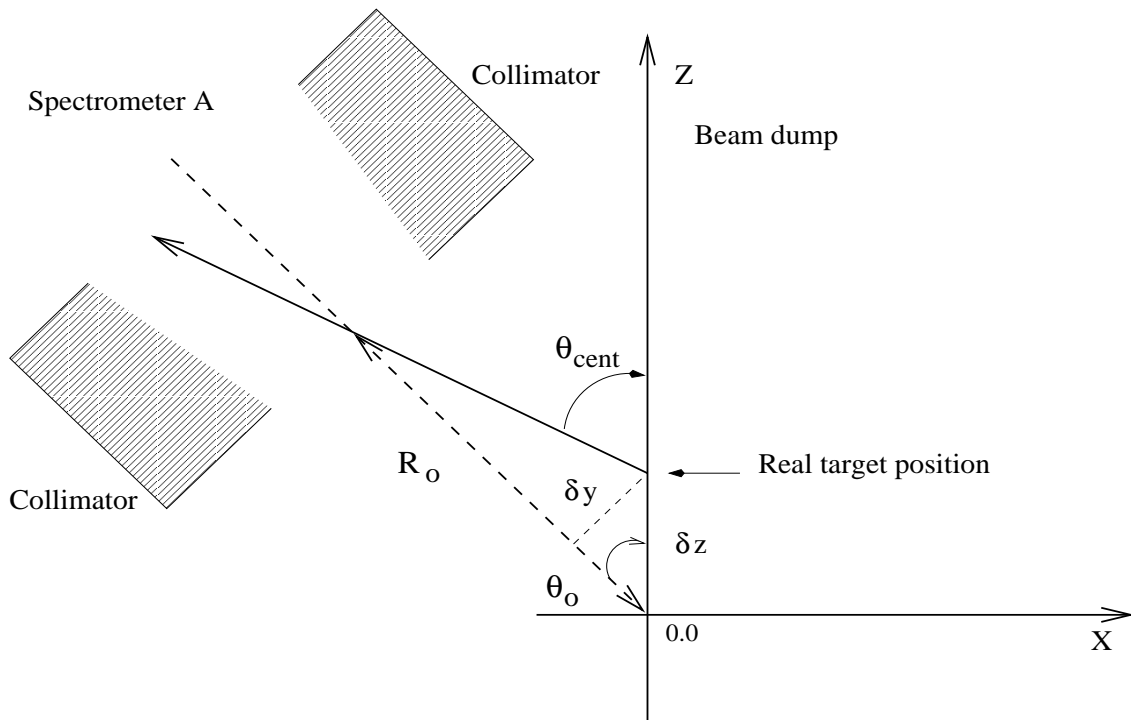


Figure 4.7: The $^{12}\text{C}(e, e')$ elastic data; the correction of the central scattering angle of the spectrometers

spot was unknown. It is possible that after usage the target suffers some radiation damage from the high beam currents, and the target thickness near the beam position may differ from its average value.

The error in the cross section due to the uncertainty in the target position was determined from the change in the cross section calculated by *MEFIT* code for a target displaced from its central position by $\pm 1\text{ mm}$. The same procedure was used to estimate the changes in the cross section due to the other large source of systematic error: the uncertainty in the horizontal beam position on the target. This was monitored using the beam cavities (see Chapter 3). For small scattering angles, knowledge of the horizontal beam position is more important than knowledge of the absolute z coordinate of the target, due to the relation between both values by $\delta z = \delta x / \tan(\theta_0)$ (see Figure 4.7). The uncertainty in the horizontal beam position

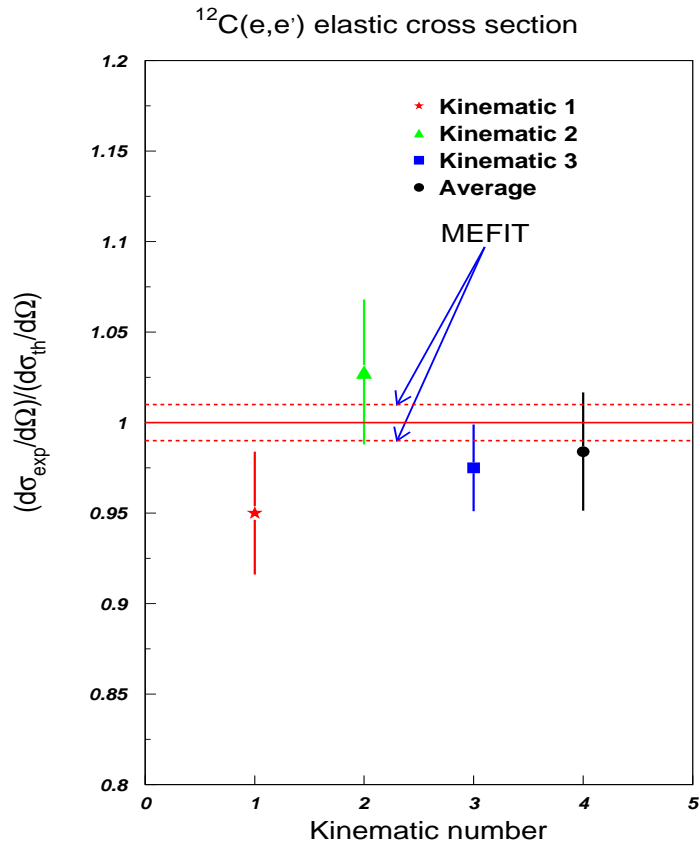


Figure 4.8: Summary of $^{12}\text{C}(e, e')$ elastic measurements

was taken as $\pm 0.5\text{ mm}$, based on observed beam-position drifts using a ZnS target.

The ALLFIT error is the sum of the statistical error and the fitting error. The last is normally small for a good quality fit. The ALLFIT error was significant only for Kinematic 3, where the target and beam-position errors were small due to the much longer distance from the target to the collimator of Spectrometer B: $\sim 314\text{ cm}$, compared to 60.5 cm for Spectrometer A.

The accuracy of the *MEFIT* predictions is estimated to be $\pm 1\%$, which is the average uncertainty for the experiment values of the elastic $^{12}\text{C}(e, e')$ cross section, that are used as input for the cross section calculations. This particular uncertainty was not taken into account when the absolute error of the experimental

	Kinematic 1	Kinematic 2	Kinematic 3
χ^2	1.28	1.16	1.4
fit sum [%]	100.00	100.07	99.98
ALLFIT error [%]	0.51	0.74	0.86
target-thickness error [%]	2.0	2.0	2.0
charge error [%]	0.1	0.1	0.1
dead-time error [%]	0.1	0.1	0.1
target-position error [%]	1.9	2.5	0.45
beam-position error [%]	1.8	2.2	0.4
beam-energy error [%]	0.7	0.7	0.7
total error [%]	3.4	4.0	2.4

Table 4.2: The summary of the fit quality parameters from ALLFIT and the individual uncertainties contributed to the total error of the $^{12}\text{C}(e, e')$ elastic cross sections ($\pm\Delta\sigma/\sigma$)

cross section was calculated.

The deadtime, and the charge collection errors were negligible ($\sim 0.1\%$) each.

Summary

The strong dependence of the elastic scattering cross section on the central scattering angle of the spectrometers, and large uncertainties in the target and beam positions, made it difficult to achieve better than 2-3 % agreement between the individual experimental results and the theoretical calculations. Nevertheless, the average cross section value is in good agreement with the MEFIT predictions (see Figure 4.8). This result confirms the absence of any significant undetected efficiency losses in the detector systems of both Spectrometers A and B, and the validity of the data analysis procedure.

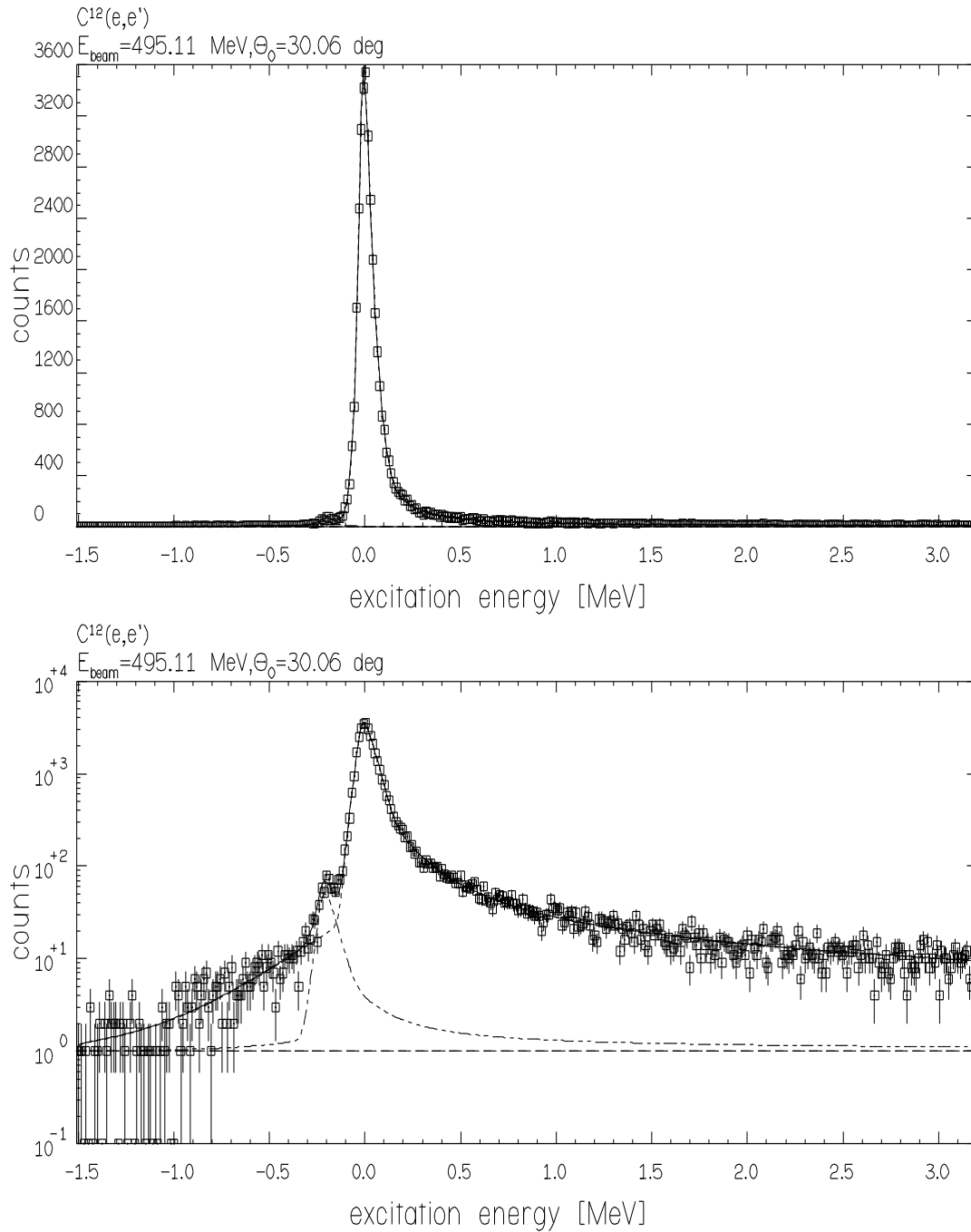


Figure 4.9: The Carbon elastic line in $^{12}\text{C}(e, e')$; the solid line shows the ^{12}C elastic peak, and the dashed line is ^{13}C background

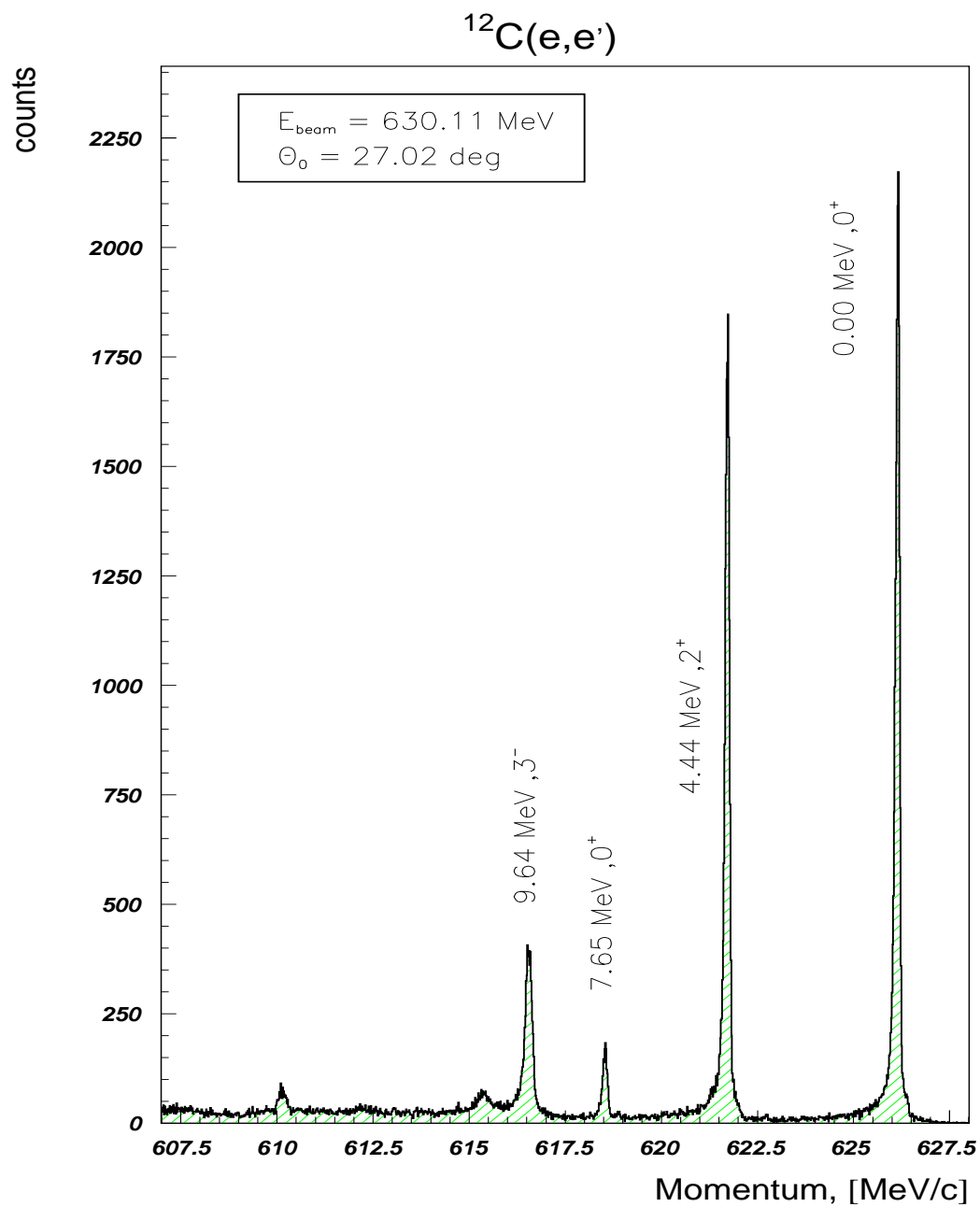


Figure 4.10: The $^{12}\text{C}(e,e')$ measurements in Kinematic 2. The electron momentum was corrected for θ_{focal} aberrations

E_{beam}	[MeV]	810.11	810.11	810.11	810.11
$\theta_{central}$	[deg]	45.0	45.0	45.0	45.0
Central momentum	[MeV/c]	585	615	645	675
total charge	[mC]	4.196	4.101	1.339	6.512
Dead time	[%]	8.7	8.7	9.095	8.31
Scaling factor		4	4	2	4

Table 4.3: The $^{12}\text{C}(e, e')$ quasi-elastic kinematics

4.4 Quasi-elastic $^{12}\text{C}(e, e')$ Measurements

The purpose of these measurements was to study the relative trigger efficiency of the individual scintillator segments of Spectrometer A. During the experiment, the same measurements were used "on-line" to correct the scintillator PMTs high voltages and increase the efficiency of a number of the scintillator segments.

To do that, Spectrometer A was set to the kinematic region corresponding to the QE peak. The QE scattering cross section changes smoothly over the acceptance range of the spectrometer, so that a large part of the focal plane is uniformly covered by scattered electrons: analogous to a "white noise" spectrum. In a few steps (see Table 4.3) with different central electron momenta for the spectrometer, the whole focal plane was studied, and the relative efficiency of all the scintillator segments was determined. This is the so-called δ -scan of the focal plane.

Data analysis

As in the case of elastic data analysis, only a coincidence of the hardware scintillator trigger with a signal from the Cherenkov detector was used as the selection criterion for real QE events. In order to compare measurements made with different central momenta, the raw counts, N_{raw} , in the momentum spectrum were

corrected for deadtime, scaling factors and luminosity:

$$N_{eff} = \frac{N_{raw} \cdot \eta_{eff}}{Q_{tot} \cdot (1 - \tau_{eff})} \quad (4.8)$$

where N_{raw} is the number of raw counts in each bin of the histogram, η_{eff} is the scaling factor, τ_{eff} is the deadtime, and Q_{tot} is the total charge collected [in mC].

As a result of these corrections, the effective number of counts N_{eff} is proportional to the QE scattering cross section. The value of N_{eff} must be the same for a given momentum value if the triggering efficiency for each scintillator segments is the same. The full momentum range of Spectrometer A is shown in Figure 4.12. The error bars shown on the plot are the statistical uncertainty in the corresponding number of raw counts in a particular histogram bin.

Results

In Figure 4.12 the following important features of the momentum spectra behaviour are clear:

- 1) The $585 \text{ MeV}/c$ data points deviate from the other settings in the momentum range between 610 and $640 \text{ MeV}/c$. A similar effect is seen in the $615 \text{ MeV}/c$ data between the 645 and $665 \text{ MeV}/c$. This inefficiency in the scintillator trigger comes from the inefficiency ($\sim 9 \%$) of segment #12 in the first dE layer of Spectrometer A (see Figure 4.11).
- 2) The data points taken at a central momentum of $675 \text{ MeV}/c$ are systematically shifted from the other measurements, due to an incorrect momentum reconstruction at this high detected momentum.

Summary

The relative efficiency of the scintillator segments was studied. The inefficiency of one particular dE segment was observed and estimated to be 9% . In the analysis of the coincidence (e,e'p) data, this inefficiency was taken into account by weighting

each event triggered in paddle #12 by a factor $w_i = 1/\epsilon_i$, where ϵ_i is the efficiency of this scintillator segment.

4.5 Elastic electron-scattering measurements on ${}^4\text{He}$

4.5.1 Introduction

The temperature and pressure of the helium gas inside the helium-target loop can be used to calculate an average helium density in the system to an accuracy $\sim 5\%$. The real density of the helium target in the area along the beam cannot be calculated in such a way, due to its dependence on the beam current (see Figure 3.8). In order to obtain the thickness of the helium target the following procedure was used:

- measurements of the elastic scattering cross sections ${}^4\text{He}(e,e')$ were made for the same beam-energy values as were used to collect the $(e,e'p)$ coincidence data;
- the theoretical elastic cross section was calculated for each kinematic, and the absolute thickness of the helium target during these measurements was determined by comparing the measured results to the predicted values.

The experimental cross sections were extracted from the elastic data with ALLFIT code, using the first estimate of the helium-target density, and then adjusting the experimental cross section value to the calculated cross section by varying the initial helium density in ALLFIT.

- Spectrometer C was positioned at a fixed angle with a fixed central momentum setting during the elastic, and the $(e,e'p)$ measurements. By using the target density obtained from the elastic data as a reference value, and the number of events detected in Spectrometer C, the real thickness of the Helium target during the $(e,e'p)$ measurements was calculated.

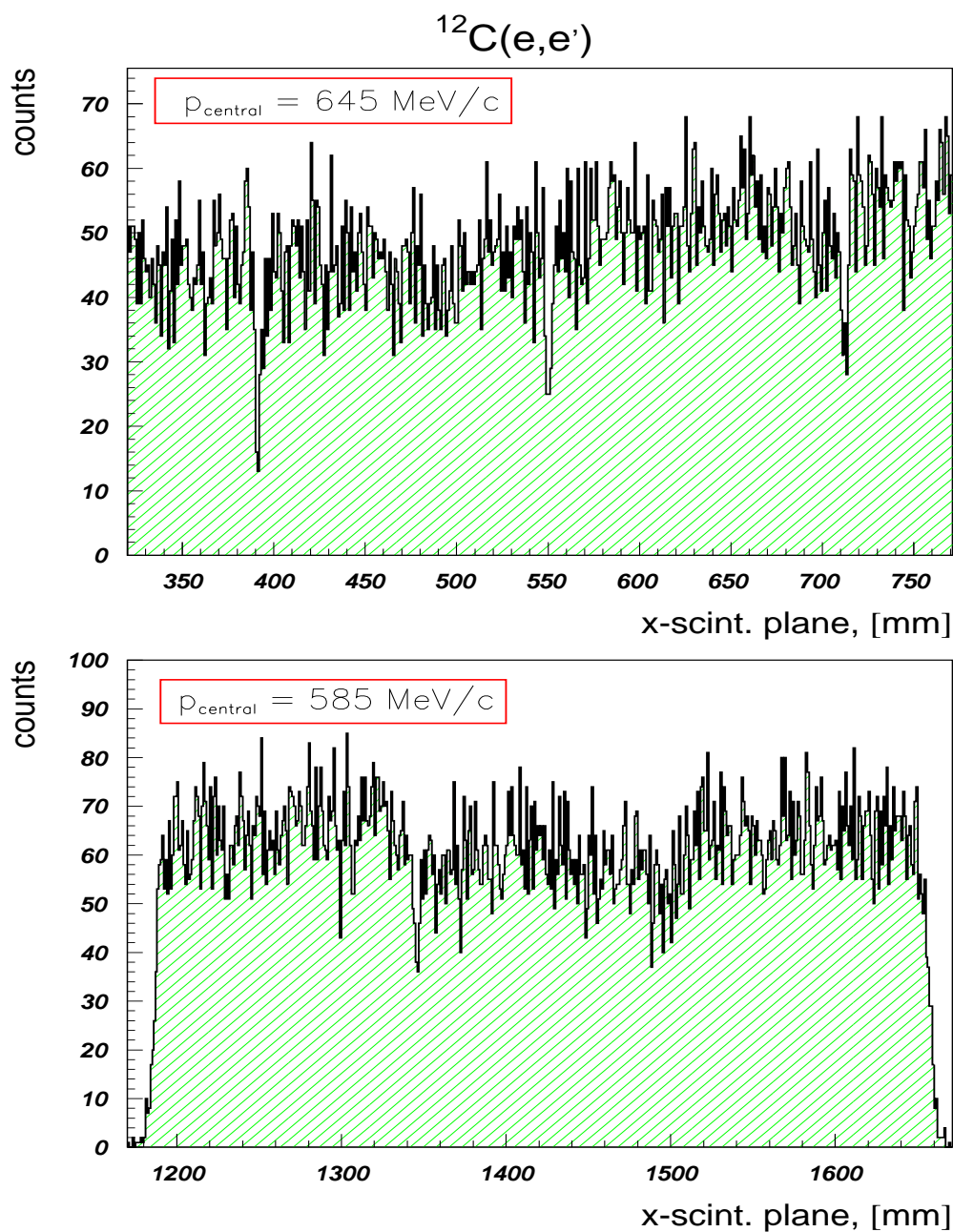


Figure 4.11: The x -scintillator plane in the $^{12}\text{C}(e,e')$ QE measurements; the efficiency losses at the edges of the scintillator segments are well seen (top); a low efficiency of the whole segment (bottom)

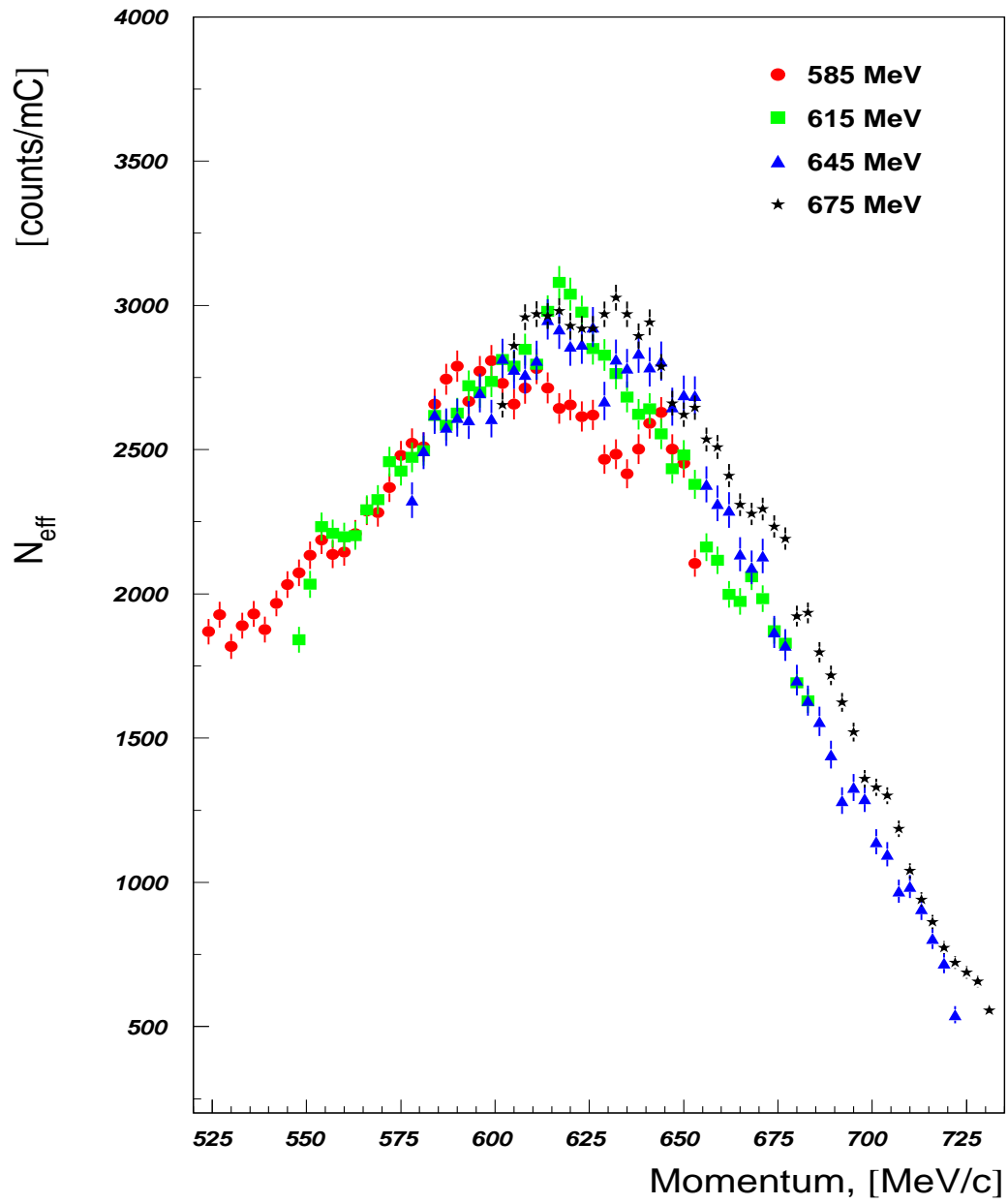


Figure 4.12: N_{eff} counts for the QE $^{12}\text{C}(e, e')$ measurements with four different central momenta in Spectrometer A

4.5.2 Theoretical helium-elastic cross section.

The theoretical cross sections for elastic scattering were calculated with a new C++ Monte-Carlo code called DUMP (described in Appendix B). These results and those obtained from reference [23] calculated with the modified version of AEEXB are compared in Table 4.4. For this comparison, it was assumed that the beam rastering amplitudes x and y were $\pm 3.5 \text{ mm}$. The target displacement along the beam line was taken as -2 mm as in reference [23]. From Table 4.4 it is clear that the differences between the results calculated by these two programs are less than 0.4 %. The one exception is the value for ${}^3\text{He}$ at $E_{beam} = 675.11 \text{ MeV}$. The statistical error in the results included in Table 4.4, and calculated with DUMP, is between 0.1 and 0.2 %. The statistical accuracy of the AEEXB predictions is unknown.

Calculations of the elastic cross section were based on the experimental values of the form factors obtained from reference [25], which provide a parameterization of the magnetic and charge form factors of ${}^4\text{He}$ and ${}^3\text{He}$. The Rosenbluth Equation was used in [25] ($h = c = 1$) to present the cross section as:

$$\left(\frac{d\sigma}{d\Omega}\right) / \left(\frac{d\sigma}{d\Omega}\right)_M = \frac{F_c^2(q^2)}{\tau} + \left[\frac{1}{2\tau} + \tan^2(\theta/2)\right] \cdot \frac{2\mu^2 F_m^2(q^2) q^2}{4m^2 Z^2} \quad (4.9)$$

$$\left(\frac{d\sigma}{d\Omega}\right)_M = \left(\frac{Z\alpha}{2E_1}\right)^2 \frac{\cos^2(\theta/2)}{\sin^4(\theta/2)} \frac{1}{1 + \frac{2E_1}{M} \sin^2(\theta/2)} \quad (4.10)$$

where m is the proton mass, $Z = 2$, E_1 is the beam energy, q^2 is the 4-momentum transfer and $\tau = 1 + q^2/4M^2$. For ${}^4\text{He}$, $\mu = 0$ and $M = 3727.41 \text{ MeV}$; so that in this case the only term left in Equation 4.9 involves the charge form-factor F_c . The ${}^4\text{He}$ data in [25] were fitted with the form-factor parameterisation:

$$F(q) = \left(1 - (a^2 q^2)^6\right) e^{-b^2 q^2} \quad (4.11)$$

where the value of a was fixed as 0.316 fm , and the best-fit value for b was 0.675 fm . For ${}^4\text{He}$ this parameterisation is correct for q^2 between 0.2 and 3.7 fm^{-2} .

	3He			4He		
E_{beam} [MeV]	540.11	675.11	855.11	540.11	675.11	855.11
Spectrometer	A	A	B	A	A	B
θ_{scat} [deg]	40	35	24.99	40	35	24.99
$\Delta\Omega_{eff}$ <i>AEEXB</i> [msr]	17.834	18.124	4.783	17.848	18.241	4.784
$\Delta\Omega_{eff}$ <i>DUMP</i> [msr]	17.854	18.169	4.798	17.854	18.169	4.798
$\frac{\Delta\Omega_{eff}^{AEEXB}}{\Delta\Omega_{eff}^{DUMP}}$	0.9989	0.9975	0.9967	0.9997	1.004	0.9970
$\frac{d\sigma}{d\Omega}$ <i>AEEXB</i> [$10^{-5} fm^2/sr$]	1.558	1.012	3.521	2.282	1.449	5.190
$\frac{d\sigma}{d\Omega}$ <i>DUMP</i> [$10^{-5} fm^2/sr$]	1.563	1.004	3.529	2.2938	1.4487	5.208
$\frac{d\sigma_{AEEXB}}{d\Omega} / \frac{d\sigma_{DUMP}}{d\Omega}$	0.9968	1.008	1.002	0.9949	1.0002	0.9965

Table 4.4: Results from AEEXB and *DUMP* Monte-Carlo codes

4.5.3 Experimental ${}^4He(e,e')$ cross section

Cross-section definition

Experimental cross sections were calculated according to the Equation:

$$\frac{d\sigma_{exp}}{d\Omega} = 10^{26} \times \frac{N_{cor} \cdot A_{He} \cdot \eta_{eff}}{\Delta\Omega_{spec} \cdot \left(\frac{Q_{tot}}{q_e}\right) \cdot \rho_{He} \cdot N_A \cdot (1 - \tau_{eff}) \cdot \epsilon_{tot}} \quad (4.12)$$

where

N_{cor} = number of counts, corrected for radiation by ALLFIT

A_{He} = 4.0 [g/mol] mass of the target

η_{eff} = effective scaling factor

$\Delta\Omega_{spec}$ = spectrometer solid angle in [sr]

Q_{tot} = total charge [in C]

$q_e = 1.602 \times 10^{-19}$ [C] elementary charge

ρ_{He} [g/cm³] = density of the 4He target

$N_A = 6.022 \times 10^{23}$ [1/mol] Avogadro number

τ_{eff} = effective dead time

$\epsilon_{tot} = \text{detectors efficiency}$

The ${}^4\text{He}$ elastic scattering measurements were performed at three beam energies (Table 4.5). Analysis of the helium elastic data were essentially the same as for carbon as shown in Figure 4.4. The only difference was that the theoretical cross sections averaged over the spectrometers acceptance were obtained from the Monte-Carlo program DUMP instead of MEFIT.

Software cuts

The same software cuts as for carbon were used to select elastically-scattered electrons. Coincidence between the scintillator trigger and a signal from the Cherenkov detector was required for background suppression.

It has been shown in reference [23] that significant acceptance losses in Spectrometer A occur for an extended target if the value of $|y_{tgt}| \geq 2\text{ cm}$. It was also mentioned that the $|\phi_{tgt}| < 75\text{ mrad}$ cut avoids such acceptance losses. This cut was used in the data analysis of all measurements with Spectrometer A, and in the Monte-Carlo simulation of the elastic helium cross section, and calculation of the effective solid angle of the spectrometer.

Background from the target cell

Another important issue was the background from the Al walls of the target cell. There are two possible ways to subtract this from the helium elastic line. First, one can apply a cut on the z target coordinate and reduce the contribution from the walls to practically zero. By doing this cut we would introduce additional systematic uncertainty into the target density, which could be large, and dependent on the accuracy of z coordinate reconstruction. The second way is to fit the background with a polynomial, and subtract its contribution from the Helium data in ALLFIT (as it is shown in Figure 4.15). This method requires a knowledge of the background behaviour under the elastic peak. In order to understand the shape

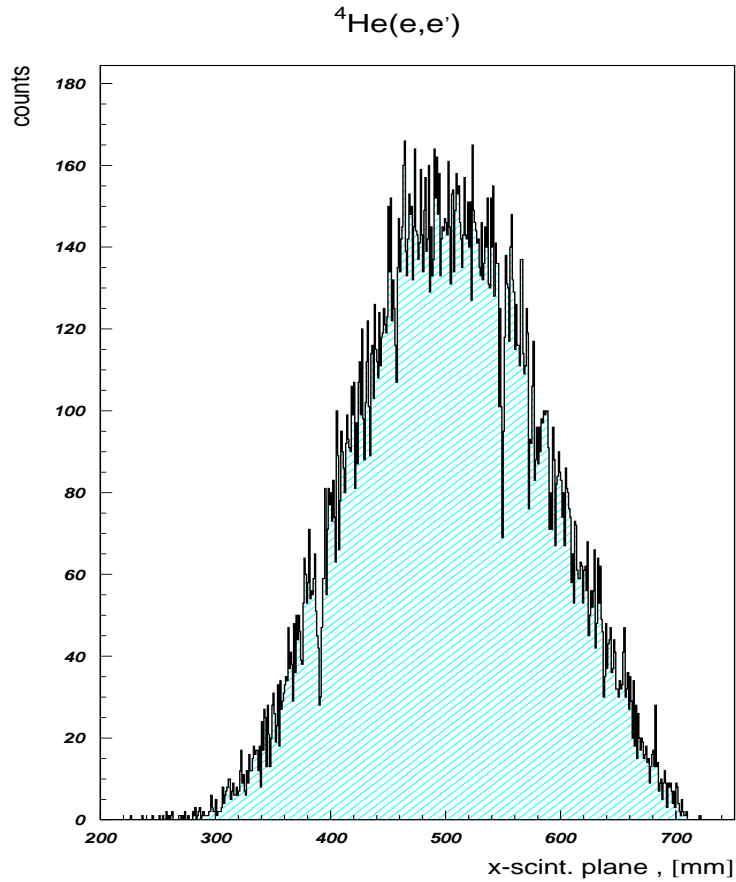


Figure 4.13: The ${}^4\text{He}$ elastic peak in Kinematic 2 projected at x scintillator plane; the trigger inefficiency is visible near $x = 395, 460$ and 550 mm

of the background, measurements with an empty Al cell were performed and analysed. In all elastic kinematics, the background from the walls was well described by a linear functional dependence and the polynomial parameters were close to the corresponding parameters in the ALLFIT background fit (Figure 4.16).

Data corrections and normalization

Due to the significant contribution of random AB coincidence events to the single elastically scattered electrons, the effective scaling factors and deadtime were calculated according to Equations 4.5 and 4.6. The total charge collected, and the

dead-time values were calculated using the Mainz COLA++ program.

The kinematically-corrected momentum p_{kin} was corrected from the aberrations caused by its dependence on θ_{focal} in the same way as for carbon, according to Equation 4.3. The effect of this correction is shown in Figure 4.14.

Significant losses of the scintillator trigger efficiency, due to the "edge effect" described in the previous sections, were observed in the case of Kinematic 2 (Figure 4.13). In calculations of the elastic cross section this effect was allowed for by using an efficiency less than 100 %, as it is shown in Table 4.5.

Reconstruction of the target cell position

The target cell was not well centered along the beam line, and its position was determined in the following way:

- the absolute position of the empty cell mounted at the target ladder was measured with theodolites, and found to be $+2 \pm 1 \text{ mm}$ in the direction of the beam dump. The measurements with the empty Al cell in Spectrometer B were used to determine the position of the real target cell.
- In data analysis with COLA++ code, the z coordinates of both walls of the empty cell were reconstructed, and the position of the center of the empty cell was determined ($+2 \text{ mm}$ in z direction). The reconstructed diameter of the empty cell was found to be equal to its real value.
- After such a "calibration", the helium elastic-scattering measurements with the real target cell were analyzed, and the target position found. It was shifted by $(-3 \pm 1) \text{ mm}$ along the beam line.

Radiative corrections

Again ALLFIT code was used to calculate the value of the radiative correction for the elastic cross section. The only difference from the analysis of the carbon data was the presence of the target cell. Therefore, in ALLFIT, a full-target thickness

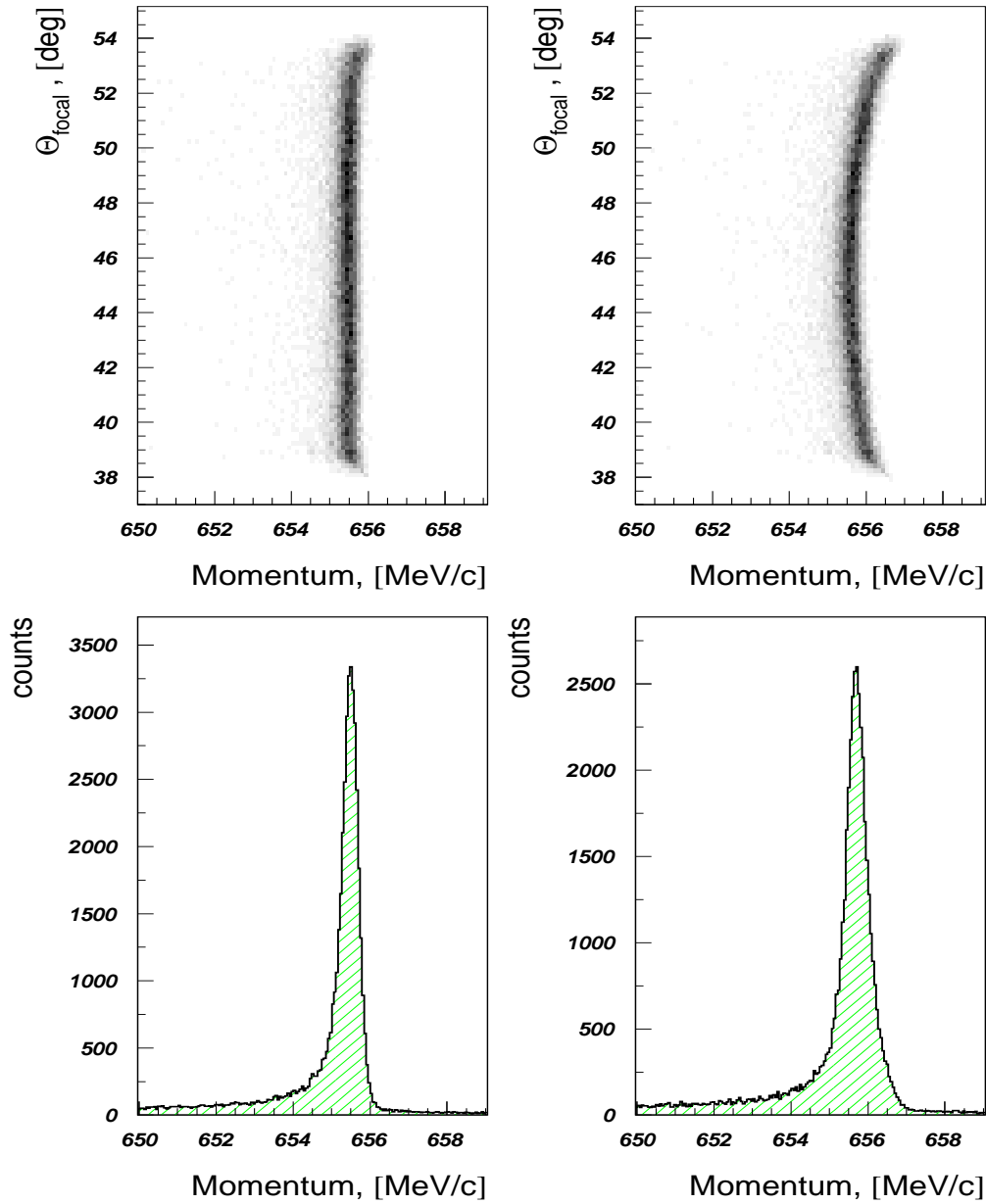
${}^4\text{He}(e, e')$ 

Figure 4.14: The ${}^4\text{He}(e, e')$ measurements, Kinematic 2.1; the kinematically-corrected momentum corrected for θ_{focal} aberrations (left) and the kinematically-corrected momentum without such correction (right)

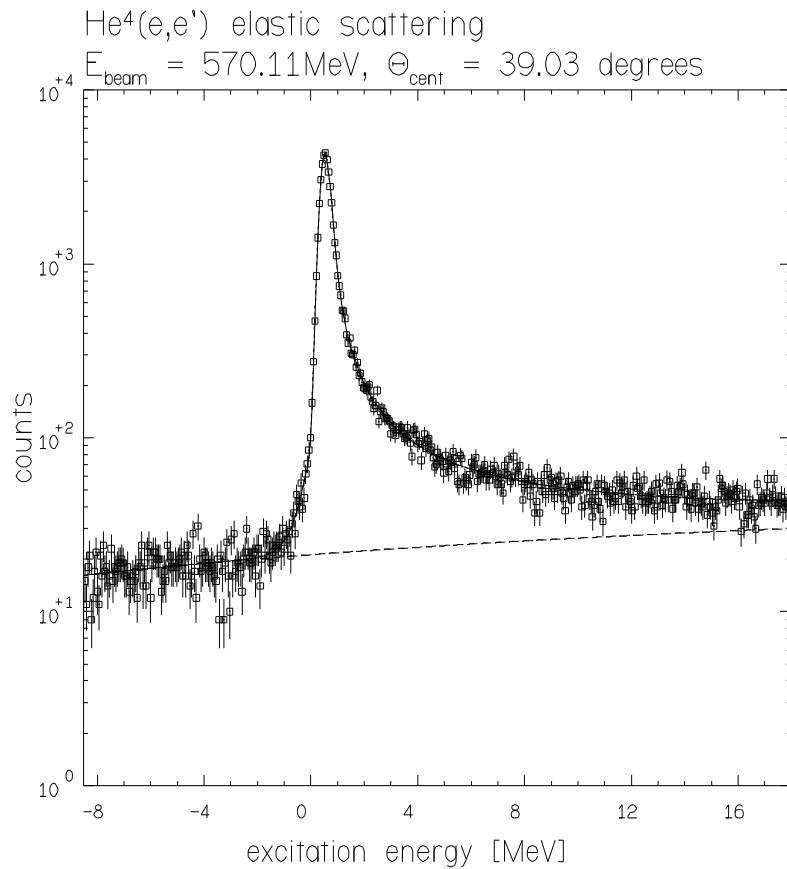


Figure 4.15: The ${}^4\text{He}$ elastic peak in Kinematic 1 (solid line); the background from the Al target cell (dashed line)

along the beam line, including the thickness of the Al walls, must be used as an input parameter in the calculation of external bremsstrahlung from the incident and outgoing electrons. Thus, an effective ${}^4\text{He} + \text{Al}$ target thickness was calculated (Table 4.5).

4.5.4 Experimental uncertainties

Details of the calculations to the error in the helium-target density are summarized in Table 4.6. The major contribution to this error was the uncertainty of the experimental ${}^4\text{He}$ form-factor used to calculate the cross section for particular

		Kin.1	Kin.2-0	Kin.2-1	Kin.3
E_{beam}	[MeV]	570.11	675.11	675.11	855.11
θ_{cent}	[deg]	39.03	32.68	32.68	25.57
beam rastering	[mm]	3×2	3×2	3×2	3×2
z_{target}	[mm]	-3 ± 1	-3 ± 1	-3 ± 1	-3 ± 1
total charge	[mC]	6.241	5.182	5.182	6.183
Dead time	[%]	6.11	10.1	10.1	10.11
Scaling factor		89.648	130	130	63.99
Trigger efficiency	[%]	99.8	99.0	99.0	100.0
${}^4He+Al$ density	[g/cm ³]	0.05604	0.05598	0.05624	0.05822
4He abundance		0.9444	0.9443	0.9447	0.9471
Al abundance		0.0556	0.0557	0.0553	0.0529
$\frac{d\sigma_{th}}{d\Omega}$	[10 ⁻⁵ fm ² /sr]	1.9217	3.0586	3.0586	4.1689
Solid angle	[msr]	17.8696	18.2919	18.2919	4.0121
N_{corr}	[counts/mC]	13938.82	12125.39	12125.39	6718.55
N_{corr}^{empty}	[counts/mC]	238.38	178.48	178.48	98.89
N_{He}^{corr}	[counts/mC]	13700.44	11946.9	11946.9	6619.66
ΔN_{He}^{corr}	[%]	0.35	0.4	0.4	0.5
4He density	[g/cm ³]	0.04012	0.04006	0.04032	0.04230

Table 4.5: Summary of the ${}^4He(e, e')$ elastic measurements

kinematical conditions. In reference [25], the total error corresponding to each form-factor value $F_c(q^2)$, is provided. Therefore the uncertainty in the calculated elastic cross section due to error in the form-factor F_c , and the corresponding helium-target density error, was calculated as $\Delta\rho_{He}/\rho_{He} = \Delta\sigma/\sigma \approx 2 \cdot (\Delta F_c/F_c)$.

The statistical error was relatively small (~ 0.5 %) and had no real effect on the total absolute error. The quality of the fitting procedure was very good, resulting in a total ALLFIT error of 0.55-0.65 %.

The sensitivity of the extracted helium density to the absolute position of the target cell was estimated by changing the target position by $\pm 1\text{ mm}$ in the Monte-Carlo calculations and extracting the density again with the new theoretical cross section value and the new spectrometer effective solid angle. The difference in the helium density, extracted in this way was small ($\sim 0.5\%$). This was partially because the change in the calculated cross section was compensated by the change in the spectrometer solid angle. However, even the change in the calculated cross section itself, due to a 1 mm shift of the target cell, was still only 0.7% . For Spectrometer B the change in solid angle due to a 1 mm shift of the target cell was negligible, but the calculated value of the average cross section changed by approximately 0.4% .

The uncertainty in the target density due to the $\pm 160\text{ keV}$ uncertainty in the beam energy was estimated by changing the input beam-energy in the Monte-Carlo code, and calculating a new value of the theoretical cross section with this changed beam energy.

The target-density error due to the software cuts was estimated by calculating the target density for the $\theta_{tgt} = \pm 60\text{ mrad}$ cut for the case of Kinematic 1. The value of this uncertainty was found to be 0.38% .

At $E_{beam} = 675.11\text{ MeV}$ two independent sets of matrix elements (the standard `qsdda495.mxl2` and the new `qsdda665.mxl` for high momenta) were used to extract the helium-target density. They correspond to Kinematic 2-1 and 2-0 in Table 4.5. The value of the deduced helium density using the different matrix elements differed by just 0.65% , which is insignificant compared to the total density error.

4.5.5 Spectrometer C

Spectrometer C was positioned at the same angle (120 degrees) during the whole experiment. Its central momentum was fixed at $340\text{ MeV}/c$. This allowed the spectrometer to be used as a monitor of the luminosity during the experiment.

	Kinem.1	Kinem.2-0	Kinem.2-1	Kinem.3
χ^2	1.0	1.2	1.0	1.1
fit sum [%]	99.98	100.12	99.97	100.02
ALLFIT error [%]	0.5	0.56	0.54	0.64
4He form-factor error [%]	1.3	1.5	1.5	1.3
angular-cut error [%]	0.4	0.4	0.4	0.4
beam-energy error [%]	0.2	0.2	0.2	0.2
charge error [%]	0.1	0.1	0.1	0.1
dead-time error [%]	0.1	0.1	0.1	0.1
target-position error [%]	0.5	0.5	0.5	0.4
total error $\Delta\rho/\rho$ [%]	1.5	1.7	1.7	1.5

Table 4.6: The contribution of the experimental uncertainties to the total error of the 4He target density ($\pm\Delta\rho/\rho$)

Software cuts

A number of software cuts were made to isolate the electrons scattered from the helium target. A coincidence between the scintillator trigger and the Cherenkov ADC signal in the range between 200 and 1500 channels was required. The momentum range was limited to between 300 and 380 MeV/c.

Helium-target density

The number of counts detected by Spectrometer C is proportional to the helium-target density. After some corrections explained below, this number was used to calculate the helium-target density during the (e,e'p) coincidence measurements. The raw number of counts in spectrometer C was first corrected for the deadtime and luminosity:

$$N_{corr} = \frac{N_{raw}}{Q_{tot} \cdot (1 - \tau_{eff})} \quad (4.13)$$

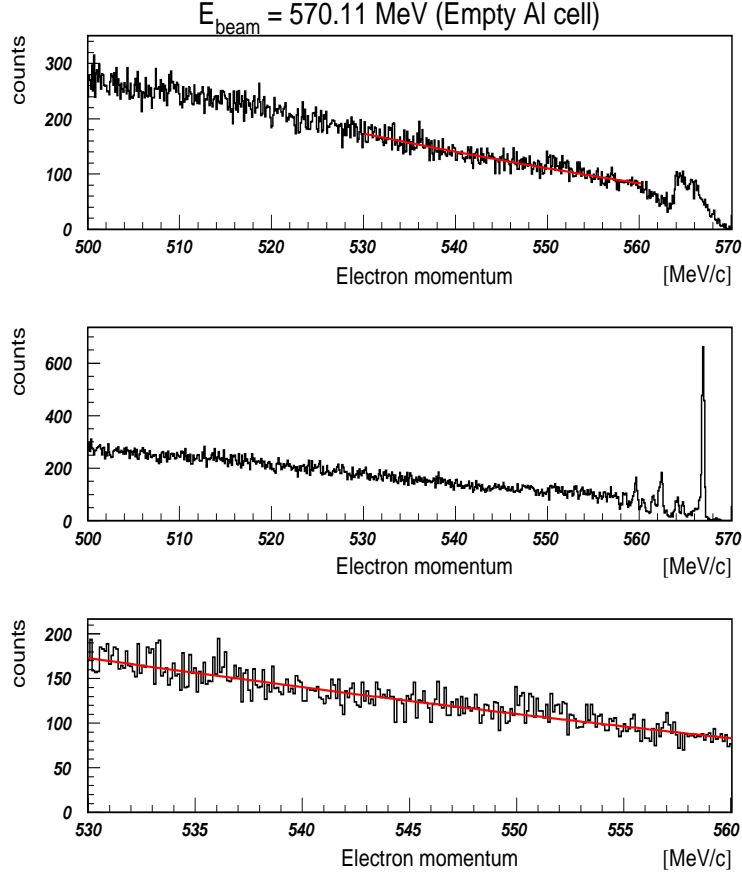


Figure 4.16: The measurements with the empty Al cell; Kinematic 1. First two histograms show a large range of the background under the elastic helium peak (positioned at approx. 550 MeV) and outside it. For the first (second) histogram the target mass equal to the ${}^4\text{He}$ (Al) mass was used to perform the kinematic calculations. The bottom histogram shows the background only under the elastic helium line (including the radiative tail).

where N_{raw} is the number of events detected in Spectrometer C after all the cuts, Q_{tot} is the total charge collected [in mC] and τ_{eff} is the deadtime. In a similar way, the measurements with the empty Al cell were analyzed, and the value N_{corr}^{empty} was extracted. The final value, N_{He}^{corr} , used as a reference number for the target-density calculations for the (e,e'p) measurements, corresponds to the number of

counts detected in Spectrometer C from the helium nuclei alone:

$$N_{He}^{corr} = N_{corr} - N_{corr}^{empty} \quad (4.14)$$

4.5.6 Summary

The helium-target density at all three beam energies used in the (e,e'p) coincidence measurements was extracted with an absolute error 2.6 – 3 %. During the measurements, the efficiency of the Phillips compressor was failing, with a corresponding loss of cooling power to the target. Small gas leaks through the valves in the 4He part of the gas system were also detected. As the result of these two effects the density of the helium gas was less for measurements done at $E_{beam} = 570.11 MeV$ than for those made at $E_{beam} = 855.11 MeV$, which were measured first. The measurements at $675.11 MeV$ were done with a target cell refilled after the emergency break. This was necessary due to failure of the compressor leading to an increase pressure in the system. Thus this last measurement cannot be compared with the previous ones in order to check consistency of the target-density values.

Chapter 5

Analysis of the coincidence (e,e'p) data

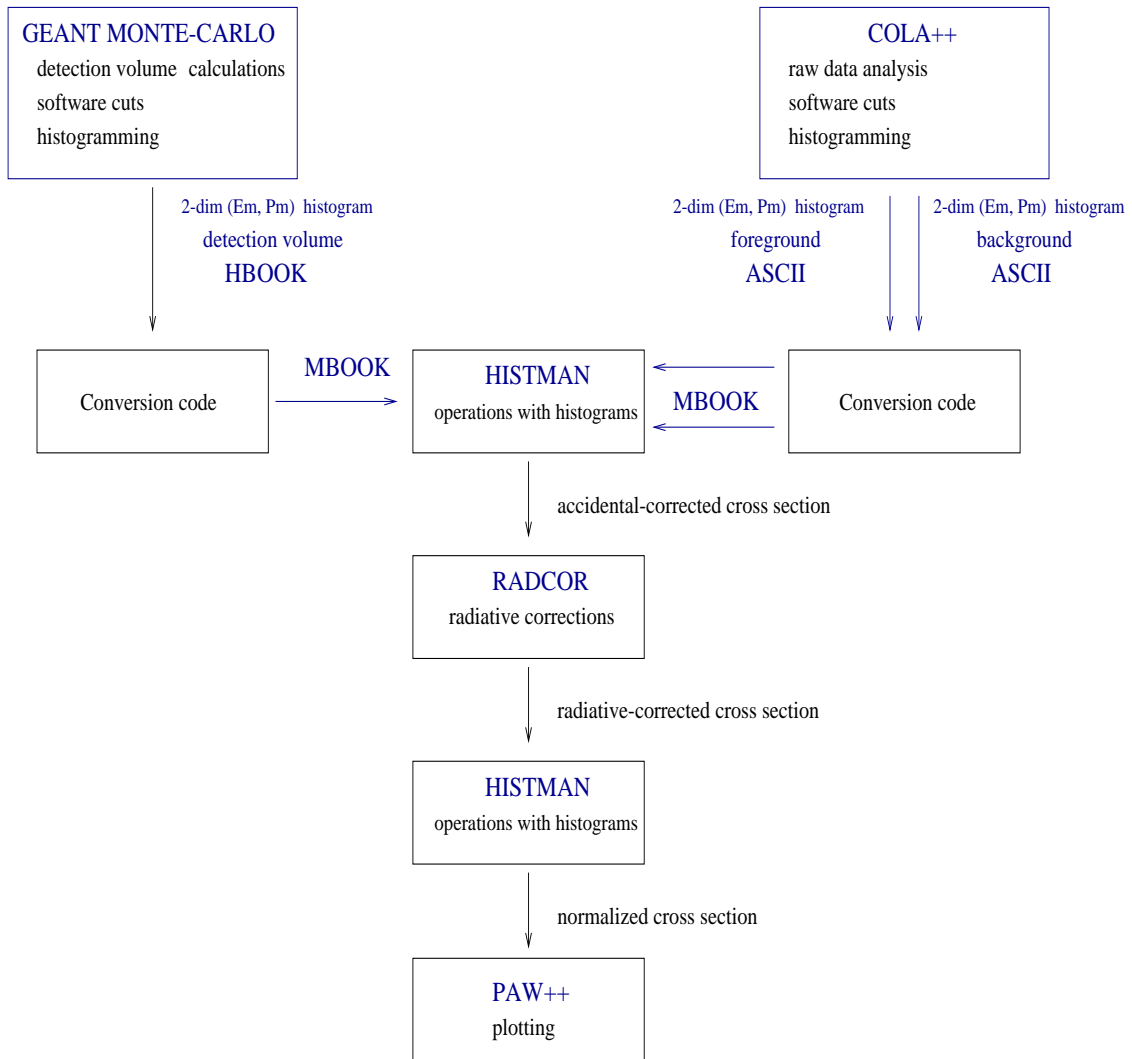
5.1 Introduction

In this chapter the analysis of the (e,e'p) data is described. It consists of several sections covering all important issues concerning the data handling, software cuts, and radiative corrections.

Section 5.2 covers matters related to the missing-energy spectra structure, and describes corrections used to improve the missing-energy resolution.

In Section 5.3 all software cuts used to reduce the background contribution to the measured (e,e'p) cross section are explained in detail. The helium-target density calculation procedure using the reference-density values for the helium gas is also described. Finally, the ω -cut used to match the range of the energy-transfer values for the three (e,e'p) kinematics, and to ensure a quality of the L/T Rosenbluth separation is mentioned.

The definitions and calculation steps for the experimental five and six-fold differential cross section, the spectral function, and the proton momentum distributions are given in Sections 5.4 - 5.6.

Figure 5.1: Analysis of the $(e,e'p)$ data

At the end of the chapter all questions concerning the radiative unfolding procedure using RADCOR code, and radiative corrections in general, are discussed in Sections 5.7 - 5.8.

A summary of kinematic information for the (e,e'p) measurements is available in Table 3.3. The major analysis steps are shown in Figure 5.1. The analysis of the raw data was performed using the Mainz COLA++ code, which was used for the data reduction, software cuts, background suppression, and histogramming. The output produced by COLA++ in the form of 2-D (E_m, p_m) histograms for the foreground and background yield was first converted into ASCII format, and then into the MBOOK format that is used in the HISTMAN package.

The detection-volume calculations were made with the new GEANT Monte-Carlo code (see Appendices A and C). This code was used to apply the same software cuts as in the analysis of the (e,e'p) data, and for the histogramming of the results of a simulation. The HBOOK output from GEANT was converted into the MBOOK format acceptable by the HISTMAN program, which was used to do all operations with histograms (adding, subtraction, scaling and slicing).

The experimental cross sections were radiatively unfolded using the RADCOR code. As an alternative, the AEEEXB Monte-Carlo code with the implemented theoretical model of the two-body-breakup and continuum channels of the (e,e'p) reaction, was used to simulate the radiative tails in the detected kinematic region.

5.2 Missing-energy spectra

Structure of the missing-energy spectra

The missing energy was calculated according to the definition given in Equation 2.11 in Chapter 2. The raw missing-energy spectrum is shown in Figure 5.2, as a 1-D projection of the 2-D (E_m, p_m) histogram. The dominant feature in this spectrum results from the two-body breakup (${}^4\text{He}(e, e'p){}^3\text{H}$) reaction channel which

is positioned at a missing-energy value of 19.8 MeV . Two other reaction channels, which create continuous strength starting from their threshold values, are the three-body breakup ${}^4\text{He}(e, e'p)nd$, and four-body breakup ${}^4\text{He}(e, e'p)pnn$. They have relatively small strength and cannot be separated one from the other.

Missing-energy resolution

The missing-energy resolution can be determined from the two-body-breakup peak in the spectrum. The full width of this peak is determined by the total resolution of the experimental setup, and was used as an input parameter in the optimization procedures described below.

For the case of high proton momenta, as were detected in Spectrometer B, the matrix elements $(\theta | \delta)$ of the standard 495 MeV matrix are no longer correct, as was shown in Chapter 4 for the kinematically-corrected momentum of elastically scattered electrons. This causes broadening of the two-body breakup peak, due to the dependence of the missing energy on θ_{focal} , and also leads to an energy assignment different from its 19.8 MeV value. Similar problems were mentioned previously in the description of the analysis of the elastic scattering from carbon and helium in Chapter 4. In order to optimize the resolution of the missing-energy spectrum, the dependence of E_m on θ_{focal} was corrected to 1st order (by a linear term) using Equation 4.3. The two-body-breakup peak before and after this correction is shown in Figure 5.3a.

The other factor, which deteriorates missing-energy resolution, is the energy-loss by ionization of the incident electrons, scattered electrons, and protons, in the helium gas and the Al walls of the target cell. This energy loss also led to a re-distribution of (e,e'p) events in the whole missing-energy spectrum due to fluctuations from the average value (Landau fluctuations). This problem will be discussed below, together with other radiation effects, such as internal and external bremsstrahlung.

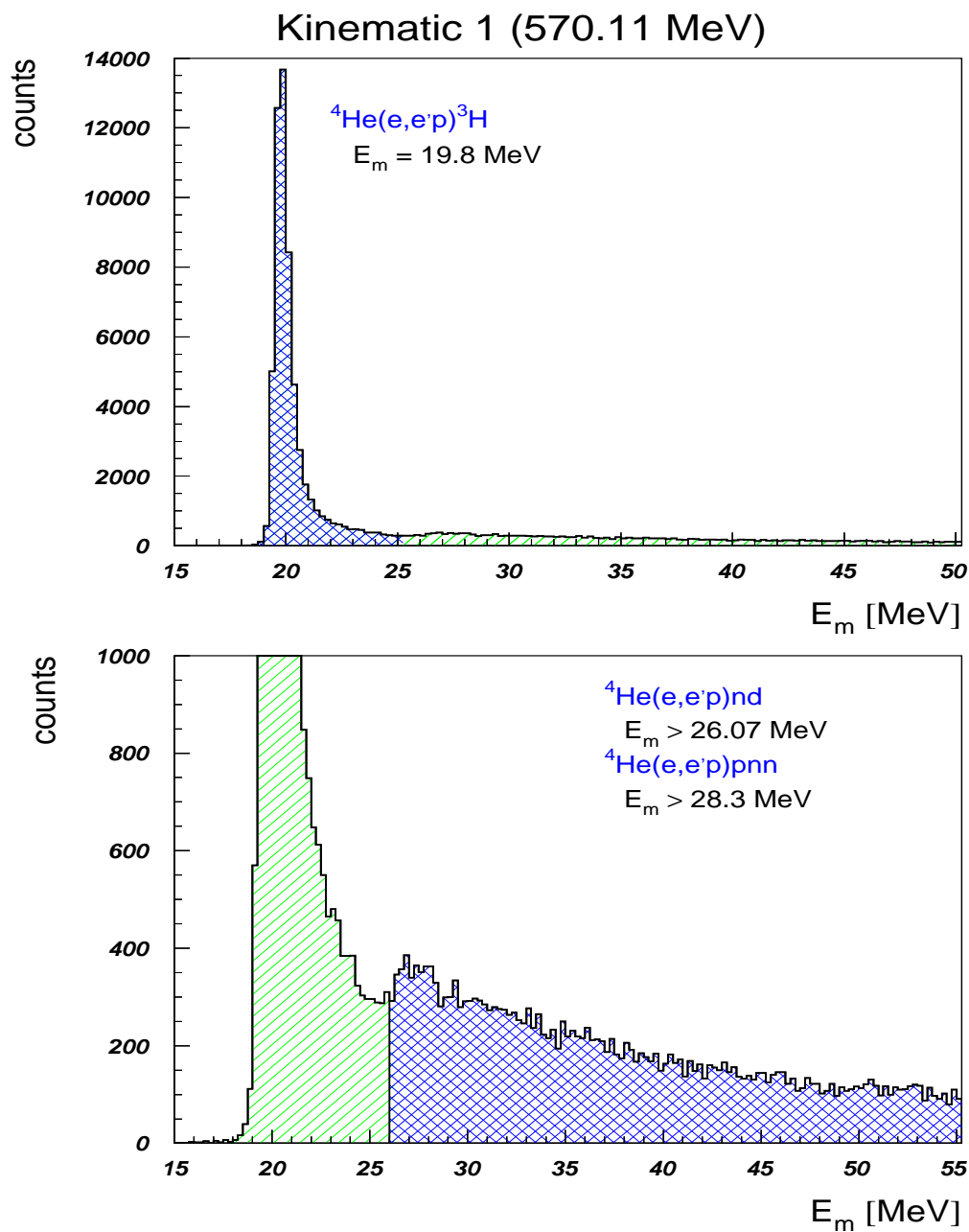


Figure 5.2: Raw missing-energy spectrum for ${}^4\text{He}(e, e'p)X$ reaction

In COLA++, the energy-loss corrections are handled by calculating the average energy-loss per unit length, for the particle. This uses the Bethe-Bloch formula, for the actual path length of the particles through the target cell. In case of the restrictive cut on the z_{vert} coordinate (explained below), the difference in path length through the target cell for particles with different vertex positions along the beam line, is not large. Therefore, the energy-loss caused only a minor dependence of E_m on the vertex position within the target cell. After the energy-loss corrections, the (e,e'p) events in the missing-energy spectrum corresponding to two-body breakup, no longer had any dependence on their vertex position along the beam line (see Figure 5.4).

After these two corrections the resulting value of the missing-energy resolution was $\sim 0.7 \text{ MeV (FWHM)}$ (Figure 5.3b).

5.3 Software cuts and background reduction

5.3.1 Overview

In order to select only events coming from the $(e, e'p)$ reaction on ${}^4\text{He}$, a number of software cuts were applied. For the electron-arm spectrometer this meant separating scattered electrons from the background formed mostly by negative pions. As was mentioned in Chapter 3, the difference in the energy deposition by electrons and pions in the scintillator segments is small, since they are both in the minimum-ionizing region. A clear separation of the scattered electrons from pions was possible using a software cut to select those events with a signal in the Cherenkov detector.

In Spectrometer B, which was the proton-arm detector, the raw ADC spectra in the scintillator segments contain a significant background of positive pions and deuterons (see Figure 5.5a). Practically all background events were removed after a coincidence timing cut, together with the Cherenkov cut in Spectrometer A as

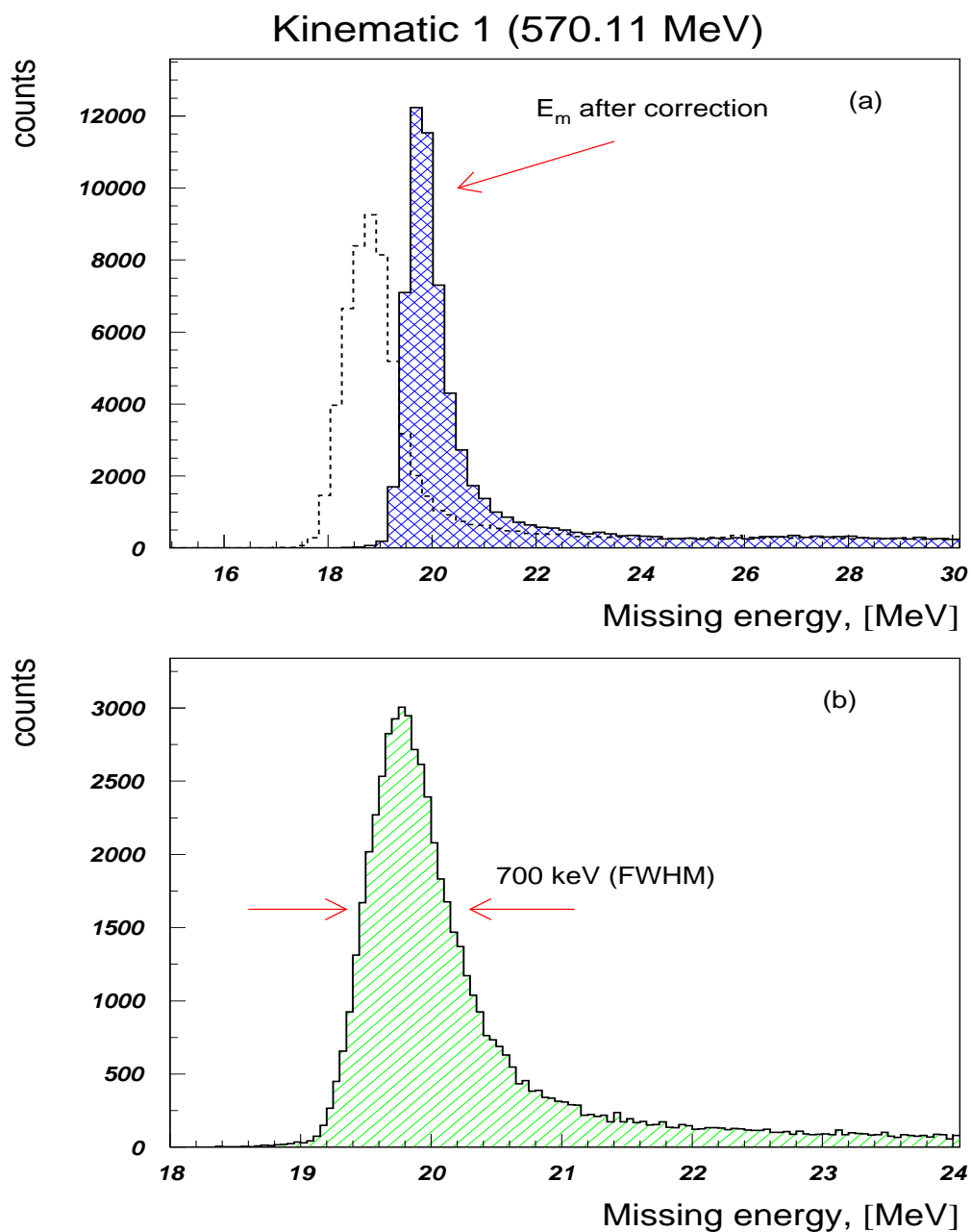


Figure 5.3: Raw missing-energy spectra; (a) the solid line is the corrected missing energy and dashed line is the missing energy not corrected from θ_{focal} dependence; (b) the two-body-breakup peak after the resolution optimization

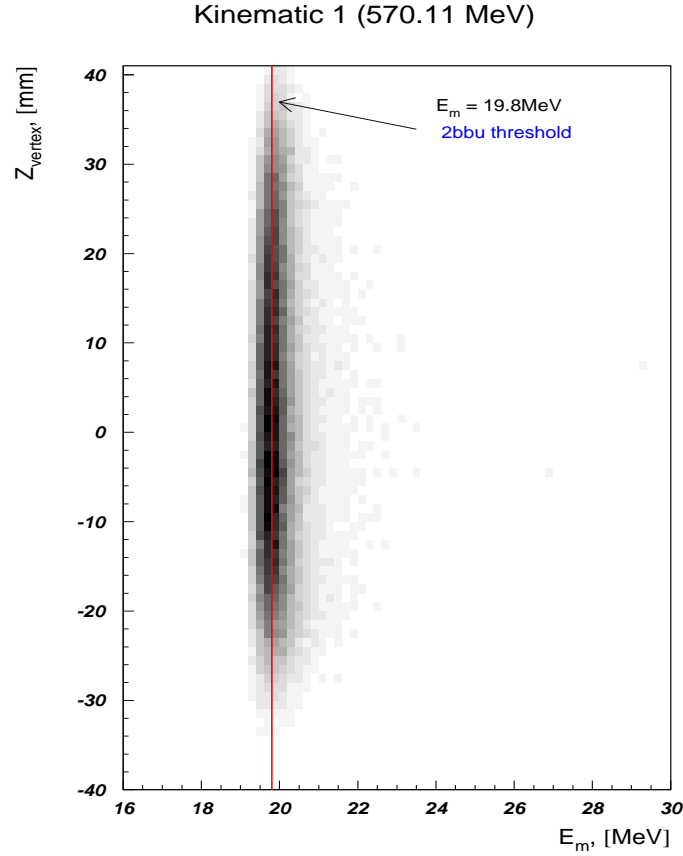


Figure 5.4: Two-body-breakup peak after correction for energy loss and θ_{focal} dependence

shown in Figure 5.5b. Thus only protons detected in coincidence with an electron remained in the spectrum.

The large part of the remaining background in the E_m spectrum was a result of particles re-scattering from the Al windows of the scattering chamber. This was removed by applying a ± 50 mrad (± 70 mrad) cut on the vertical angle θ_{tgt} in Spectrometer B(A).

A cut on the reaction vertex coordinate z_{vert} , equal to ± 2 cm, was used to limit the acceptance by both spectrometers to a region which was fully defined by the collimator geometry. This cut removed most of the background contribution from the walls of the Al target cell.

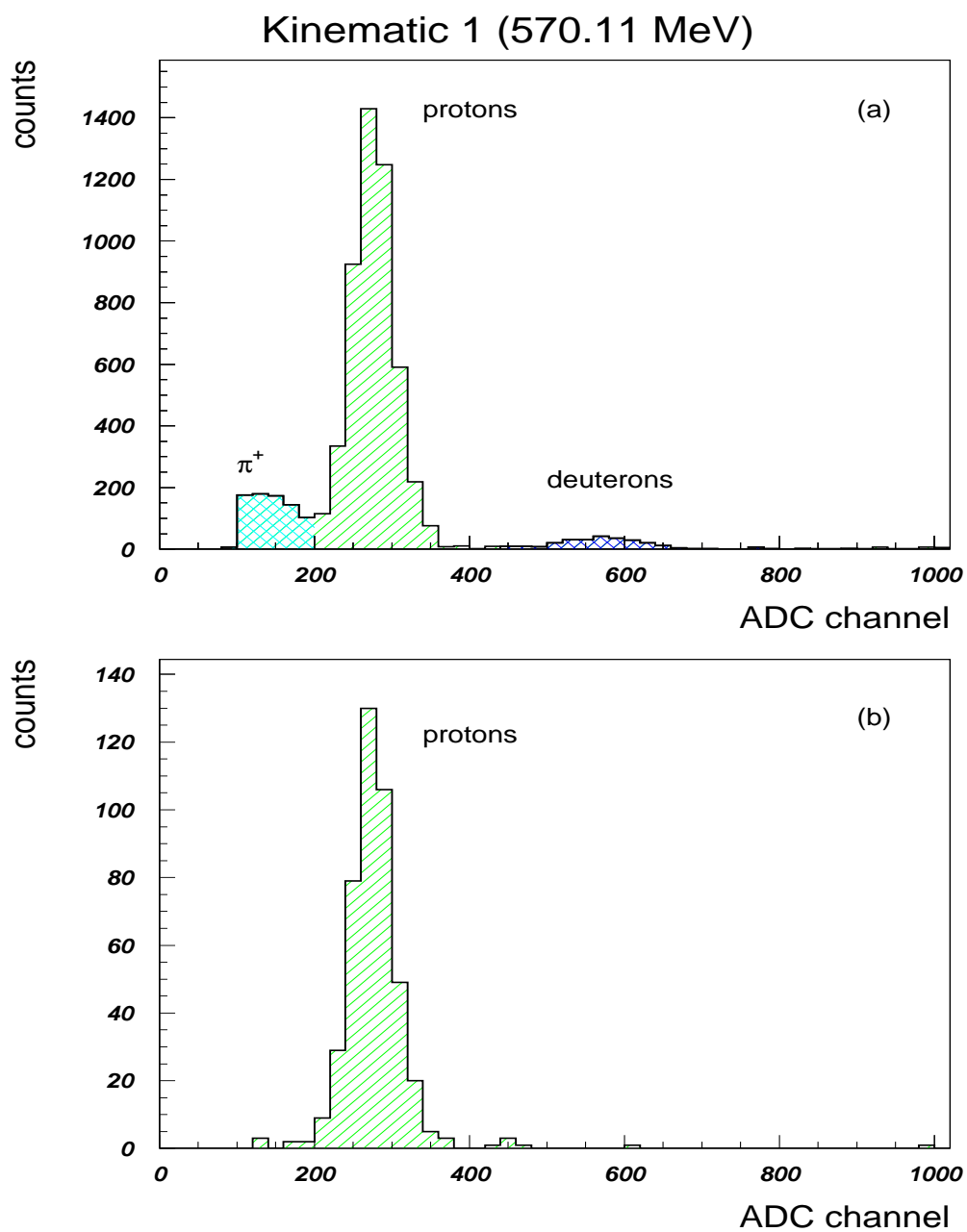


Figure 5.5: ADC spectra for scintillator of Spectrometer B before the timing cut (a) and after it (b)

Florizone [23] reported a large acceptance loss in Spectrometer A when an extended target was used, for a horizontal spectrometer angle $|\phi_{tgt}| \geq 75 \text{ mrad}$. Thus, a cut on this angle of $|\phi_{tgt}| \leq 75 \text{ mrad}$ was applied to limit the spectrometer acceptance.

In addition, the momentum acceptance of Spectrometer A was limited to $\pm 10 \%$ and Spectrometer B to $\pm 7.5 \%$ corresponding to their nominal acceptance values (see Chapter 3).

5.3.2 Coincidence timing

ToF corrections

The raw coincidence timing is about 10 nsec wide (Figure 5.6a). In the analysis with COLA++, the raw timing was corrected for a number of factors which caused its broadening:

- 1) the individual TDC offsets for the segments of the scintillator layer, which defines the coincidence timing (in this measurement the second dE layer) were adjusted so that the width of the coincidence-timing distribution was minimized;
- 2) the time required for photons to reach PMTs viewing each scintillator segment was calculated, and a corresponding correction to the coincidence timing was introduced. This time depends on the non-dispersive coordinate value y_{scint} , and the effective speed of light in the scintillator material, which is ~ 1.4 times less than the c/n value obtained from the known refraction index value. Dependence of the timing signal on the pulse height in the scintillator was decreased.
- 3) the time-of-flight for a particle with velocity β to travel from the target to the focal plane detectors was taken into account.

Although for most of (e,e'p) events the coincidence timing was a Gaussian distribution with a FWHM of 1.4 nsec (Figure 5.6b), some events fall outside this peak,

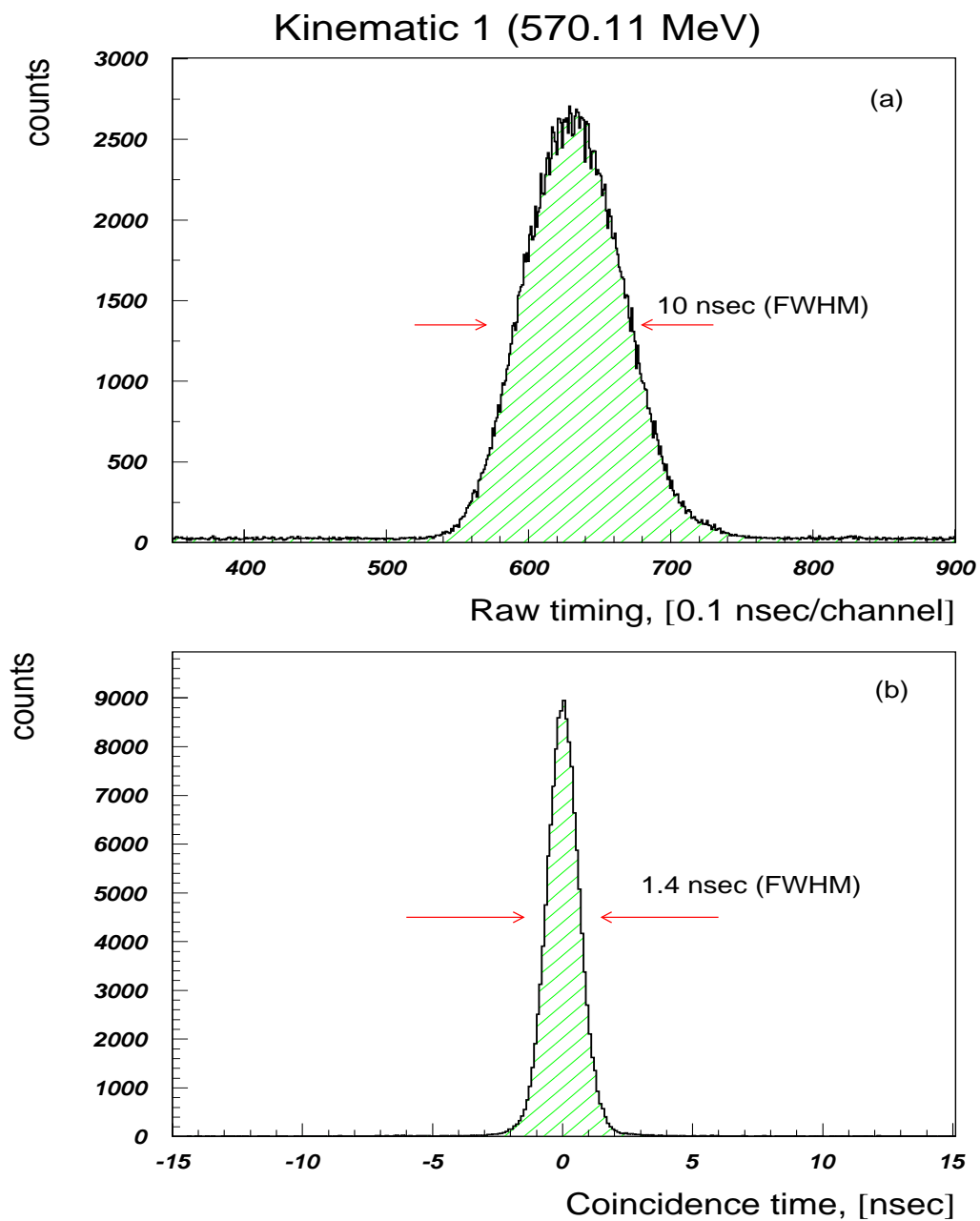


Figure 5.6: Raw coincidence time (a); corrected timing (b)

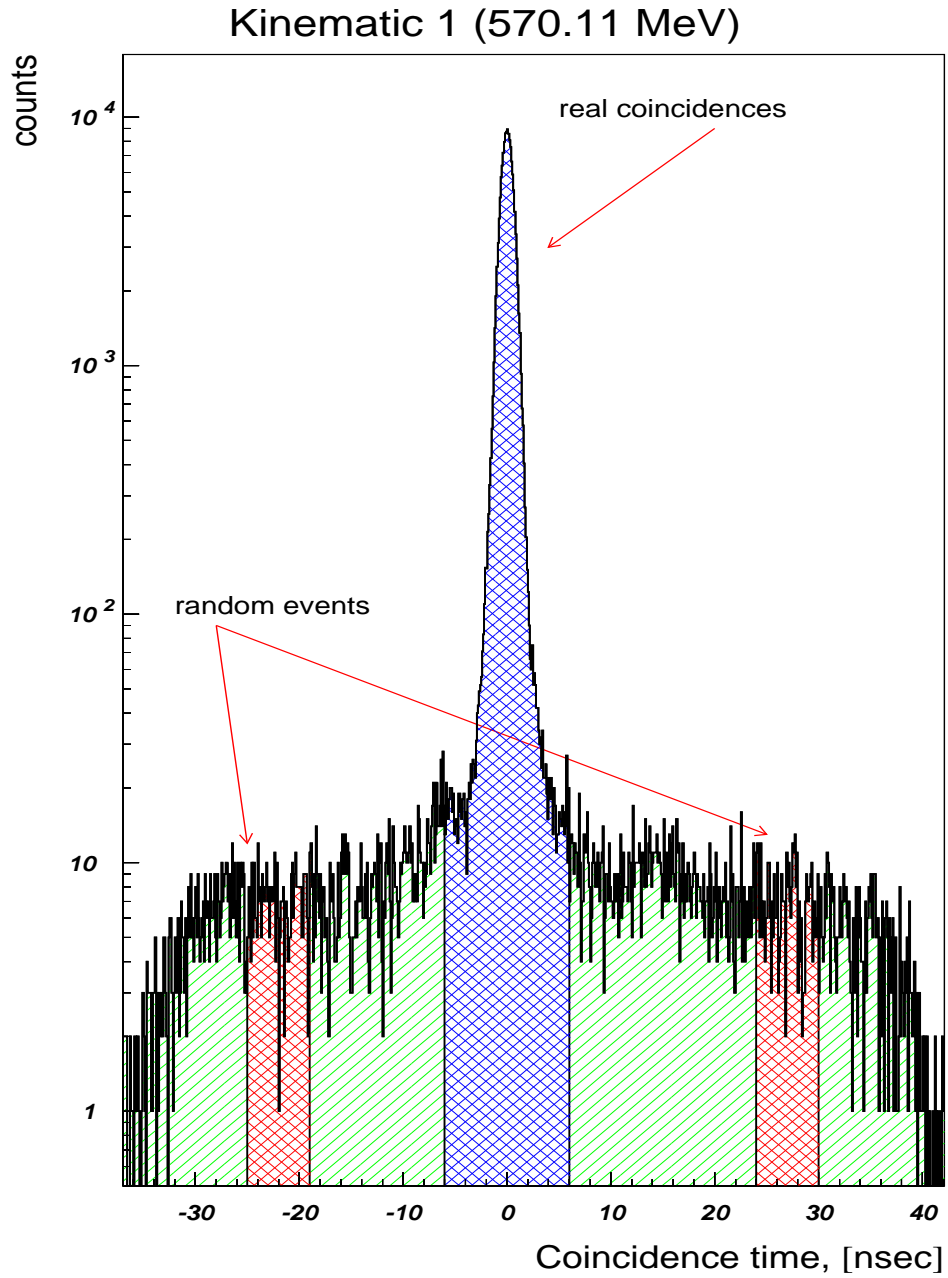


Figure 5.7: Coincidence timing; the foreground and background windows are shown

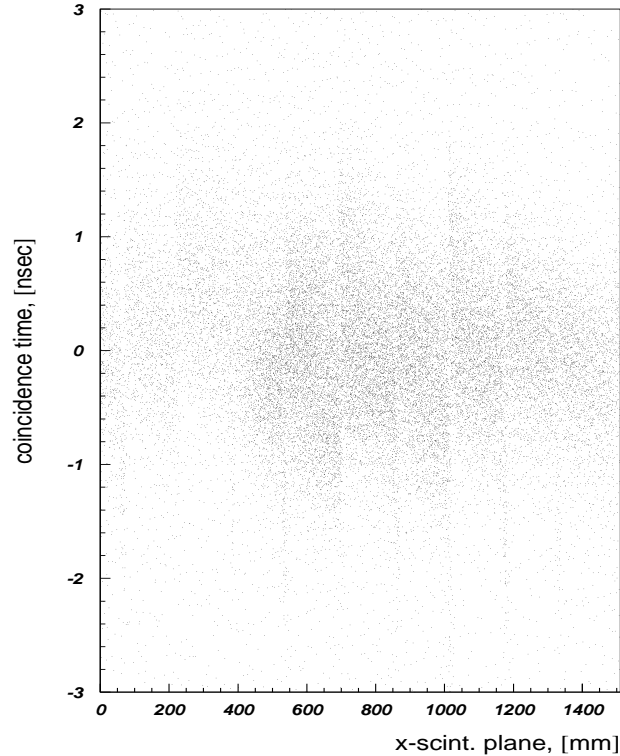


Figure 5.8: Dependence of the coincidence timing from the dispersive x-scint. coordinate near the edges of the scintillator segments

as shown in Figure 5.7. This non-Gaussian part of the timing distributions comes from particles crossing the scintillator layers near a gap between two scintillator paddles. In this case the pulse height in either paddle is reduced, and a shift in the coincidence timing is observed. The combination of such events in both spectrometers leads to long (up to 10 nsec) tails at both sides of the coincidence peak, which can be observed in Figure 5.7. In Figure 5.8, where the coincidence timing is plotted as a function of the focal plane coordinate $x - scintillator\ plane$, the individual scintillator segments are evident. Narrow vertical lines correspond to events hitting the edges of the scintillator paddles. By using a wide ($\pm 6\ nsec$) timing cut in the data analysis, most of these events were included in the foreground yield.

Foreground and background yield

It is clear from Figure 5.7 that the number of "true" coincidences N_{true} can be determined as:

$$N_{true} = N_{real} - N_{rand} \quad (5.1)$$

where N_{real} is a number of events inside the ± 6 nsec timing cut on the coincidence peak, and N_{rand} is a sum of events from two 6-nsec-wide windows in a region far away from the coincidence peak, (see also Figure 5.7).

Loss of (e,e'p) events in the ToF cut

A small number of coincidence (e,e'p) events were outside the ± 6 nsec timing cut. The inefficiency due to this cut was estimated from the ratio of the two-body-breakup strength outside the ToF window, to the total number of detected (e,e'p) events (see Figure 5.9). The absolute value of this inefficiency is 0.3 – 0.4 % for all kinematics.

5.3.3 Background processes

In the coincidence-time spectrum (Figure 5.10) one can see two peaks separated by approximately 6 nsec. The left peak is due to detection of a proton in coincidence with a π^- .

In Kinematic 1, (see Table 3.3) negative pions with momentum equal to the central momentum of Spectrometer A ($p_{cent}^A = 236$ MeV/c) have a full energy $E_{\pi^-} = \sqrt{p_{\pi^-}^2 + m_{\pi^-}^2} \approx 274$ MeV, and a corresponding velocity $\beta_{cent} \approx 0.86$. The time-of-flight for particles with a velocity β through Spectrometer A is equal to $t_A \approx L_{cent}/(0.3 \cdot \beta)$ [nsec], where the length of the central trajectory for Spectrometer A is $L_{cent} \approx 10.8$ m. It is clear that an approximate time-of-flight difference between electrons and pions is approximately $\Delta T \approx 3.33 L_{cent} \cdot (\beta_{e^-} - \beta_{\pi^-}) \approx 5$ nsec. In reality, this value is a slightly larger (6 nsec) since most of the pions were detected

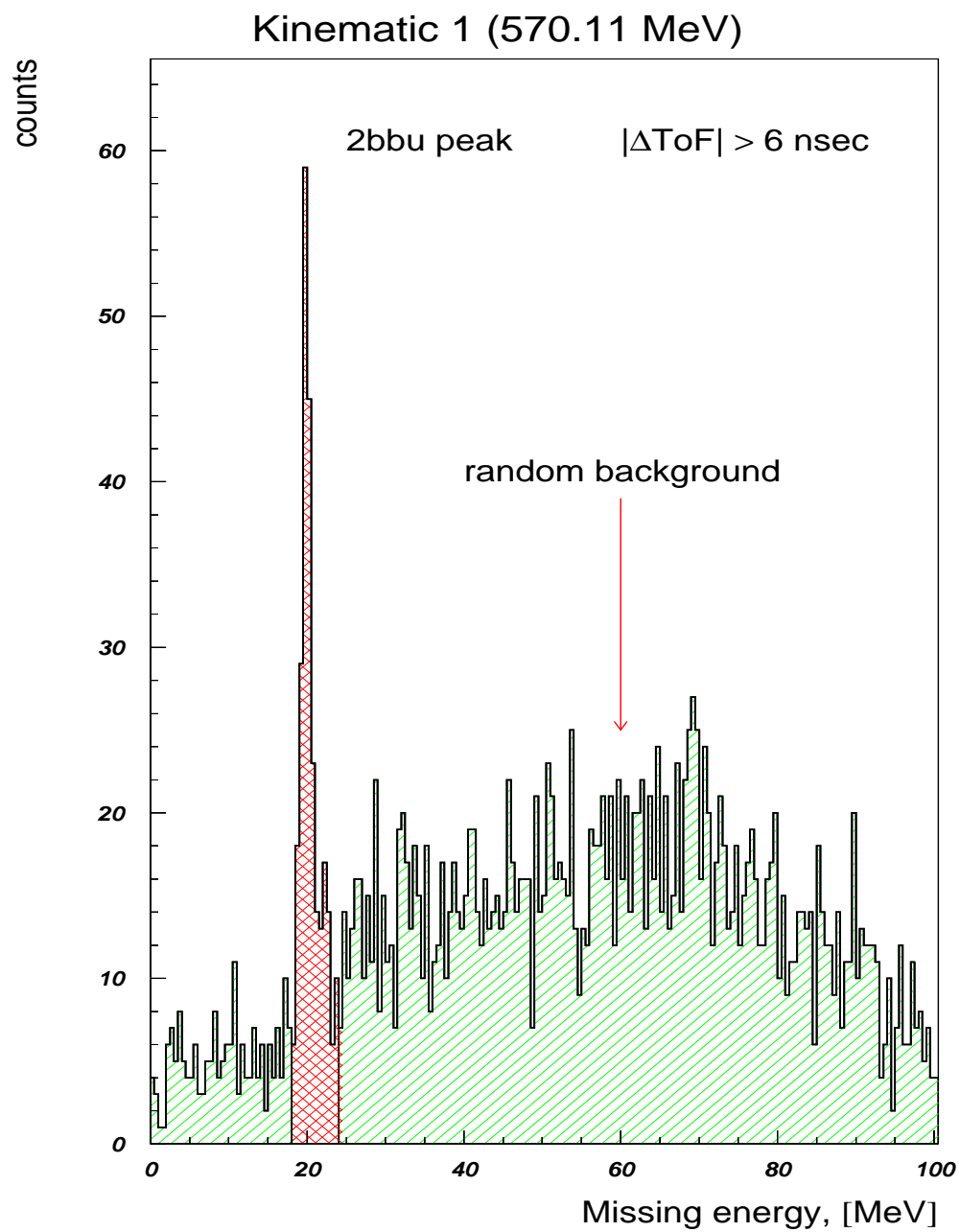


Figure 5.9: Inefficiency of the coincidence-timing cut

on the low-momentum side of the focal plane, and have momenta lower than the central value. By requiring the signal from the Cherenkov detector to be non-zero, practically 100 % of the $(\pi^- + p)$ coincidences can be removed from the coincidence-time spectra, as shown in Figure 5.10.

5.3.4 Cut on target length

The helium target cell has a diameter $\approx 8\text{ cm}$, which cannot be fully used in the (e,e'p) data analysis. Only half of the target thickness was used, and the vertex coordinate z_{vert} was limited to a $|z_{vert}| \leq 2\text{ cm}$ range. First of all, it was necessary to limit the spectrometer coordinate y_{tgt} to a range where the acceptance of the spectrometers is well-understood and defined by the collimator geometry. At the same time, this cut safely removes the major background contribution from the Al walls of the target cell.

The behaviour of the missing-energy spectrum at high missing energies is clear from Figure 5.11a, where the results for three different z_{vert} cuts are shown. The spectra look very similar for the $\pm 25\text{ mm}$ and $\pm 20\text{ mm}$ cuts, and show a significant reduction of the measured strength for $E_m \geq 50\text{ MeV}$. This is an indication that cutting more closely than $\pm 20\text{ mm}$ would not improve the background at high missing energies. A tighter cut would simply increase the statistical uncertainty of the results by reducing the data available for analysis.

The same conclusion is reached from the reconstructed position of the target-cell walls from the data taken with the empty Al cell. The $\pm 2\text{ cm}$ region of the reconstructed z -coordinate histogram for (e,e'p) events is almost zero (Figure 5.11b).

The fraction of coincidence Al(e,e'p)X events remaining in the measured (e,e'p) data was estimated from the measurements with the empty cell, where the same software cuts were used. After the $\pm 20\text{ mm}$ cuts on the vertex coordinate z_{vert} , the number of events detected in the missing-energy spectrum from interactions in the cell walls was scaled according to the total charge collected at the target in both

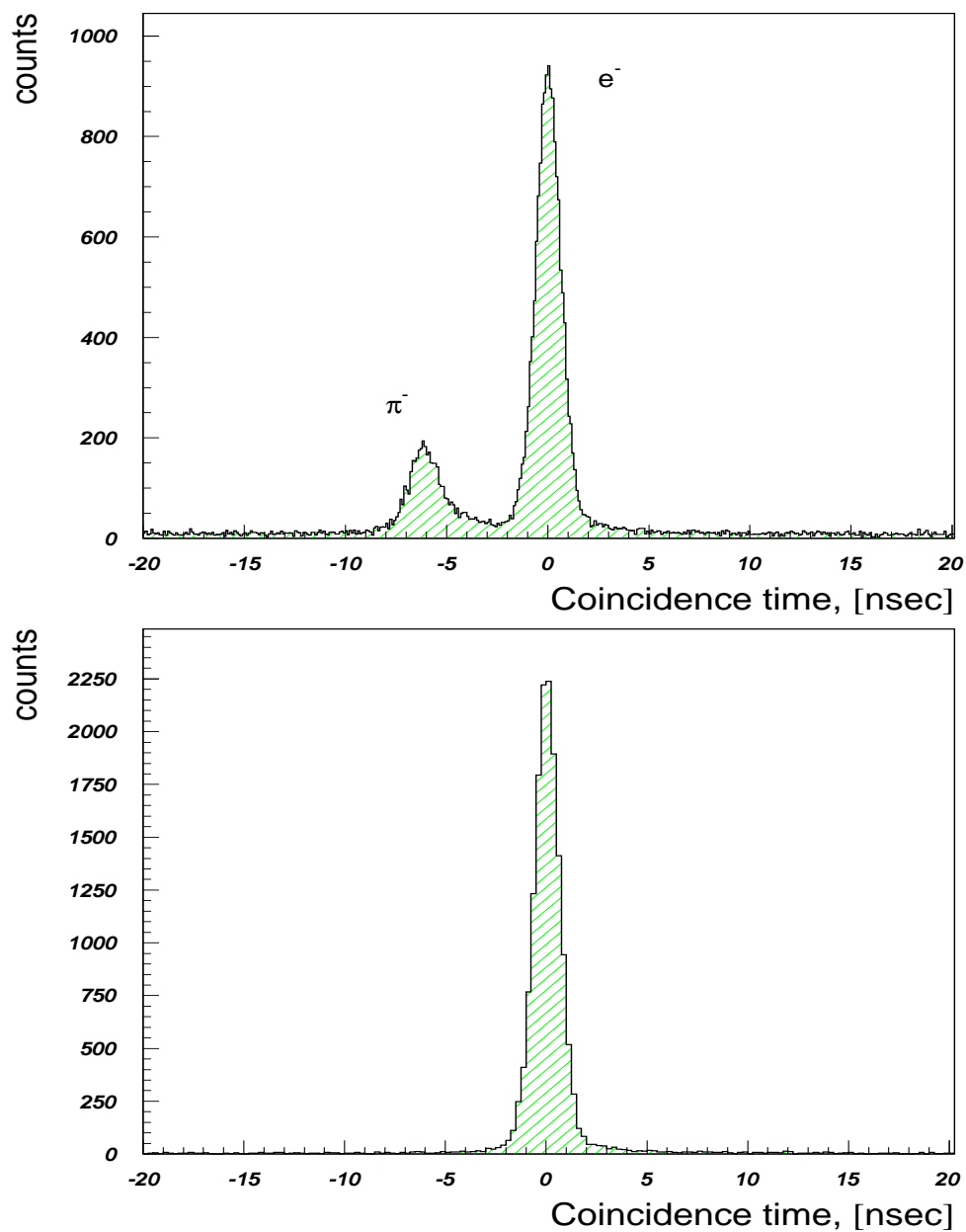


Figure 5.10: $E_{beam} = 570.11$ MeV, the central momentum in Spectrometer A $P_{cent}^A = 236$ MeV/c. Pions background in ToF (top); ToF after the Cherenkov cut (bottom)

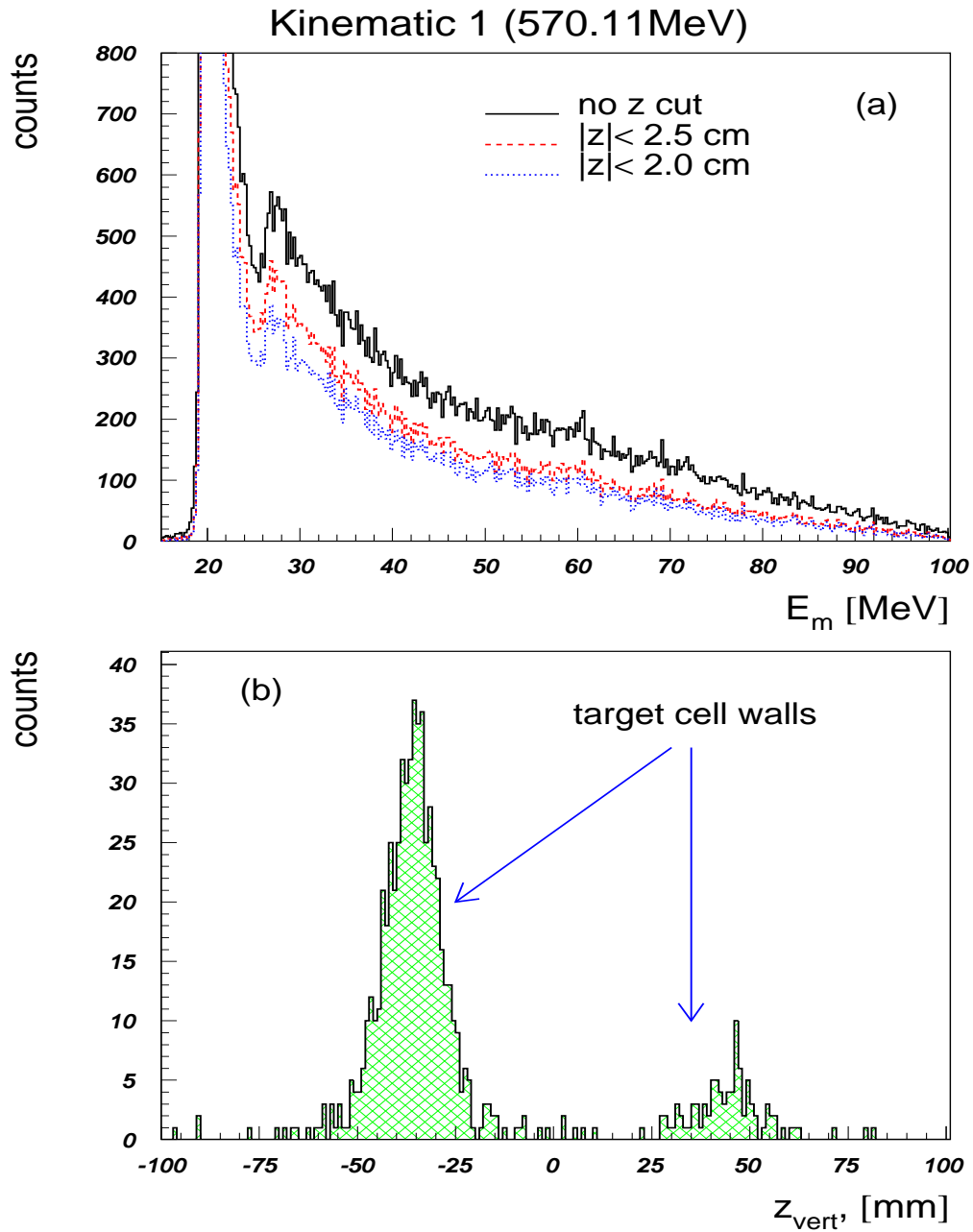


Figure 5.11: (a) The missing-energy spectra (from top to bottom): no cut on z , $|z| \leq 2.5$ cm and $|z| \leq 2.0$ cm; (b) z -coordinate at the target for the walls of the empty cell

measurements. Using such a procedure, the portion of $\text{Al}(e,e'p)X$ events in the collected $(e,e'p)$ data was found to be less than 0.1 %.

5.3.5 Background contribution from the scattering chamber windows

The source of the background

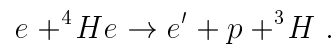
The scattering chamber was built with a narrow (50 mm wide) Al window as shown in Figure C.1. Particles passing through this window suffer multiple scattering and energy loss due to ionization and radiation processes. This caused deflection of some electrons and protons (which were originally outside the spectrometers acceptance), to be detected in Spectrometers A and B. Since these particles lost energy in the Al they were observed mostly in the high-missing-energy region. If the vertical position of the scattering chamber was misaligned relative to the beam line, the effect of re-scattering becomes more visible and more difficult to remove. This re-scattering was observed for the first time during the $(e,e'p)$ measurements with ${}^3\text{He}$. It appears as a large bump in the high missing-energy region, where practically no strength was observed before. This effect was very significant due to the lower proton momenta detected in Spectrometer B, and a significant misalignment (-8 mm) of the scattering chamber. For ${}^4\text{He}$, the average energy-loss for protons in the 1.8-cm thick Al window, when detected in Spectrometer B is $\sim 15 \text{ MeV}$. Consequently, this background appeared in the missing-energy region of the three and four-body breakup channels, where the statistical uncertainty is relatively large. This caused problems in identifying it.

The missing-energy and angular dependence of this background in Spectrometers A and B was studied using measured $(e,e'p)$ data, and GEANT simulations of the $(e,e'p)$ reaction.

Spectrometer B

Modeling of the experimental setup using GEANT was used to study both the significance of this background process at different missing-energies, and the efficiency of the software cuts used for its reduction. Details of the new Monte-Carlo code are given in Appendices A and C.

In Figure 5.12, one can see the results of simulations for the two-body-breakup reaction channel



Each picture contains the missing-energy spectrum for the fully opened collimator of Spectrometer B, and the missing-energy spectrum obtained for one of the four different positions of the vertical collimator (60, 55, 50, and 45 mrad). In all these plots, an enhancement of the number of detected events at $E_m \approx 37 \text{ MeV}$, corresponding to protons losing energy in the scattering chamber, is visible. The collimator positions are equivalent to cuts on the vertical angle θ_{tgt}^B of the same absolute value. None of these cuts is 100 % efficient, but the number of background events was reduced significantly already by a $\pm 50 - 55 \text{ mrad}$ cuts.

The optimum value of the cut is $|\theta_{tgt}^B| \leq 50 \text{ mrad}$, which effectively suppresses re-scattering and does not unnecessarily reduce the volume of the (e,e'p) data.

A similar background study was carried out for the measured missing-energy spectra. This was done by selecting (e,e'p) events detected in the range of the vertical angles θ_{tgt}^B close to the limit of the spectrometer acceptance, as shown in Figure 5.13. The missing-energy spectra selected for θ_{tgt}^B ranging between 60 and 70 mrad, show significant strength around $E_m \approx 34 \text{ MeV}$, comparable with three-body breakup. This additional strength disappears only for $|\theta_{tgt}^B| \leq 50 \text{ mrad}$, providing additional confirmation of the effectiveness of this cut.

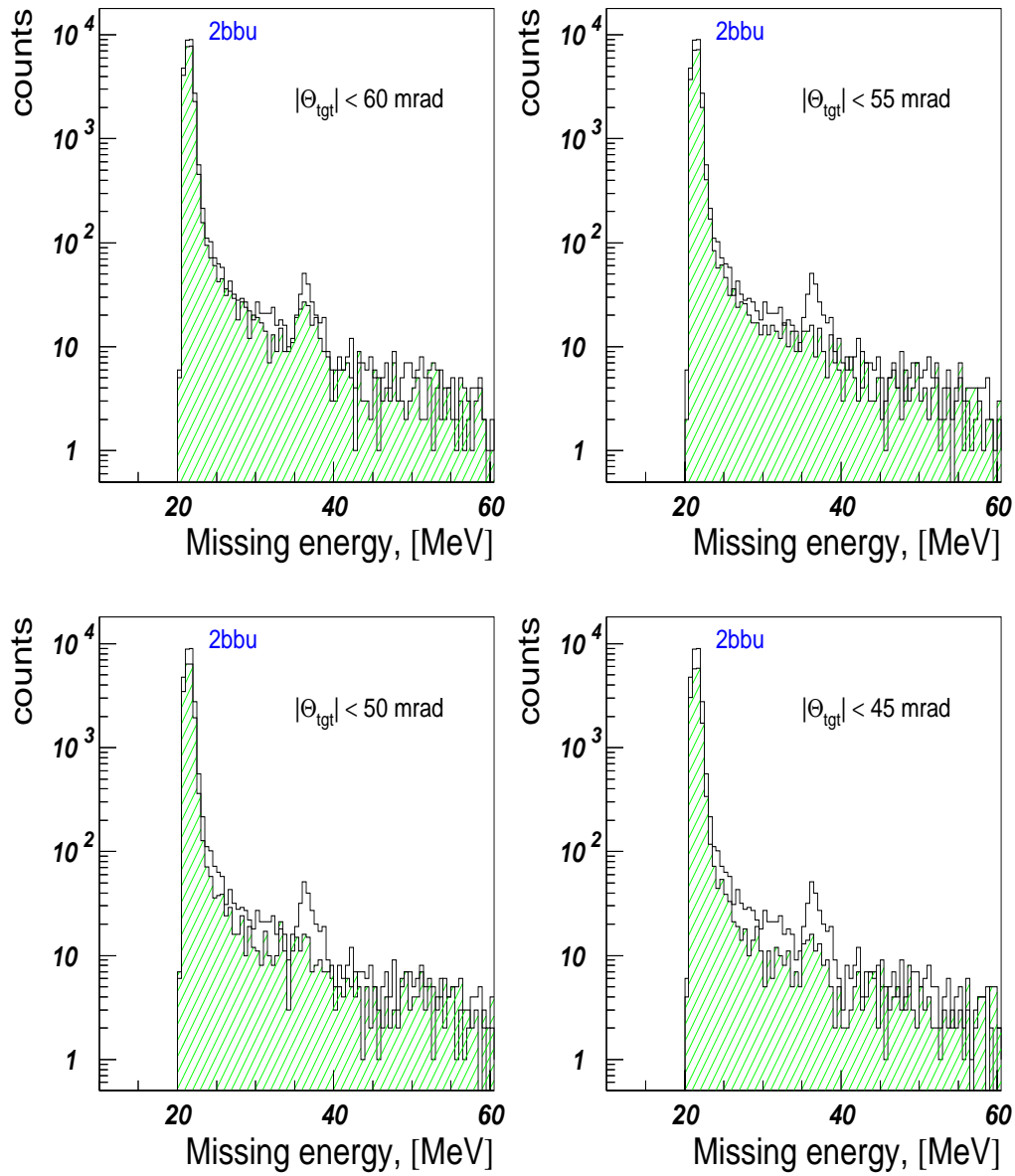


Figure 5.12: Simulated missing-energy spectra : solid line - collimator B is opened by 70 mrad in the vertical direction. Hatch style histograms contain the missing-energy spectra for the different values of the vertical acceptance: 60, 55, 50 and 45 mrad. The scattering-chamber position is -3 mm in the vertical direction

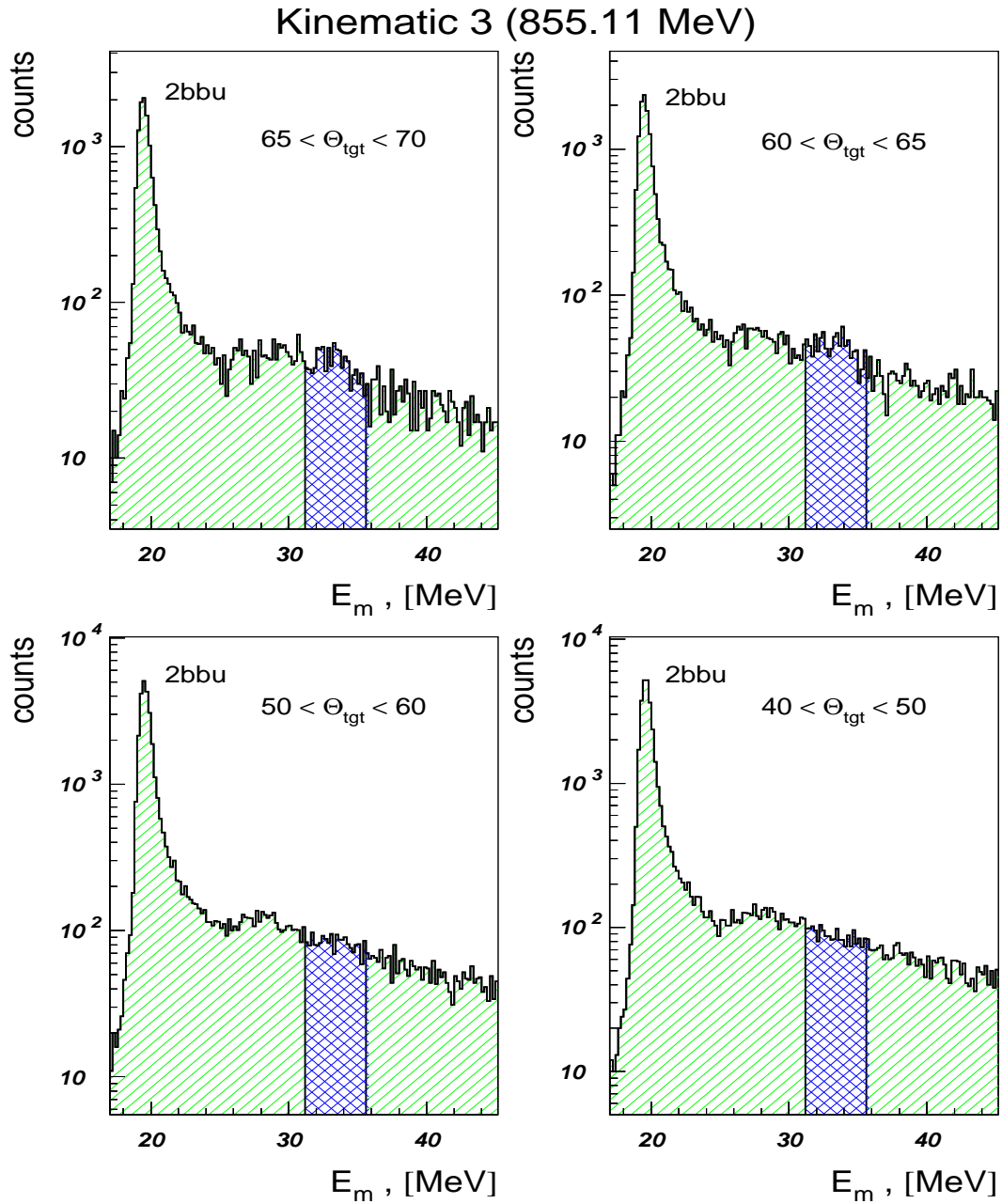


Figure 5.13: Kinematic 3, the measured data; the background at missing energies around 34 MeV from the protons losing energy in the scattering-chamber window

Spectrometer A

Electrons detected in Spectrometer A can also be scattered from the window of the scattering chamber. Because the electron mass is much less than the proton mass, the radiation losses become very important. Protons lose energy only due to ionization losses in the Al window and thus the majority of the background events appear in some defined missing-energy region (see Figure 5.15b and 5.16b). Electrons on the other hand can radiate much more energy in the form of one or more hard photons, and therefore contribute to the background at much higher missing energies.

In the measured (e,e'p) data, the background from the scattered electrons was clearly observed as a broad peak at missing energies up to 70 MeV. This is shown in Figure 5.14, where the (e,e'p) events were selected by the software cut $\theta_{tgt} \geq 70 \text{ mrad}$. This background shows a clear dependence on the momentum of the detected electrons (see Figure 5.15a, 5.16a and 5.14). At higher electron momenta, the background is less, in agreement with the dependence on the multiple scattering angle $\theta_0 \sim \frac{1}{p}$, (p is the scattered momentum). In Kinematic 3, for electron momenta near 550 MeV/c, this type of background disappears in both the experimental data and the Monte-Carlo simulations.

Summary

The angular, and missing-energy dependence of the background due to particles scattered from the scattering-chamber window and detected in both Spectrometers A and B was studied. It was found that the major part of this background can be excluded from the final results by introducing two software cut on the vertical angle of both spectrometers. For Spectrometer B the value of this cut was $|\theta_{tgt}^B| \leq 50 \text{ mrad}$, and for Spectrometer A a value $|\theta_{tgt}^A| \leq 70 \text{ mrad}$ cut.

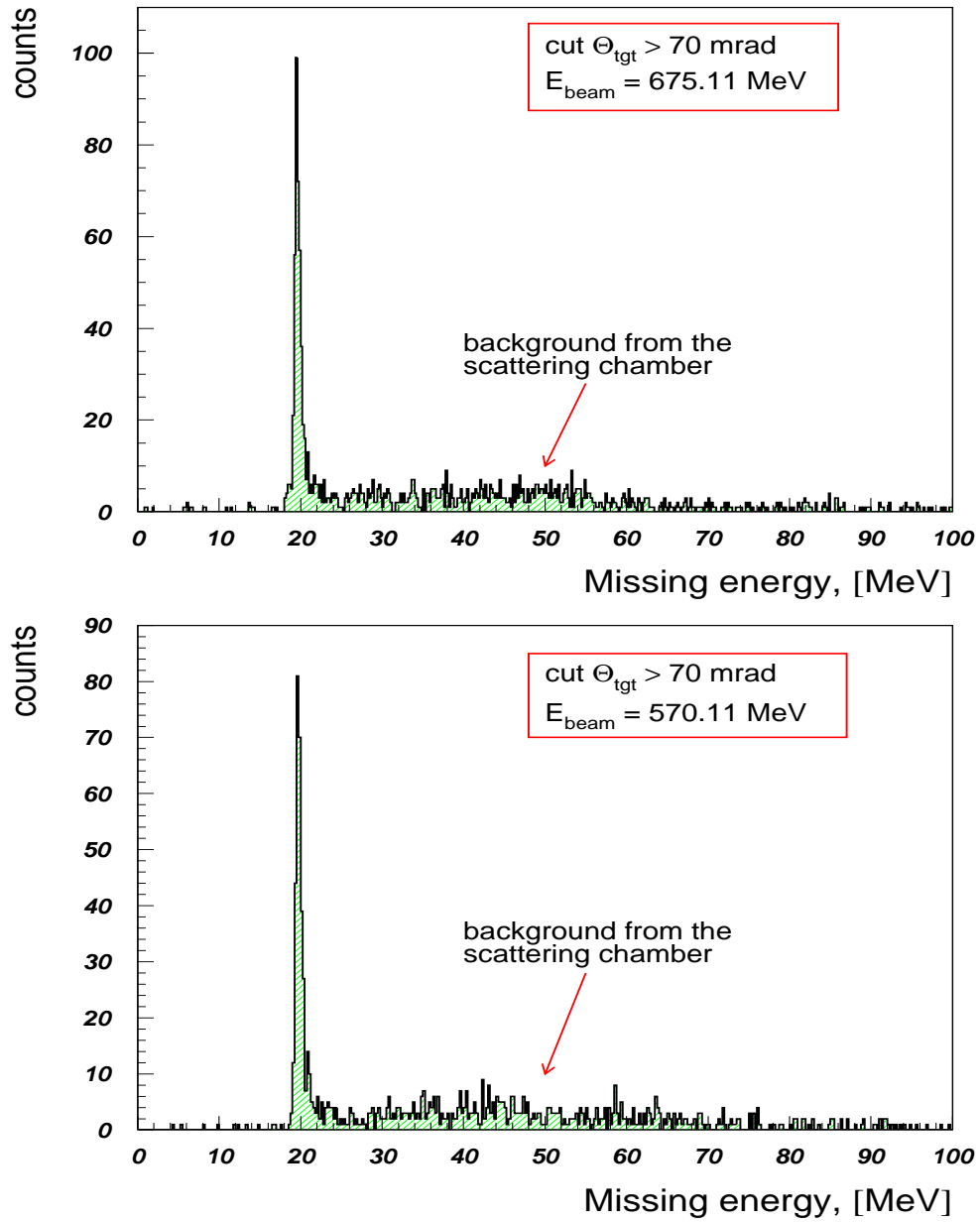


Figure 5.14: Kinematic 1 & 2, the measured data; the background from the electrons losing their energy in the scattering chamber window

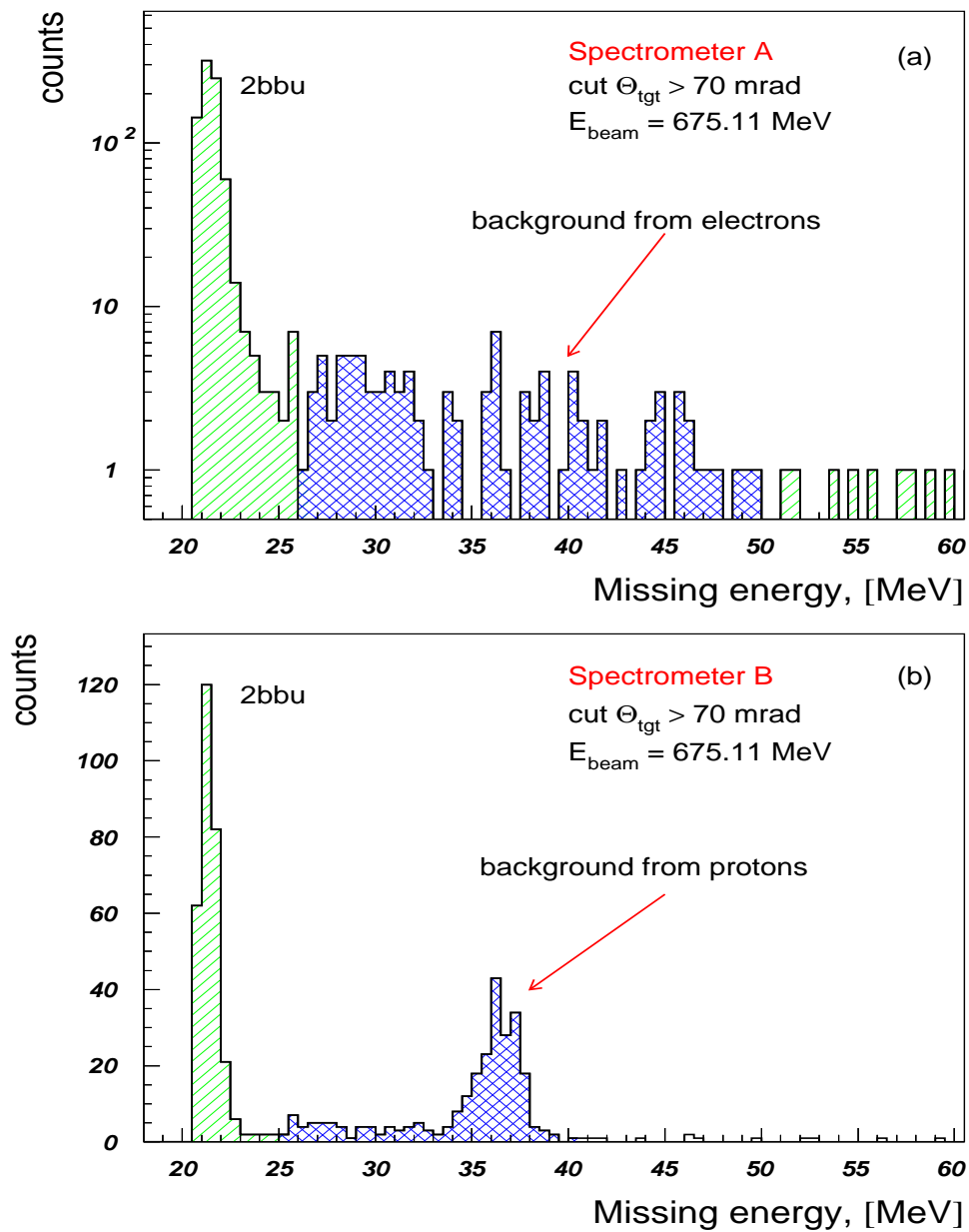


Figure 5.15: GEANT simulation for the Kinematic 2, of the background contribution at a high missing energy from the electrons and protons losing part of their energy in the scattering chamber window

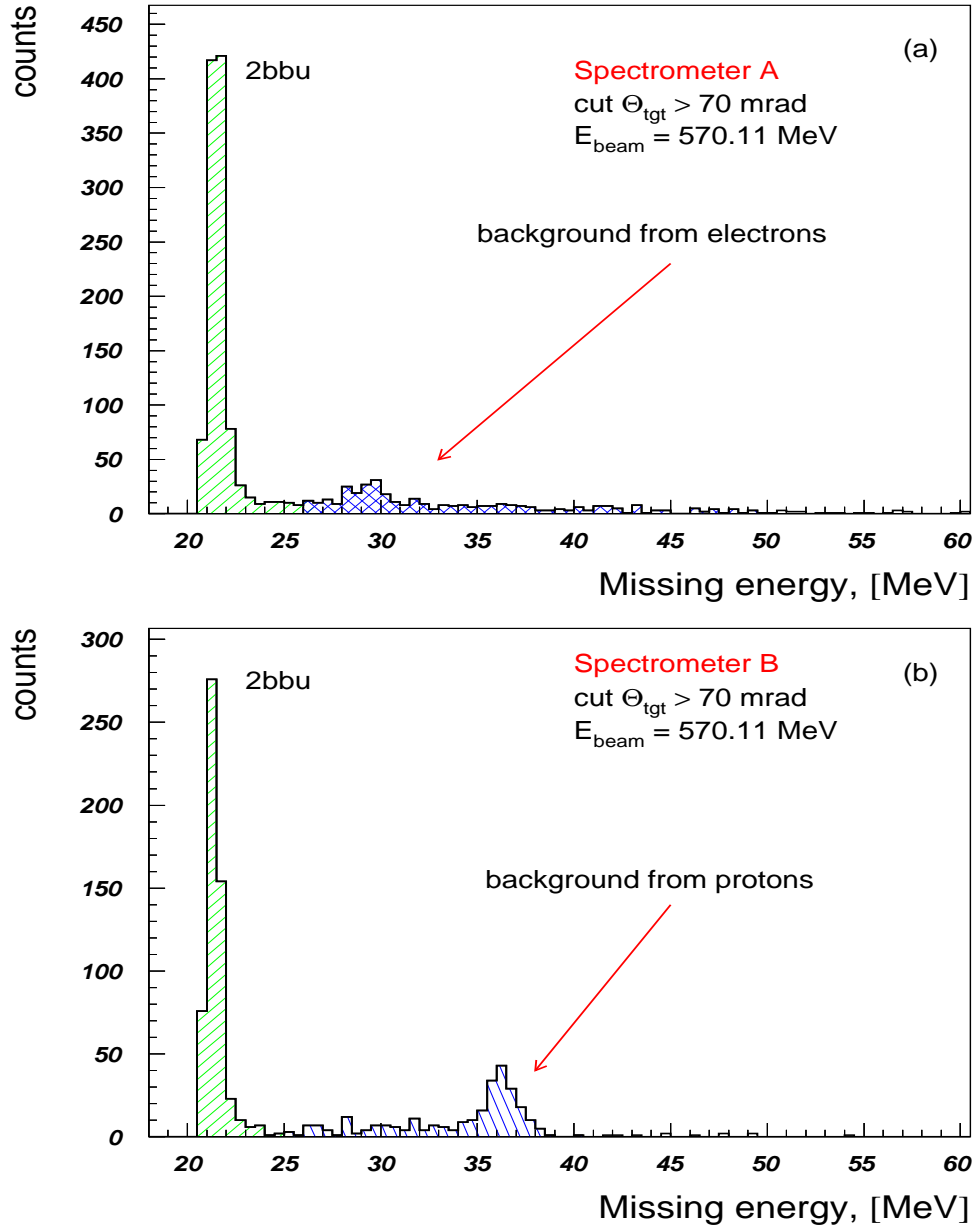


Figure 5.16: GEANT simulation for the Kinematic 1, of the background contribution at a high missing energy from the electrons and protons losing part of their energy in the scattering chamber window

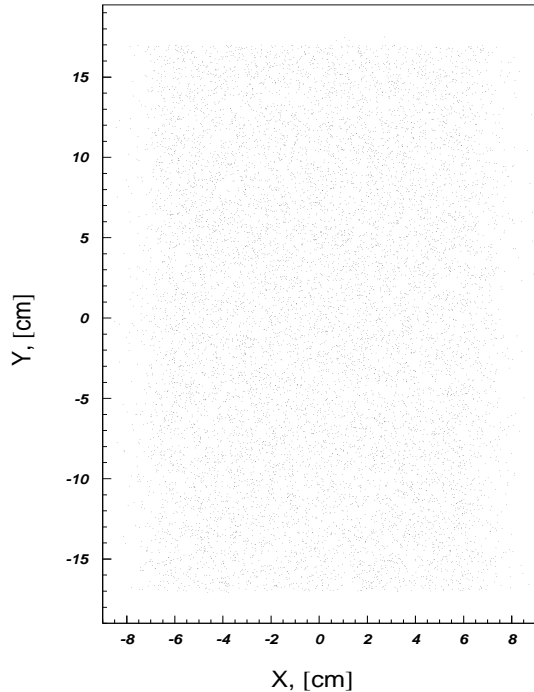


Figure 5.17: Image of Spectrometer B collimator ($E_m \geq 50 \text{ MeV}$)

5.3.6 Background at $E_m \geq 50 \text{ MeV}$

In reference [23] significant strength was observed at $E_m \geq 50 \text{ MeV}$ due to re-scattering of protons from the collimator edges of Spectrometer B with momentum around $500 \text{ MeV}/c$. In order to study the importance of this effect in these measurements, the particle's coordinates in the spectrometer systems were reconstructed at the collimator positions for both Spectrometer A and B. Using the vertex coordinates at the target and the distance to the collimators, the horizontal x and vertical y coordinates of the particles were reconstructed according to Equations B.6 and B.7. An additional software cut of $E_m \geq 50 \text{ MeV}$ was used to select only the high-missing-energy region, where the larger contribution of the background was expected.

The resulting image for the collimator of Spectrometer B is shown in Fig-

ure 5.17. The distribution of (e,e'p) events is purely random, with no indication of peaking near the collimator edges. The vertical acceptance of Spectrometer B is defined in this case by a cut on θ_{tgt} equal to ± 50 mrad. A similar uniform distribution of coincidence electrons was observed in Spectrometer A. From these results it was possible to conclude that most of the events at high missing-energies are not the result of scattering from the edges of the collimators.

5.3.7 Thickness of the helium target

Calculation technique

The single arm (e,e') data from Spectrometer C were used to extract the helium-target thickness for the (e,e'p) runs, using the reference value of the helium density calculated for elastic scattering from helium at the same beam energy (see Chapter 4). The number of raw counts detected in Spectrometer C was corrected for the deadtime τ_{eff} , scaling factor η_{eff} , total charge collected at the target Q_{tot} . Thus the corresponding N_{corr} values were calculated as:

$$N_{corr} = \frac{N_{raw} \eta_{eff}}{Q_{tot}(1 - \tau_{eff})} \quad (5.2)$$

where N_{corr} is the number of events detected in Spectrometer C due to scattering from both ${}^4\text{He}$ gas and Al walls of the target cell. The contribution of the walls was subtracted from N_{corr} according to Equation 4.14. These final values, called N_{He}^{corr} , are given in Tables D.1, D.3 and D.5. The density of the helium gas was calculated for each individual (e,e'p) run by comparing these N_{He}^{corr} values with the reference value from the elastic scattering measurements:

$$\rho_{He}^{(e,e'p)} = \rho_{He}^{elast} \times \frac{N_{corr}^{He}(e,e'p)}{N_{corr}^{He}(elast)} \quad (5.3)$$

The helium density ρ_{He}^{tot} in Tables D.1, D.3 and D.5 was obtained from the density values corresponding to individual runs weighted by the charge collected during

these runs as follows:

$$\rho_{He}^{tot} = \frac{\sum_{i=1}^n \rho_{He}^i \cdot Q_i^{AB}}{\sum_{i=1}^n Q_i^{AB}} \quad (5.4)$$

where n is the total number of runs.

Experimental uncertainty

The absolute uncertainty in the helium-target density for the each (e,e'p) run was determined as :

$$\Delta\rho_{He}^{(e,e'p)} \approx \Delta\rho_{He}^{elast} + \Delta N_{He}^{corr} \quad (5.5)$$

The total absolute error $\Delta\rho_{He}^{(e,e'p)}$ was calculated by weighting the individual errors with the charge collected during the n individual runs:

$$\Delta\rho_{He}^{tot} = \frac{\sum_{i=1}^n \Delta\rho_{He}^i \cdot Q_i^{AB}}{\sum_{i=1}^n Q_i^{AB}} \quad (5.6)$$

5.3.8 ω -cut

The (e,e'p) measurements were performed at three different beam energies, so that the absolute values of the detected electron momenta and corresponding ω values were also different (see Figure 5.18). The experimental results obtained for these kinematics in the form of (E_m, p_m) histograms are compared in Chapter 6. Since the experimental cross sections are reduced to a function of these two variables only, (e,e'p) events with different ω values can contribute to the same (E_m^i, p_m^i) bin. Therefore, in order to compare the resulting cross section for different kinematics in the same kinematical region of the QE peak, an ω -cut which matches the acceptance for all measurements was used (see Figure 5.18).

The ω -range was limited to between 310.4 and 357.6 MeV, which corresponds to the acceptance of Spectrometer A for Kinematic 1. As a result of this cut, the (E_m, p_m) phase-space became almost identical for all kinematics, Figure 5.19.

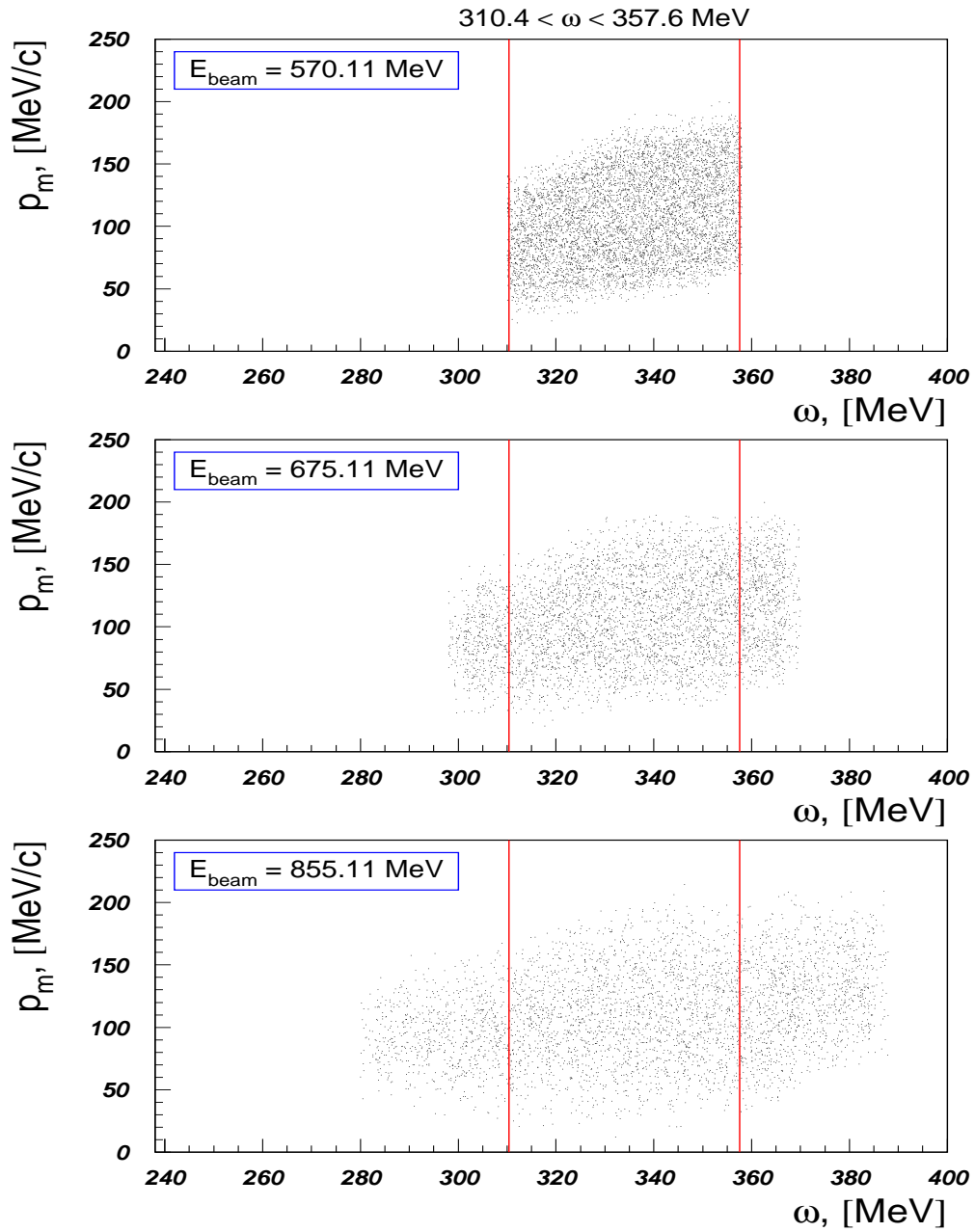


Figure 5.18: The cut on ω used to match the phase-space for the different kinematics of the (e,e'p) data

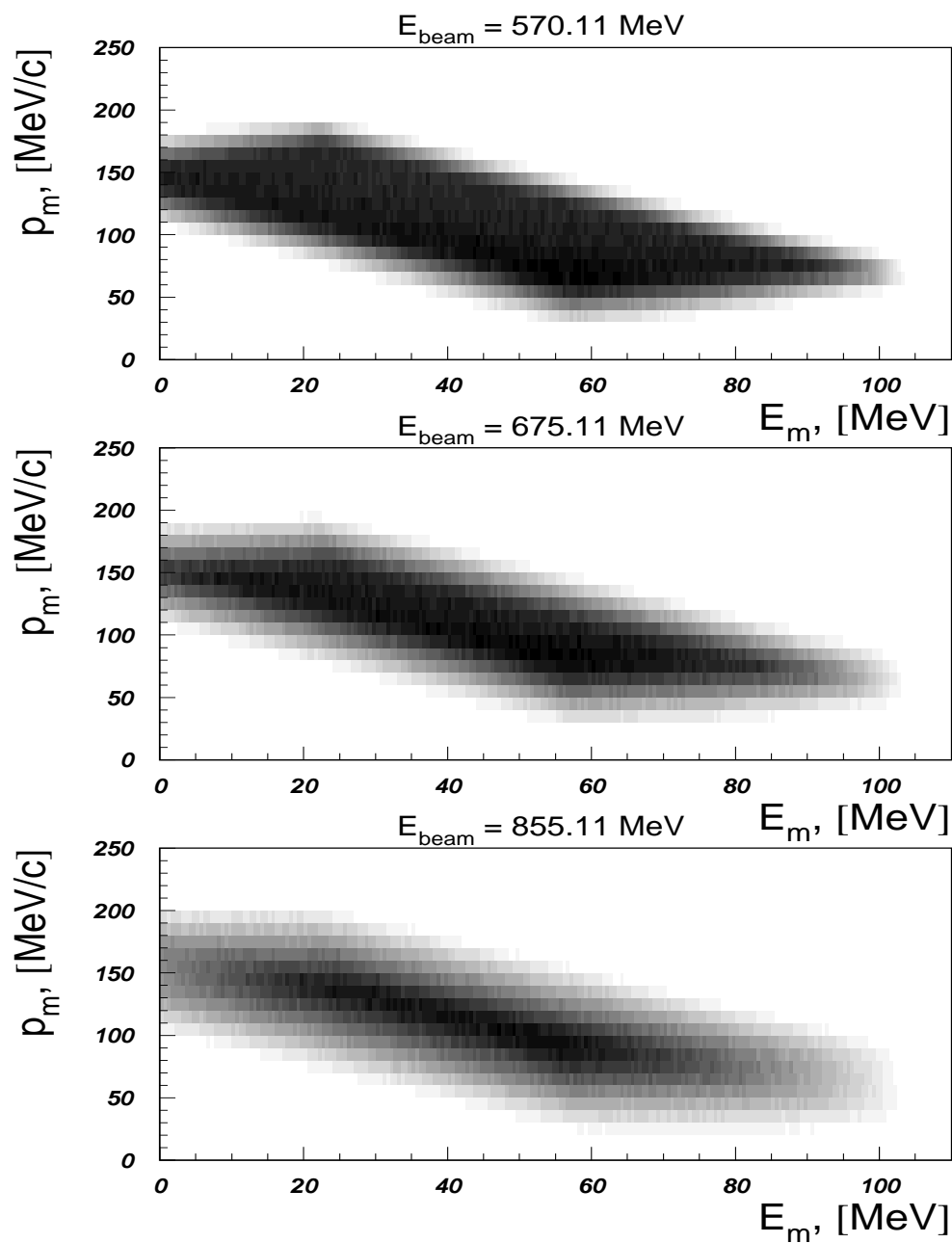


Figure 5.19: The (E_m, p_m) phase-space after the cut on ω

5.4 Six-fold differential cross section

Cross section definition

The experimental six-fold cross section was determined as:

$$\frac{d^6\sigma}{d\Omega_e d\Omega_p dp_e dp_p} = 10^{26} \times \frac{N[E_m^i, p_m^i] \cdot A_{He}}{\left(\frac{Q_{tot}^{AB}}{q_e}\right) \cdot N_A \cdot \rho_{He} \cdot (1 - \eta_{tot}) \cdot \epsilon_{tot} \cdot \Delta V(E_m^i, p_m^i)} \quad (5.7)$$

The cross section unit is: $\left[\frac{fm^2}{(MeV/c)^2 \cdot sr^2} \right]$

where

A_{He} is the Helium mass in [g/mol]

Q_{tot}^{AB} is total charge collected in [C]

$q_e = 1.602 \times 10^{-19}$ [C] (the elementary charge)

N_A is the Avogadro number in [1/mol]

η_{tot} is weighted dead-time value

ϵ_{tot} is a total efficiency of the setup

ρ_{He} is the helium-target density in [g/cm³]

$\Delta V(E_m^i, p_m^i)$ is the detection volume in $\left[\frac{1}{(MeV/c)^2 \cdot sr^2} \right]$

The detection volume $\Delta V(E_m^i, p_m^i)$ was calculated with the new GEANT Monte-Carlo code described in Appendices A and C as:

$$\Delta V(E_m^i, p_m^i) = \frac{N_{det}(E_m^i, p_m^i)}{N_{trials}} \Delta p_e \Delta p_p \Delta \Omega_e \Delta \Omega_p \quad (5.8)$$

where N_{det} is the number of events detected in bin (E_m^i, p_m^i) , N_{trials} is the total number of events generated in the full volume $\Delta p_e \Delta p_p \Delta \Omega_e \Delta \Omega_p$ sampled in the simulations. This volume was selected to include the entire experimental momentum and angular acceptance ranges of the spectrometers.

Absolute normalization of the measured cross section

Calculation of the cross section requires knowledge of the total charge collected at the target, the full data-acquisition deadtime, the total efficiency of the

experimental setup and the helium-target density.

The helium-target density was calculated from the values obtained for each (e,e'p) run according to the Equation 5.4. As for the elastic data analysis, the total charge collected at the target, Q_i^{AB} , and dead-time values η_i corresponding to the individual runs, were calculated using the COLA++ code. These dead-time values were weighted by the charge collected at the target during these runs, and the final dead-time value η_{tot} was obtained as:

$$\eta_{tot} = \frac{\sum_{i=1}^n \eta_i \cdot Q_i^{AB}}{\sum_{i=1}^n Q_i^{AB}} \quad (5.9)$$

The efficiency value ϵ_{tot} was introduced to compensate for the loss of (e,e'p) events as a result of the ToF-cut (see Section 5.3.2). The inefficiency of this cut was calculated as a fraction of (e,e'p) events in the two-body breakup peak that were outside the 12 *nsec* coincidence window.

5.5 Five-fold differential cross section

For the two-body breakup reaction channel, the observed missing-energy spectra contain peaks with a width determined by the experimental energy resolution; but in reality they are δ -functions. Thus, this reaction channel can be described by five kinematic variables only: one of the six variables mentioned above is redundant. However, due to the additional dependence of the two-body-breakup cross section on the missing energy, the measured strength must be integrated over the missing-energy region, where we expect this strength to be non-zero.

Thus the cross section for this reaction channel is obtained by integrating the six-fold cross section over the selected region of the missing energy $E_1 \leq E_m \leq E_2$ as:

$$\frac{d^5\sigma}{d\Omega_e d\Omega_p dp_e} = \int_{E_1}^{E_2} \frac{d^6\sigma}{d\Omega_e d\Omega_p dp_e dp_p} \frac{1}{\left| \frac{\partial E_m}{\partial p_p} \right|} \quad (5.10)$$

where the Jacobian $|\frac{\partial E_m}{\partial p_p}|$ was calculated from the definition of E_m from Equation 2.11 as:

$$\frac{\partial E_m}{\partial p_p} = -\frac{p_p}{E_p} + \frac{\vec{p}_p \cdot \vec{p}_B}{p_p E_B} \quad (5.11)$$

where $E_B = \sqrt{p_B^2 + m_{A-1}^2}$ and m_{A-1} is the mass of the A-1 nucleus, as defined in Chapter 2.

In order to perform these calculations the six-fold cross section differential in missing energy is calculated first as:

$$\frac{d^6 \sigma}{d\Omega_e d\Omega_p dp_e dE_m} = 10^{26} \times \frac{N[E_m^i, p_m^i] \cdot A_{He}}{\left(\frac{Q_{tot}^{AB}}{q_e}\right) \cdot N_A \cdot \rho_{He} \cdot (1 - \eta_{tot}) \cdot \epsilon_{tot} \cdot \Delta V_{jac}(E_m^i, p_m^i)} \quad (5.12)$$

where $\Delta V_{jac}(E_m^i, p_m^i)$ is the detection volume calculated in the same way as the detection volume used in Equation 5.7, but weighted by a factor $|\frac{\partial E_m}{\partial p_p}|$:

$$\Delta V_{jac}(E_m^i, p_m^i) = \frac{N_{det}^{jac}(E_m^i, p_m^i)}{N_{trials}} \Delta p_e \Delta p_p \Delta \Omega_e \Delta \Omega_p \quad (5.13)$$

where each event $N_{det}(E_m^i, p_m^i)$ is weighted by $|\frac{\partial E_m}{\partial p_p}|$. As the last step, the five-fold cross section is calculated by integrating over the defined range of missing energy:

$$\frac{d^5 \sigma}{d\Omega_e d\Omega_p dp_e} = \sum_{E_1}^{E_2} \frac{d^6 \sigma}{d\Omega_e d\Omega_p dp_e dE_m} \Delta E_m \quad (5.14)$$

5.6 The experimental spectral function

The experimental (“distorted”) spectral function can be extracted from the experimental cross section according to Equation 2.22. In data analysis it was obtained using a formula similar to Equation 5.7, except that the detection volume was weighted by the factor $p_p^2 \cdot \sigma_{ep}$:

$$S(E_m^i, p_m^i) = 10^{26} \times \frac{N[E_m^i, p_m^i] \cdot A_{He}}{\left(\frac{Q_{tot}^{AB}}{q_e}\right) \cdot N_A \cdot \rho_{He} \cdot (1 - \eta_{tot}) \cdot \epsilon_{tot} \cdot \Delta V_{ep}(E_m^i, p_m^i)} \quad (5.15)$$

The detection volume was calculated as:

$$\Delta V_{ep}(E_m^i, p_m^i) = \frac{N_{det}^{ep}(E_m^i, p_m^i)}{N_{trials}} \Delta p_e \Delta p_p \Delta \Omega_e \Delta \Omega_p \quad (5.16)$$

where $N_{det}^{ep}(E_m^i, p_m^i)$ for each event during the Monte-Carlo simulations was weighted by the $p_p^2 \cdot \sigma_{ep}$.

The proton momentum-density distribution

Integration of the proton spectral function $S(E_m, p_m)$ over the missing-energy region corresponding to one of the reaction channels, gives the proton momentum density distribution $\rho(p_m)$ for this channel:

$$\rho(p_m) = \int_{E_{m1}}^{E_{m2}} S(E_m, p_m) dE_m \quad (5.17)$$

In the next chapter, the proton-momentum distributions $\rho_{3,4}(p_m)$ for the three-body and four-body-breakup reaction channels will be calculated by integrating the measured spectral function over the missing-energy region between 25 and 45 MeV.

5.7 Radiative corrections with RADCOR

5.7.1 Introduction

Electrons can be easily deflected in the electromagnetic field of the nucleus, and radiate both real and virtual photons. This radiation creates an unwanted background in the missing-energy spectrum, and produces errors in the measured (e,e'p) cross section. Much of the strength in the low missing-energy region of the spectrum

is shifted to higher missing energies, creating visible strength in the uncorrected raw spectra.

The average energy loss of the incident electron beam ($\sim 0.3 \text{ MeV}$), scattered electron ($\sim 0.5 \text{ MeV}$) and protons ($\sim 0.9 \text{ MeV}$) due to ionization of the target medium was taken into account in the raw data analysis using COLA++. Other physical processes, which lead to a re-distribution of the (e,e'p) events in the measured (E_m, P_m) phase-space, such as external and internal bremsstrahlung and Landau straggling, were corrected separately using the RADCOR program. Corrections due to external and internal bremsstrahlung are described below in detail. The correction factor for Landau straggling was equal to 1.000 for both electrons and protons in the experimental kinematic range, and is not discussed in this thesis. The RADCOR version at Mainz, written by Rokavec [34], was used. This incorporates improvement in the calculation of external bremsstrahlung (see also ref. [23]) by taking into account the contribution from the walls of the Al target cell.

5.7.2 Schwinger radiation

The question of the radiative corrections to electron-scattering data caused by virtual photons was intensively studied between 1950 and 1970. Figure 5.20 shows some of the diagrams describing the emission and re-absorption of virtual photons. Diagrams A) and B) are the electron self-energy diagrams, and lead to mass and electron wave function renormalization. Diagram C) describes the vertex renormalization and D) is the "vacuum polarization" (photon self-energy) diagram, which modifies the photon propagator and renormalizes the electron charge.

Schwinger [35] showed that in an experiment performed with a finite energy resolution ΔE , the elastic scattering process is indistinguishable from the process in which a soft, real photon (of energy $k \leq \Delta E$) is emitted in the electromagnetic field of the target nucleus involved in the elastic scattering. One thus has to include in the cross section calculation (and the radiative correction) the diagrams from

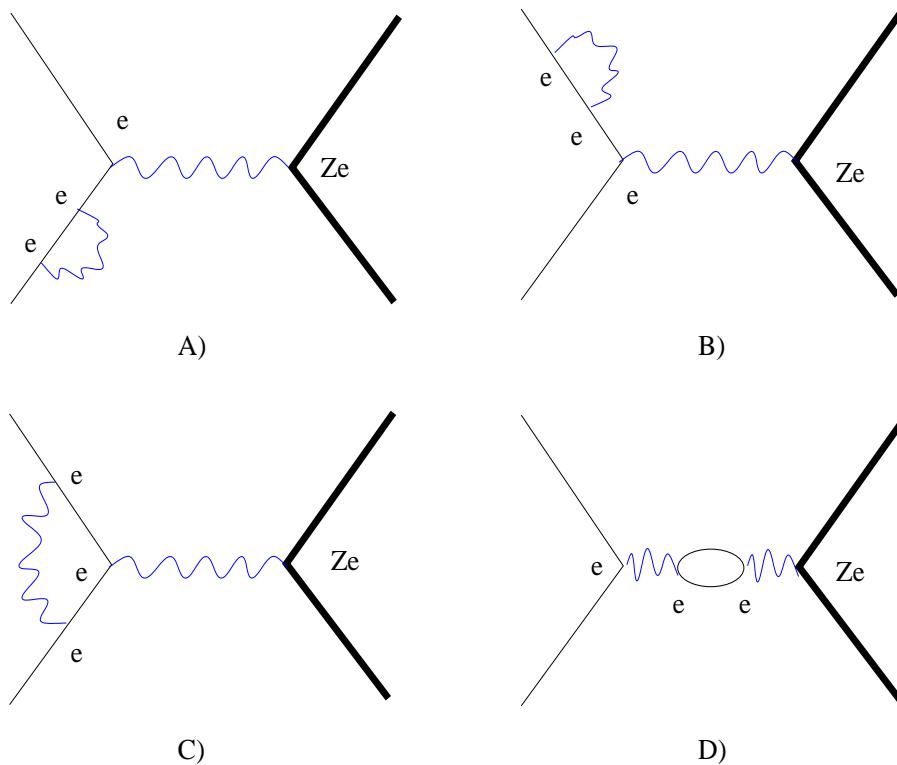


Figure 5.20: Radiative correction diagrams for electron-nucleus scattering

Figure 5.21 in which one soft, real bremsstrahlung photon is emitted following the electron-nucleus interaction. Diagrams C) and D) of Figure 5.21 are proportional to a factor of $1/M$, where M is the nuclear mass, and being small are not taken into account in most of the cases. Therefore the experimental cross section for the elastic scattering below the ΔE cut-off energy can be written as

$$\frac{d\sigma(\Delta E)}{d\Omega} = \frac{d\sigma^{th}}{d\Omega} (1 - \delta_s) \quad (5.18)$$

where $\frac{d\sigma^{th}}{d\Omega}$ is a theoretical cross section, and δ_s is the Schwinger correction for elastic scattering [36]. In case of the (e,e'p) process the correction factor for Schwinger radiation proposed by Penner [37] was used in RADCOR:

$$K_s = \frac{e^{\delta_{real}}}{1 + \delta_{virt}} \quad (5.19)$$

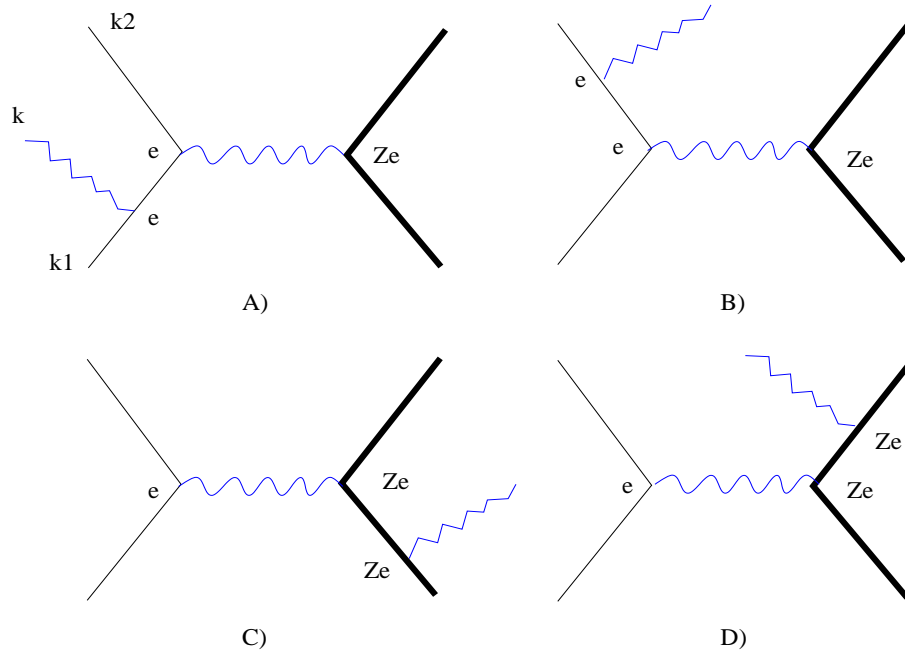


Figure 5.21: Diagrams for photon emission during electron-nucleus scattering

The contribution of real photons was taken as:

$$\delta_{real} = \frac{\alpha}{\pi} \left[\ln \frac{E_i E_f b}{\eta^2 \Delta E^2} \right] \left[\ln \left(\frac{-q_\mu q^\mu}{m_e^2} \right) - 1 \right] \quad (5.20)$$

where ΔE is the resolution cut-off energy and b , η and $q_\mu q^\mu$ have the following definitions:

$$b = 1 + \frac{2\omega}{M} \sin^2 \left(\frac{\theta_e}{2} \right)$$

$$\eta = 1 + \frac{2E_i}{M} \sin^2 \left(\frac{\theta_e}{2} \right)$$

$$q_\mu q^\mu = \omega^2 - (\vec{q})^2$$

The contribution of virtual photons was taken as:

$$\delta_{virt} = \frac{\alpha}{\pi} \left[\frac{13}{6} \left[\ln \frac{-q_\mu^\mu}{m_e^2} - 1 \right] - \frac{17}{18} - \frac{\pi^2}{6} - \frac{1}{2} \ln^2 \left(\frac{E_i}{E_f} \right) + L_2 \cos^2 \left(\frac{\theta_e}{2} \right) \right] \quad (5.21)$$

where the Spence function $L_2(x)$ is:

$$L_2(x) = \int_0^x \frac{\ln(1-y)}{y} dy \quad (5.22)$$

or

$$L_2(x) = \sum_{i=1}^{\infty} \frac{x^i}{i^2} \quad (5.23)$$

E_i and E_f in all equations are the initial and final energy of the electron, M is the target-nucleus mass and α is the electromagnetic coupling constant.

The correction factor for Schwinger radiation calculated with RADCOR was approximately 17, 20 and 25 % for Kinematics 1, 2 and 3 respectively (see Table 3.3).

5.7.3 External bremsstrahlung

Although the Schwinger correction for radiation is the major part of the radiative correction, so-called external bremsstrahlung must also be taken into account. External bremsstrahlung are produced when an incident or scattered electron radiates a real photon in the electromagnetic field of the target nuclei other than those involved in the (e,e'p) reaction. An approximate radiation correction for external bremsstrahlung was suggested by Friedrich [38]:

$$K_{ap}^{ext}(\Delta E) = 1 - \int_0^{E_{beam} - \Delta E} f^{rad} dE_f = 1 - \delta^{rad} \quad (5.24)$$

where f^{rad} is the probability for the emission of one real photon:

$$f^{rad}(E_f) = t_{eff} \frac{1}{\Delta E} [1 - \eta R + R^2] \quad (5.25)$$

$$\eta = \frac{2}{3} - \frac{1}{9} (\ln 183 Z^{-1/3})^{-1} \quad (5.26)$$

where $R = E_{beam}/E_f$, $t_{eff} = t/X_0$ is the effective target thickness in radiation lengths, t is the target thickness, X_0 is the radiation length in $[g/cm^2]$ and

$$\delta^{rad} = exp \left[t_{eff} \left[-\left(\zeta - \frac{1}{2}\right) + \zeta \ln \frac{E}{\Delta E} + \zeta \frac{\Delta E}{E} - \frac{1}{2} \left(\frac{\Delta E}{E}\right)^2 \right] \right] \quad (5.27)$$

$$\zeta = \frac{1}{9} \left[12 + \frac{(Z+1)}{l_1 Z + l_2} \right] \quad (5.28)$$

$$X_0 = 716.405 \frac{A_{eff}}{Z_{eff}} \frac{1}{(Z_{eff} \cdot (l_1 - f_c) + l_2)} \quad (5.29)$$

Z_{eff}	l_1	l_2
1	5.31	6.114
2	4.79	5.621
3	4.74	5.805
4	4.71	5.924
≥ 5	$5.216 - \frac{1}{3} \ln(Z_{eff})$	$7.085 - \frac{2}{3} \ln(Z_{eff})$

Table 5.1: Parameters for calculation of the radiation length in RADCOR

in the above l_1 and l_2 are parameters for calculating the radiation length (Table 5.1) and f_c is a correction describing charge-screening of the nucleus

$$f_c = (Z_{eff} \alpha)^2 \left[1.202 + (Z_{eff} \alpha)^2 \left(-1.0369 + 1.008 \frac{(Z_{eff} \alpha)^2}{((Z_{eff} \alpha)^2 + 1)} \right) \right] \quad (5.30)$$

Z_{eff} and A_{eff} are the effective equivalents of charge Z and A :

$$Z_{eff} = \sum_i w_i Z_i \quad (5.31)$$

$$A_{eff} = \sum_i w_i A_i \quad (5.32)$$

Here Z_i , A_i , w_i are the charge, mass number and weighting of atoms of type i in the target.

The correction factor for external bremsstrahlung calculated with RADCOR was approximately 2.1, 2.5 and 2.9 % for Kinematics 1, 2 and 3 respectively (see Table 3.3).

External bremsstrahlung from the target cell material

The target cell material was *Al* plus a small amounts of heavier metals like *Zn* and *Cu* (see Table 3.2). In order to calculate with RADCOR the contribution of external bremsstrahlung from the wall materials, the total target thickness d_{tot}

was calculated:

$$d_{tot} = d_{He} + d_{Al} + d_{Cu} \quad (5.33)$$

where d_{He} is a thickness of 4He ($\sim 0.154 g/cm^2$), d_{Al} is a thickness of the Al ($0.0575 g/cm^2$), and d_{Cu} is a thickness of a heavy metals like Cu ($\sim 0.016 g/cm^2$).

An effective total radiation length X_0^{tot} was calculated according to reference [40] as:

$$X_0^{tot} = \frac{1}{(d_{He}/d_{tot})/X_0^{He} + (d_{Cu}/d_{tot})/X_0^{Cu} + (d_{Al}/d_{tot})/X_0^{Al}} \quad (5.34)$$

where X_0^{He} is the radiation length in 4He , X_0^{Al} is the radiation length in Al ($24 g/cm^2$), X_0^{Cu} is the radiation length in Cu ($12.86 g/cm^2$). The total effective radiation length of the target material was approximately $43 g/cm^2$.

5.7.4 Limitations of the unfolding procedure with RADCOR

The major problems appearing during the radiative unfolding with RADCOR were caused by the following two reasons.

First of all, the radiative corrections are performed in a 2-dimensional (E_m, p_m) phase-space, and as an input RADCOR requires a 2-D cross section histogram. This is produced by division of the 2-D histogram for the experimental yield by the 2-D detection-volume histogram, according to Formula 5.7. Thus the available kinematic information about the individual (e,e'p) events is limited by these two values plus the beam energy value. In order to compensate for the lack of information about each coincidence (e,e'p) event, the following assumptions are made during the RADCOR initialization:

- 1) the momentum transfer \vec{q} , and the proton angle are fixed at their central value;
- 2) the angle between $p_m^{\vec{}}$ and \vec{q} is set to zero;

Therefore, the radiative tail trajectories calculated with RADCOR can differ from reality, resulting in an unpredictable systematic error for the unfolding procedure.

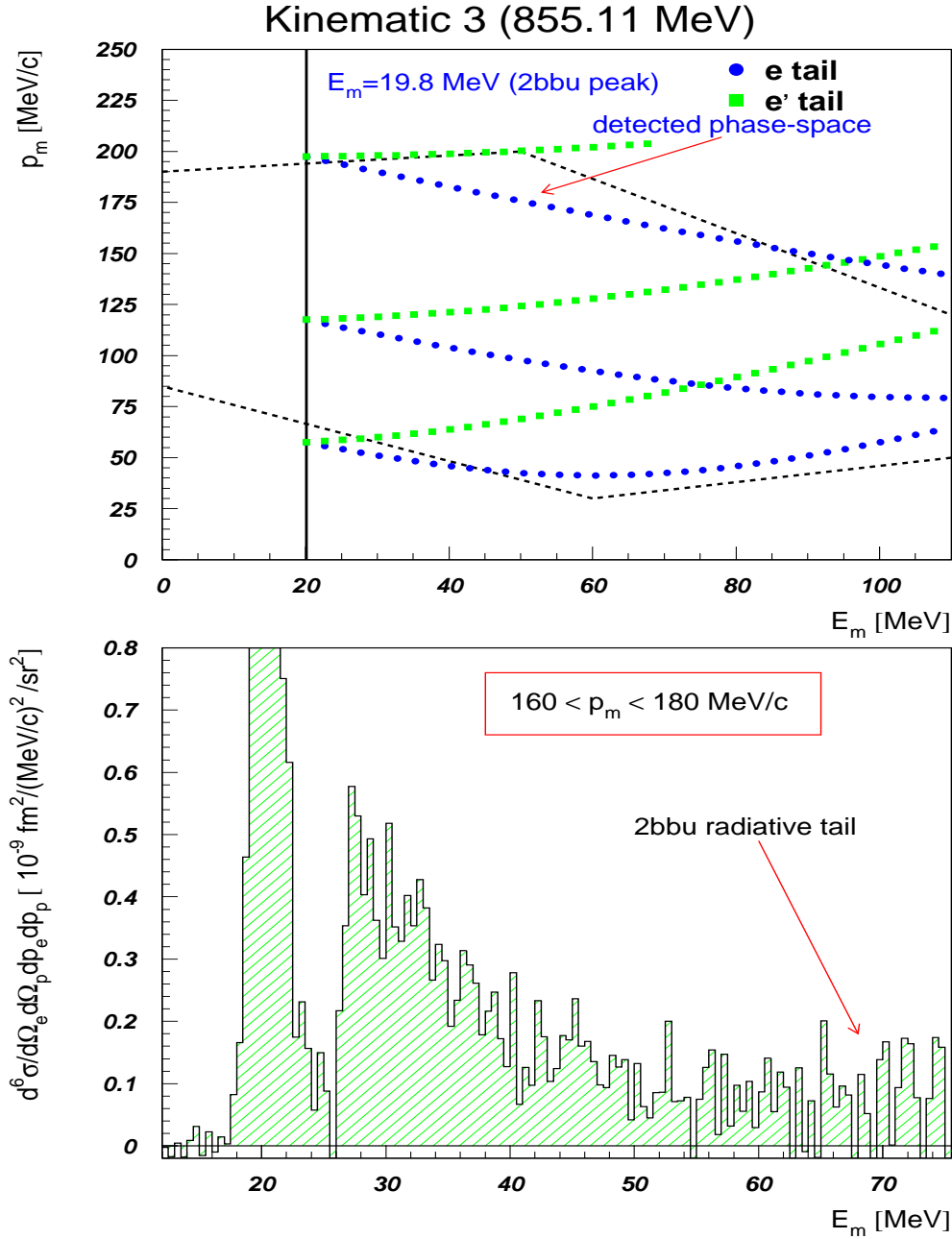


Figure 5.22: Radiative tails from the incident and scattered electrons (top). Continuum cross section corrected for radiation using RADCOR (bottom); significant radiative contribution (from the two-body-breakup peak at a higher p_m) is expected in the missing-energy region shown as the “2bbu radiative tail” (bottom)

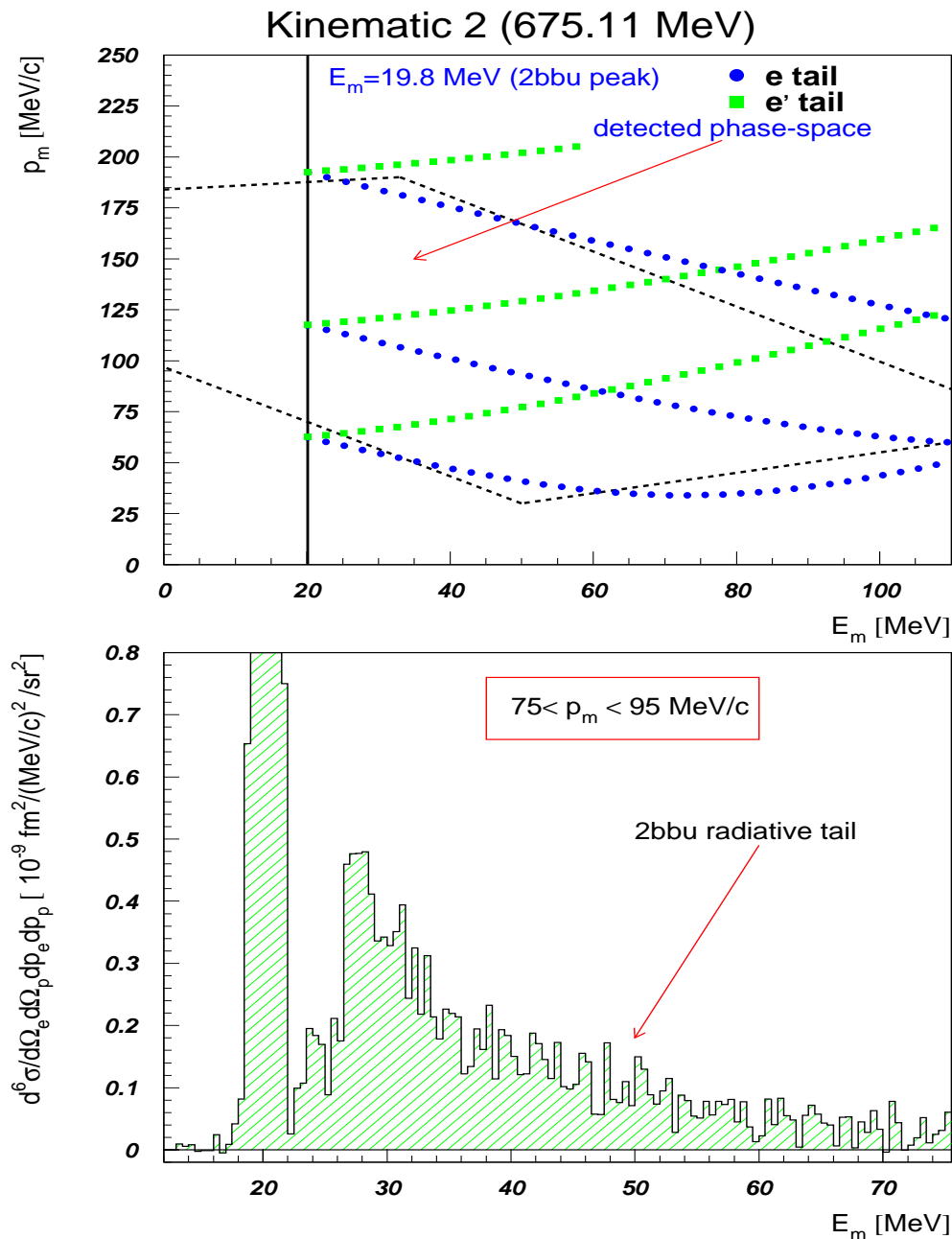


Figure 5.23: Radiative tails from the incident and scattered electrons (top). Continuum cross section corrected for radiation using RADCOR (bottom); significant radiative contribution (from the two-body-breakup peak at a lower p_m) is expected in the missing-energy region shown as the “2bbu radiative tail” (bottom)

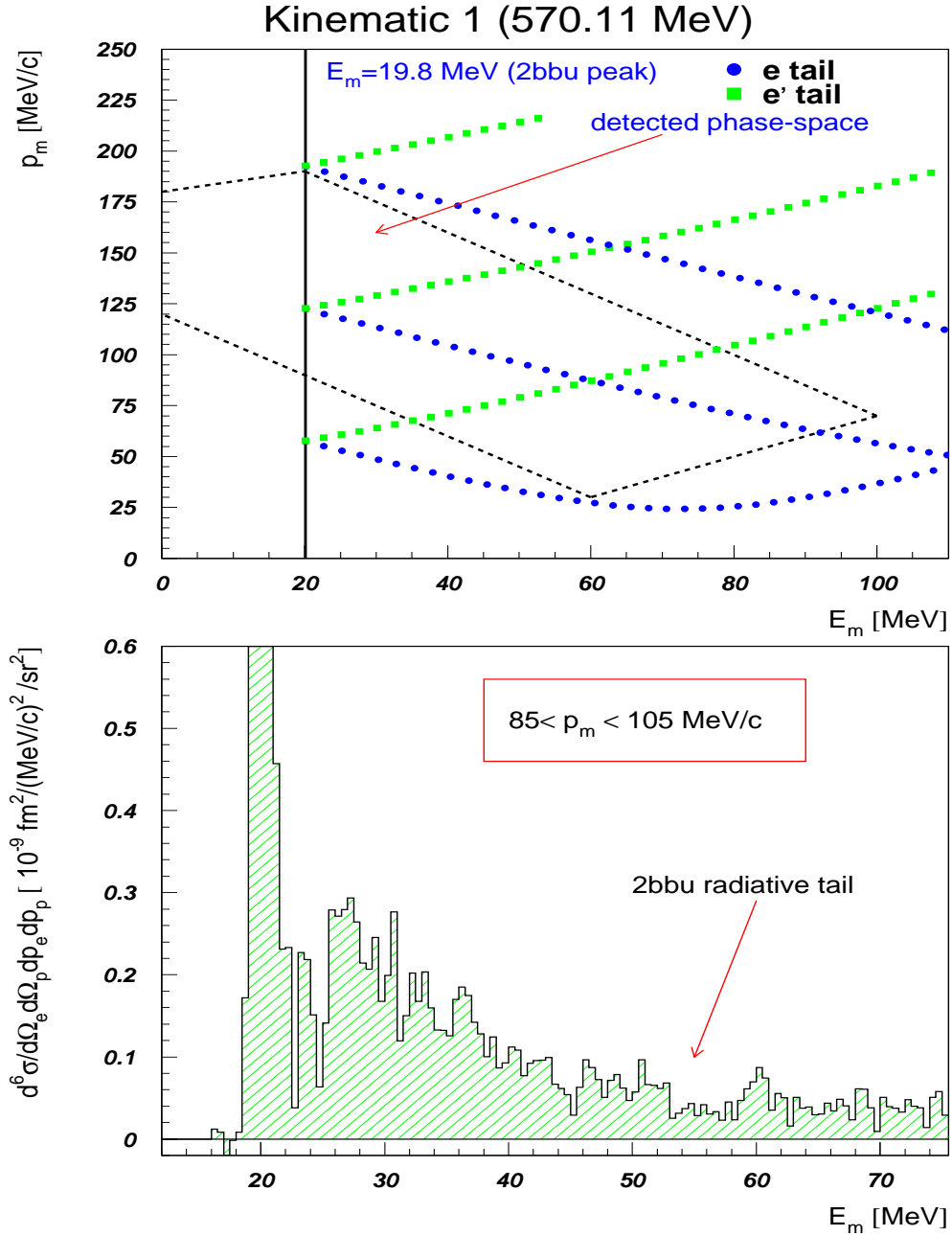


Figure 5.24: Radiative tails from the incident and scattered electrons (top). Continuum cross section corrected for radiation using RADCOR (bottom); significant radiative contribution (from the two-body-breakup peak at a lower p_m) is expected in the missing-energy region shown as the “2bbu radiative tail” (bottom)

The second major problem is due to the limited size of the 2-D cross section histogram, a large part of the (E_m, p_m) phase-space cannot be unfolded correctly. This happens because the radiative tails come from *outside* the detected (E_m, p_m) space. This effect is shown in Figures 5.22, 5.23 and 5.24. In these pictures the two-body-breakup radiative tail from the incident and scattered electrons are shown separately. Thus, previously unfolded histograms always contain some contribution from the (E_m, p_m) regions, which are outside of the spectrometer acceptance. This fact could cause a serious problem, and mistakes in interpretation of the results of the unfolding procedure. An uncertainty in the two-body breakup cross section due to the unfolding procedure should be in the range of a few per cent, but interpretation of the data corresponding to the three and four-body breakup channels is much more complicated.

In addition to the problem caused by the external radiative tails, two other factors are important for the three and four-body breakup channels. First, the value of the radiative correction is comparable to or larger than the cross-section value. Second, the uncertainty in the radiative tail trajectories increases in the high-missing-energy region.

For each kinematic, the behaviour of the radiative tail from the dominant two-body-breakup channel was studied, and the range of (E_m, p_m) phase-space, where the continuum-breakup reaction channels are free from the external radiative tails, was determined. Outside this phase-space region, a non-zero cross section in the missing-energy range 50–100 MeV is observed, which consists mostly of the external radiation tail contribution (Figure 5.22, 5.23 and 5.24).

Due to the large difference in the (E_m, p_m) phase-space region measured in each of the $(e, e'p)$ kinematics, the safe regions where cross sections for the three and four-body breakup channels can be extracted, are not the same. For Kinematic 1, only a tiny fraction of the measured (E_m, p_m) phase space can be used.

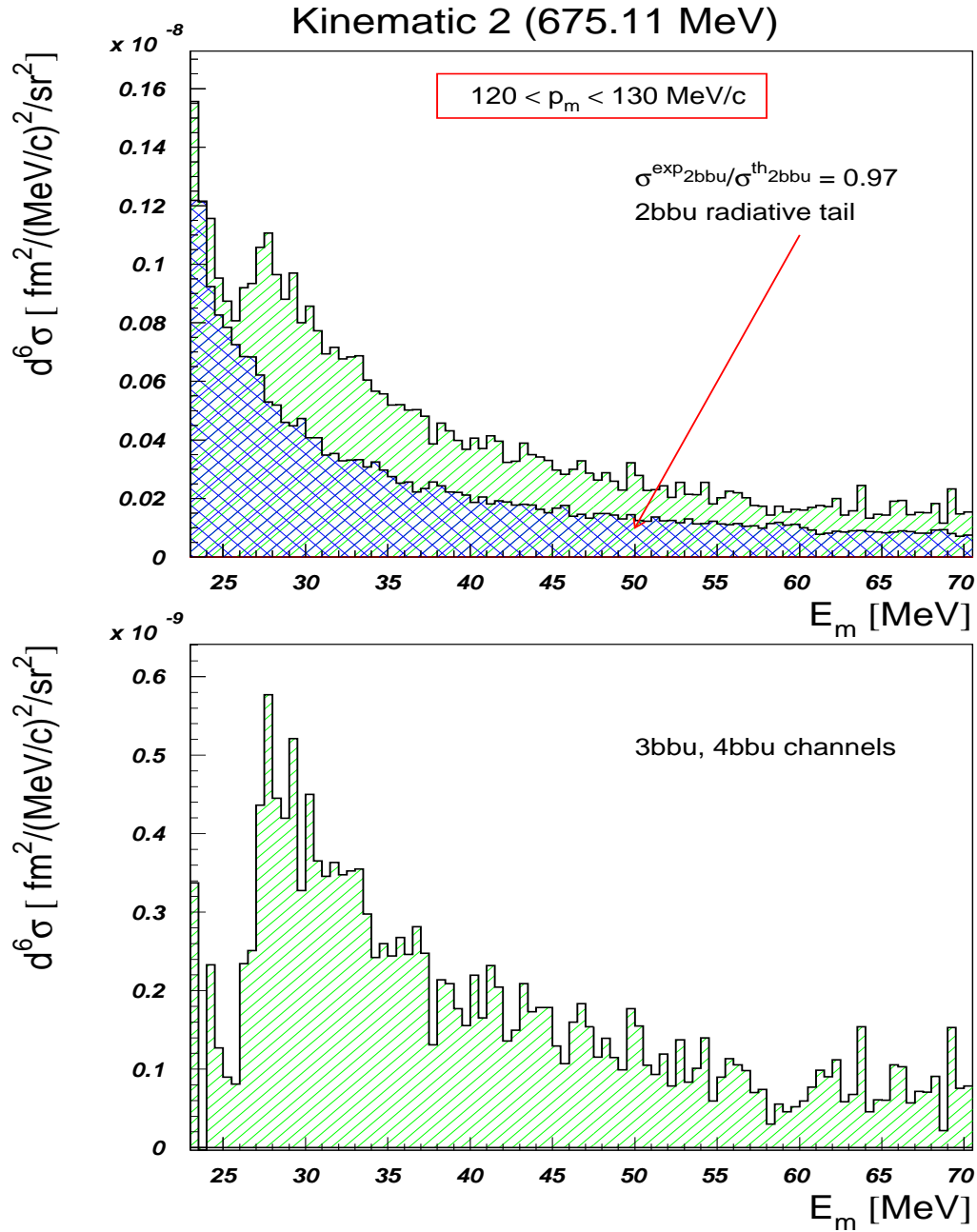


Figure 5.25: AEEXB simulation of the two-body breakup radiative tail (received from Templon [31]) positioned on top of the radiatively uncorrected six-fold cross section (top); this six-fold cross section after subtraction of the two-body breakup radiative tail (AEEXB)

5.8 Monte-Carlo simulations of the radiative tail

Instead of doing the radiative unfolding of the experimental data, one can also use a Monte-Carlo technique to simulate radiative effects using a theoretical model for the spectral function. This method has some advantages, and is more reliable at high missing energies, when the standard unfolding procedure gives results with large uncertainty. The AEEXB code [42] was modified to include both external and internal bremsstrahlung computations. The cross section was computed from the spectral function and the off-shell $e - p$ cross section in the *cc1* prescription. All details about the simulation code, and cross section model are given in reference [41] and [43].

As was already shown, the most serious problem during the unfolding with RADCOR was that the (E_m, p_m) data contains a radiative contribution from outside the spectrometer acceptance. This effect becomes more important at higher missing energies, and close to the boundaries of the measured (E_m, p_m) phase-space. The Monte-Carlo theoretical model covers a much larger region of phase-space, and the full kinematic information is available for each generated event, so that behaviour of the radiative tails can be accurately calculated. In order to adjust the measured strength for the two-body breakup to the theory prediction, the latest was multiplied by factor 0.75.

Several problems still have to be solved for this type of computations. Calculations based on the theoretical model, which deviates from the experimental results from one missing-momentum value to other (one can see this in Fig.6.13). As a pure technical problem was that external bremsstrahlung from the heavy-metal components (details are in Table 3.2) of the cell material was not taken into account. At the moment the AEEXB program cannot be used to extract the actual cross-section values. Nevertheless, the Monte-Carlo technique was used to provide an additional and important test of the RADCOR unfolding procedure at missing energies higher than 40-45 MeV.

In Figure 5.25 the radiative tails from the two-body breakup (calculated using AEEXB) are shown in comparison with the radiatively uncorrected six-fold differential cross section (top picture). The continuum cross section after subtraction of the two-body breakup radiative contribution calculated using AEEXB (shown in the top histogram) is given in the bottom histogram. One can see that the $(e,e'p)$ cross section is not zero in the whole missing-energy range, since radiative corrections still have to be applied to the continuum channels in this case. This non-zero strength (at high missing energies) belongs to the three and four-body radiative tails. The full AEEXB simulation results that support this statement are shown in Figure 6.1.

In the next chapter the simulated six-fold differential cross section will be compared with the measured data. This will provide an independent test of the RADCOR unfolding procedure in the high missing-energy region.

Chapter 6

Results

Overview

This chapter describes the experimental results obtained for the two-body breakup and continuum channels of the ${}^4\text{He}(e, e'p)$ reaction. First, the measured 6-fold differential cross sections for the three kinematics corresponding to the three different values of the virtual-photon polarization ϵ are presented in Section 6.1. The nature of the $(e, e'p)$ cross section for the continuum channels in the high missing-energy region is discussed here. Both results corrected for radiation with RADCOR, and those obtained from the AEEXB simulations are compared.

Section 6.2 is devoted to the two-body breakup channel. Here the results for the 5-fold differential cross section, and proton-triton momentum distributions are shown in figures and tables both with the ω -cut (see Chapter 5) used to match the detected energy-transfer region for all kinematics, and without it. The proton-momentum distributions were compared with the earlier experimental results, and three different theoretical models. The model-independent ratio for the longitudinal (σ_L) and transverse (σ_T) response functions was obtained via the Rosenbluth separation, and compared to that from the σ_{cc1} off-shell $e - p$ cross-section model of de Forest [14].

The spectral functions and proton-momentum distributions corresponding to

the continuum channels of the ${}^4\text{He}(e, e'p)$ reaction are presented in Section 6.3. The experimental results are also compared to the theoretical calculations from ref.[55]. A model-independent study for the σ_L/σ_T ratio as a function of the missing energy was performed using the Rosenbluth separation technique. The resulting ratio for the longitudinal and transverse response functions was also compared to the prediction of the σ_{cc1} off-shell $e - p$ cross-section model of de Forest.

The errors given in the tables and plots contain the statistical errors of experimental data, statistical uncertainties of the Monte-Carlo detection-volume calculations, and the RADCOR error resulting from the radiative unfolding procedure. The systematic-error estimate for the measured cross sections ($\pm 2.2 - 2.4$ %) was not included here, and is described in Section 6.4.

6.1 Six-fold differential cross section

6.1.1 AEEEXB simulations

Simulated cross section

The theoretical proton-triton momentum distribution was used to model the two-body breakup cross section. This momentum distribution was calculated employing the variational Monte-Carlo (VMC) for Argonne v18 N-N potential ref. [50] and Urbana IX ref. [51] the three-nucleon interaction (TNI) as described in [48]. The theoretical spectral function for the continuum was obtained from ref. [54]. This ${}^4\text{He}$ spectral function was calculated with the Lorentz integral transform method (see reference [55]).

The processes of internal and external bremsstrahlung were included into the Monte-Carlo simulation. The theoretical cross section was reduced by approximately 25 % in order to match with the measured two-body strength at the missing momentum value $p_m = 115 \pm 5 \text{ MeV}/c$.

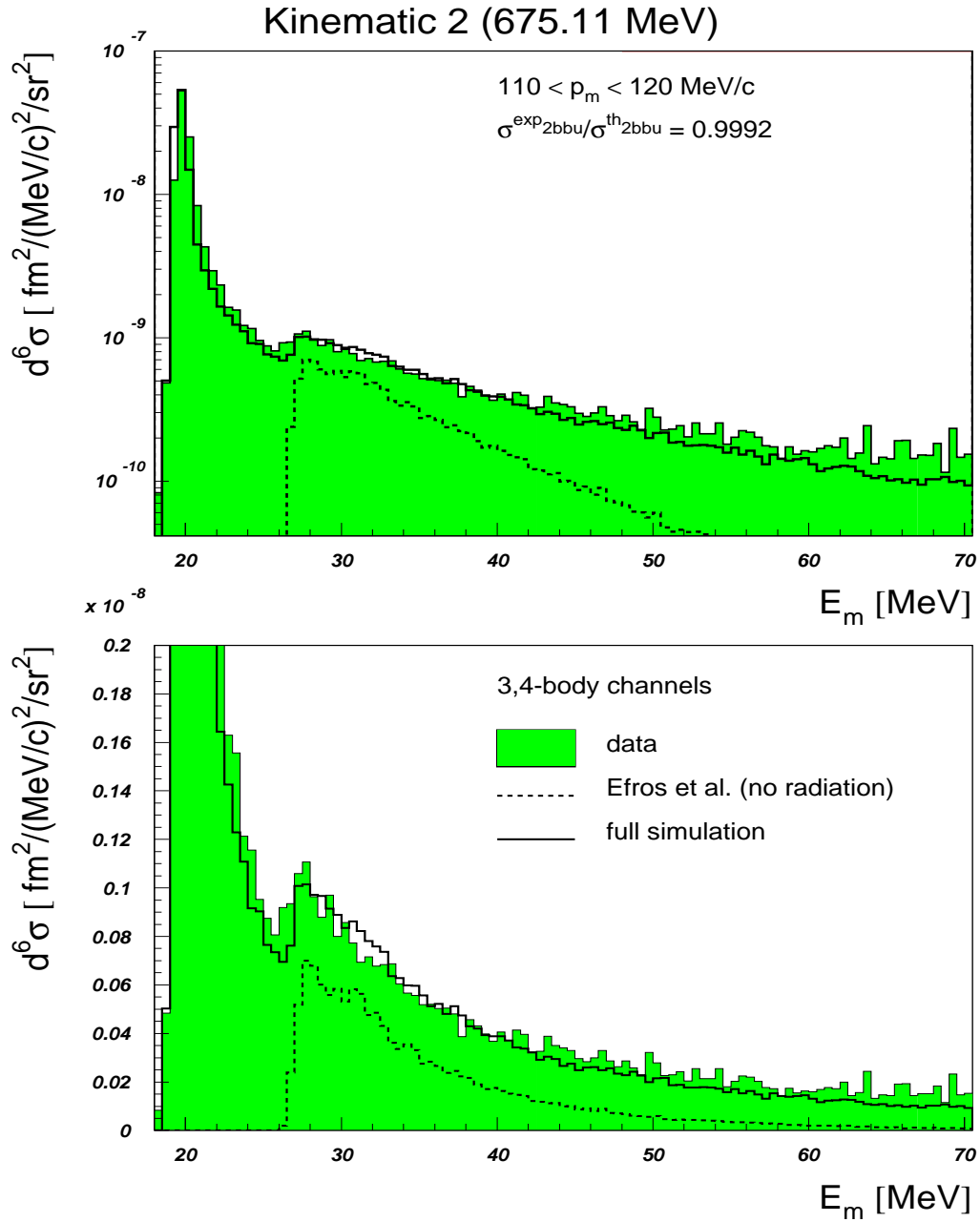


Figure 6.1: AEXB simulation of the 6-fold differential cross section (received from Templon [31]). The solid line shows the simulation result for all channels of the ${}^4\text{He}(e, e'p)$ reaction. The dashed line is the theoretical cross section for the continuum without radiation, calculated from the theoretical spectral function [55]

Results

The simulated cross section was compared to the radiatively uncorrected measured cross section in Figure 6.1. In general, agreement between the experimental results and simulation is good over the entire missing-energy range. Insignificant deviation of the simulation from the data near the three-body threshold comes from the resolution effects. The simulation is also slightly lower than the measured data for the missing energies larger than 50 MeV. This might disappear after the including the effect of external bremsstrahlung from the heavy-metal components of the target-cell material. This was not yet incorporated into the code as mentioned in Chapter 5. But even now, one can conclude that no significant deviation from the theoretical model can be observed up to the $E_m = 70 \text{ MeV}$.

6.1.2 RADCOR unfolding

Radiatively-corrected missing-energy spectra

The missing-energy spectra after the radiative unfolding with RADCOR are shown in Figures 6.2 and 6.3. For comparison, the raw (not corrected for radiation) missing-energy spectra are also shown there. For all three kinematics the radiative corrections allowed a clear separation of the two-body-breakup channel from the continuum to be made. Almost all radiative contribution from the two-body breakup in the missing-energy region between those reaction channels was removed. The three-body-breakup channel, which starts at $E_m \sim 26.07 \text{ MeV}$ is clearly visible. The four-body-breakup channel starts at $E_m \sim 28.3 \text{ MeV}$ and cannot be separated from the three-body breakup channel. From the missing-energy plots one can see that the effect of radiative corrections is very large in the continuum region: this causes also a large systematic uncertainty in the continuum cross section.

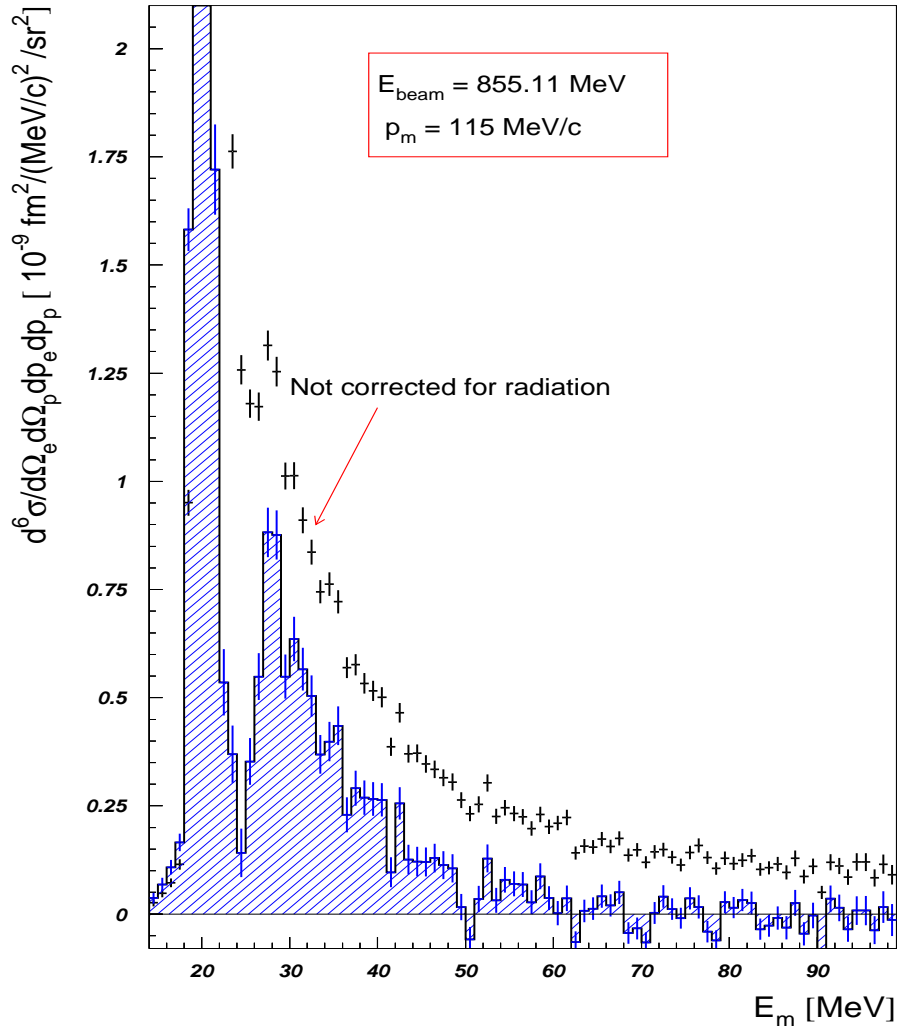


Figure 6.2: Six-fold differential cross section radiatively corrected with RADCOR

Cross-section behaviour at high missing energies

As mentioned in Chapter 5, the (E_m, p_m) spectra radiatively unfolded with RADCOR may still contain some contribution from the external radiative tails. As the missing energy increases, and the absolute cross section value decreases, this radiative contribution may play an increasingly important role. In order to understand to what extent the measured strength at high missing energies consists of

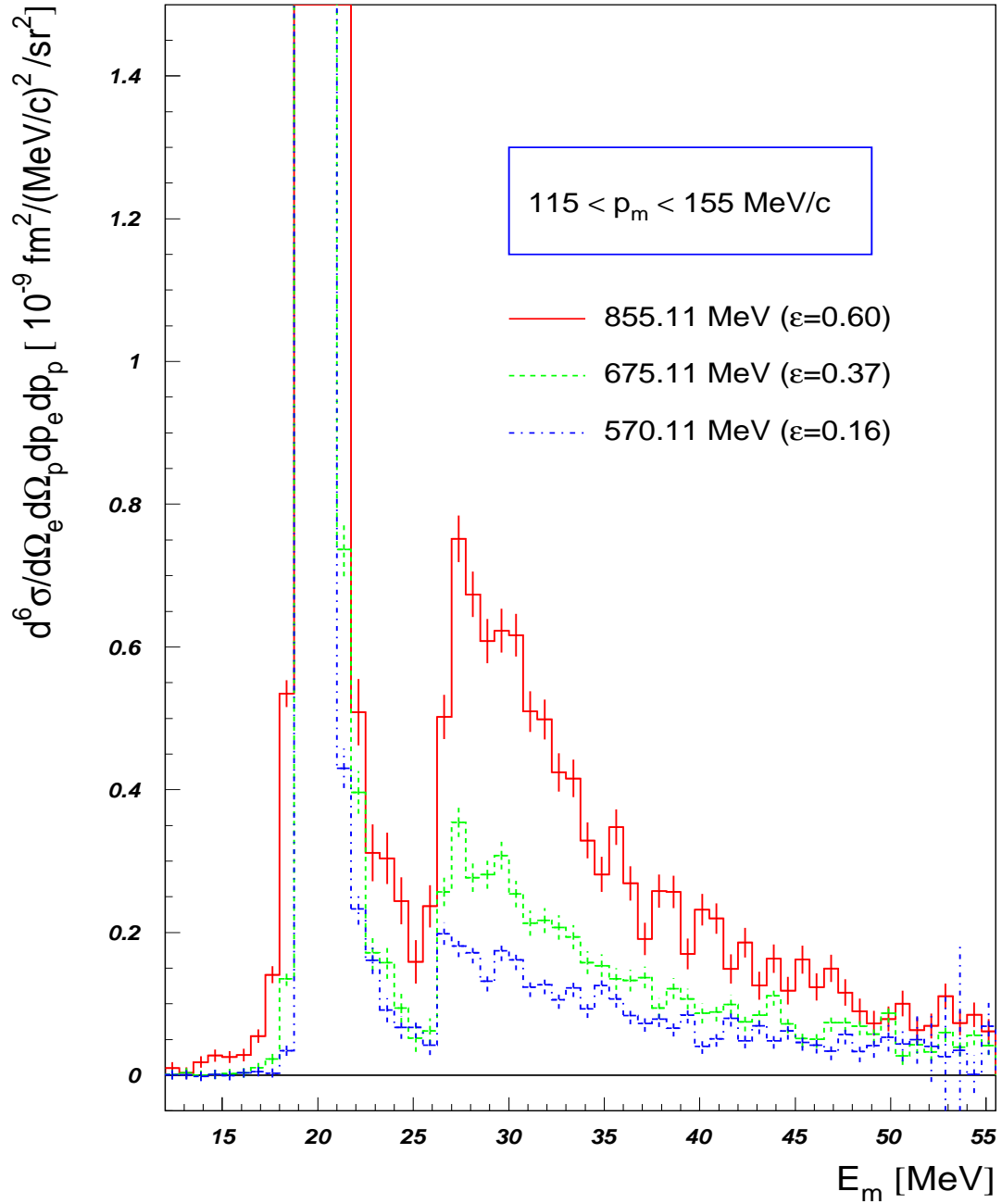


Figure 6.3: Six-fold differential cross section radiatively corrected with RADCOR

this background contribution, the central part of the missing-momentum acceptance was selected, and is shown in Figure 6.2. It is clear from this plot, that already at $E_m \sim 50 \text{ MeV}$ the cross section value is small and consistent with zero in the range of $E_m = 55 - 100 \text{ MeV}$. At these missing energies the radiative corrections become equal to or even larger than the radiatively corrected (e,e'p) cross section. Two other kinematics cannot be used to study the nature of the (e,e'p) strength at such high missing energies due to the much smaller size of the detected phase-space. This fact makes them vulnerable to the external radiative contribution as was mentioned in Chapter 5 (see Figures 5.23 and 5.24). The cross-section behaviour for all three kinematics is shown in Figure 6.3. The cross-section value for each kinematic is generally equal or less than approximately $0.5 \cdot 10^{-10} \text{ fm}^2/(\text{MeV}/c)^2/\text{sr}^2$ for the missing energies from the 45-50 MeV and higher. All this is an indication that in the high-missing-energy region the measured cross section consists almost entirely of the background resulting from the radiative tails.

Summary

The two-body-breakup channel was clearly separated from the continuum-reaction channels, as a result of the radiative unfolding procedure applied to the raw (E_m, p_m) spectra. This provided an opportunity to carry out a separate study for those reaction channels. The six-fold differential radiatively-corrected cross sections were obtained for all three kinematics in the missing-energy range between 25 and 45-50 MeV. For $E_m \geq 50 \text{ MeV}$ only qualitative result can be delivered. In this missing-energy region the (e,e'p) cross section was found to be consistent with the theoretical cross section for the continuum calculated from the theoretical spectral function [55], as shown in Figure 6.21. It was not possible to study the L/T behaviour of the (e,e'p) cross section for $E_m \geq 50 \text{ MeV}$, since the cross section for this missing-energy region can be determined only for one beam-energy value.

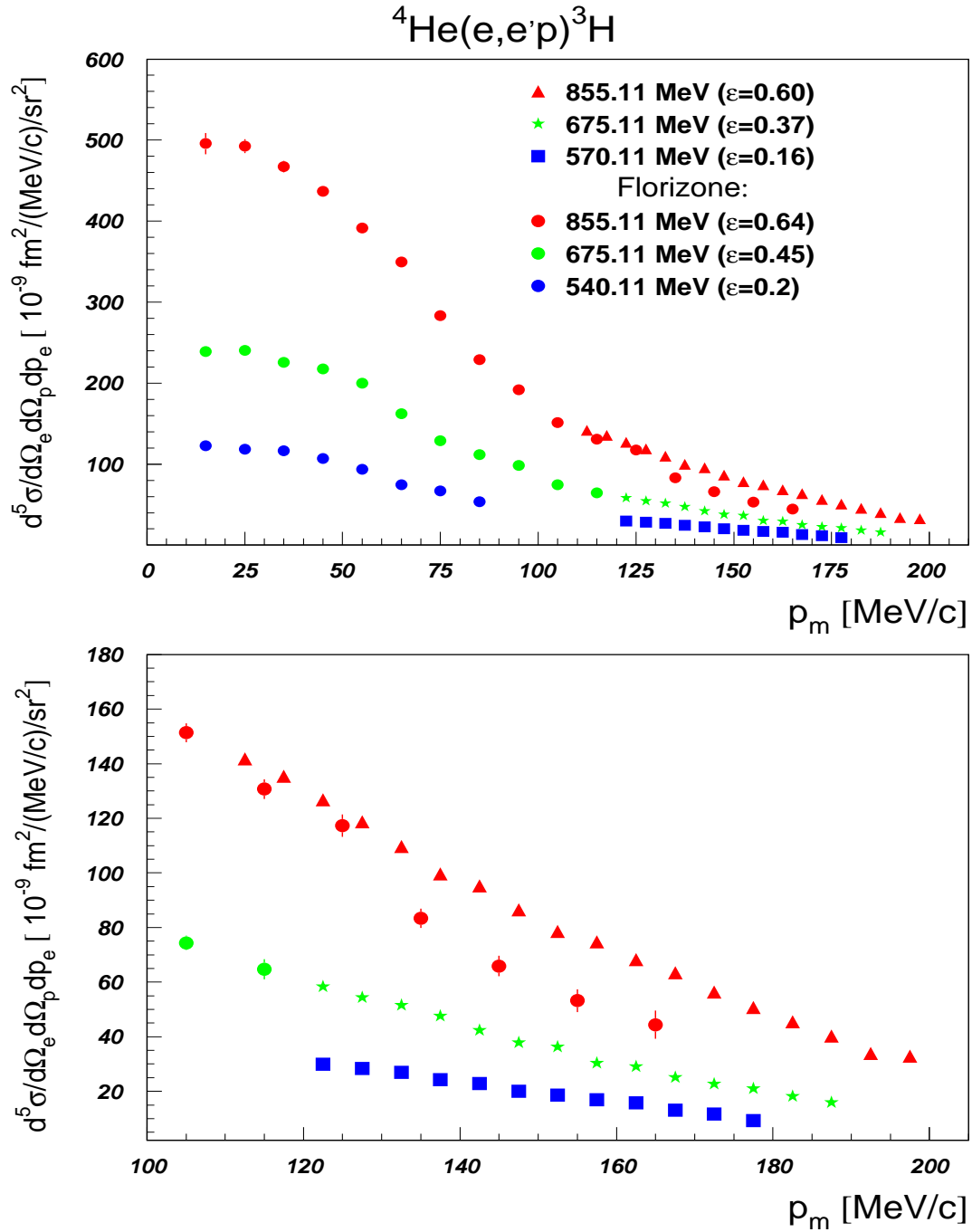


Figure 6.4: ${}^4\text{He}(e,e'p){}^3\text{H}$ cross section (without the ω -cut)

6.2 Two-body-breakup channel

All results for the two-body breakup channels were obtained by integrating the measured strength in the missing-energy region $17 \leq E_m \leq 25 \text{ MeV}$, as was described in Chapter 5. The five-fold differential cross sections and the proton-triton momentum distributions are presented here for the case when the ω -cut (see Chapter 5 for details) was used and without it. The five-fold differential cross sections were separated into the longitudinal ($K \cdot \sigma_L$) and transverse ($K \cdot \sigma_T$) components using the Rosenbluth formula. These cross section components were used to calculate the model-independent ratio for the σ_L and σ_T response functions (defined in Chapter 2). This ratio was compared to the prediction from the σ_{cc1} model, which was calculated by averaging the response functions from σ_{cc1} over the experimental acceptance using the Monte-Carlo technique.

6.2.1 Five-fold differential cross section

The 5-fold differential cross section for the ${}^4\text{He}(e, e'p){}^3\text{H}$ reaction channel was extracted according to the procedure explained in Section 5.5. The resulting values are given in Figure 6.4. The error bars are too small to be visible in the plot. In this figure the cross sections for the three kinematics are shown, together with the results obtained for the top of the QE peak by Florizone [23] for similar kinematical conditions. The shape of the cross section is similar for all three kinematics, although the magnitude varies significantly as a function of incident electron energy.

The resulting cross sections are given as a function of the missing momentum in Table 6.1 with the ω -cut, (used to match the acceptance for all kinematics) and without it. The errors given in this table include the statistical errors for the experimental yield, the statistical errors for the detector volume calculated with the Monte-Carlo method, and the uncertainty due to the unfolding procedure with RADCOR.

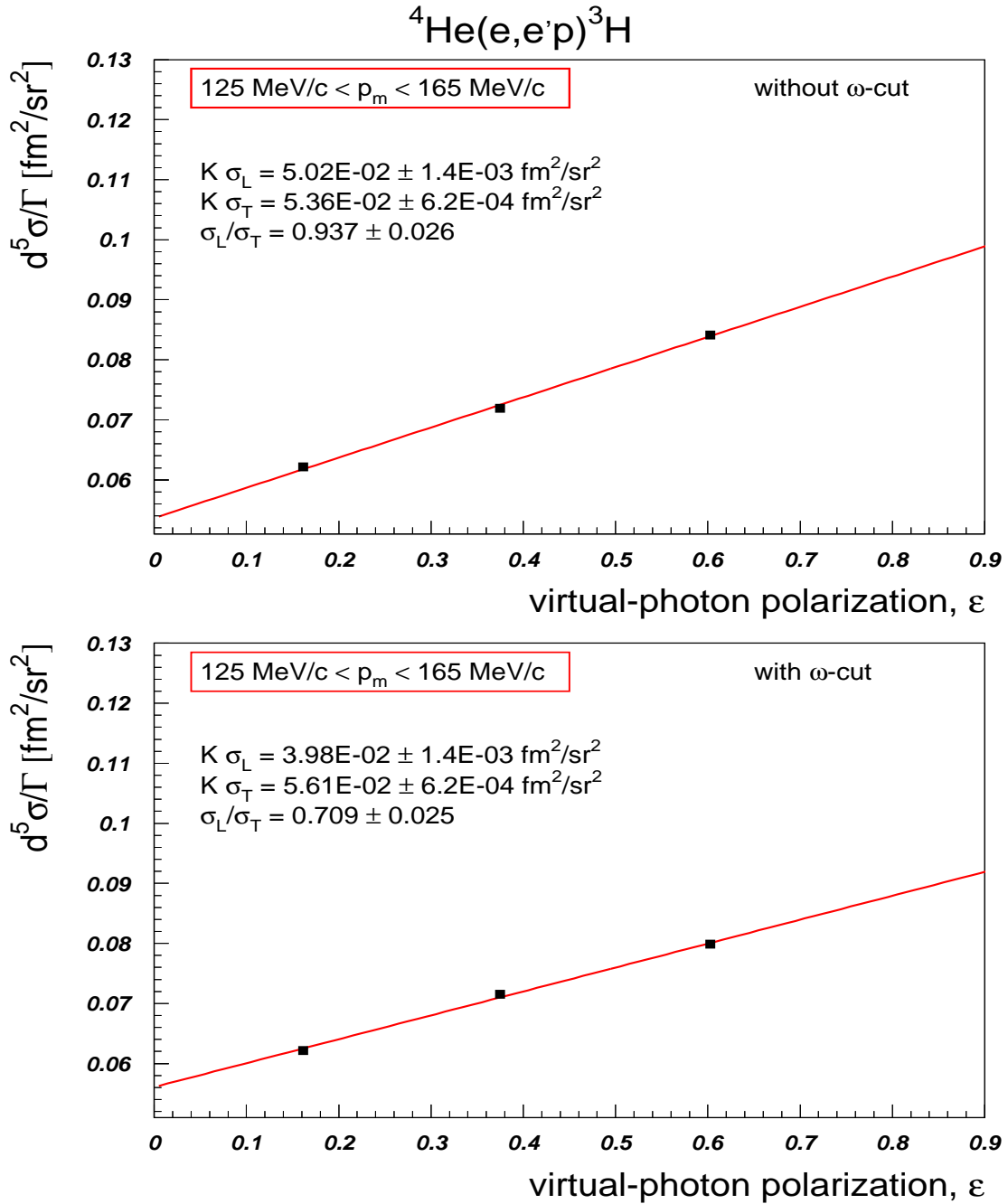


Figure 6.5: Rosenbluth plot for the case of the two-body breakup reaction channel

p_m $\frac{MeV}{c}$	5-fold cross section [$10^{-9} fm^2/(MeV/c)/sr^2$]				
	855.11 MeV	855.11 MeV*	675.11 MeV	675.11 MeV*	570.11 MeV
117.5	135.45 ± 1.25	117.43 ± 1.57	-	-	-
122.5	126.77 ± 1.21	113.01 ± 1.46	58.28 ± 0.78	55.32 ± 0.81	29.86 ± 0.56
127.5	118.74 ± 1.18	106.55 ± 1.33	54.44 ± 0.76	52.81 ± 0.76	28.3 ± 0.55
132.5	109.69 ± 1.15	100.21 ± 1.24	51.63 ± 0.74	51.16 ± 0.74	27.01 ± 0.53
137.5	99.69 ± 1.13	92.61 ± 1.16	47.54 ± 0.72	47.49 ± 0.72	24.34 ± 0.51
142.5	95.30 ± 1.14	89.94 ± 1.14	42.34 ± 0.68	42.36 ± 0.68	22.80 ± 0.49
147.5	86.51 ± 1.13	83.90 ± 1.12	37.78 ± 0.64	37.80 ± 0.64	20.03 ± 0.47
152.5	78.57 ± 1.13	77.94 ± 1.13	36.25 ± 0.64	36.28 ± 0.64	18.57 ± 0.45
157.5	74.80 ± 1.16	74.79 ± 1.16	30.40 ± 0.61	30.44 ± 0.61	16.96 ± 0.43
162.5	68.22 ± 1.18	68.36 ± 1.18	29.10 ± 0.63	29.16 ± 0.63	15.73 ± 0.41
167.5	63.46 ± 1.21	63.63 ± 1.21	25.06 ± 0.63	25.15 ± 0.64	13.03 ± 0.38
172.5	56.35 ± 1.24	56.54 ± 1.24	22.79 ± 0.67	22.91 ± 0.68	11.62 ± 0.38
177.5	50.74 ± 1.28	51.03 ± 1.29	21.01 ± 0.74	21.21 ± 0.75	9.23 ± 0.39
182.5	45.43 ± 1.35	45.81 ± 1.36	18.23 ± 0.83	18.49 ± 0.85	-
187.5	40.30 ± 1.46	40.92 ± 1.48	15.91 ± 1.05	16.31 ± 1.09	-
192.5	33.89 ± 1.63	34.95 ± 1.70	-	-	-
197.5	32.86 ± 2.18	36.01 ± 2.48	-	-	-

Table 6.1: ${}^4He(e, e'p){}^3H$ cross section (* indicates the cross section calculated with the ω -cut)

6.2.2 Rosenbluth L/T separation

Analysis

In order to obtain a model-independent result for the behaviour of the longitudinal and transverse responses, the Rosenbluth separation technique was used. The 5-fold differential cross section was averaged over the missing-momentum range

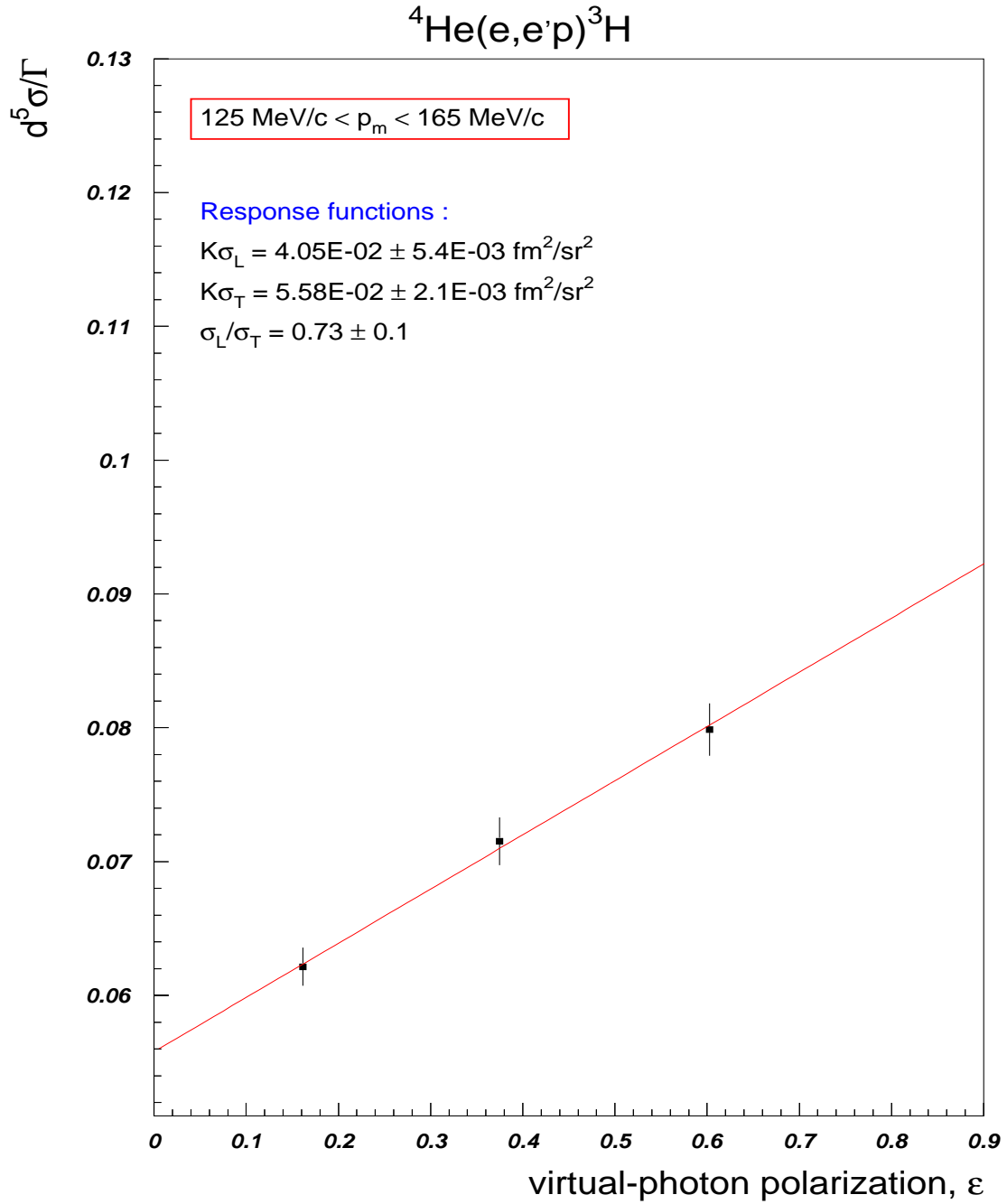


Figure 6.6: Rosenbluth plot for the case of the two-body breakup reaction channel (the systematic error is included)

between the 125 and 165 MeV/c in order to reduce systematic and statistical errors for the measured cross section, so as to produce a Rosenbluth plot of good quality. This missing-momentum range corresponds to the central region of the measured (E_m, p_m) phase-space, and is far away from its boundaries. It is important since the detector volume is very sensitive to a precise knowledge of the spectrometers acceptance. Thus in the selected central part of the acceptance the systematic error due to the detector-volume calculation is reduced to a minimum.

Subsequently, the five-fold differential cross section, $d^5\sigma$, was divided by the virtual-photon flux Γ calculated for each kinematic according to Equation 2.14. The Rosenbluth separation, was thus performed on the $d^5\sigma/\Gamma$. This produced the response functions σ_L and σ_T multiplied by the kinematic factor K in units fm^2/sr^2 according to Equation 2.19.

Using these longitudinal and transverse components of the $d^5\sigma$ cross section one can obtain the ratio of the nuclear response functions σ_L/σ_T defined in Chapter 2 (Equations 2.15 and 2.16), or the ratio R_L/R_T (Equations 2.17 and 2.18). These values can then be compared with the theoretical predictions.

The theoretical value of σ_L/σ_T was estimated by averaging over the spectrometer acceptance using the GEANT Monte-Carlo code the corresponding nuclear responses σ_L and σ_T calculated from the *cc1* off-shell model of de Forest. This calculation of the σ_L/σ_T ratio was done for each generated event using the same software cuts as were applied to the experimental data. The ratio σ_L/σ_T is unit less, and was found to be approximately 1.06. By comparing the experimental result to this value one can conclude whether or not the L/T ratio is reduced compared to the theory.

Results

In Figure 6.5 the Rosenbluth plots are shown for the case when the ω -cut was not applied (top picture) and with the ω -cut (lower plot). The data points for the different virtual-photon polarization were fitted with a straight line using a least-

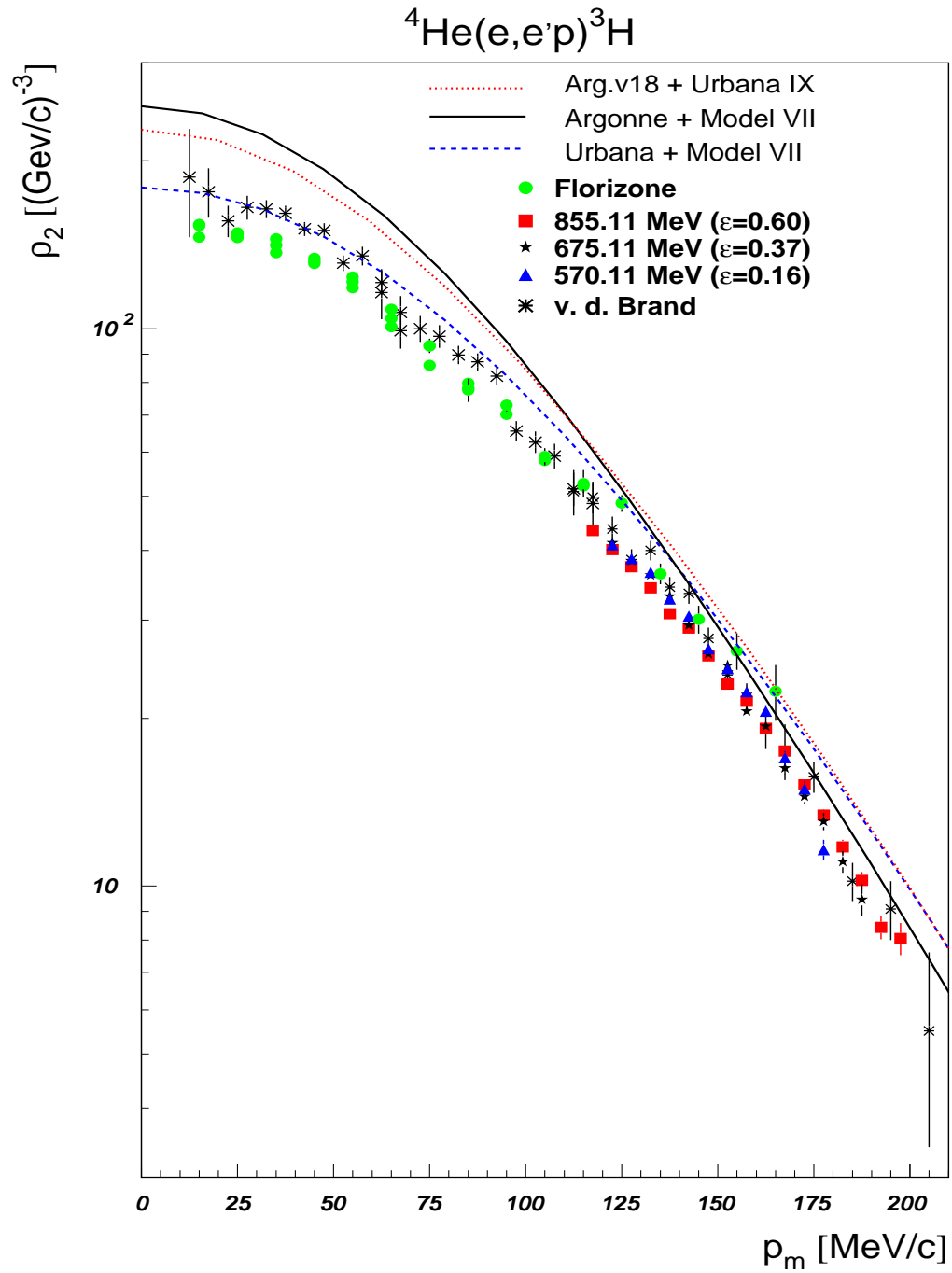


Figure 6.7: The proton-triton momentum distributions (without the ω -cut)

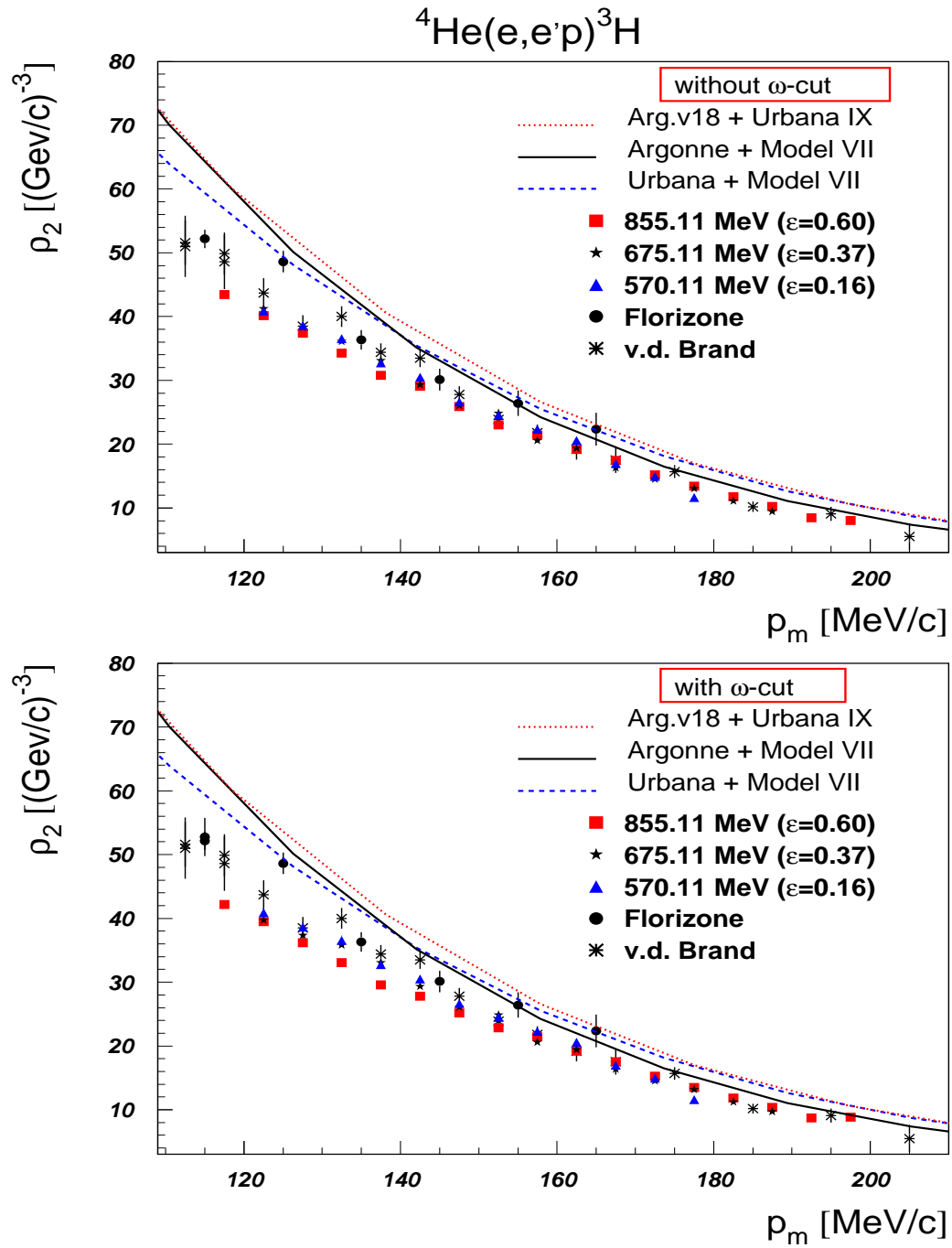


Figure 6.8: The proton-triton momentum distributions

square method. The error bars are too small to be visible at the plot.

It is clear from these plots that the resulting cross-section values for all three kinematics are consistent with each other and linear. The ω -cut was found to produce a significant effect on the σ_L/σ_T ratio. With the ω -cut the ratio σ_L/σ_T was 33 % lower than the value predicted by the σ_{cc1} model. When the ω -cut was not used, the reduction of the σ_L/σ_T ratio was only 12 %.

Since the ω -cut is supposed to reduce the systematic error for the Rosenbluth separation and ensure that the ω -range contributing to the measured cross section is the same for all kinematics, the result obtain with the ω -cut should be physically more correct. This means that the measured σ_L/σ_T ratio for our kinematical conditions is equal to 0.71 ± 0.025 , and the $(\sigma_L/\sigma_T)^{exp}/(\sigma_L/\sigma_T)^{cc1}$ is approximately 0.67 ± 0.024 .

When the full systematic error ($\pm 2.2 - 2.4$ %) in the cross-section value is taken into account the $(\sigma_L/\sigma_T)^{exp}/(\sigma_L/\sigma_T)^{cc1}$ is approximately 0.69 ± 0.09 as shown in Figure 6.6.

6.2.3 The proton-triton momentum distribution

The proton-momentum distributions were obtained by dividing of the measured cross section by the kinematical factor $p_p^2 \cdot \sigma_{cc1}$ as was explained in Chapter 5. Although these momentum distributions are model-dependent, they can be used to provide a detailed comparison between the experimental results obtained in this work and the data measured by other groups. They also allow comparison between theory and experiment.

The measured momentum distributions are shown in Figures 6.8 and 6.7 as a function of missing momentum. Also shown are the theoretical calculations of Schiavilla *et al.* [45] and Forest *et al.* [48], together with experimental results from Florizone [23] and van den Brand [52]. The resulting proton-momentum distribu-

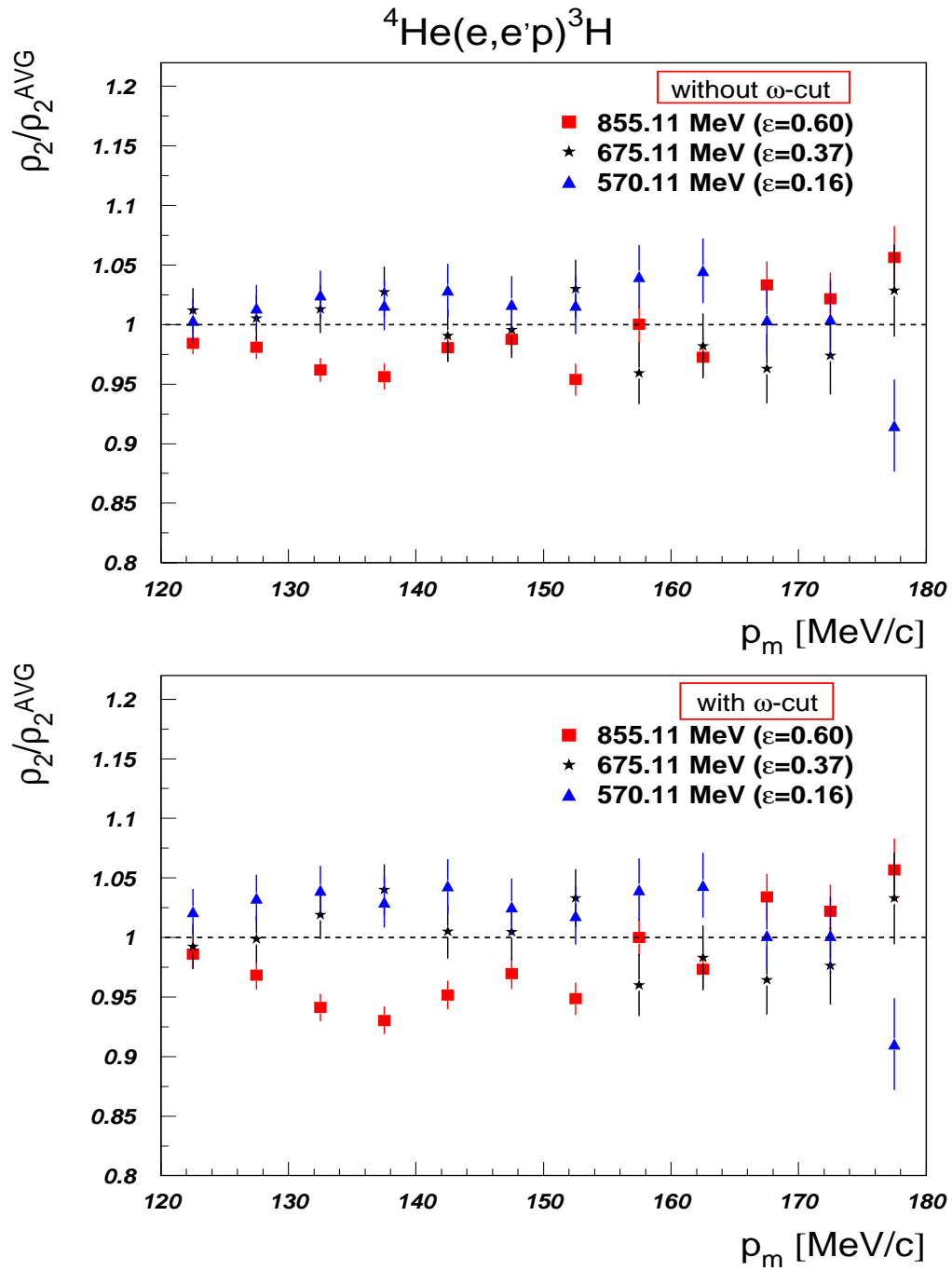


Figure 6.9: The proton-triton momentum distributions compared to the averaged over the three kinematics value

p_m $\frac{MeV}{c}$	$\rho_2(p_m) [(GeV/c)^{-3}]$				
	855.11 MeV	855.11 MeV*	675.11 MeV	675.11 MeV*	570.11 MeV
117.5	43.42 ± 0.39	42.17 ± 0.55	-	-	-
122.5	40.12 ± 0.38	39.47 ± 0.50	41.25 ± 0.55	39.74 ± 0.57	40.91 ± 0.76
127.5	37.37 ± 0.37	36.21 ± 0.45	38.31 ± 0.53	37.35 ± 0.53	38.63 ± 0.74
132.5	34.30 ± 0.36	33.08 ± 0.40	36.12 ± 0.51	35.82 ± 0.51	36.55 ± 0.72
137.5	30.82 ± 0.34	29.59 ± 0.37	33.11 ± 0.49	33.07 ± 0.49	32.74 ± 0.68
142.5	29.05 ± 0.34	27.80 ± 0.35	29.35 ± 0.47	29.36 ± 0.47	30.48 ± 0.66
147.5	25.87 ± 0.33	25.19 ± 0.33	26.08 ± 0.44	26.10 ± 0.44	26.65 ± 0.61
152.5	23.03 ± 0.33	22.86 ± 0.33	24.88 ± 0.44	24.90 ± 0.44	24.54 ± 0.59
157.5	21.46 ± 0.33	21.45 ± 0.33	20.57 ± 0.41	20.60 ± 0.41	22.32 ± 0.56
162.5	19.17 ± 0.33	19.21 ± 0.33	19.36 ± 0.42	19.40 ± 0.42	20.60 ± 0.54
167.5	17.48 ± 0.33	17.52 ± 0.33	16.29 ± 0.41	16.34 ± 0.41	16.98 ± 0.49
172.5	15.19 ± 0.33	15.24 ± 0.33	14.49 ± 0.43	14.56 ± 0.43	14.94 ± 0.48
177.5	13.40 ± 0.34	13.48 ± 0.34	13.05 ± 0.46	13.18 ± 0.46	13.05 ± 0.46
182.5	11.76 ± 0.35	11.86 ± 0.35	11.07 ± 0.50	11.23 ± 0.51	-
187.5	10.23 ± 0.37	10.38 ± 0.37	9.45 ± 0.62	9.69 ± 0.65	-
192.5	8.43 ± 0.41	8.69 ± 0.42	-	-	-
197.5	8.05 ± 0.53	8.81 ± 0.60	-	-	-

Table 6.2: The proton-triton momentum distributions (* indicates the momentum distributions calculated with the ω -cut)

tions are given in Table 6.2 with the ω -cut and without it.

Theoretical momentum distributions

The proton-triton momentum distributions used for comparison with the measured proton distributions for the two-body breakup channel were calculations of Schiavilla *et al.* [45] (variational Monte-Carlo) and also Forest *et al.* [48]. The cal-

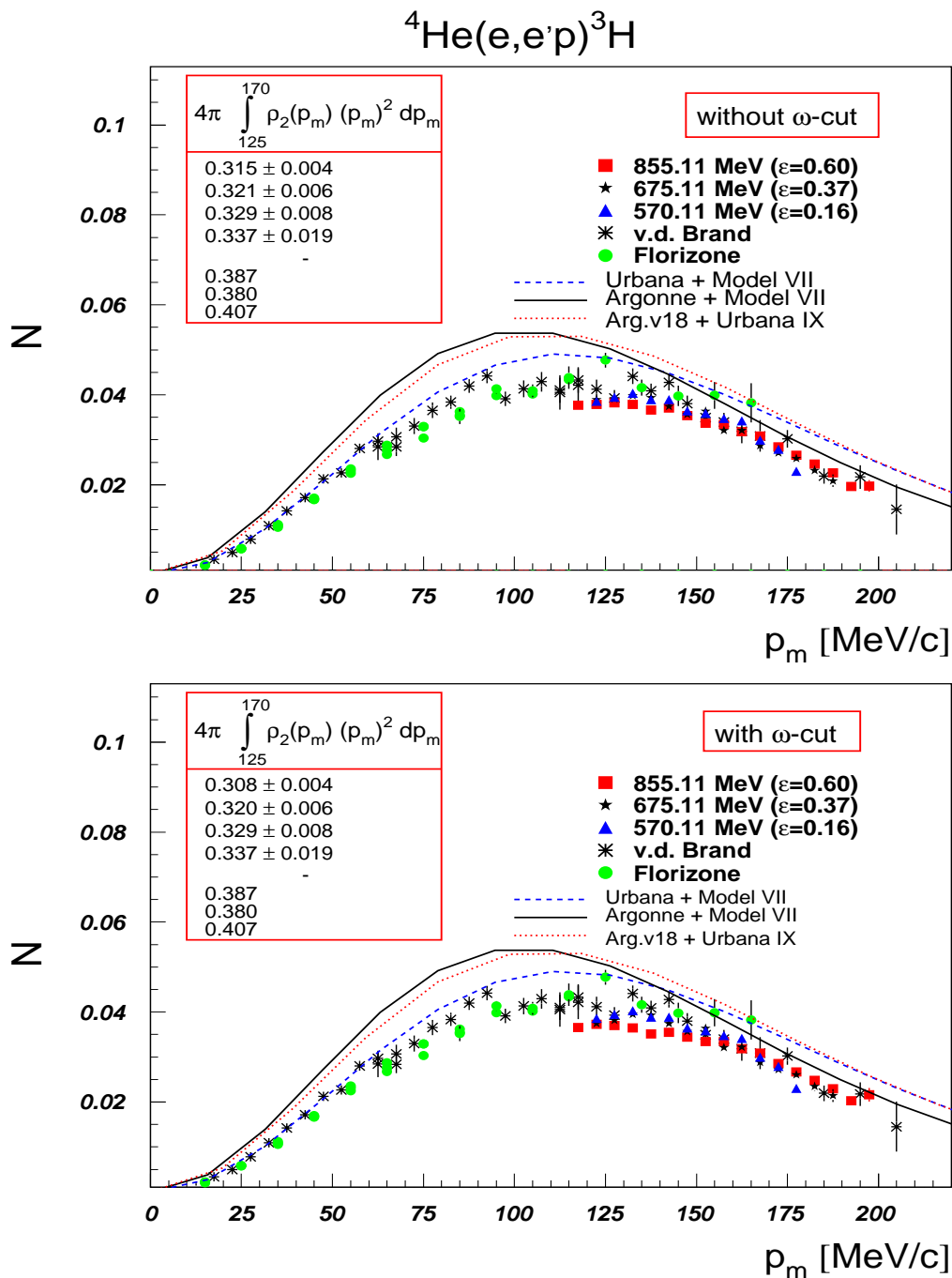


Figure 6.10: The $\langle N \rangle$ value (for each p_m bin) calculated for the proton-triton momentum distributions

culations in ref. [45] were performed using the Urbana [46] and Argonne [47] models for the N-N interactions, and the three-nucleon interaction model VII. The third theoretical $p-{}^3H$ momentum distribution was calculated employing the VMC for Argonne v18 N-N potential [50] and Urbana IX [51] TNI as described in ref. [48], and is available at ref. [49].

Experimental momentum distributions

Earlier, the proton-triton momentum distributions using similar kinematical conditions were measured by Florizone [23] at MAMI in order to study the L/T behaviour of the (e,e'p) cross section on 4He . These measurements were also performed for three different ϵ values (0.2, 0.45 and 0.64) with corresponding beam energy 540.11, 675.11 and 855.11 MeV. The 3-momentum transfer was the same as for our measurements (685 MeV/c), but the ω -value was 242.7 MeV, corresponding to the top of the QE peak, where the scaling factor $y = 0$. All momentum distributions in [23] were also extracted using the σ_{cc1} prescription for the off-shell $e-p$ cross section. The systematic uncertainty for these results is 5-6 %. The error bars shown in all figures are statistical only.

Another experimental result, which was compared with our measurements over the entire missing-momentum p_m region, were measured at NIKHEF by van den Brand *et al.* [52]. These data, referred to in ref. [52] as Kinematic I, were collected at a lower momentum transfer ($|\vec{q}| = 431 \text{ MeV}/c$), and the virtual-photon polarization was $\epsilon = 0.48$. The perpendicular kinematic, where $\vec{p}_m \perp \vec{q}$ was used. Again, the σ_{cc1} off-shell $e-p$ cross section was used to calculate the proton-triton momentum distribution. The error bars shown in Figures 6.8 and 6.8 for these results are also statistical. The total systematic error in ref. [52] was estimated to be $\sim 6 \%$.

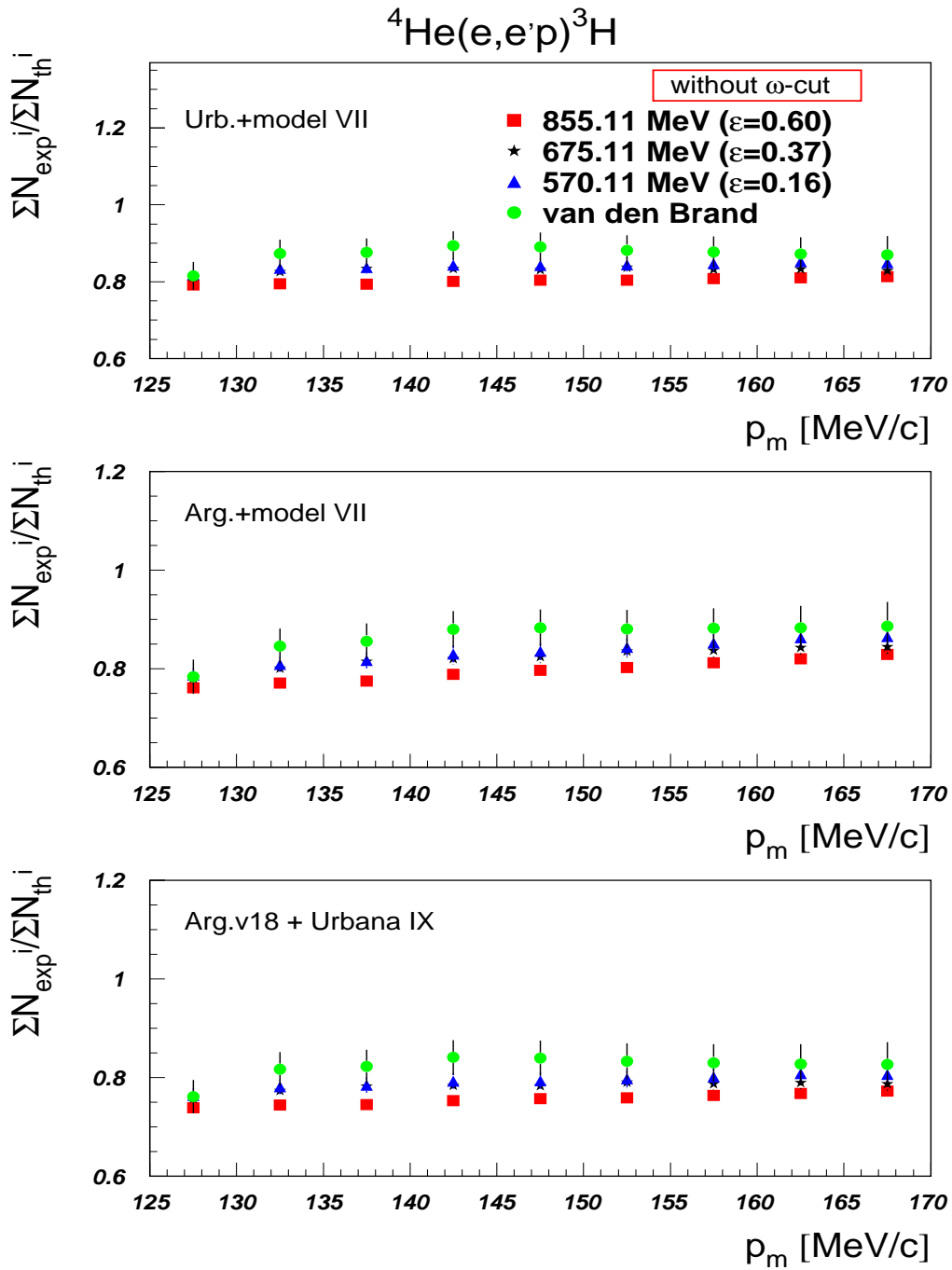


Figure 6.11: The ratio between the experimental data and several theoretical models for proton-triton momentum distributions (without the ω -cut)

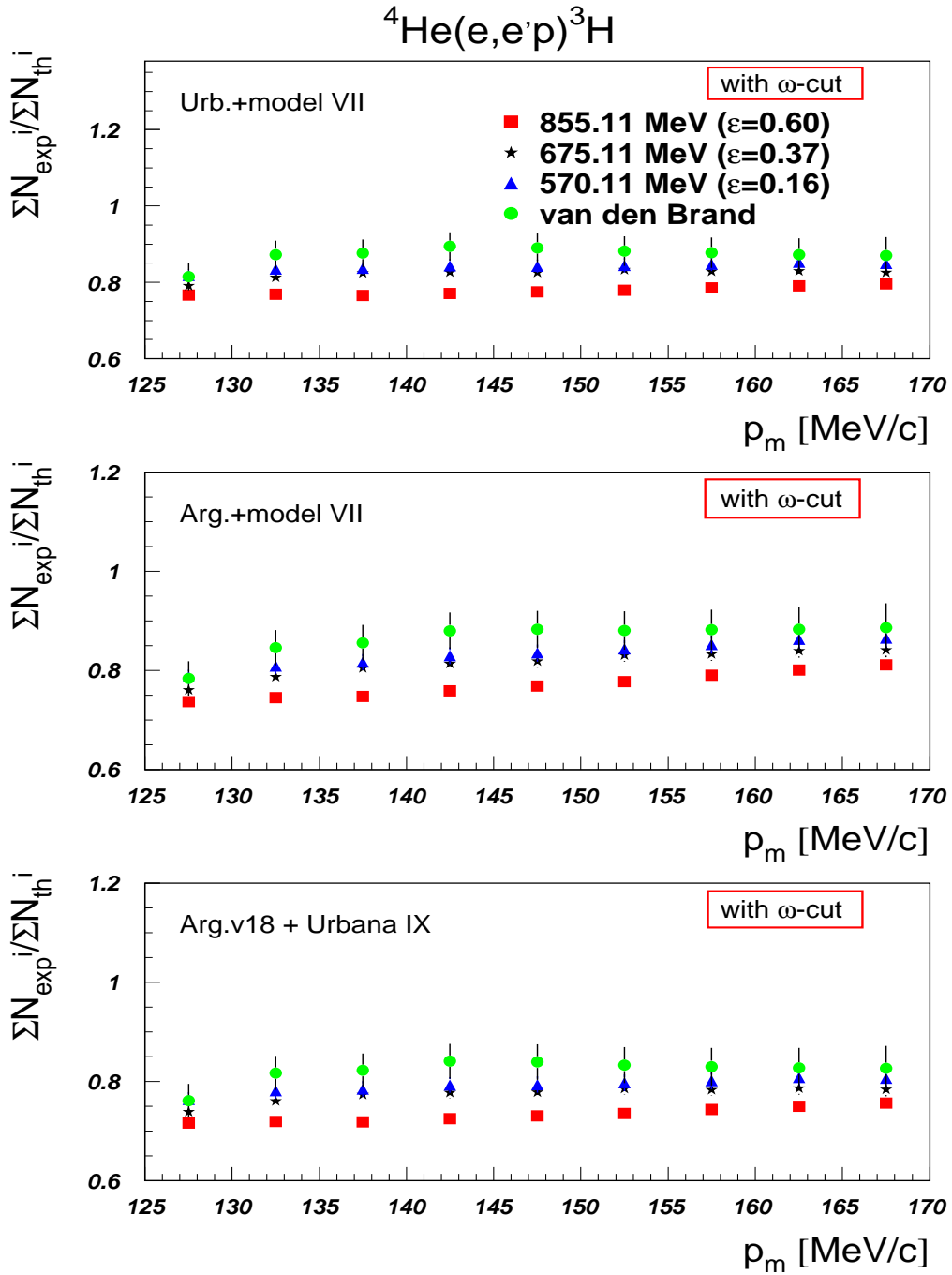


Figure 6.12: The ratio between the experiment and several theoretical models for proton-triton momentum distributions (with the ω -cut)

Analysis

The normalization requirement in the PWIA calculation is that the momentum distribution, $\rho(p_m)$, for a fully occupied orbital with total angular momentum j is normalized to its occupancy [53], such that

$$4\pi \int dp_m p_m^2 \rho_j(p_m) = 2j + 1 \quad (6.1)$$

for the independent-particle shell model. Thus, the following integral was calculated for comparison of the measured proton-triton momentum distribution

$$\langle N \rangle = 4\pi \int_{125}^{170} dp_m p_m^2 \rho_2(p_m) \quad (6.2)$$

This was done for the missing-momentum range p_m between the 125 and 170 MeV/c, which corresponds to the overlap region of the three kinematics for the two-body breakup channel. The averaged value $\langle N \rangle$ for the our three kinematics, the results of van den Brand, and several theoretical models are given in Figure 6.10.

The ϵ -dependence of the $\rho_2(p_m)$ was studied in three different ways.

First, the ρ_2/ρ_2^{AVG} ratio

$$\frac{\rho_2}{\rho_2^{AVG}} = \frac{\rho_2(p_m, \epsilon)}{\frac{1}{3} \sum_{\epsilon} \rho_2(p_m, \epsilon)} \quad (6.3)$$

for each p_m bin was calculated. This ratio shows how much the momentum distribution for each individual measurement deviates from the averaged ρ_2^{AVG} value for a particular p_m bin.

Second, the ratio

$$\frac{\langle N \rangle_{exp}^i}{\langle N \rangle_{th}^i} = \frac{\rho_2^{exp}(p_m^i)}{\rho_2^{th}(p_m^i)} \quad (6.4)$$

for each missing-momentum bin p_m^i was determined (see Figures 6.13 and 6.14). In order to calculate the ρ_2^{th} value for each missing-momentum bin, the theoretical

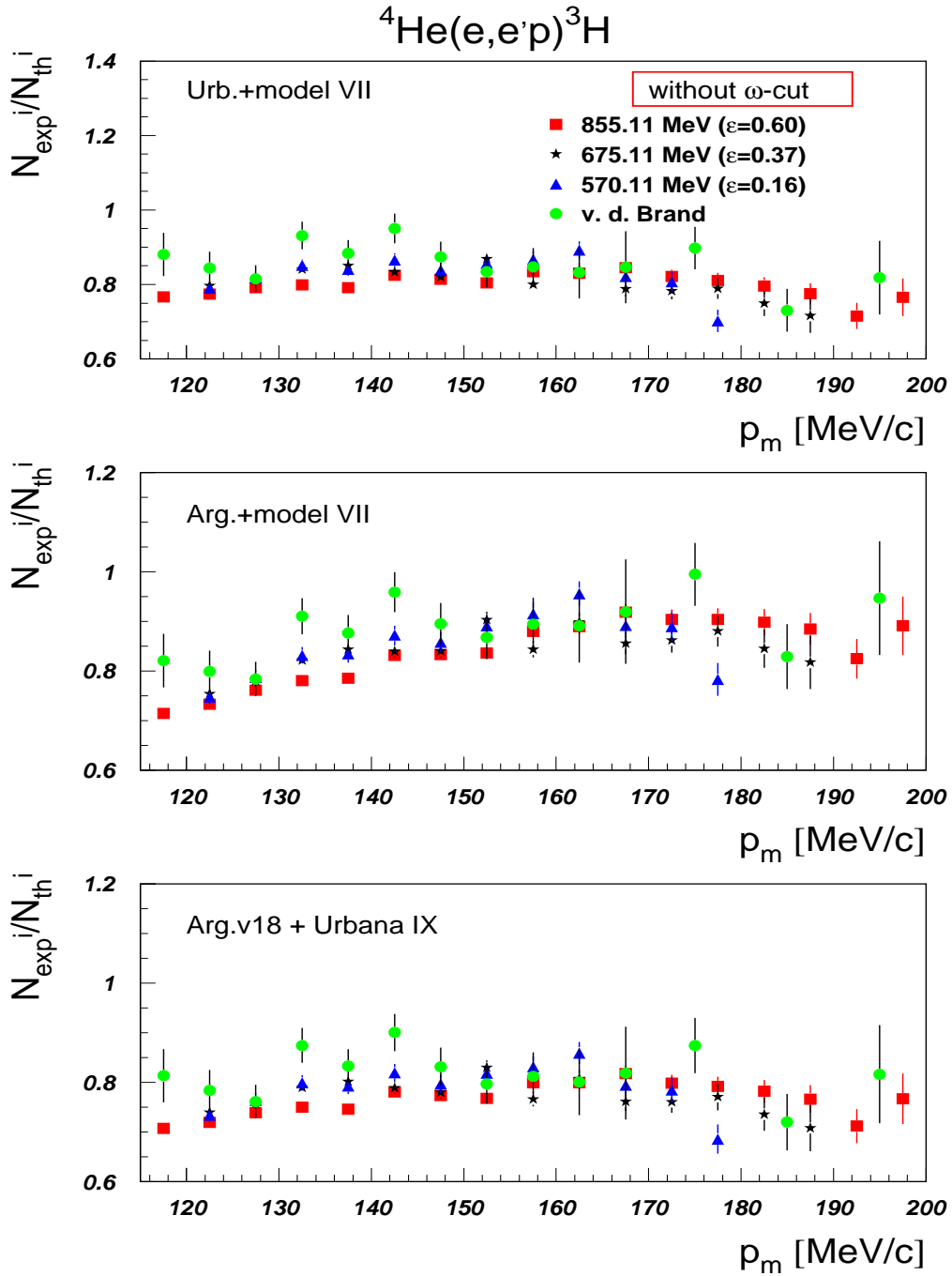


Figure 6.13: The ratio between the experiment and several theoretical models for the proton-triton momentum distributions (without the ω -cut)

data points were fitted with a high-order polynomial, so that the functional dependence $\rho_2^{th}(p_m)$ was extracted. After that the ρ_2^{th} was calculated for the missing-momentum value corresponding to the middle of each missing-momentum bin. This ratio gives us the deviation of the experimental $\rho_2^{exp}(p_m)$ momentum distribution from the theoretical predictions.

Third, the development of the sum's ratio

$$\frac{\sum_i \langle N \rangle_{exp}^i}{\sum_i \langle N \rangle_{th}^i} = \frac{\sum_i \int dp_m \left[(p_m^i)^2 \rho_2^{exp}(p_m^i) \right]}{\sum_i \int dp_m \left[(p_m^i)^2 \rho_2^{th}(p_m^i) \right]} \quad (6.5)$$

was studied as a function of the missing momentum as shown in Figure 6.11.

Results

Most of the difference between the cross sections measured at different ϵ (see Figure 6.4) is removed by dividing the cross sections by the factor $p_p^2 \cdot \sigma_{ep}^{cc1}$. Nevertheless, even after this the measured proton-momentum distributions show some systematic dependence on ϵ . In Figure 6.9, the data points measured at an incident electron energy of 570.11 MeV are systematically higher than the data collected at 855.11 MeV. The overall difference is small ($\sim 5\%$) and the fluctuations from one missing-momentum bin to another are large for each spectrum.

After the ω -cut the difference between the 855.11 MeV kinematic and the other measurements increased by 2-3%. The same dependence can be clearly observed in Figures 6.11 and 6.12, where the value of a $\sum \langle N \rangle_{exp}^i / \sum \langle N \rangle_{th}^i$ is shown for several theoretical models. The fluctuations are reduced on these plots, and a clear, although small, systematic shift for all three ϵ can be observed. The final value for $\langle N \rangle$ is approximately 4.3% different for the lowest and highest incident electron energies without the ω -cut (Figure 6.10). This difference increased to 6.6% after including the ω -cut. It must be mentioned that this result is difficult to interpret

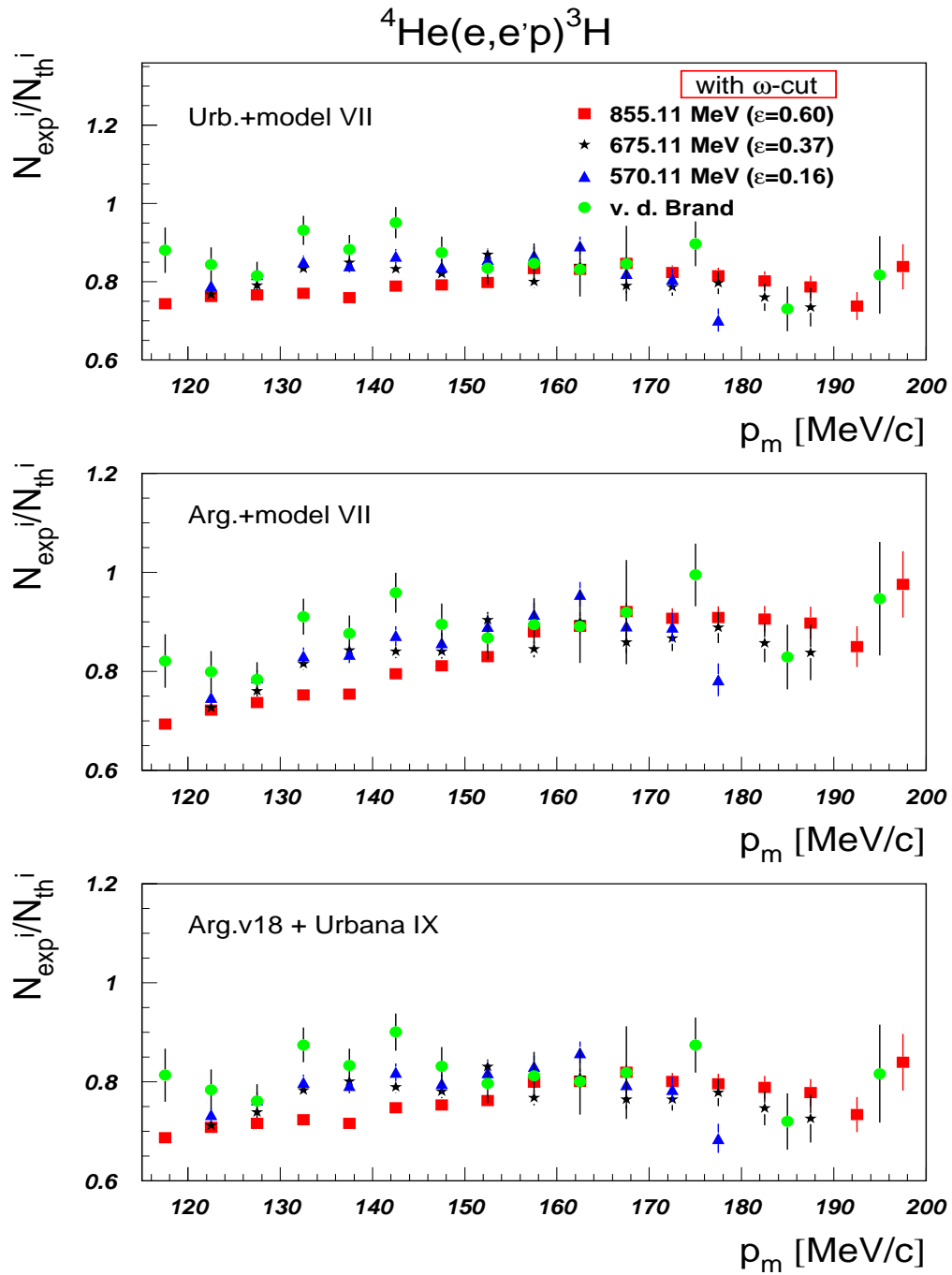


Figure 6.14: The ratio between the experiment and several theoretical models for proton-triton momentum distributions (with the ω -cut)

uniquely due to the systematic uncertainty of $\pm 2.2 - 2.4$ %. Nevertheless, a clear linear ϵ -dependence of the proton-momentum distributions for all three kinematics is a good indication that this ϵ -dependence is more than just an accidental coincidence.

Figures 6.8 and 6.7 show the measured momentum distributions compared with the experimental results obtained earlier in Mainz (reference [23]), and the NIKHEF data of van den Brand [52]. The agreement with the NIKHEF data is good in the complete missing-momentum range $115 \leq p_m \leq 200$ MeV/c, although our results are statistically more accurate. At lower missing momenta our momentum distributions are slightly lower compared to NIKHEF (see Figures 6.13 and 6.14). Results measured at MAMI by Florizone also show satisfactory agreement with our results in the overlap region of the kinematics, although there are some points, where the disagreement is substantial. It is probably significant that where the data by Florizone does not match our data, it also disagrees with the NIKHEF data.

The experimental momentum distributions were found to be approximately 15 - 25 % lower than the predictions of the several theoretical models as shown in Figures 6.12 and 6.11. Moreover, all three theoretical models show quite different missing-momentum dependence for the ratio of the experimental and the theoretical results. This is complicated by the ϵ -dependence of the experimental results (see Figures 6.13, 6.14). At least part of this difference is due to the final-state interaction effect between the detected proton and the rest of the nuclear system, which is not included in the theoretical calculations.

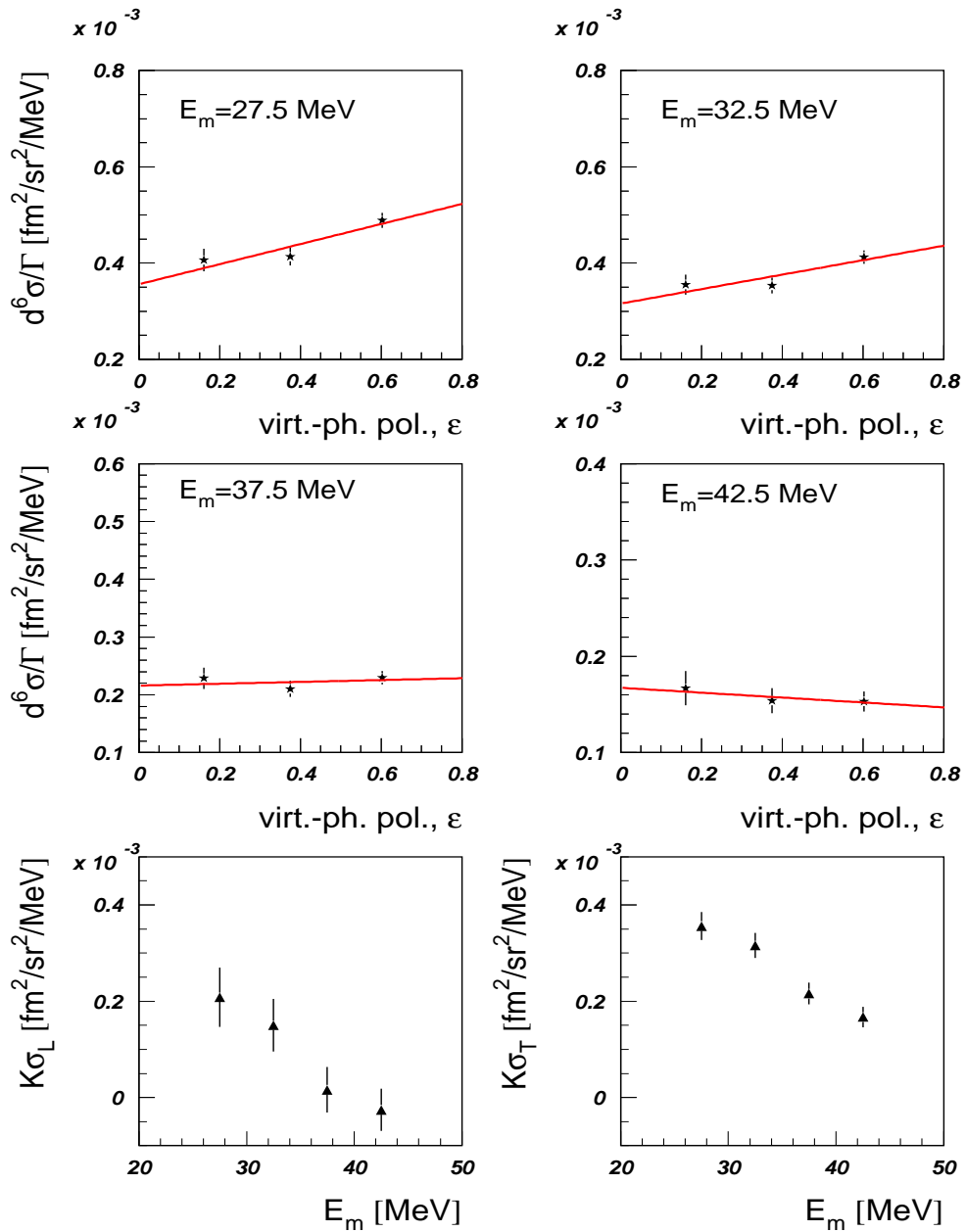
Continuum channels (without ω -cut)

Figure 6.15: Rosenbluth plots for the continuum region (5 MeV missing-energy bins)

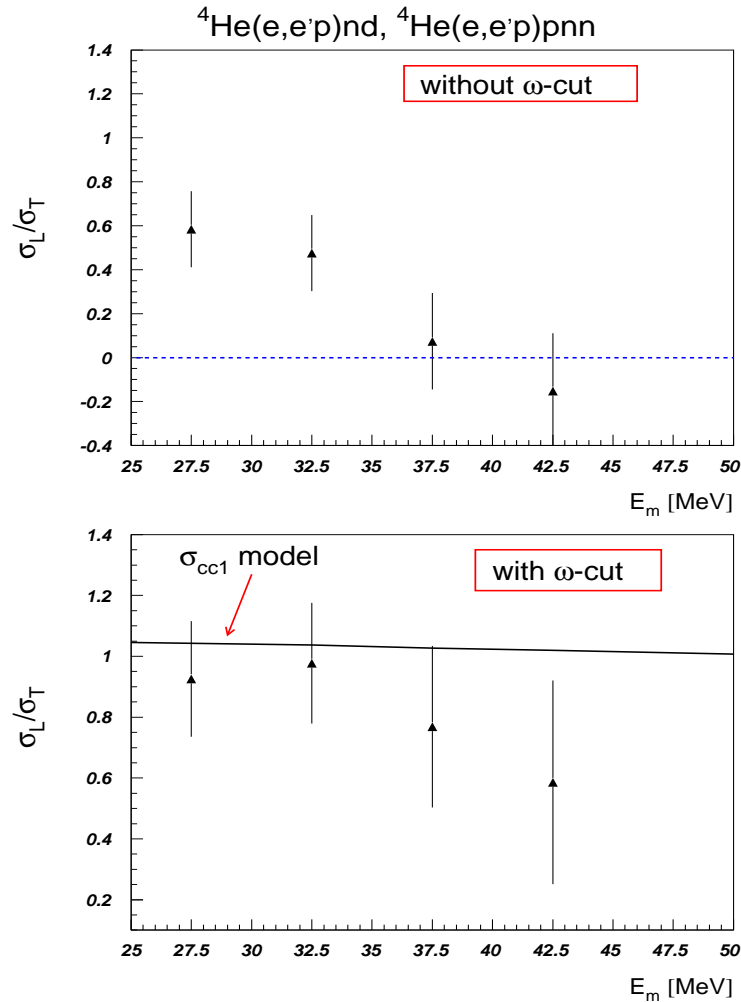


Figure 6.16: Ratio σ_L/σ_T as a function of the missing energy (5 MeV missing-energy bins)

6.3 Three and four-body breakup channels

6.3.1 Rosenbluth L/T separation

Compared to the two-body-breakup cross section, the cross section for the continuum region is much smaller, and the statistical and systematic uncertainties are relatively larger. Nevertheless, it was possible to perform the Rosenbluth separation for the continuum cross section as a function of the missing energy. This

method can provide more detailed information about the L/T behaviour of the continuum cross section, than the momentum distributions, where the continuum strength is integrated over the entire missing-energy range.

Analysis

To perform the Rosenbluth separation, the six-fold differential cross section $d^6\sigma$ was averaged over the missing-momentum range between 115 MeV/c and 155 MeV/c. This was done to reduce the statistical and systematic uncertainties and to ensure the quality of the Rosenbluth plots. The missing-energy range, where the continuum cross section was found to be non-zero (25 - 45 MeV), was divided into the 2, 4 or 5 bins as shown in Figures 6.15, 6.17, 6.18 and 6.19. Different size missing-energy bins were used to determine whether the results of the Rosenbluth separation depended on how the averaging of the cross section was performed over the missing-energy range. In addition, the $d^6\sigma$ cross section for each kinematic was divided by the virtual-photon flux calculated according to Equation 2.14. The Rosenbluth plots, thus were performed for the $d^6\sigma/\Gamma$ variable. This allows the values of σ_L and σ_T multiplied by the kinematical factor K to be obtained according to Equation 2.19 in units $fm^2/MeV/sr^2$.

Using these longitudinal and transverse parts of the $d^6\sigma$ cross section one can obtain the ratio of the nuclear response functions σ_L/σ_T as a function of missing energy as defined in Chapter 2 (Equations 2.15 and 2.16), and compare these with the theoretical predictions.

The theoretical σ_L/σ_T value was estimated using the Monte-Carlo code by averaging over the acceptance the corresponding nuclear responses σ_L and σ_T from the σ_{cc1} off-shell model of de Forest. This was done by calculating the σ_L/σ_T ratio for each generated event accepted by the same software cuts, as were applied to the experimental data. The ratio σ_L/σ_T is unit-less, and was found to be approximately

1.02 – 1.045 for different missing-energy values. By comparing these with the experimental results one can conclude whether or not the L/T ratio is reduced compared to theory.

Results

As in case of the L/T separation for the two-body breakup cross section, the L/T cross section behaviour in the continuum was also studied with and without the ω -cut. The Rosenbluth separation without the ω -cut was done only for the case of 5 MeV missing-energy bins in order to understand the influence of this cut on the resulting σ_L/σ_T ratio.

The effect of this cut appeared to be more significant compared to the two-body breakup case. Without the ω -cut, the Rosenbluth plots show some chaotic behaviour at high missing energies, with the $K \cdot \sigma_L$ being negative for the last E_m bin. The Rosenbluth plots after the ω -cut are more self-consistent and linear.

The ratio σ_L/σ_T for both cases is shown in Figures 6.16, 6.18 and 6.19. The ratio σ_L/σ_T shows a similar dependence on the missing energy for the different E_m bin size, and is close to ~ 1 at low missing-energy values, in good agreement with the σ_{cc1} predictions. As the missing energy increases, σ_L/σ_T becomes less than 1, and reaches the value (for the highest missing-energy bin): 0.69 ± 0.21 (10 MeV bins), 0.59 ± 0.33 (5 MeV bins) and 0.43 ± 0.36 for the 4 MeV missing-energy bins, although the error bars are quite large.

These results indicate that the transverse part of the (e,e'p) cross section becomes larger than that predicted by the σ_{cc1} model for missing energies greater than 35 MeV. In one of the plots (Figure 6.19), the $K \cdot \sigma_T$ is even increasing at the highest missing-energy bin ($E_m = 43 \text{ MeV}$).

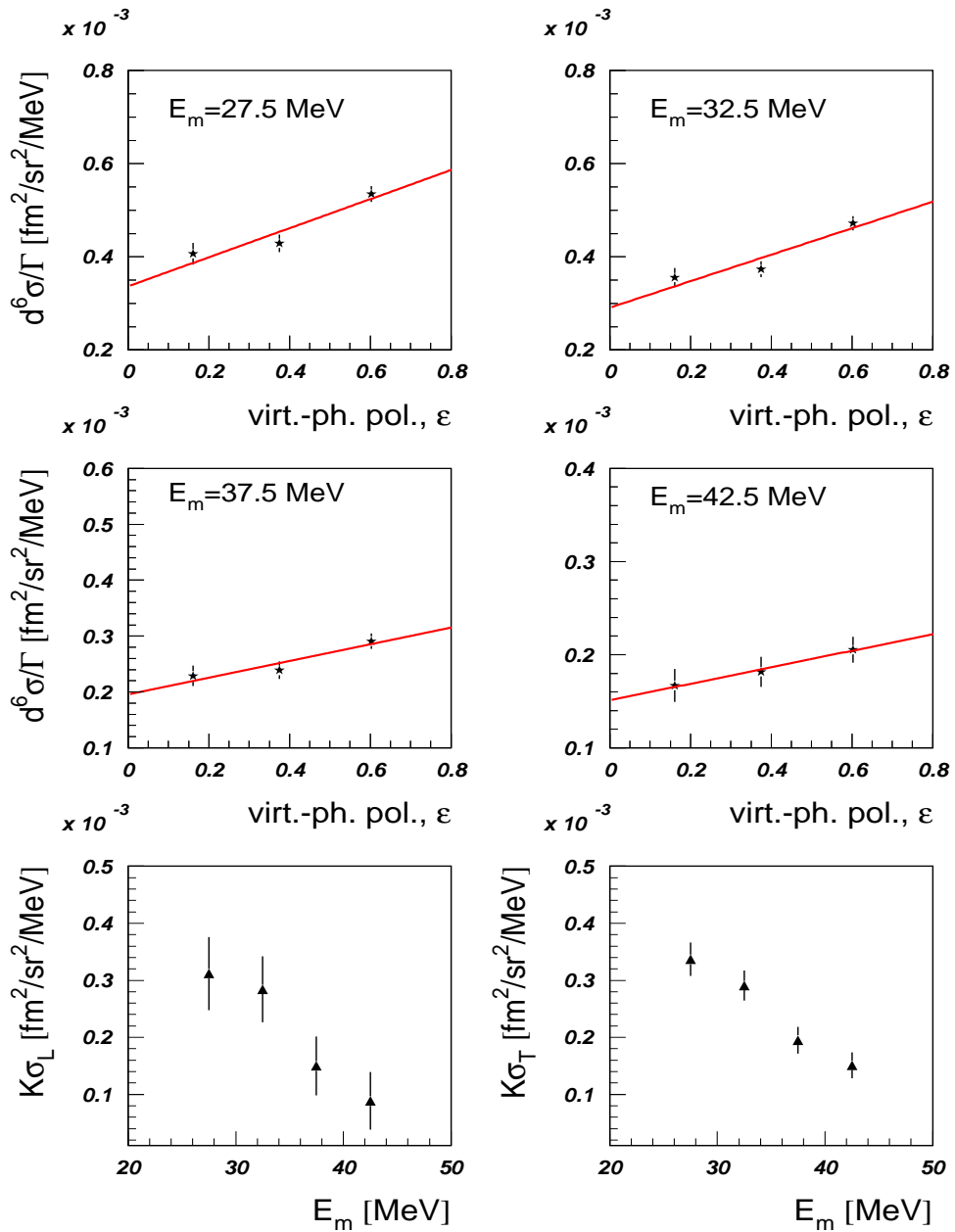
Continuum channels (with ω -cut)

Figure 6.17: Rosenbluth plots for the continuum region (5 MeV missing-energy bins)

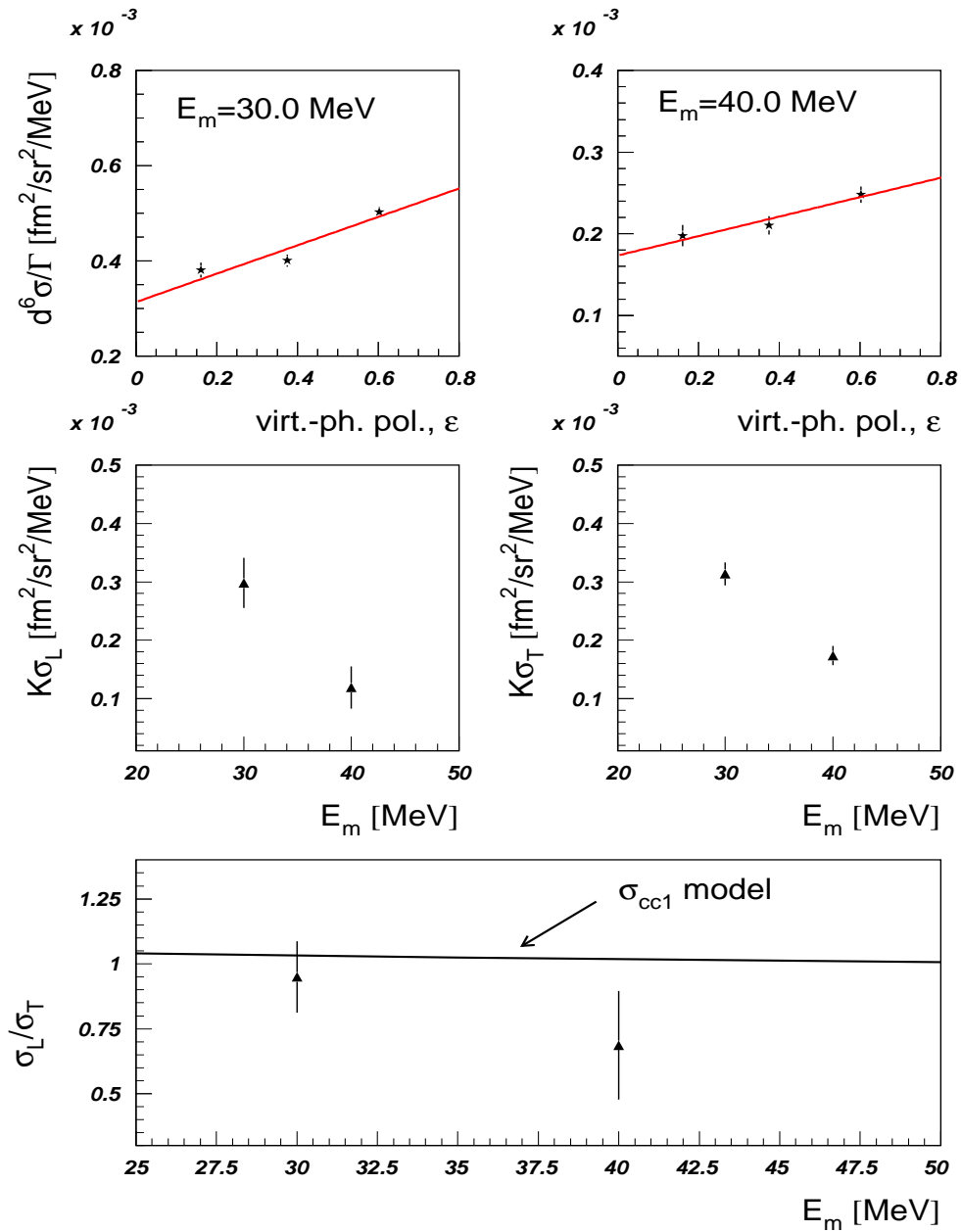
Continuum channels (with ω -cut)

Figure 6.18: Rosenbluth plots for the continuum region (10 MeV missing-energy bins)

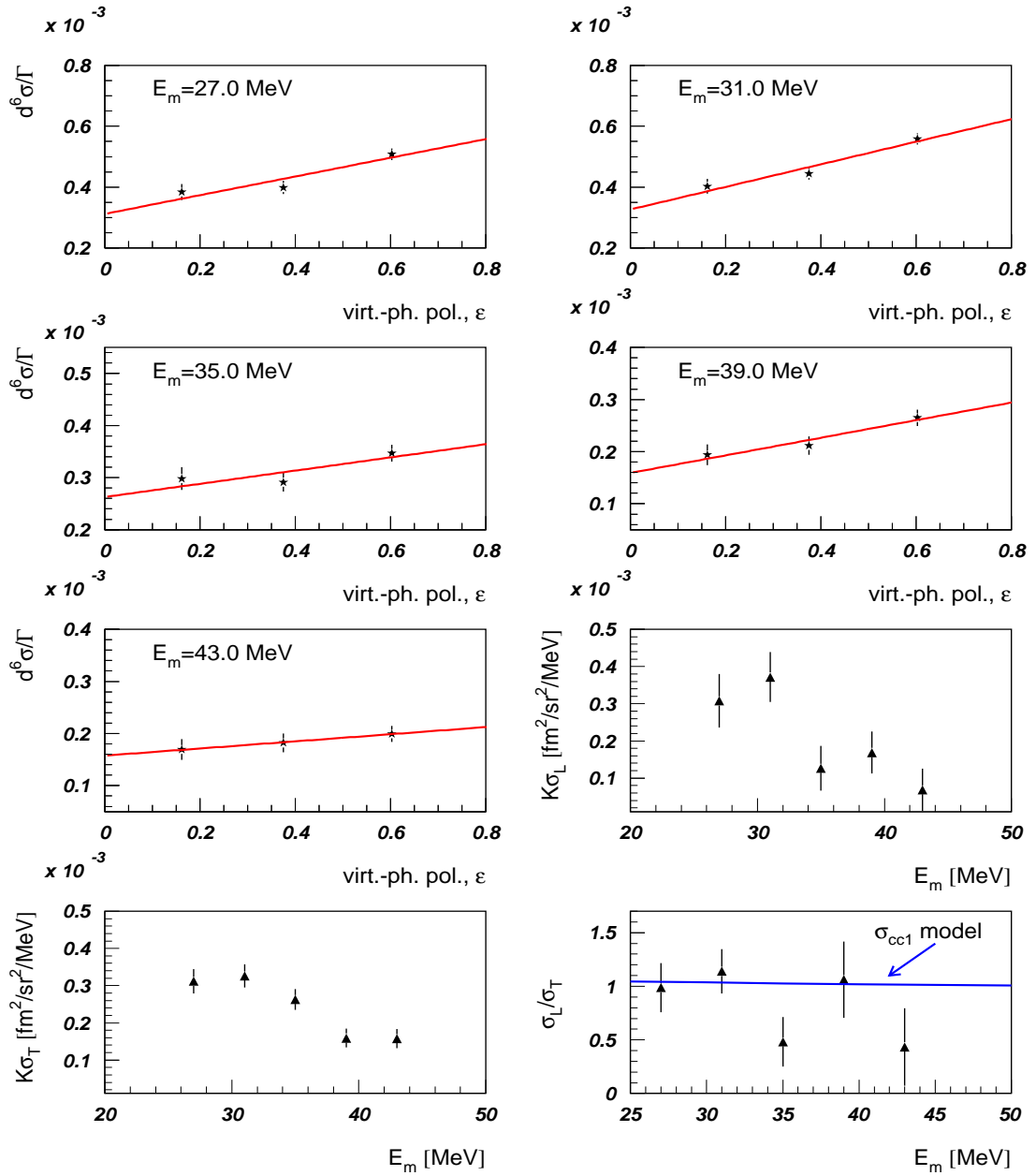
Continuum channels (with ω -cut)

Figure 6.19: Rosenbluth plots for the continuum region (4 MeV missing-energy bins)

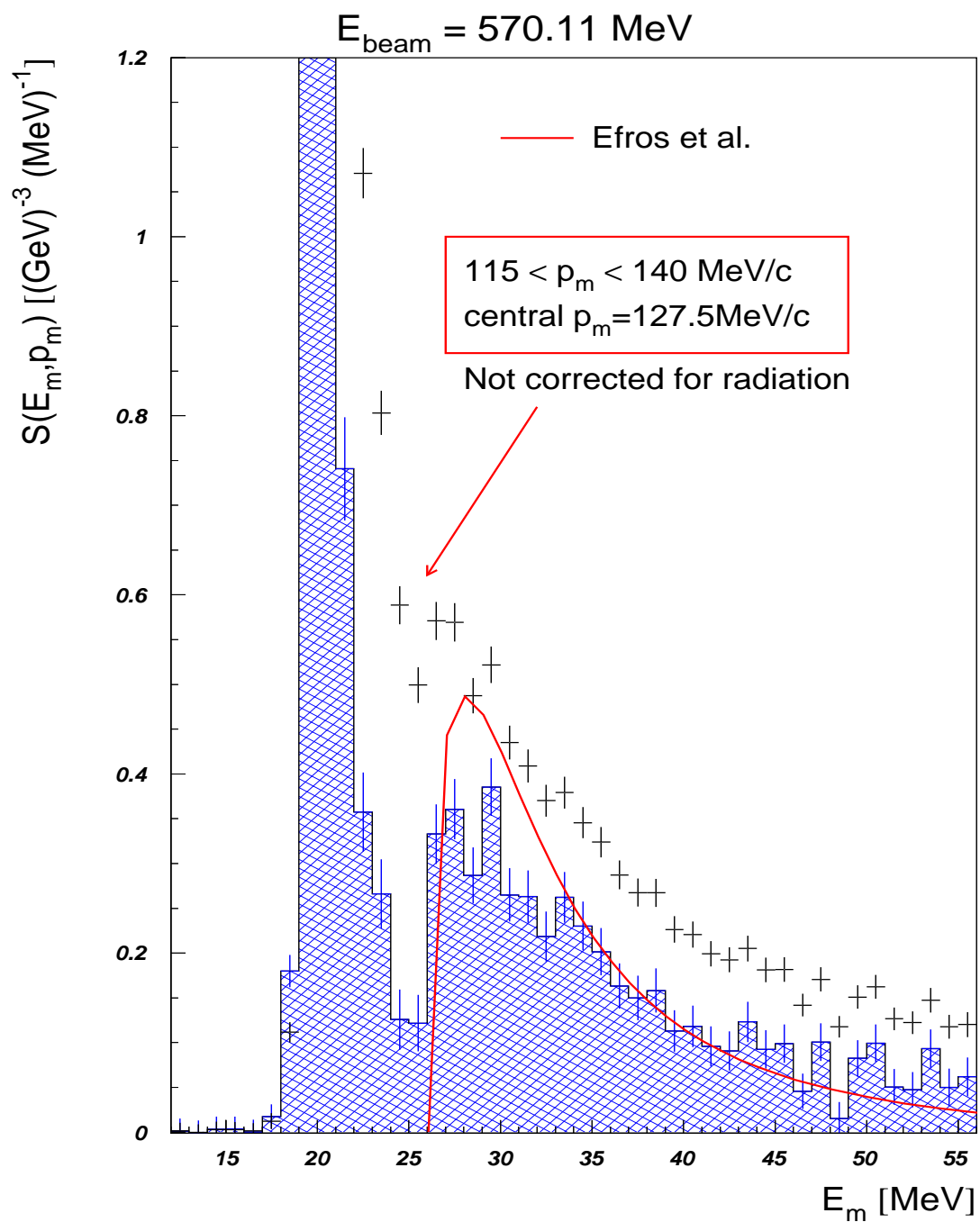


Figure 6.20: Measured spectral function in Kinematic 1

6.3.2 Spectral function

Experimental spectral function

The experimental spectral functions were extracted from the experimental cross section using the elementary off-shell electron-proton cross section model σ_{cc1} . This procedure is fully described in Chapter 5 (see Eq. 5.15). Most of the difference observed between the six-fold differential cross sections for kinematics with different virtual-photon polarizations was removed after division by a factor $p_p^2 \cdot \sigma_{cc1}$.

Theoretical spectral function

The theoretical spectral function used for comparison with the experimental results was obtained from ref. [54]. This ${}^4\text{He}$ spectral function was calculated with the Lorentz integral transform method over a large missing-momentum range (see reference [55]). The semi-realistic Trento nuclear-potential model (central force describing 1S_0 and 3S_1 phase shifts up to the pion threshold) was used. The final-state interaction in the residual 3N system was completely taken into account; although the final-state interaction between the detected proton and the residual 3N system is not included.

Results

The experimental spectral functions were compared with the theoretical calculations for two missing-momentum values (127.5 MeV/c and 147.5 MeV/c) for Kinematics 2 and 3 as shown in Figures 6.21 and 6.22. The measured spectral function for the lowest beam energy was compared with the theory only at one missing-momentum value (127.5 MeV/c), due to the fact that the (E_m, p_m) phase-space covered in this kinematic is smaller compare to others, and is shown in Figure 6.20. Due to the low statistics for the continuum channels, the experimental spectral functions were averaged over the missing momentum $\pm 12.5 \text{ MeV}/c$ in all cases. Each of

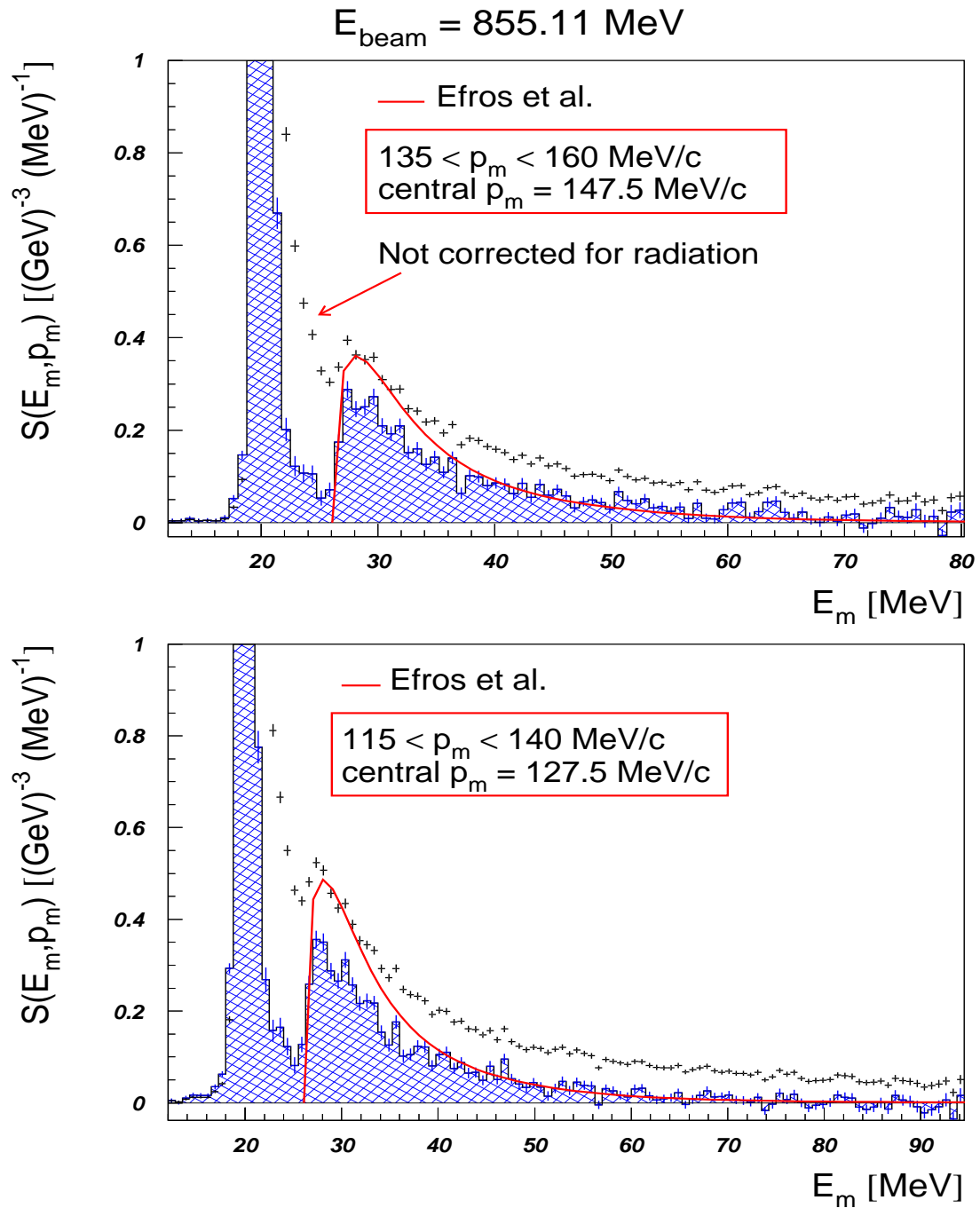


Figure 6.21: Measured spectral function in Kinematic 3

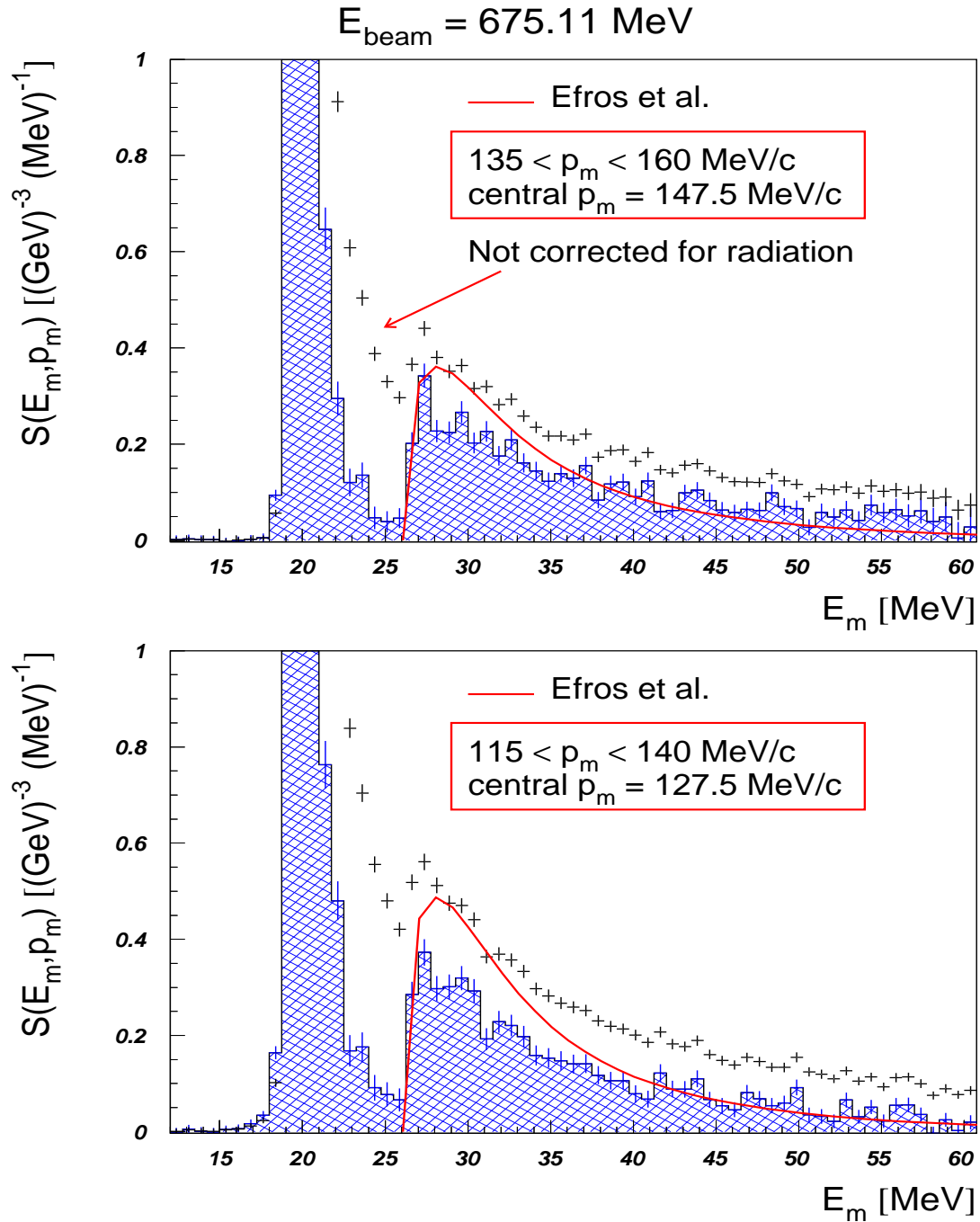


Figure 6.22: Measured spectral function in Kinematic 2

these plots also shows a spectral function extracted from the radiatively-uncorrected experimental cross section. This is to show the magnitude of the radiative corrections. The measured spectral functions for all three experimental kinematics are shown together in Figure 6.23.

In general the agreement between the theory and the experiment is satisfactory. The deviation of the experimental spectral function from the model at low missing energies can be partially explained by the final-state interaction effect between the proton and residual $3N$ system. From both Figures 6.22 and 6.21 one important feature in the spectral function behaviour is apparent. The agreement between the theory and the experiment improves at higher missing-momentum values. This is probably an indication that the final-state interaction effect decreases, when the initial proton momentum in the He nucleus is higher, and the interaction in the $p - 3N$ system is reduced.

In Fig 6.21 the theoretical and measured spectral function show good agreement even at high missing energies ($E_m = 50 - 95 MeV$). This is especially evident for the bottom histogram ($p_m = 127.5 MeV/c$) where the central part of the phase-space is shown. However, care must be exercised in the interpretation of the results at high missing energies in case of Kinematic 1 and 2. For these kinematics the experimental spectral function shown in Figures 6.22 and 6.20 contains a certain background contribution from the external radiative tails at $E_m \geq 45 - 50 MeV$ (see Fig. 5.23 and 5.24). In all cases the size of radiative corrections in this missing-energy region even from the detected strength at lower missing energies is larger than the actual value of the experimental spectral function. The influence of the external radiative tails is also increased in this region. In other words, due to the existing experimental uncertainties the measured spectral function can be safely determined for all three kinematics only for the missing-energy range $26 MeV \leq E_m \leq 45 - 50 MeV$.

In Figure 6.23 the experimental spectral functions for three different virtual-photon polarizations ϵ are shown. No significant dependence on ϵ can be observed.

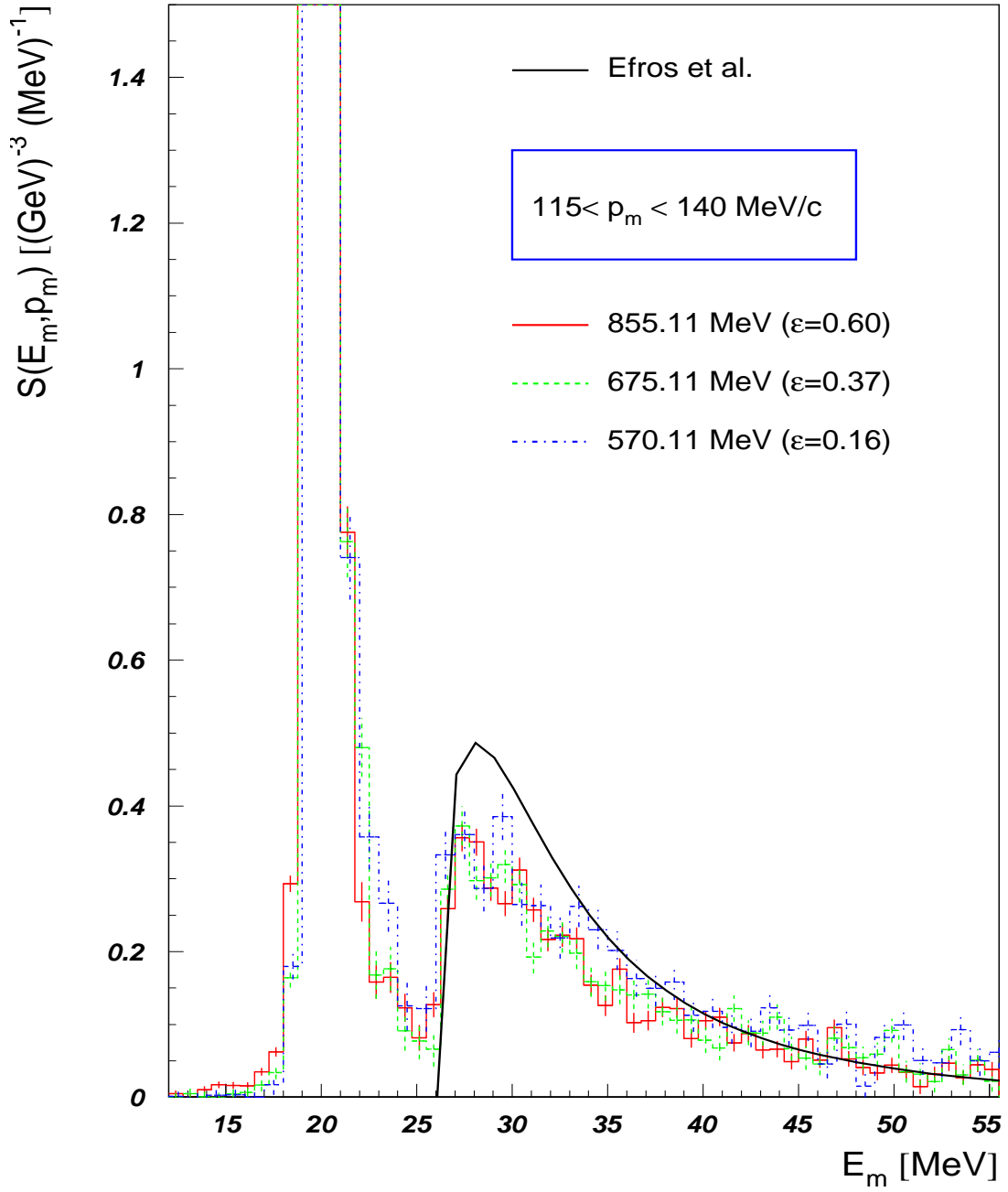


Figure 6.23: Measured spectral function for all three kinematics

All measured spectral functions show a similar dependence from the missing energy in a shape and magnitude.

6.3.3 The proton-momentum distribution

p_m $\frac{MeV}{c}$	$\rho_{3,4}(p_m) [(GeV/c)^{-3}]$				
	855.11 MeV	675.11 MeV	855.11 MeV*	675.11 MeV*	570.11 MeV
87.5	5.25 ± 0.24	-	-	-	-
92.5	5.05 ± 0.22	-	-	-	-
97.5	4.77 ± 0.21	5.18 ± 0.30	-	-	-
102.5	4.42 ± 0.20	4.48 ± 0.28	-	-	-
107.5	4.23 ± 0.20	4.70 ± 0.28	-	-	-
112.5	3.97 ± 0.19	4.47 ± 0.28	4.67 ± 0.25	-	-
117.5	3.48 ± 0.19	3.99 ± 0.28	4.20 ± 0.23	4.21 ± 0.28	4.80 ± 0.41
122.5	3.68 ± 0.19	3.53 ± 0.27	4.39 ± 0.22	3.70 ± 0.27	4.01 ± 0.39
127.5	3.19 ± 0.18	3.08 ± 0.26	3.79 ± 0.21	3.23 ± 0.26	4.12 ± 0.39
132.5	3.28 ± 0.18	3.40 ± 0.26	4.18 ± 0.21	3.51 ± 0.26	4.08 ± 0.38
137.5	3.08 ± 0.18	2.87 ± 0.25	3.90 ± 0.21	3.04 ± 0.25	3.21 ± 0.36
142.5	2.95 ± 0.17	2.93 ± 0.24	3.69 ± 0.22	3.19 ± 0.26	3.15 ± 0.35
147.5	2.51 ± 0.17	2.94 ± 0.24	3.37 ± 0.23	3.19 ± 0.27	3.28 ± 0.35
152.5	2.62 ± 0.17	2.90 ± 0.23	3.55 ± 0.25	3.36 ± 0.29	4.08 ± 0.38
157.5	2.42 ± 0.17	3.08 ± 0.24	-	-	-
162.5	2.25 ± 0.18	-	-	-	-
167.5	2.01 ± 0.18	-	-	-	-
172.5	1.88 ± 0.19	-	-	-	-

Table 6.3: $\rho_{3,4}(p_m)$ momentum distributions for ${}^4He(e, e'p)nd$ and ${}^4He(e, e'p)nnp$ reaction channels ($mark^*$ is corresponding to the momentum distributions calculated with the ω -cut)

As was already shown in the previous section, the experimental spectral functions for the three virtual-photon polarization values are similar within the detected range of missing energy and missing momentum. In order to make more a detailed comparison between these results, the experimental proton-momentum distributions were calculated according to Equation 5.17 as:

$$\rho_{3,4}(p_m) = \int_{25}^{45} S(E_m, p_m) dE_m \quad (6.6)$$

The lower limit was selected to be less than the three-body breakup threshold in order to include the continuum strength shifted to this region due to the finite experimental energy resolution. All results were obtained for the case, both with and without the ω -cut.

Theoretical momentum distribution

The theoretical momentum distribution $\rho_{3,4}(p_m)$ was computed according to Equation 6.6 using the theoretical spectral function obtained from ref. [54]. This ${}^4\text{He}$ spectral function was calculated with the Lorentz integral transform method over a large missing-momentum range (see reference [55]). The semi-realistic Trento N-N potential model was used. The final-state interaction in the residual three-nucleon system was completely taken into account.

Further calculations that include the FSI effect between the detected proton and the recoiling $3N$ system are required to compare the "distorted" experimental proton-momentum distributions directly to the theoretical calculations.

Earlier experimental momentum distribution

Earlier the proton-momentum distributions for similar kinematical conditions were measured by Florizone [23] at MAMI. These measurements were also performed to study the L/T behaviour of the ${}^4\text{He}(e, e'p)$ cross section for three different ϵ

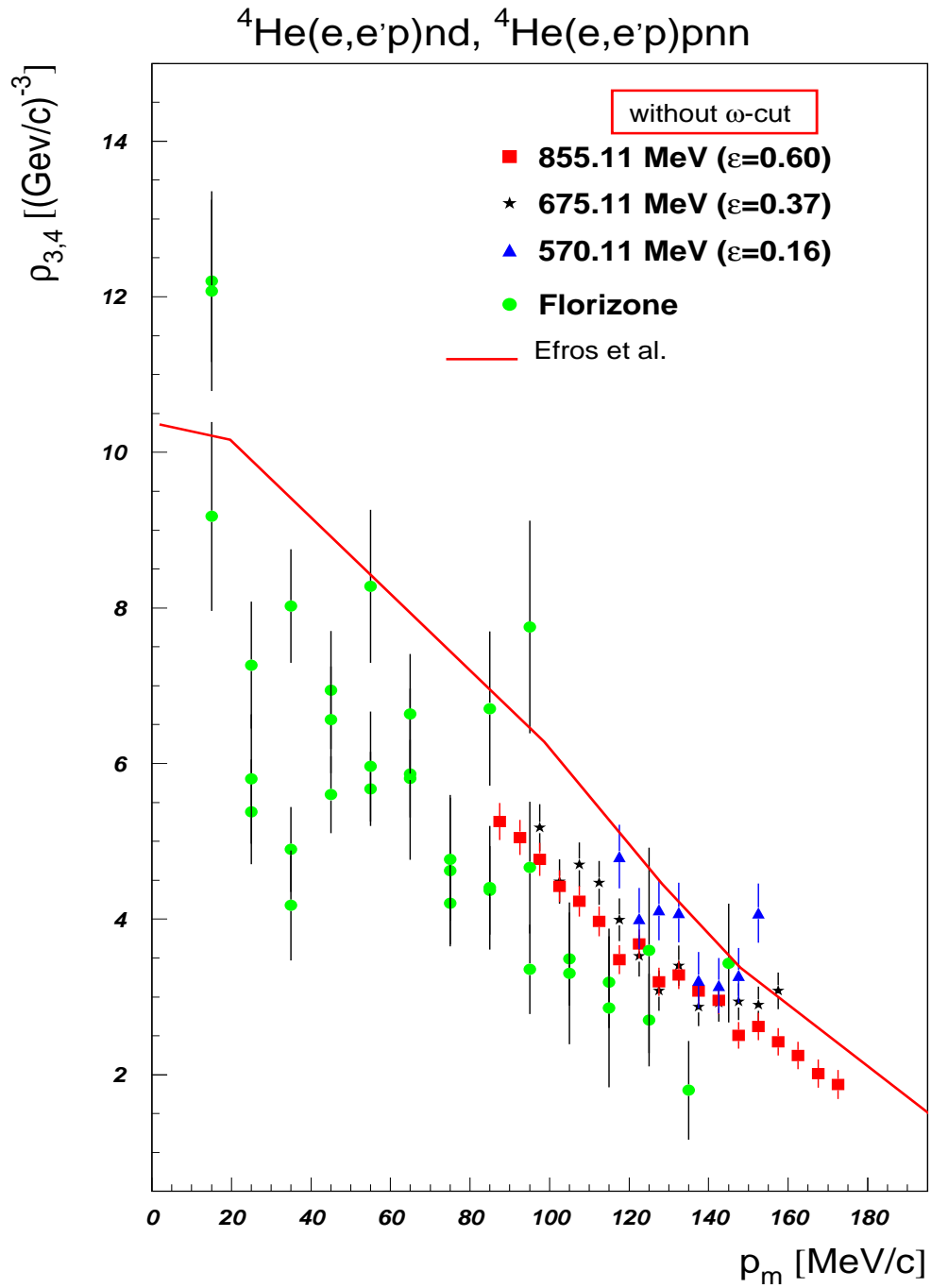


Figure 6.24: The proton-momentum distribution $\rho_{3,4}$ as a function of the missing momentum

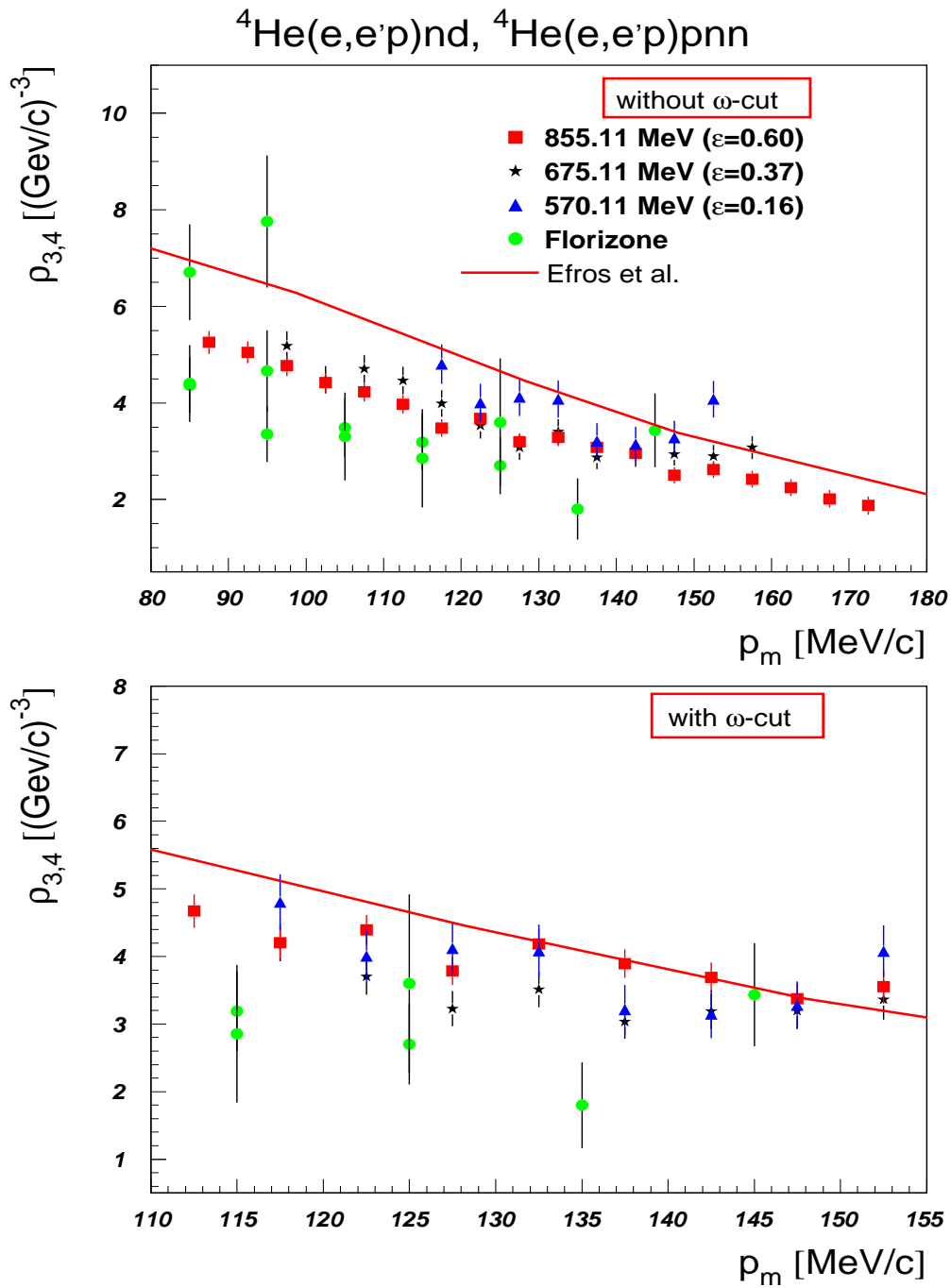


Figure 6.25: The proton-momentum distribution $\rho_{3,4}$ as a function of the missing momentum

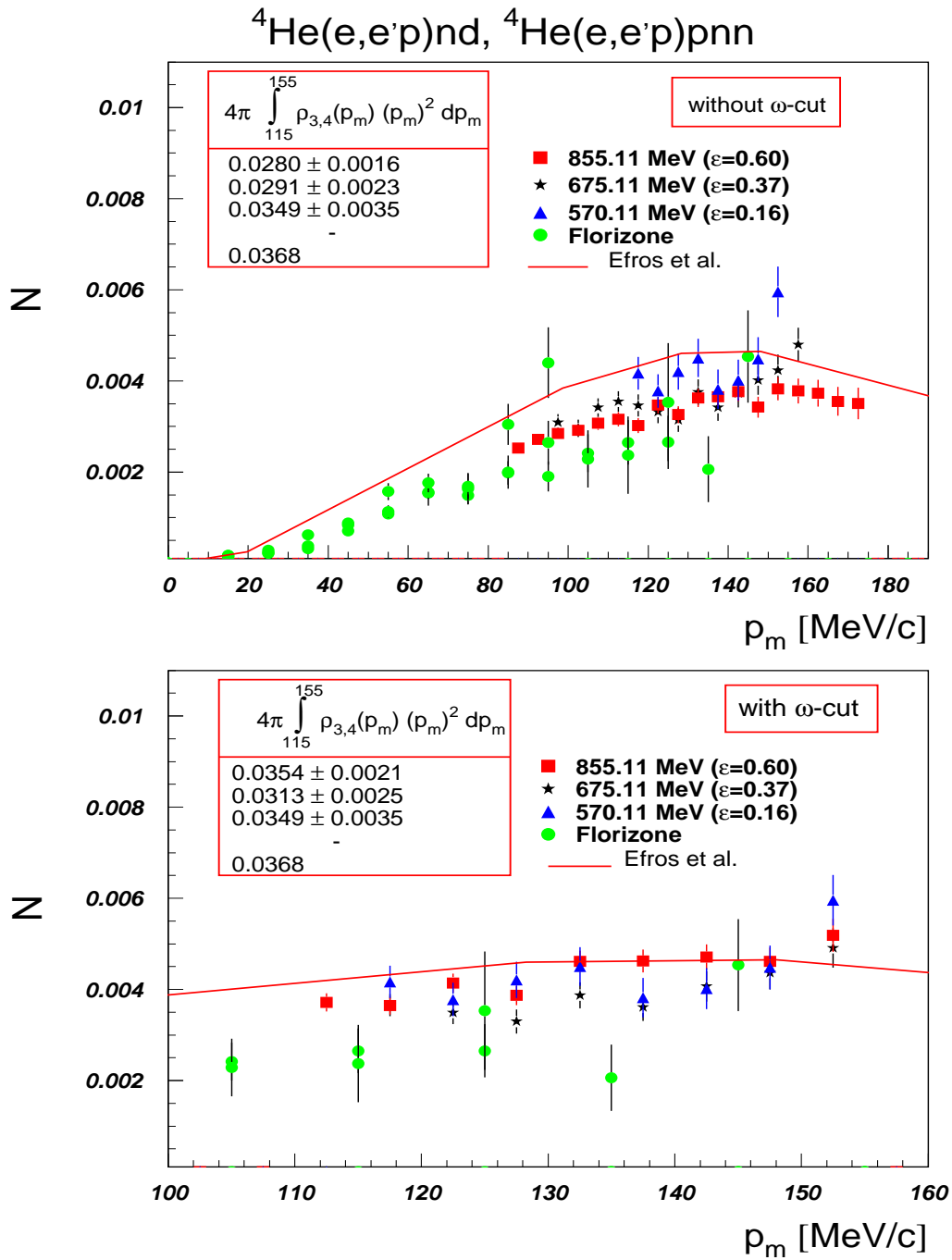


Figure 6.26: $\langle N \rangle$ value as a function of the missing momentum (calculated for each missing-momentum bin)

values (0.2, 0.45 and 0.64) and corresponding the beam energies of 540.11, 675.11 and 855.11 MeV. The momentum transfer \vec{q} was the same as for our measurements (685 MeV/c), but the ω -value was 242.7 MeV, which corresponds to the top of the quasi-elastic peak, where the scaling factor $y = 0$. All momentum distributions in [23] were also extracted using the σ_{cc1} prescription for the off-shell electron-proton cross section. The systematic uncertainty for these results is 5-6 %. The error bars shown in Figure 6.24 are statistical only. The major part of the data points correspond to the lower missing momenta, but the overlap region between our results is large and allows comparison with our measurements.

Analysis

Similar to the case of the two-body-breakup data analysis, the following dimensionless integral was calculated for comparison of the measured proton-momentum distributions with the theory and each other

$$\langle N \rangle = 4\pi \int_{115}^{155} dp_m p_m^2 \rho_{3,4}(p_m) \quad (6.7)$$

for the missing-momentum range p_m between the 115 and 155 MeV/c, which corresponds to the overlap region of the three kinematics for the continuum channels. This averaged value $\langle N \rangle$ for the our kinematics and the theory is given in Figure 6.26.

The ϵ -dependence of the $\rho_{3,4}(p_m)$ was studied in the same way as for the two-body breakup channel. First, the ratio

$$\frac{\rho_{3,4}}{\rho_{3,4}^{AVG}} = \frac{\rho_{3,4}(p_m, \epsilon)}{\frac{1}{3} \sum_{\epsilon} \rho_{3,4}(p_m, \epsilon)} \quad (6.8)$$

for each missing-momentum bin was calculated. This ratio shows how much the momentum distribution for each individual measurement deviates from the averaged $\rho_{3,4}^{AVG}$ value for the particular p_m bin. Second, the ratio

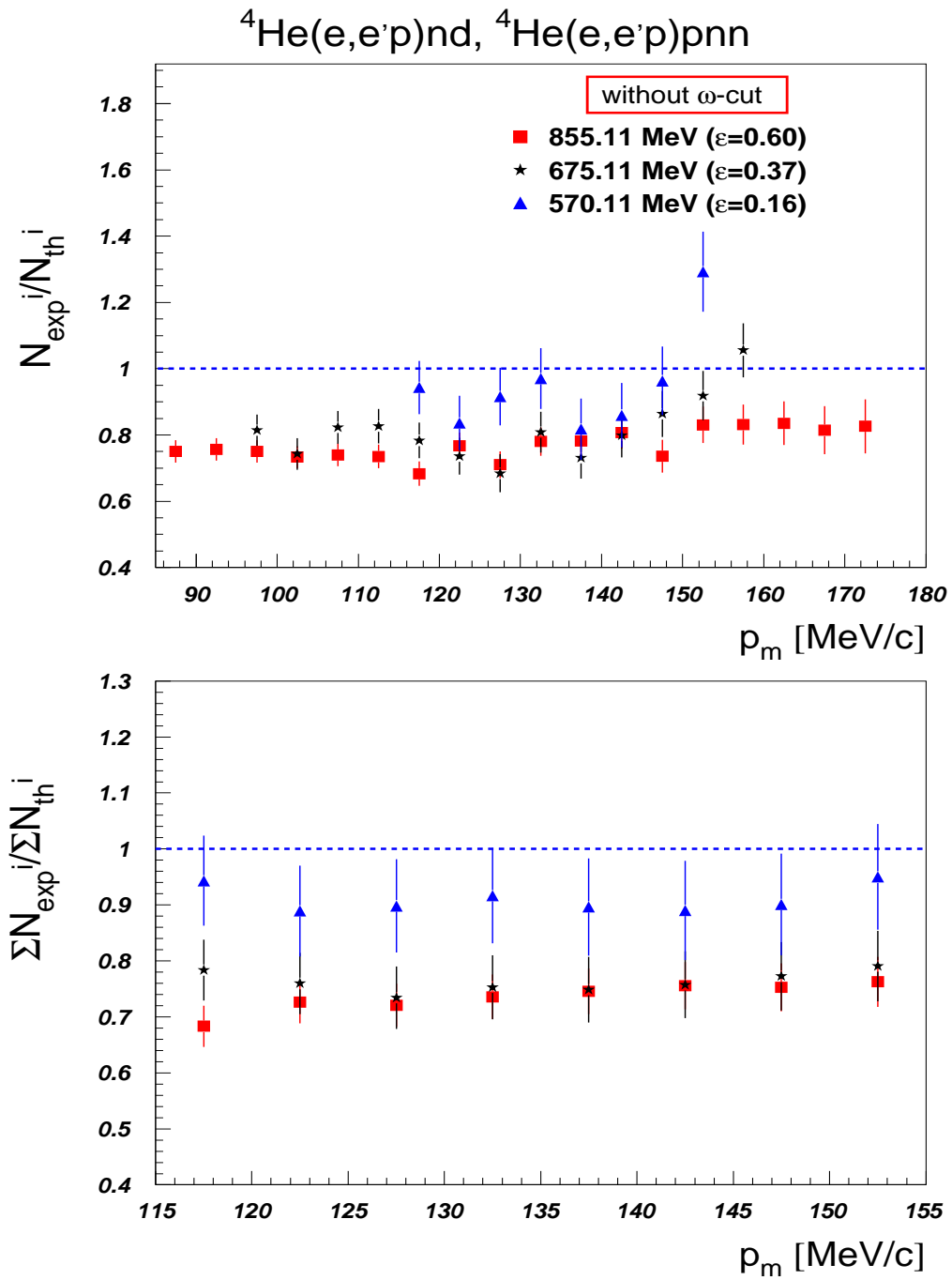


Figure 6.27: Ratio for the experimental and theoretical momentum distributions as a function of the missing momentum

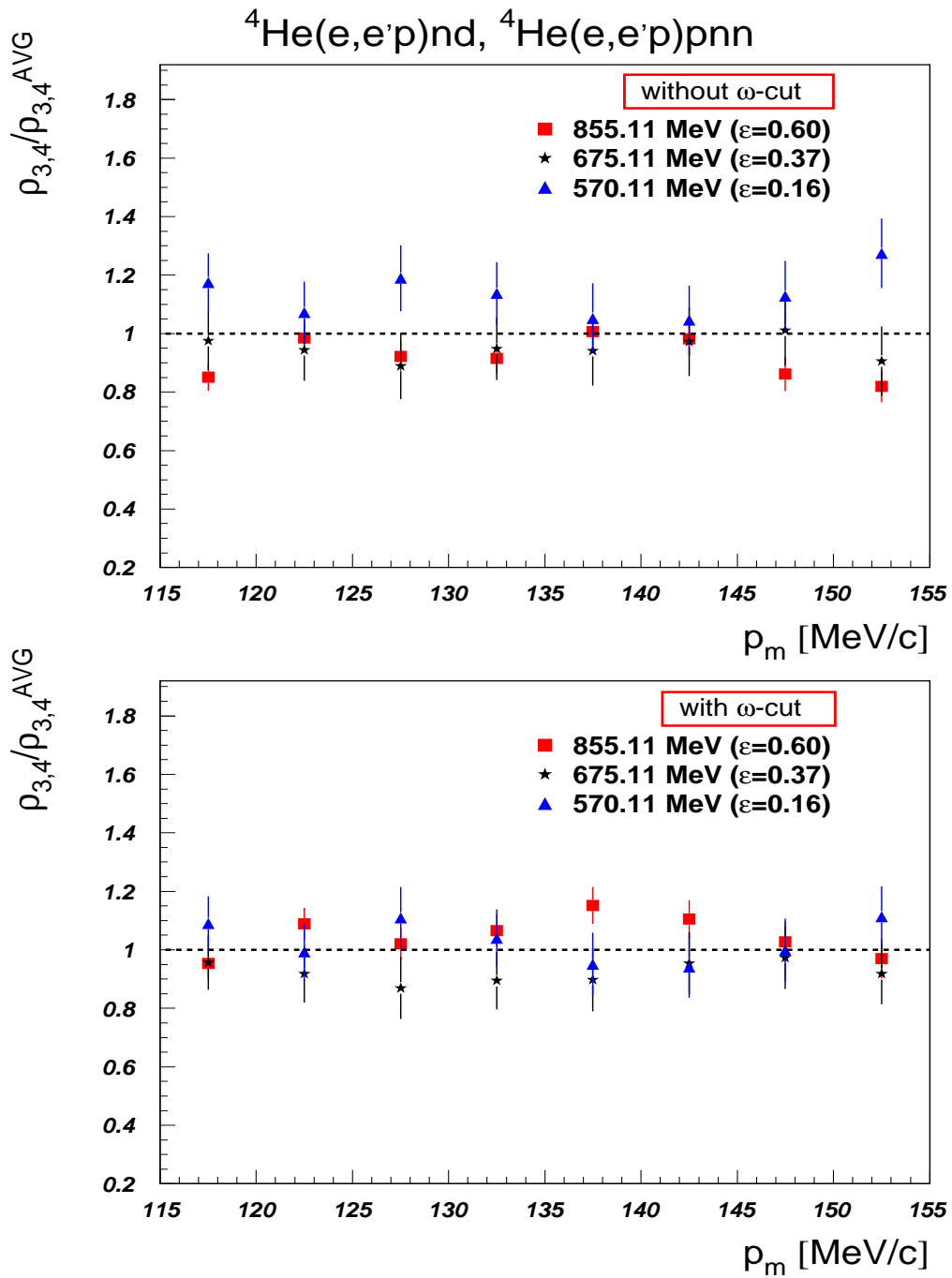


Figure 6.28: The proton-momentum distributions compared to the averaged over the three kinematics value

$$\frac{\langle N \rangle_{exp}^i}{\langle N \rangle_{th}^i} = \frac{\rho_{3,4}^{exp}(p_m^i)}{\rho_{3,4}^{th}(p_m^i)} \quad (6.9)$$

for each missing-momentum bin i (see Figures 6.27 and 6.29) was calculated. In order to calculate the $\rho_{3,4}^{th}$ value for each missing-momentum bin, the theoretical data points were fitted with a high-order polynomial, so that the functional dependence $\rho_{3,4}^{th}(p_m)$ was extracted. The systematic uncertainty created by this procedure was less than 2-3 %. After that the $\rho_{3,4}^{th}$ was calculated for the missing-momentum value corresponding to the middle of each missing-momentum bin. This ratio gives the deviation of the experimental $\rho_{3,4}^{exp}(p_m)$ momentum distribution from the theory prediction as a function of the missing momentum. Third, the development of the sum's ratio

$$\frac{\sum_i \langle N \rangle_{exp}^i}{\sum_i \langle N \rangle_{th}^i} = \frac{\sum_i \int dp_m \left[(p_m^i)^2 \rho_{3,4}^{exp}(p_m^i) \right]}{\sum_i \int dp_m \left[(p_m^i)^2 \rho_{3,4}^{th}(p_m^i) \right]} \quad (6.10)$$

was studied as a function of the missing momentum as shown in Figures 6.27 and 6.29.

Results

The large kinematic dependence seen for the data measured at different ϵ in the 6-fold cross section was removed by dividing the cross sections by the factor $p_p^2 \sigma_{ep}^{cc1}$. The remaining dependence from the virtual-photon polarization ϵ was studied both with and without the ω -cut. When this cut is not used, the measured momentum distributions show a significant systematic dependence on ϵ . In Figure 6.28 (top picture), the data points measured at 570.11 MeV incident-electron energy are systematically 15-20 % higher than the data collected at 855.11 MeV and 675.11 MeV, although the statistical uncertainty is large and the $\rho_{3,4}/\rho_{3,4}^{AVG}$ value

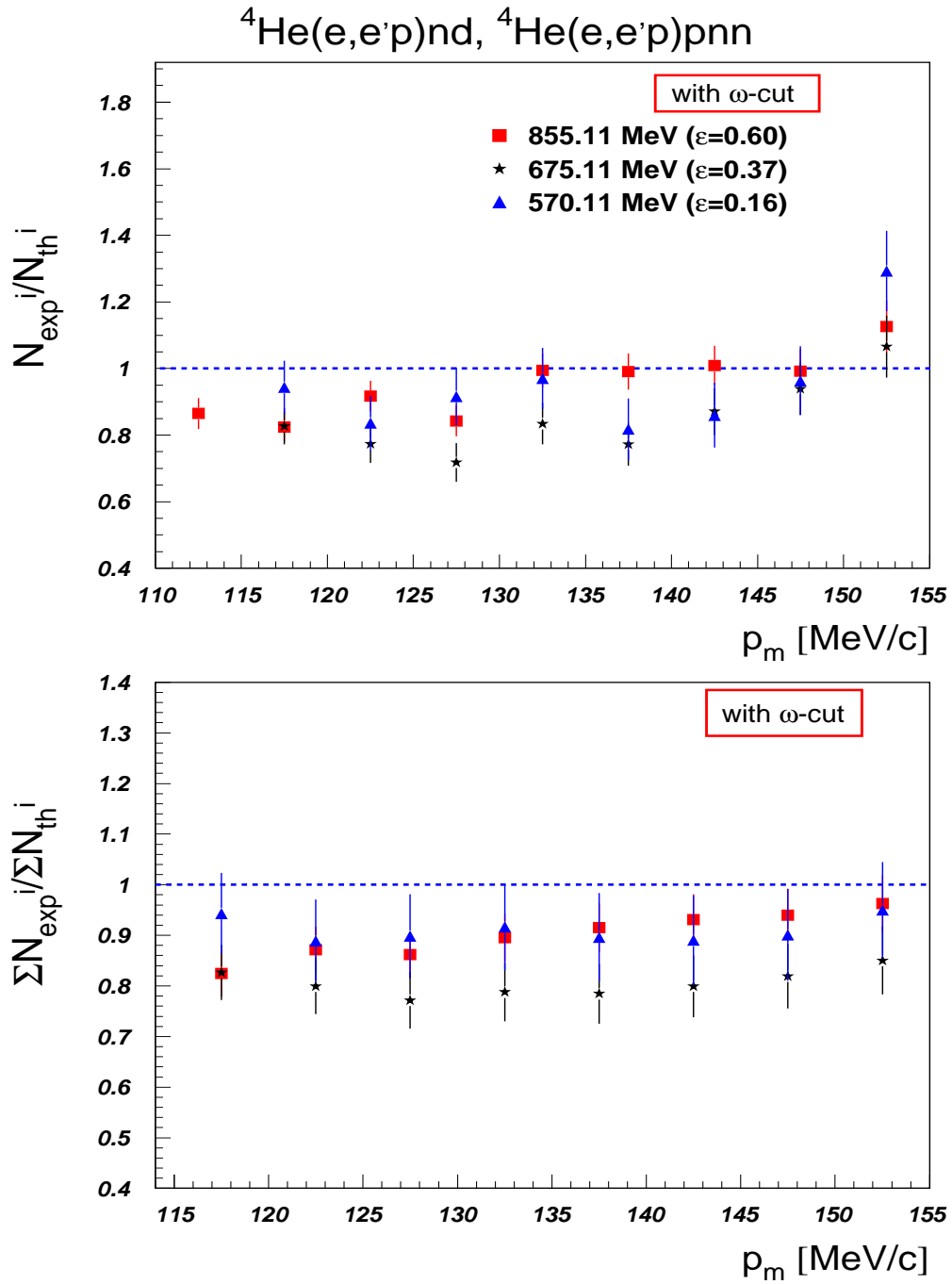


Figure 6.29: Ratio for the experimental and theoretical momentum distributions as a function of the missing momentum

fluctuates from point to point. This dependence can be better observed in Figure 6.27, where the $\sum \langle N \rangle_{exp}^i / \sum \langle N \rangle_{th}^i$ (bottom picture) and $\langle N \rangle_{exp}^i / \langle N \rangle_{th}^i$ values are shown. The integral value $\langle N \rangle$ calculated for the three kinematics and the theoretical value are given in Figure 6.26. When the ω -cut is not used, $\langle N \rangle$ value is higher by approximately 20 % for the Kinematic 1 ($\epsilon = 0.16$) compare to the integral value measured for the Kinematic 3 ($\epsilon = 0.6$).

This strong ϵ -dependence completely disappears in the data obtained with the ω -cut. In Figure 6.28 (bottom picture), no systematic ϵ -dependence can be observed. The integral $\langle N \rangle$ value is also independent of the virtual-photon polarization (see Figure 6.26).

In Figures 6.24, 6.24 and 6.26 measured-proton-momentum distributions are also compared to the experimental results obtained earlier in Mainz and mentioned in reference [23]. The agreement between those results and our measurements is good, but the large statistical uncertainty for the data points from [23] are not allowed more detailed study. In general, results measured at MAMI by Florizone are lower by the 10-20 % compare to our measurements.

Without the ω -cut the experimental momentum distributions are approximately 10-20 % lower than the theory predictions as shown in Figure 6.27. This cuts removes almost all data dependence on ϵ and increases the $\langle N \rangle_{exp}^i / \langle N \rangle_{th}^i$ up to 0.9 - 0.95.

This number is approximately 10 % higher than that for the two-body breakup channel, where the experimental data points were approximately 20 % lower than the theoretical predictions.

6.4 Systematic error estimate

The calculation of the systematic error due to the normalization procedure was described in Chapter 4. It consists of a number of systematic uncertainties, and

is given in Table 4.6. The helium-target density value for elastic scattering, which includes this systematic error, was used to calculate the helium-target density for the individual (e,e'p) runs. The systematic uncertainty for the latest value includes, in addition, a statistical error for the number of events detected in Spectrometer C, and can be calculated from Equation 5.5. The next step is to calculate the systematic normalization error for each kinematic according to Equation 5.6.

The total systematic error ($\pm\Delta\sigma/\sigma$) in the (e,e'p) cross-section value due to the helium-density calculation procedure was approximately 2.0 %, 2.2 % and 2.2 % for Kinematic 1, 2 and 3 respectively.

The other systematic uncertainties were insignificant. The uncertainty in total charge collected at the target and the coincidence dead-time error were of the order of 0.1 % each, and were neglected. The sensitivity of the final cross section to the uncertainty in the beam energy and target-position error must be also small, because even for the elastic measurements characterized by a strong angular dependence these errors were of the order of 0.2 - 0.5 %. The contribution of the uncertainty due to the software angular cuts was taken the same as for the elastic measurements on *He* ($\sim 0.4 - 0.6$ %).

Thus, the full systematic uncertainty ($\pm\Delta\sigma/\sigma$) for the (e,e'p) cross section measured in this experiment is 2.2-2.4 %.

Chapter 7

Conclusion

A high-resolution study of the ${}^4\text{He}(e, e'p)$ reaction was performed. The high resolution of the Mainz spectrometers made it possible to study the two-body breakup and continuum reaction channels separately. These measurements are also characterized by a very low background, and therefore high data quality. The systematic error estimate for these measurements is $\pm 2.2 - 2.4\%$. The following results were obtained:

- Two independent analysis methods (AEEXB simulations and RADCOR unfolding) give a similar result concerning the problem of "unexpectedly large" cross section for proton knockout observed in earlier (e,e'p) experiments in the high missing-energy region (see Chapter 1). No such phenomenon was observed in our measurements as shown in Figures 6.2, 6.21 and 7.1a. A large strength observed in the raw (E_m, p_m) spectra in the high missing-energy region was formed by the radiative tails from the lower missing-energy regions. The significant non-zero strength seen in the high missing-energy region (and also close to the phase-space boundaries) after the RADCOR unfolding belongs mostly to the external radiative tails from the outside of the detected (E_m, p_m) region.

- The 6-fold differential cross section for the continuum channels of the ${}^4\text{He}(e, e'p)$ reaction were measured in the missing-energy range $25 \leq E_m \leq 45 - 50 \text{ MeV}$. The $(e, e'p)$ cross section for $E_m \geq 50 \text{ MeV}$ shows no significant deviation from the model based on the theoretical spectral function from ref. [55]. At these missing energies the measured strength is small and dominated by the radiative background.
- The Rosenbluth separation was performed for the two-body breakup cross section averaged over the missing-momentum range $125 \leq p_m \leq 165 \text{ MeV}/c$. The experimental ratio for the longitudinal and transverse response functions was calculated and compared to the prediction from the σ_{cc1} off-shell $e - p$ model of de Forest. The σ_L/σ_T value was 0.71 ± 0.025 , which is 33 % lower than that from the σ_{cc1} model. After including the systematic error the σ_L/σ_T value was 0.73 ± 0.1 (31 % \pm 13 % below the prediction based on the σ_{cc1} model as shown in Figure 7.1c). This value is in a good agreement with the earlier results presented by Ducret *et al.* [8], where the reduction of the L/T ratio compare to the theory prediction was observed for the similar momentum transfer \vec{q} values.
- The proton-triton momentum distributions also show systematic ϵ -dependence, with a 6.6 % difference for the integral $\langle N \rangle$ value between the kinematics with the smallest and largest ϵ .
- The measured proton-triton momentum distributions were found to be 15 - 25 % below the predictions from different theoretical models.
- The Rosenbluth separation was also performed for the continuum cross section averaged over the missing-momentum range $115 \leq p_m \leq 155 \text{ MeV}/c$ for a number of the missing-energy values. The experimental ratio for the longitudinal and transverse responses was calculated and compared to the prediction from the σ_{cc1} off-shell $e - p$ model of de Forest. The σ_L/σ_T value was found

to be in good agreement with the σ_{cc1} model at low missing energies. In the high missing-energy region of the measured (e,e'p) cross section, the L/T ratio is significantly reduced compared to the model as shown in Figure 7.1c. The ratio $(\sigma_L/\sigma_T)^{exp}/(\sigma_L/\sigma_T)^{cc1}$ was found to be (for the analysis with the different missing-energy bin size): 0.67 ± 0.21 ($E_m = 40 \text{ MeV}$), 0.59 ± 0.34 ($E_m = 42.5 \text{ MeV}$), and 0.43 ± 0.35 ($E_m = 43 \text{ MeV}$).

- The distorted spectral function was measured in the missing-energy range $25 \leq E_m \leq 45 - 50 \text{ MeV}$ for all three kinematics. It was found that the spectral function shows no significant deviation from the theoretical spectral function (ref. [55]) at $E_m \geq 50 \text{ MeV}$ (Fig. 6.21).
- No significant ϵ -dependence was observed for the spectral functions calculated for the different kinematics (see Figure 7.1b).
- No ϵ -dependence was observed for the proton-momentum distributions for the continuum channel, when comparison is done for the same range of the energy-transfer values. This result does not disagree with the Rosenbluth separation, where the deviation from the σ_{cc1} model was observed. In fact, the weight of the events from the high missing-energy region is not large in the total integral value. The Rosenbluth separation thus permitted the L/T cross section dependence to be studied in a more detailed way.
- The proton-momentum distributions for the continuum channel were 4 - 15 % below the theory prediction, when comparison is done for the same range of the energy-transfer values.

In short, we can conclude: the majority of ϵ -dependence seen in the (e,e'p) cross section for different kinematics is removed by division by the elementary $e - p$ cross section in $cc1$ prescription of de Forest. A small remaining ϵ -dependence, which probably indicates excess transverse strength is difficult to interpret uniquely due

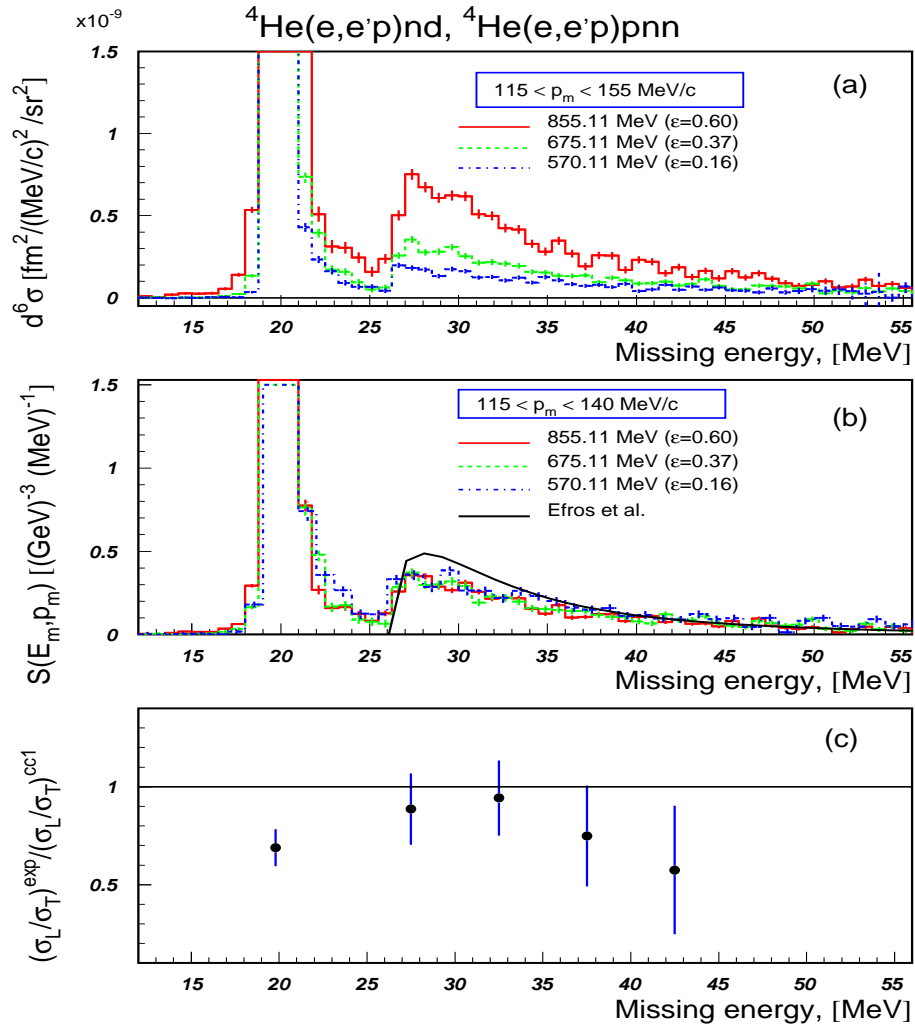


Figure 7.1: Results shown as a function of missing energy. (a) Six-fold differential cross section for the three values of the virtual-photon polarization ϵ in the missing-momentum range from 115 to 155 MeV/c. (b) Spectral function. (c) The ratio σ_L/σ_T (both the 2-body and continuum channels)

to the relatively large systematic uncertainties. Further attempts must be done to reduce the systematic uncertainty due to the absolute data normalisation and radiative unfolding procedure. More complete theoretical calculations that include additional effects beyond PWIA (FSI, meson exchange currents and others) are also

required to make more detailed comparison between the experimental and theoretical results.

Appendix A

A.1 GEANT model of the collimators

This part of the Appendix describes the GEANT models used to simulate the collimators of the spectrometers in the new GEANT Monte-Carlo. The general structure of the program is given in the Appendix C. Detailed description of the collimators shape, and the computer codes used to generate the geometrical equivalents of the collimators are included. The formulas used to calculate the geometrical and angular constrains of the collimator of the Spectrometer B are also presented.

The shape of the collimators is quite complicated with the multiple faces in the horizontal and vertical directions. In the new GEANT Monte-Carlo code described in detail in Appendix C the collimators of Spectrometer A and B were both simulated using the GEANT geometry package (reference [44]), with input parameters for the real geometrical dimensions obtained from the original technical drawings.

A.1.1 The collimator of Spectrometer A

This collimator with an acceptance angle of 21 msr was successfully described with 7 trapezoids of a *TRD2* type (see reference [44]) which have x and y dimensions both varying along the z axis as shown in Figure A.1. Both collimators were manufactured from a heavy alloy containing 95 % of Tungsten with a density of approximately 18 g/cm^3 , which was reproduced in the simulations. All trapezoids were

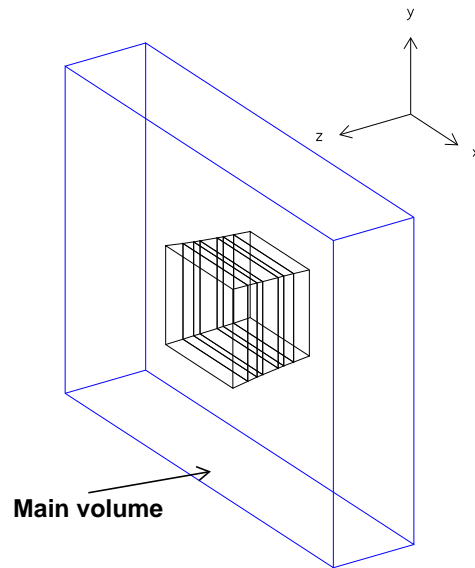


Figure A.1: The collimator of Spectrometer A, the view from the spectrometer side filled with the vacuum and positioned inside the main volume filled with Tungsten. (Figure A.1).

A.1.2 The collimator of Spectrometer B

This collimator consists of four independent parts which can be moved in order to set desired vertical angular acceptance values between 0 and 70 mrad and horizontal angular acceptance between 0 and 20 mrad. The geometry of the collimator is described in details in Figure A.3, where the θ and ϕ are the nominal values of the vertical and horizontal acceptance respectively. By using the relations between the angular acceptance of the collimator and its geometrical dimensions (shown in Figure A.3), an exact model of the collimator was implemented in the GEANT simulation program. Figures A.4 and A.5 show how both the horizontal and vertical components of the collimator were simulated by a number of trapezoids of *TRD2* type.

```

Main volume
PAR(1) = 40/2. ! x/2
PAR(2) = 30/2. ! y/2
PAR(3) = 8./2. ! z/2
call GSVOLU('AKOL','BOX ',2,PAR,3,IVOL)
rtf(1) = 60.55
rtf(2) = t0es
rtf(3) = f0es
call XYZRTP(xyzlab,rtf(1))
call GSPOS('AKOL',1,'BOX0',x,y,z,1,'ONLY')
1st volume
PAR(1) = 8.7211/2. ! x/2 at -z
PAR(2) = 8.8273 /2. ! x/2 at +z
PAR(3) = 7.9554/2. ! y/2 at -z
PAR(4) = 8.1511/2. ! y/2 at +z
PAR(5) = 1.600/2. ! z/2
call GSVOLU('HOA1','TRD2',3,PAR,5,IVOL)
x = 0.
y = 0.
z = -3.2
call GSPOS('HOA1',1,'AKOL',x,y,z,0,'ONLY')
2nd volume
PAR(1) = 8.8273/2. ! x/2 at -z
PAR(2) = 8.9356/2. ! x/2 at +z
PAR(3) = 8.1511/2. ! y/2 at -z
PAR(4) = 8.2734/2. ! y/2 at +z
PAR(5) = 1./2. ! z/2
call GSVOLU('HOA2','TRD2',3,PAR,5,IVOL)
x = 0.
y = 0.
z = -1.9
call GSPOS('HOA2',1,'AKOL',x,y,z,0,'ONLY')
3rd volume
PAR(1) = 8.9356/2.
PAR(2) = 9.0006/2.
PAR(3) = 8.2734/2.
PAR(4) = 8.3573/2.
PAR(5) = 0.6/2.
call GSVOLU('HOA3','TRD2',3,PAR,5,IVOL)
x = 0.
y = 0.
z = -1.1
call GSPOS('HOA3',1,'AKOL',x,y,z,0,'ONLY')
4th volume
PAR(1) = 9.0006/2.
PAR(2) = 9.2412/2.
PAR(3) = 8.3573/2.
PAR(4) = 8.5811/2.
PAR(5) = 1.6/2.
call GSVOLU('HOA4','TRD2',3,PAR,5,IVOL)
x = 0.
y = 0.
z = 0.
call GSPOS('HOA4',1,'AKOL',x,y,z,0,'ONLY')
5th volume
PAR(1) = 9.2412/2.
PAR(2) = 9.3568/2.
PAR(3) = 8.5811/2.
PAR(4) = 8.6650/2.
PAR(5) = 0.6/2.
call GSVOLU('HOA5','TRD2',3,PAR,5,IVOL)
x = 0.
y = 0.
z = 1.1
call GSPOS('HOA5',1,'AKOL',x,y,z,0,'ONLY')
6th volume
PAR(1) = 9.3568/2.
PAR(2) = 9.5494/2.
PAR(3) = 8.6650/2.
PAR(4) = 8.8224/2.
PAR(5) = 1./2.
call GSVOLU('HOA6','TRD2',3,PAR,5,IVOL)
x = 0.
y = 0.
z = 1.9
call GSPOS('HOA6',1,'AKOL',x,y,z,0,'ONLY')
7th volume
PAR(1) = 9.5494/2.
PAR(2) = 9.9253/2.
PAR(3) = 8.8224/2.
PAR(4) = 9.0743/2.
PAR(5) = 1.6/2.
call GSVOLU('HOA7','TRD2',3,PAR,5,IVOL)
x = 0.
y = 0.
z = 3.2
call GSPOS('HOA7',1,'AKOL',x,y,z,0,'ONLY')

```

Figure A.2: GEANT simulation of the collimator of Spectrometer A

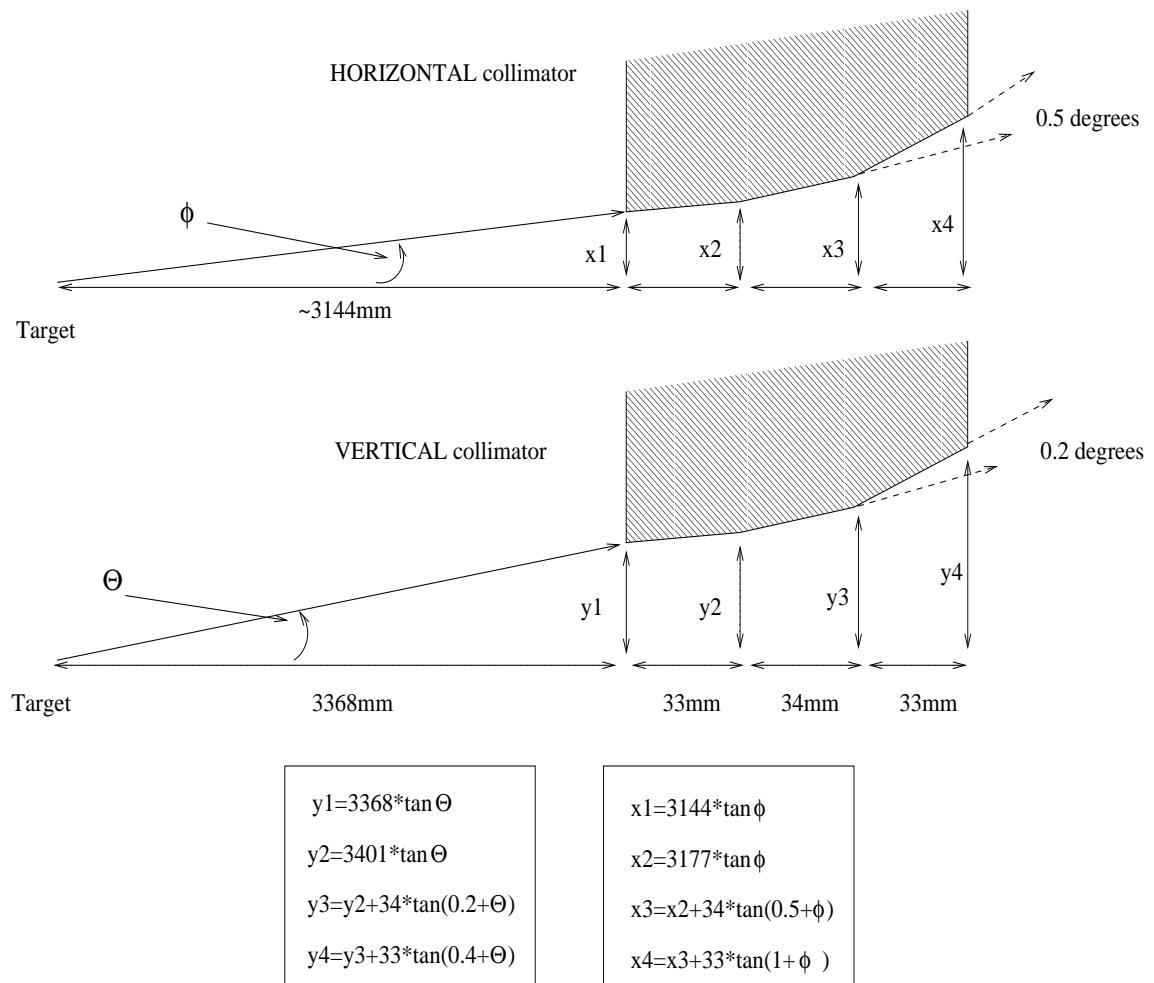


Figure A.3: The geometry of the collimator of Spectrometer B, where θ and ϕ are the angular acceptance values for a point target

```

Main volume
xtop=336.8*tan(colli(3)/1000.)
xbott=336.8*tan(colli(4)/1000.)
PAR(1)= 60./2. ! x/2
PAR(2)= 90./2. ! y/2
PAR(3)= 10./2. ! z/2
call GSVOLU('BKOV', 'BOX ',3,PAR,3,IVOL)
rtf(1)= 336.8+5.0 !dist. to the middle of vert.colli
rtf(2)= t0ps
rtf(3)= f0ps
call XYZRTP(xyzlab,rtf(1))
call GSPOS('BKOV',1,'BOX0',x,y,z,2,'ONLY')
1st Top part
PAR(1)=50./2.
PAR(2)=50./2.
PAR(3)=20./2.
PAR(4)=PAR(3)-3.3*tan(colli(3)/1000.)
PAR(5)=3.3/2.
call GSVOLU('HBT1', 'TRD2 ',2,PAR,5,IVOL)
x=0.
y=xtop+20./2.
z=-5.+3.3/2.
call GSPOS('HBT1',1,'BKOV',x,y,z,0,'ONLY')
2nd Top part
PAR(1)=50./2.
PAR(2)=50./2.
PAR(3)=PAR(4)
PAR(4)=PAR(3)-3.4*tan(colli(3)/1000.+0.2*PI/180.)
PAR(5)=3.4/2.
call GSVOLU('HBT2', 'TRD2 ',2,PAR,5,IVOL)
x=0.
y=y
z=0.
call GSPOS('HBT2',1,'BKOV',x,y,z,0,'ONLY')
3rd Top part
PAR(1)=50./2.
PAR(2)=50./2.
PAR(3)=PAR(4)
PAR(4)=PAR(3)-3.3*tan(colli(3)/1000.+0.4*PI/180.)
PAR(5)=3.3/2.

call GSVOLU('HBT3', 'TRD2 ',2,PAR,5,IVOL)
x=0.
y=y
z=5.-3.3/2.
call GSPOS('HBT3',1,'BKOV',x,y,z,0,'ONLY')
1st Bottom part
PAR(1)=50./2.
PAR(2)=50./2.
PAR(3)=20./2.
PAR(4)=PAR(3)-3.3*tan(colli(4)/1000.)
PAR(5)=3.3/2.
call GSVOLU('HBB1', 'TRD2 ',2,PAR,5,IVOL)
x=0.
y=-xbott-20./2.
z=-5.+3.3/2.
call GSPOS('HBB1',1,'BKOV',x,y,z,0,'ONLY')
2nd Bottom part
PAR(1)=50./2.
PAR(2)=50./2.
PAR(3)=PAR(4)
PAR(4)=PAR(3)-3.4*tan(colli(4)/1000.+0.2*PI/180.)
PAR(5)=3.4/2.
call GSVOLU('HBB2', 'TRD2 ',2,PAR,5,IVOL)
x=0.
y=y
z=0.
call GSPOS('HBB2',1,'BKOV',x,y,z,0,'ONLY')
3rd Bottom part
PAR(1)=50./2.
PAR(2)=50./2.
PAR(3)=PAR(4)
PAR(4)=PAR(3)-3.3*tan(colli(4)/1000.+0.4*PI/180.)
PAR(5)=3.3/2.
call GSVOLU('HBB3', 'TRD2 ',2,PAR,5,IVOL)
x=0.
y=y
z=5.-3.3/2.
call GSPOS('HBB3',1,'BKOV',x,y,z,0,'ONLY')

```

Figure A.4: GEANT simulation of the vertical collimator of Spectrometer B

```

Main volume
xleft=314.4*tan(colli(1)/1000.)
xrigh=314.4*tan(colli(2)/1000.)
PAR(1)= 60/2. ! x/2
PAR(2)= 70/2. ! y/2
PAR(3)= 10/2. ! z/2
call GSVOLU('BKOH', 'BOX ',3,PAR,3,IVOL)
rtf(1)= 314.4+5.0 ! distance to the middle of horiz.colli
rtf(2)= t0ps
rtf(3)= f0ps
call XYZRTP(xyzlab,rtf(1))
call GSPOS('BKOH',1,'BOX0',x,y,z,2,'ONLY')
1st left part
PAR(1)=20./2.
PAR(2)=PAR(1)-3.3*tan(colli(1)/1000.)
PAR(3)=57./2.
PAR(4)=PAR(3)
PAR(5)=3.3/2.
call GSVOLU('HBL1','TRD2 ',2,PAR,5,IVOL)
x=-xleft-10.
y=0.
z=-5.+3.3/2.
call GSPOS('HBL1',1,'BKOH',x,y,z,0,'ONLY')
2nd left part
PAR(1)=PAR(2)
PAR(2)=PAR(1)-3.4*tan(colli(1)/1000.+0.5*PI/180.)
PAR(3)=57./2.
PAR(4)=57./2.
PAR(5)=3.4/2
call GSVOLU('HBL2','TRD2 ',2,PAR,5,IVOL)
x=x
y=0.
z=0.
call GSPOS('HBL2',1,'BKOH',x,y,z,0,'ONLY')
3rd left part
PAR(1)=PAR(2)
PAR(2)=PAR(1)-3.3*tan(colli(1)/1000.+1.*PI/180.)
PAR(3)=57./2.
PAR(4)=57./2.
PAR(5)=3.3/2.

call GSVOLU('HBL3','TRD2 ',2,PAR,5,IVOL)
x=x
y=0.
z=5.-3.3/2.
call GSPOS('HBL3',1,'BKOH',x,y,z,0,'ONLY')
1st right part
PAR(1)=20./2.
PAR(2)=PAR(1)-3.3*tan(colli(2)/1000.)
PAR(3)=57./2.
PAR(4)=PAR(3)
PAR(5)=3.3/2.
call GSVOLU('HBR1','TRD2 ',2,PAR,5,IVOL)
x=xrigh+10.
y=0.
z=-5.+3.3/2.
call GSPOS('HBR1',1,'BKOH',x,y,z,0,'ONLY')
2nd right part
PAR(1)=PAR(2)
PAR(2)=PAR(1)-3.4*tan(colli(2)/1000.+0.5*PI/180.)
PAR(3)=57./2.
PAR(4)=PAR(3)
PAR(5)=3.4/2.
call GSVOLU('HBR2','TRD2 ',2,PAR,5,IVOL)
x=x
y=0.
z=0.
call GSPOS('HBR2',1,'BKOH',x,y,z,0,'ONLY')
3rd right part
PAR(1)=PAR(2)
PAR(2)=PAR(1)-3.3*tan(colli(2)/1000.+1.*PI/180.)
PAR(3)=57./2.
PAR(4)=PAR(3)
PAR(5)=3.3/2.
call GSVOLU('HBR3','TRD2 ',2,PAR,5,IVOL)
x=x
y=0.
z=5.-3.3/2.
call GSPOS('HBR3',1,'BKOH',x,y,z,0,'ONLY')

```

Figure A.5: GEANT simulation of the horizontal collimator of Spectrometer B

Appendix B

B.1 Monte-Carlo for calculations of ${}^{3,4}\text{He}(e, e')$ elastic cross sections

B.1.1 Overview

The new Monte-Carlo is the C++ code with two different operation modes, (see Figure B.1). In the first mode it calculates the cross section for elastic scattering from ${}^{3,4}\text{He}$ averaged over the acceptance of Spectrometer A or B, based on the known values of the helium form-factors from Equations 4.9 and 4.11. In the second mode it returns the effective solid angle of Spectrometer A or B dependent on different factors such as the beam rastering, extended target geometry, target cell offset and the non-trivial geometrical shape of the collimators.

The new Monte-Carlo code took advantage of the C++ variant of the CERN HBOOK libraries available in Mainz. These *HMBook* C++ libraries provide convenient graphical output of all required values in a format used by the Mainz COLA++ program. This feature makes control of the calculations much easier and more efficient.

slit #	x_i [cm]	y_i [cm]	R_0^i [cm]
1	4.3606	3.9777	56.55
2	4.4137	4.0756	58.15
3	4.4678	4.1367	59.15
4	4.5003	4.1787	59.75
5	4.6206	4.2906	61.35
6	4.6784	4.3325	61.95
7	4.7747	4.4112	62.95
8	4.9626	4.5371	64.55

Table B.1: The horizontal x_i and vertical y_i dimensions of the 21 *msr* collimator of Spectrometer A and the corresponding distances R_0^i from the target

B.1.2 Events generation

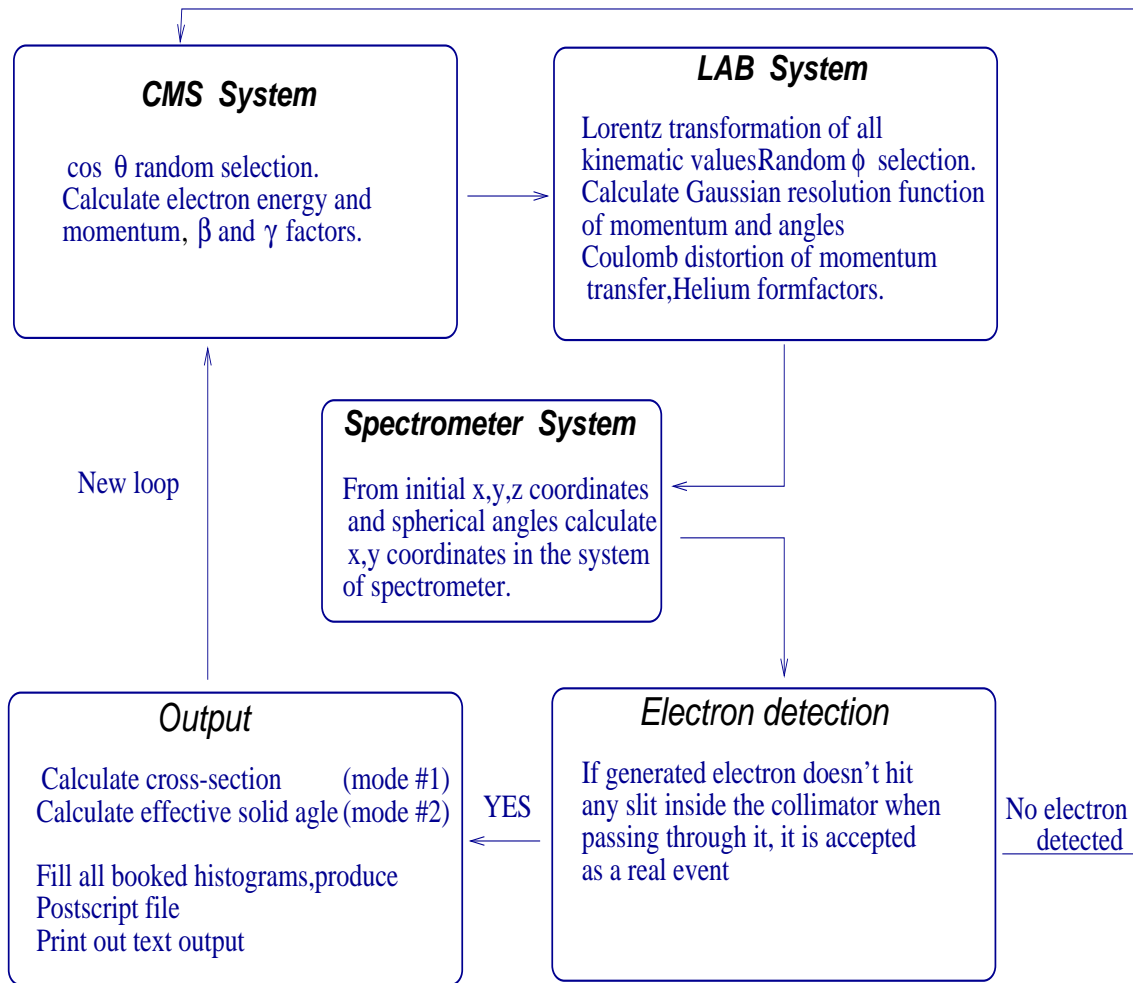
The spectrometer effective solid angle Ω_{eff} was determined as a fraction of a total solid angle Ω_{tot} sampled in the simulation:

$$\Omega_{eff} = \frac{N_{det} \cdot \Omega_{tot}}{N_{tot}} \quad (\text{B.1})$$

where N_{det} is the number of events accepted by the spectrometer, Ω_{tot} and N_{tot} are the full solid angle and the number of events entering this solid angle. Ω_{tot} was limited by the range of preselected spherical angles θ and ϕ to save the CPU time:

$$\Omega_{tot} = 4\pi \frac{(\cos(\theta_{min}) - \cos(\theta_{max}))}{2} \frac{(\phi_{max} - \phi_{min})}{360} \quad (\text{B.2})$$

The cross section calculations are made in the center-of-mass system and the Lorentz transformation is used to obtain the corresponding values in the laboratory system. The Ω_{eff} calculations were done completely in the laboratory frame.

Figure B.1: Simplified structure of the *DUMP* Monte-Carlo code

B.1.3 Simulation of physical processes

In order to obtain values for the cross section and effective solid angle that were as close as possible to reality, the following setup details and corrections were included in the calculations:

- beam rastering amplitudes;
- spherical shape of the target cell;
- possibility of changing the position of the target cell along the beam line;
- possibility of applying cuts on both θ_{tgt} and ϕ_{tgt} angles, as is done in the analysis of the experimental data;
- average beam-energy losses in the helium gas and Al walls.

There were between 70 and 600 KeV for helium of density $0.04 g/cm^3$ depending on the vertex position inside the target cell.

- Coulomb distortion of momentum transfer.

When electrons approach the nucleus, the Coulomb field accelerates them so that a larger momentum transfer occurs. In the experimental form factors, used to make predictions of the elastic cross section, the effect of Coulomb distortion was taken into account. During the analysis of our experimental data, this effect remains and therefore distortion of "pure" form factors by the nuclear Coulomb field was accounted for by introducing an effective momentum transfer q_{eff} (see ref. [32]). This resulted in $\sim 2\%$ reduction of the calculated cross section:

$$q_{eff} = q \cdot \left(1 + \frac{1.5 Z \alpha \hbar c}{p_{beam} R_{eq}}\right) \quad (B.3)$$

where $R_{eq} = 1.12 \cdot A^{1/3}$ is the equivalent radius of a hard sphere, q is the 3-momentum transfer [MeV], $\hbar c = 197.327$ [Mev fm], $\alpha = 1/137$, p_{beam} is the electron beam momentum [MeV] , $A=4$ and $Z=2$.

- the simulation of momentum and angle resolution by Gaussian distributions based on the experimental resolution of the spectrometers.

For these purposes the *gasdev* function obtained from reference [33], which gen-

erates a random Gaussian distribution with Mean=0 and $\sigma=1$ was used.

B.1.4 Particles tracking through the collimators

In the code, the shape of the 21 *msr* collimator of Spectrometer A was simulated by a number of slits of defined size, obtained from the original technical drawings. The geometry of the collimator of Spectrometer B was calculated each time using two input parameters for its vertical and horizontal acceptance as it is shown in Figure A.3.

The following algorithm was used to simulate the correct tracking of the electrons through a collimator. When an electron is passing through the collimator, the x and y coordinates in the spectrometer coordinate system are calculated for each slit of the collimator from the spherical θ_e and ϕ_e angles and the initial (x_w, y_w, z) position of the reaction vertex according to Equations B.6 and B.7. This calculation requires the introduction of two additional variables, θ_x and R_0^{corr} , defined in Equations B.4 and B.5.

$$\theta_x = \text{atan}(\tan(\theta_e)) \cdot \cos(\phi_0 - \phi_e) \quad (\text{B.4})$$

where ϕ_0 is equal to 180 degrees for Spectrometer A and 0 degrees for Spectrometer B. θ_x is in a reality a projection of θ_e on the horizontal $x - z$ plane. R_0^{corr} is a distance from the reaction vertex (x_w, y_w, z) to a particular slit of the collimator:

$$R_0^{corr} = R_0 - (z_{beam} + z_{abs}) \cdot \cos(\theta_0) - x_w \cdot \sin(\theta_0) \quad (\text{B.5})$$

where R_0 is a distance from the center of coordinates, where $(x_w = 0, y_w = 0, z = 0)$ to a particular slit of the collimator in the horizontal $x - z$ plane, θ_0 is the central scattering angle of the spectrometer, z_{beam} is the vertex position inside the target cell and z_{abs} is an absolute displacement of the target cell along the z axis. By using all these variable the horizontal x and vertical y coordinates in the system of coordinates of the spectrometers are calculated as:

$$x = R_0^{corr} \cdot \tan(\theta_x - \theta_0) - (z_{beam} + z_{abs}) \cdot \sin(\theta_0) + x_w \cdot \cos(\theta_0) \quad (\text{B.6})$$

$$y = \sqrt{(R_0^{corr})^2 + x^2} \cdot \sin(\theta_x) \cdot \tan(\phi_0 - \phi_e) + y_w \quad (\text{B.7})$$

The vertical θ_{spec} and horizontal ϕ_{spec} angles at the target in the spectrometers coordinate system were calculated as:

$$\theta_{spec} = \text{atan}(y/R_0^{corr}) \quad (\text{B.8})$$

$$\phi_{spec} = \theta_0 - \theta_x \quad (\text{B.9})$$

These two variables are used to place the cuts identical to those used during the analysis of the experimental data.

For each slit the absolute x and y coordinates in the spectrometers coordinate system were compared to the known geometrical dimensions corresponding to a particular slit of the collimator. The *true* event means the electron drift through a collimator volume without touching its walls.

B.1.5 Effective solid angle of the spectrometers

The solid angle of the spectrometers depends from the target position along the y_0 coordinate of the spectrometer. A shift of the target position causes a change of the absolute value of the spectrometer solid angle and the range of accessible horizontal and vertical angles. By using a realistic model of the collimators these changes were taken into account in calculating the elastic scattering cross sections from carbon and helium targets. The range of effective solid angles for Spectrometers A and B is shown in Figure B.2 as a function of y_0 . All the data points shown at the plot were calculated using the *DUMP* Monte-Carlo code.

The effective solid angle of the spectrometers for the extended targets shows only a minor dependence on y_0 . This is more evident for Spectrometer B, which has much longer distance from the target to the collimator compared to Spectrometer A. For Spectrometer A, the effective solid angle dependence, even for the maximum extended target length of $y_0 = 2.5 \text{ cm}$, is reduced by only $\sim 0.7 \%$ compared to its nominal value. In case of point targets, especially when the measured cross section

shows a strong angular dependence, changes of angular acceptance must be carefully taken into account.

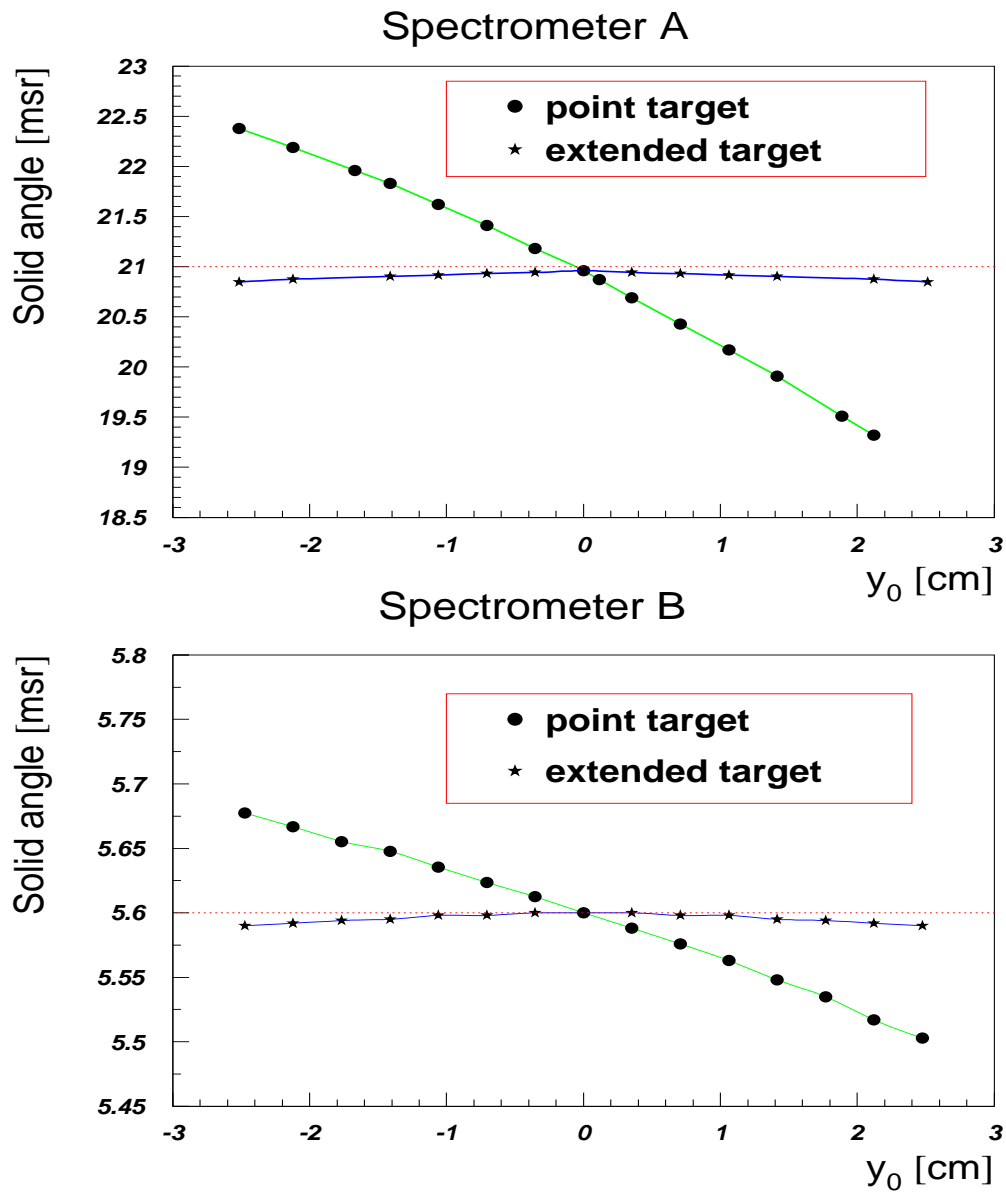


Figure B.2: The solid angle of Spectrometer A(B) as a function of the spectrometer y_0 coordinate in case of 21(5.6) msr collimator

Appendix C

C.1 GEANT Monte-Carlo code

C.1.1 Modeling of the experimental setup

As was explained in the Appendix A, realistic models of the collimators were developed to describe the complicated geometrical acceptance of Spectrometers A and B. The target cell was simulated as an *Al* cylinder filled with ^4He gas of density as used in the experiment. It was assumed that 0.012 *cm* of mylar, and an air of thickness of 6 *cm* (Spectrometer A) and 12 *cm* (Spectrometer B) were between the target and the spectrometers. The scattering chamber was simulated as an *Al* cylinder with a defined window size. It can be moved up and down by changing one parameter in the GEANT input file. This option was incorporated to study the effects of re-scattering from the scattering chamber windows. Details of the scattering chamber geometry are given in Figure C.1.

C.1.2 Operation modes

The new program can be used in the following modes:

- 1) The simulation of the two-body and continuum breakup reactions on ^3He and ^4He start from the *centre - of - mass* system (CMS).

In this mode the program generates only events allowed by the energy-momentum

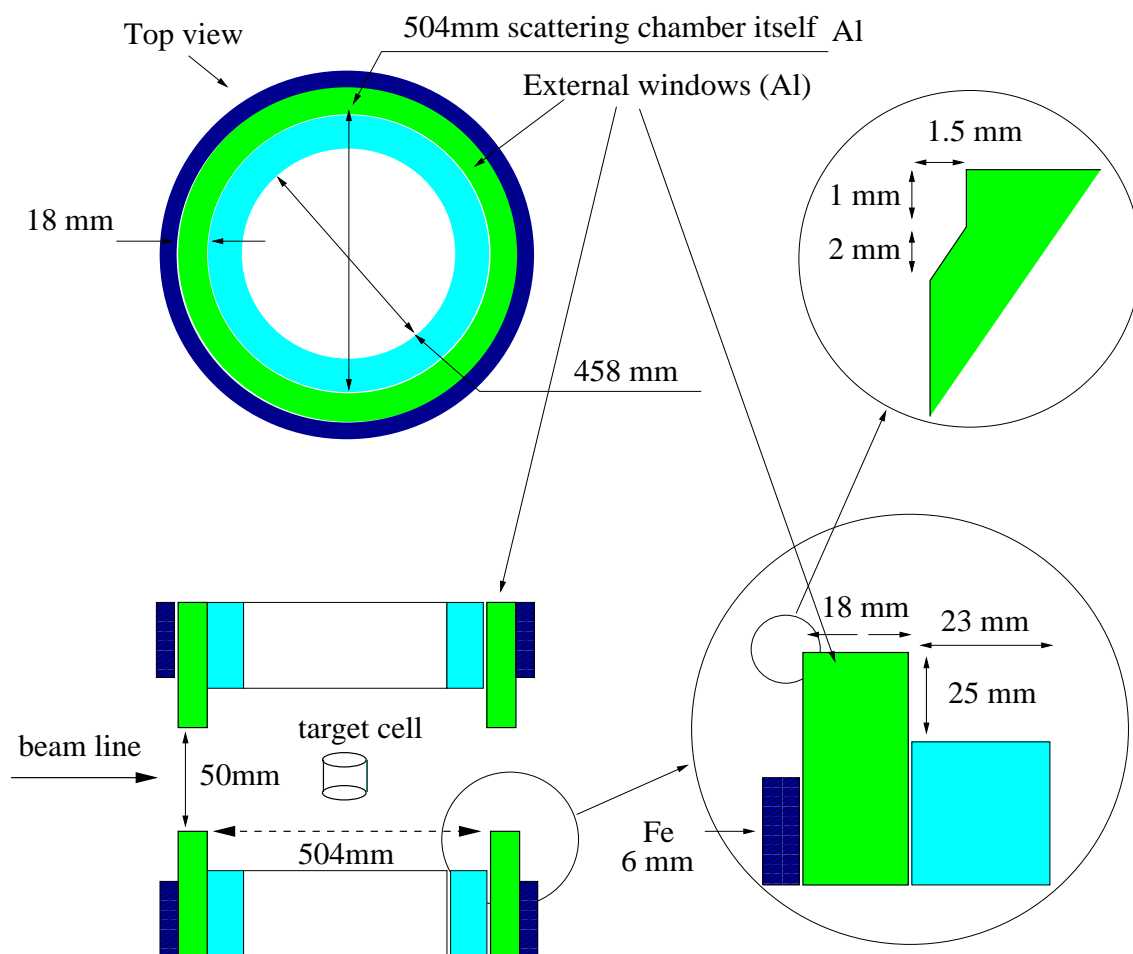


Figure C.1: Scattering chamber

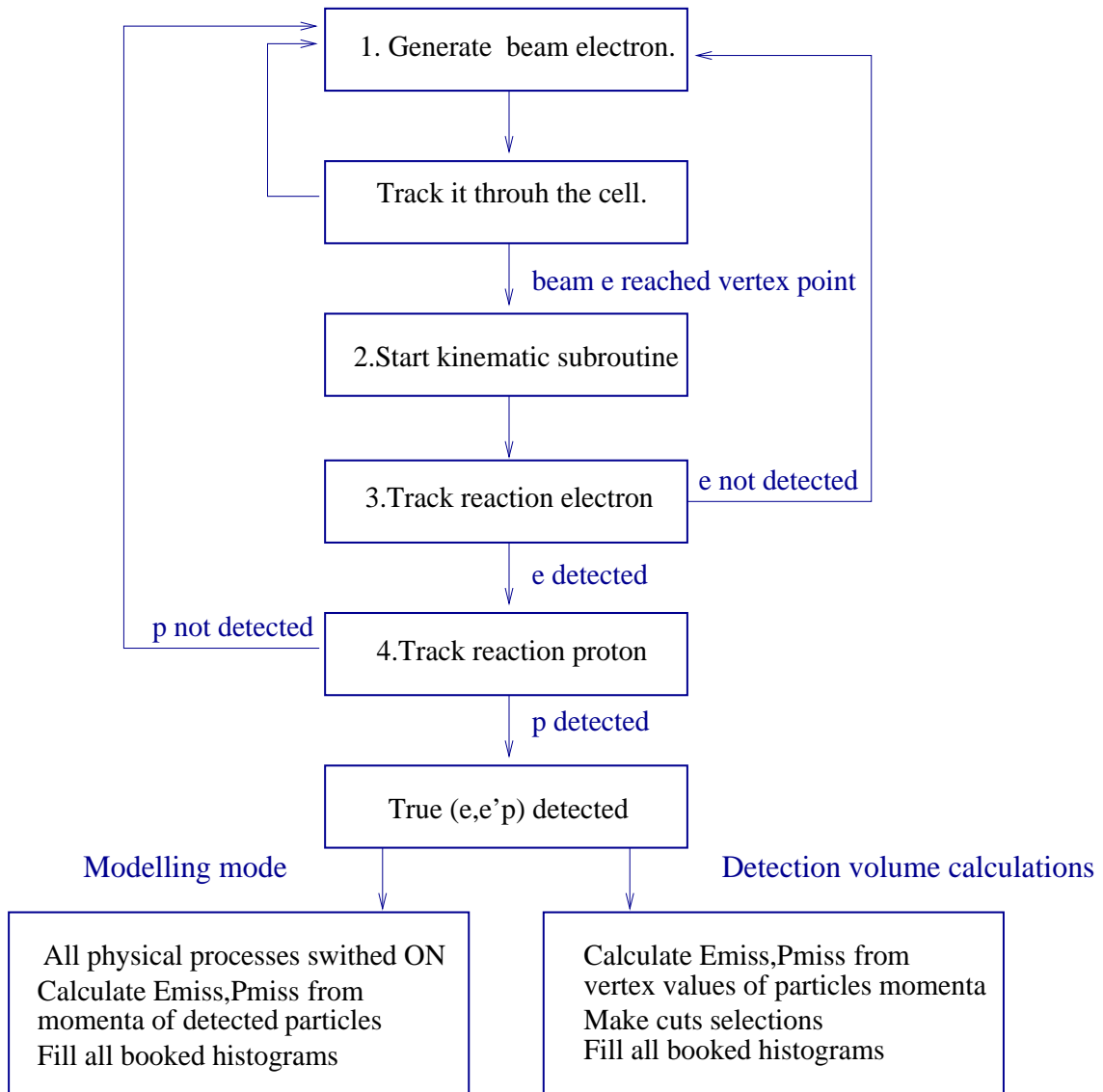
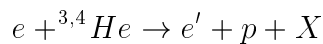


Figure C.2: General structure of the GEANT Monte-Carlo code

conservation and can be used to reaction and background simulations. All physical processes, including nuclear interactions, can be switched on by setting the corresponding parameters in the code input file. Internal bremsstrahlung also can be included by using the method of two external effective radiators, which placed before and after the reaction vertex (see reference [39]).

- 2) This mode is almost the same as the first mode, except that the electron arm of the reaction is simulated in the laboratory frame . Again, only events allowed by the energy-momentum conservation are generated. Further decay of the excited compound particle X from the ${}^{3,4}\text{He}(e, eX)$ reaction is simulated in the CMS. The mode was developed to save CPU time and improve a productivity of the code.
- 3) The detection-volume calculations were done completely in the laboratory frame for the reaction:



by uniformly sampling the 6-dimensional volume $dp_e dp_p d\Omega_e d\Omega_p$. In this mode, external and internal bremsstrahlung are switched off, and particle ionization losses are calculated as an average. Various software cuts identical to those used in the analysis of the experimental data can be applied. Calculations of the off-shell σ_{ep} cross section in the *cc1* prescription of de Forest are also included.

Appendix D

D.1 Helium-target density for the (e,e'p) runs

In this section, the luminosity information for the individual runs of ${}^4\text{He}(e, e'p)$ measurements done at MAMI during June of 1998 is presented. For each kinematic, two tables were used to give the information about the coincidence AB runs, and a single Spectrometer C data.

In Tables D.1, D.3 and D.5 the luminosity information for Spectrometer C is given. The values for total charge collected at the target Q^C , the data-acquisition deadtime, and the scaling factors for the single events detected in Spectrometer C are shown there. The helium-target density ρ_{He} and the statistical error for the number of single events detected in Spectrometer C are also included. More information about these values can be find in Chapter 5.

In Tables D.2, D.4 and D.6 the total charge collected at the target for the coincidence AB events and the coincidence dead-time values are shown. In addition, the thickness of the helium target after the cut ($\pm 2\text{ cm}$) on z -target coordinate is included.

The information included in these tables is sufficient to normalize the experimental yield, and calculate the cross-section values.

Run number	Q^C [mC]	deadtime [%]	Scaling	N_{He}^{corr}	ρ_{He} [g/cm ³]	ΔN_{He}^{corr} [%]
980618151844	95.859	2.0	25	12911.7	0.037810	0.45
980618161729	89.781	1.8	23	12997.4	0.038061	0.44
980618171815	89.584	1.9	23	13070.4	0.038275	0.44
980618181907	89.522	1.9	23	13083.8	0.038314	0.44
980618192129	92.623	1.9	23	12978.0	0.038005	0.44
980618203226	89.660	1.9	23	13006.6	0.038088	0.44
980618213309	90.581	1.9	23	13036.3	0.038175	0.44
980618223435	93.086	1.9	23	12970.8	0.037983	0.44
980618233733	36.511	1.9	23	13066.2	0.038263	0.70

Table D.1: Helium-target density at $E_{beam} = 570.11 MeV$

Run number	Q^{AB} [mC]	deadtime %	ρ_{He} [mg/cm ²]
980618151844	95.856	6.0	151.24
980618161729	89.778	5.0	152.24
980618171815	89.589	5.0	153.10
980618181907	89.519	5.0	153.26
980618192129	92.628	5.0	152.02
980618203226	89.673	5.0	152.35
980618213309	90.584	5.0	152.70
980618223435	93.084	5.0	151.93
980618233733	36.514	5.0	153.05
Total	767.225	5.125	152.38

Table D.2: Helium-target thickness at $E_{beam} = 570.11 MeV$

Run number	Q^C [mC]	Deadtime [%]	Scaling	N_{He}^{corr}	ρ_{He} [g/cm ³]	ΔN_{He}^{corr} [%]
980620133354	89.379	1.8	20	11275.7	0.038055	0.45
980620143509	89.637	1.8	20	11185.2	0.037749	0.45
980620153604	89.328	1.8	20	11251.7	0.037974	0.45
980620163743	92.394	1.8	20	11244.2	0.037949	0.44
980620174037	67.531	1.8	20	11295.5	0.038122	0.51
980620184440	87.499	1.8	20	11212.7	0.037842	0.45
980620195512	34.667	1.8	20	11341.5	0.038277	0.71
980620202218	39.746	1.8	20	11246.3	0.037955	0.67
980620205440	20.187	1.5	20	11333.6	0.038250	0.93
980620214002	54.948	1.6	20	11362	0.038346	0.57

Table D.3: Helium-target density at $E_{beam} = 675.11 MeV$

Run number	Q^{AB} [mC]	Deadtime %	ρ_{He} [mg/cm ²]
980620133354	89.385	7.5	152.2
980620143509	89.651	7.5	151.0
980620153604	89.332	7.5	151.9
980620163743	92.399	7.5	151.8
980620174037	67.533	7.5	152.5
980620184440	87.502	7.5	151.4
980620195512	34.671	7.6	153.1
980620202218	39.749	7.5	151.8
980620205440	20.194	6.9	153.0
980620214002	54.947	6.9	153.4
Total	665.363	7.4	152.0

Table D.4: Helium-target thickness at $E_{beam} = 675.11 MeV$

Run number	Q^C [mC]	Deadtime [%]	Scaling	N_{He}^{corr}	ρ_{He} [g/cm ³]	ΔN_{He}^{corr} [%]
980617044906	64.076	1.8	12	6054.85	0.038691	0.56
980617053232	45.233	1.8	12	6118.67	0.039099	0.66
980617060332	43.384	1.7	12	6071.33	0.038796	0.68
980617074433	45.223	1.7	12	6094.29	0.038943	0.67
980617081518	45.349	1.7	12	6066.06	0.038762	0.67
980617084825	45.897	1.7	12	6087.98	0.038903	0.66
980617092758	45.177	1.7	12	6065.73	0.038760	0.67
980617101452	47.124	1.7	12	6058.84	0.038716	0.65
980617110437	45.878	1.8	12	6104.03	0.039005	0.66
980617114913	45.266	1.7	12	6118.08	0.039095	0.66
980617122003	44.738	1.7	12	6103.54	0.039002	0.67

Table D.5: Helium-target density at $E_{beam} = 855.11 MeV$

Run number	Q^{AB} [mC]	Deadtime %	ρ_{He} [mg/cm ²]
980617044906	64.090	14.1	154.764
980617053232	45.254	14.1	156.396
980617060332	43.397	14.2	155.184
980617074433	45.242	14.1	155.772
980617081518	45.359	14.1	155.048
980617084825	45.922	14.2	155.612
980617092758	45.189	14.0	155.040
980617101452	47.147	14.4	154.864
980617110437	45.894	14.1	156.020
980617114913	45.274	14.1	156.380
980617122003	44.755	14.0	156.008

Table D.6: Helium-target thickness at $E_{beam} = 855.11 MeV$

Bibliography

- [1] γ -dependence of Response-Function Separations on ${}^{3,4}\text{He}$ for $0 \leq E_{\text{miss}} \leq 100 \text{ MeV}$, Proposal A1/3-96, Institut fuer Kernphysik, Mainz University, unpublished (<http://wwwa1.kph.uni-mainz.de/A1/proposals.html>)
- [2] J. J. van Leeuwe *et al*, High missing-momentum components in ${}^4\text{He}$ studied with the (e,e'p) reaction, Proceedings of the 15th European Conf. on Few-Body Problems in Physics, Peniscola, 1995
- [3] R. W. Lourie *et al*, Phys. Rev. Lett. **56**, 2364 (1986)
- [4] L. B. Weinstein *et al*, Phys. Rev. Lett. **64**, 1646 (1990)
- [5] L. J. H. M. Kester *et al*, Phys. Rev. Lett. **B366**, 44 (1996)
- [6] P. E. Ulmer *et al*, Phys. Rev. Lett. **59**, 2259 (1987)
- [7] G. van der Steenhoven *et al*, Nucl. Phys. **A484**, 445 (1988)
- [8] J.E. Ducret *et al*, Nucl. Phys. **A553** (1993) 697
- [9] R. Schiavilla, Phys. Rev. Lett. **65** (1990) 835
- [10] Frank J, Hertz G 1914 Verh. Deutschen Phys. Ges. **16** 457
- [11] Fregeau J, Hofstadter R 1955 Phys. Rev. **99** 1503
- [12] T.W. Donnelly Advances in Nuclear Physics, Vol.22, p.67

- [13] S. Boffi *et al.*, Nuclear Physics **A435** (1985) 697
- [14] T. de Forest, Nucl. Phys., **A392**, 232 (1983)
- [15] G.G. Simon *et al.*, Nuclear Physics **A333** (1980), 381
- [16] D. Mittwich, Diploma thesis, University of Mainz, unpublished, 1992
- [17] S. Schardt, PhD thesis, University of Mainz, unpublished, 1994
(available at <http://www1.kph.uni-mainz.de/A1/publications.html#doc>)
- [18] Boeglin W.U. Czechoslovak J. of Physics, Vol.45 (1995), No.4/5
- [19] K.I.Blomqvist *et al.*, Nucl. Instr. and Meth., **A403** (1998), 263-301
- [20] M.W. Kuss, Technische Universitaet Darmstadt, PhD thesis, unpublished, 1996
(available at <http://www1.kph.uni-mainz.de/A1/publications.html#doc>)
- [21] H.Merkel, Internal report, Institut fuer Kernphysik, Mainz University, 1997
- [22] K. W. Krygier, PhD thesis, University of Mainz, unpublished, 1996
(available at <http://www1.kph.uni-mainz.de/A1/publications.html#doc>)
- [23] R. Florizone, MIT, PhD thesis, unpublished, 1998
(available at <http://www1.kph.uni-mainz.de/A1/publications.html#doc>)
- [24] J. Kelly, MIT, PhD thesis, unpublished, 1981
- [25] C. R. Otterman *et al.*, NPA436 (1985) 688
- [26] J. Friedrich, University of Mainz, private communication
- [27] T. Pospischil, University of Mainz, private communication
- [28] M. Weis, University of Mainz, private communication
- [29] K. Merle, PhD thesis, University of Mainz, unpublished, 1976

- [30] M. Korn, PhD thesis, University of Mainz, unpublished, 1995
(available at <http://www1.kph.uni-mainz.de/A1/publications.html#doc>)
- [31] J. Templon, University of Georgia, private communication
- [32] J. Heisenberg and H.P. Block, *Ann. Rev. Nucl. Part. Sci.* **33** (1983) 569
- [33] W.H. Press *et al.*, *Numerical recipes in C*, Cambridge University Press
- [34] A. Rokavec, University of Ljubljana, PhD thesis, unpublished, 1994
- [35] J. Schwinger, *Phys. Rev.* **76**, 790 (1949)
- [36] J. Schwinger, *Phys. Rev.* **75**, 898 (1949)
- [37] S. Penner, *Nuclear Structure Physics*, Proceedings of the 18th Scottish University Summer School in Physics 1977
- [38] J. Friedrich, *Nucl. Instr. Meth.* **129** (1975) 505
- [39] L.W. Mo, Y.S. Tsai, *Reviews of Modern Physics*, Vol.41, N.1, January 1969
- [40] W.R. Leo *Techniques for Nuclear and Particle Physics Experiments*, p.40
(Springer-Verlag, Berlin, 1987)
- [41] J.A. Templon, *Radiative-Tail Simulations for Mainz Expt. A1/1-93* (1998), Internal report, University of Georgia
- [42] C. E. Vellidis, *AEEXB: A Program for Monte Carlo Simulations of coincidence electron-scattering experiments*, OOPS Collaboration Internal Report, MIT-Bates Accelerator Laboratory, 1998
- [43] J. A. Templon, C. E. Vellidis, R. E. J. Florizone, A. J. Sarty *Phys. Rev. C* **61**, 014607 (2000)
- [44] GEANT, CERN Program Library, Detector Description and Simulation Tool

- [45] R. Schiavilla *et al.*, Nucl. Phys. **A449** 219 (1986)
- [46] I. E. Lagaris and V. R. Pandharipande, Nucl. Phys. **A359** (1981) 331
- [47] R. B. Wiringa *et al.*, Phys. Rev. **C29** (1984) 1207
- [48] J.L. Forest *et al.*, Phys. Rev **C54**, 646 (1996)
- [49] <http://www.phy.anl.gov/theory/research/overlap/he4.tp>
- [50] R. B. Wiringa *et al.*, Phys. Rev. **C51** (1995) 38
- [51] B. S. Pudliner *et al.*, Phys. Rev. Lett. **74** (1995) 4396
- [52] J.F.J. van den Brand *et al.*, Nucl. Phys. **A534** (1991) 637
- [53] J.J. Kelly Advances in Nuclear Phys., vol.23, p.75
- [54] W. Leidemann, Trento University, private communication
- [55] V. D. Efros, W. Leidemann, G. Orlandini, Phys. Rev. **C58** (1998) 582